

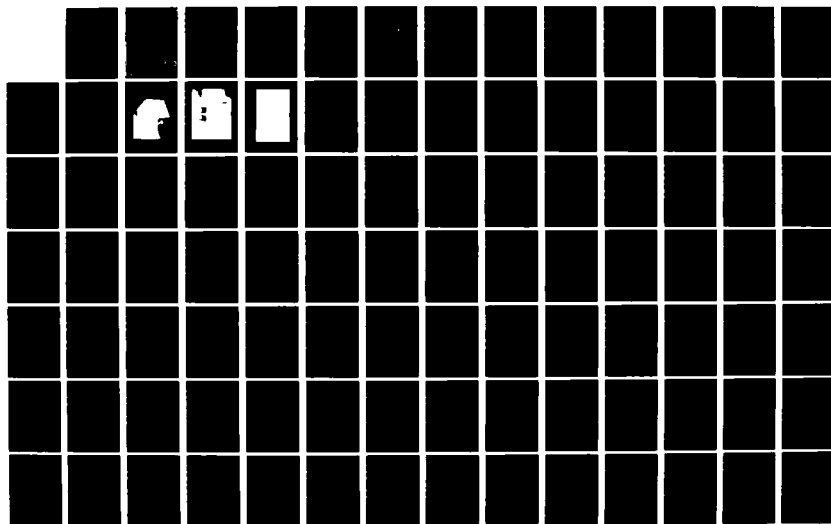
AD-A121 994

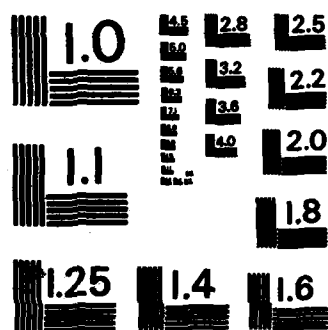
STUDY AND ANALYZE ENERGETIC PARTICLE AND MAGNETIC
ACTIVITY DATA(U) EMMANUEL COLL BOSTON MASS PHYSICS
RESEARCH DIV L GENTILE ET AL. JUN 82 AFGL-TR-82-0217
F19628-79-C-0102 F/G 3/2

1/4

UNCLASSIFIED

NL





MICROCOPY RESOLUTION TEST CHART
NATIONAL BUREAU OF STANDARDS-1963-A

AFGL-TA- 82-0217

STUDY AND ANALYZE ENERGETIC PARTICLE AND MAGNETIC ACTIVITY DATA

L. Gentile
E.G. Holeman
A. Huber
J. Pantazis
D.R. Parsignault
Y.V. Rao
M.P. Hagan

The Trustees of Emmanuel College
400 The Fenway
Boston, Massachusetts 02115

Final Report
01 April 1979 - 31 March 1982

June 1982

Approved for public release; distribution unlimited

AIR FORCE GEOPHYSICS LABORATORY
AIR FORCE SYSTEMS COMMAND
UNITED STATES AIR FORCE
HANSCOM AFB, MASSACHUSETTS 01731

DTIC
ELECTE
NOV 30 1982
S D
E

AD A121994

DTIC FILE COPY

2 11 30 084

**Qualified requestors may obtain additional copies from the
Defense Technical Information Center. All others should
apply to the National Technical Information Service.**

Unclassified

MIL-STD-847A
31 January 1973

SECURITY CLASSIFICATION OF THIS PAGE (When Data Entered)

REPORT DOCUMENTATION PAGE		READ INSTRUCTIONS BEFORE COMPLETING FORM
1. REPORT NUMBER AFGL-TR-82-0217	2. GOVT ACCESSION NO. AD-A121994	3. RECIPIENT'S CATALOG NUMBER
4. TITLE (and Subtitle) Study and Analyze Energetic Particle and Magnetic Activity Data		5. TYPE OF REPORT & PERIOD COVERED Final 01 Apr 79 - 31 Mar 82
		6. PERFORMING ORG. REPORT NUMBER
7. AUTHOR(s) L. Gentile J. Pantazis M.P. Hagan E.G. Holeman D.R. Parsignault A. Huber Y.V. Rao		8. CONTRACT OR GRANT NUMBER(s) F19628-79-C-0102
9. PERFORMING ORGANIZATION NAME AND ADDRESS Emmanuel College Physics Research Division 400 The Fenway, Boston, MA 02115		10. PROGRAM ELEMENT, PROJECT, TASK AREA & WORK UNIT NUMBERS 61102F 2311G1AK
11. CONTROLLING OFFICE NAME AND ADDRESS Air Force Geophysics Laboratory Hanscom AFB MA 01731 Contract Manager: Irving Michael/PHG		12. REPORT DATE June 1982
14. MONITORING AGENCY NAME & ADDRESS (if different from Controlling Office)		13. NUMBER OF PAGES 336
		15. SECURITY CLASS. (of this report) Unclassified
		15a. DECLASSIFICATION DOWNGRADING SCHEDULE
16. DISTRIBUTION STATEMENT (of this Report) Approved for public release; distribution unlimited		
17. DISTRIBUTION STATEMENT (of the abstract entered in Block 20, if different from Report)		
18. SUPPLEMENTARY NOTES		
19. KEY WORDS (Continue on reverse side if necessary and identify by block number) See other side.		
20. ABSTRACT (Continue on reverse side if necessary and identify by block number) See Page 1 for Summary		

DD FORM 1 JAN 73 1473 EDITION OF 1 NOV 65 IS OBSOLETE

Unclassified

SECURITY CLASSIFICATION OF THIS PAGE (When Data Entered)

Unclassified

SECURITY CLASSIFICATION OF THIS PAGE (When Data Entered)

19. Key Words

active shielding
auroral x-ray contaminator
background radiation
Bevelac
bulk etching rate
CIRRIS
collimator
cosmic ray trajectory
detectors
discharge system
DMSP satellite
electron spectrometer
electronic logic
high energy range head assembly
ion spectrometer
LDEF (Long Duration Exposure Facility)
LEPS (Low Energy Proton Spectrometer)
lost count problem
low energy range head assembly
magnetic assembly
Meteosat-F2 satellite
passive shielding
polar cap protons
Protel
proton fluxes
range-energy parameters
S3-2 satellite
S3-3 satellite
Sky Anchor XIII
SSJ3 electrostatic analyzer
SSJ4 electrostatic analyzer

Unclassified

SECURITY CLASSIFICATION OF THIS PAGE (When Data Entered)

TABLE OF CONTENTS

LIST OF FIGURES

LIST OF TABLES

I. SSJ4 ELECTRON AND ION SPECTROMETER FOR DMSP

1.0 Introduction

2.0 Instrument Description

2.1 Analyzers

2.2 Detectors

2.3 Electronics

2.3.1 Preamp discriminators

2.3.2 Log counters

2.3.3 Control and data logic

2.3.4 Power converter and sun sensor

2.3.5 Plate voltage regulator

2.3.6 Background measurement

2.4 Testing

2.5 Calibration

II. PROTEL

1.0 Physical Principles

2.0 Description of the Instrument

2.1 The High-Energy-Range Head Assembly

2.1.1 Collimator

2.1.2 Magnetic assembly

2.1.3 Detector system

2.1.4 Passive shielding

2.1.5 Active shielding

2.1.6 Description of the electronic logic

2.2 The Low-Energy-Range Head Assembly

2.2.1 Collimator

2.2.2 Magnetic assembly

2.2.3 Detector system

2.2.4 Passive shielding

2.2.5 Active shielding

2.2.6 Description of the electronic logic

Accession For	
NTIS GRA&I	<input checked="" type="checkbox"/>
DTIC TAB	<input checked="" type="checkbox"/>
Unannounced	<input type="checkbox"/>
Justification	
By	
Distribution/	
Availability Codes	
Dist	Avail and/or Special
<input checked="" type="checkbox"/>	

Page

vi

x

2

2

12

13

13

13

18

18

18

21

22

23

26

29

29

31

31

38

41

42

46

46

46

48

51

51

	<u>Page</u>
3.0 Discrimination against Background Radiation	
3.1 Theoretical Consideration	54
3.2 Background Estimates for the High-Energy-Range Head Assembly	61
3.3 Background Estimates for the Low-Energy-Range Head Assembly	69
4.0 Calibration	73
III. SOLID STATE NUCLEAR TRACK DETECTORS	
1.0 Experiments at Brookhaven National Laboratory	76
2.0 Experiments at NASA-Lewis Research Center	79
3.0 Long Duration Exposure Facility (LDEF)	82
4.0 Cosmic Ray Exposure I	84
5.0 Passive Energetic Particle Detector Experiment with CIRRIIS on an early Space Shuttle System	86
6.0 Cosmic Ray Exposure II (SKY ANCHOR XIII)	88
7.0 Heavy Ion Experiments at BEVALAC (Lawrence Berkeley Laboratory)	89
8.0 Measurement of bulk etching rate	90
9.0 Range-Energy parameters	93
10.0 Technical Developments	94
IV. THE PLASMA EXPERIMENT ON BOARD METEOSAT-F2	
1.0 Introduction	120
2.0 The Spacecraft	120
3.0 The electrostatic analyzer (SSJ3)	
3.1 Physical principle	121
3.2 Physical description	122
3.3 The detectors	125
4.0 The Electronics	
4.1 The preamplifiers	126
4.2 The logarithmic counters	126
4.3 The control logic and data output	129
4.4 The power supply	131
4.5 The high voltage stepping circuit	131

	<u>Page</u>
5.0 The Data	
5.1 Presentation of the data	132
6.0 First Results from Meteosat-2 discharge experiments - ESA Bulletin, February 1982.	138
 V. DATA ANALYSIS AND INTERPRETATION	
1.0 Polar Cap Protons - Auroral X-Ray Contamination of the Low-energy Spectrometer on the S3-2 satellite in the Polar Regions	145
2.0 LEPS - Investigation of the Lost Count Problem of the Instrument	147
3.0 S3-2, S3-3, and LEPS - Proton Fluxes (0.08 - 100 MeV) as measured by the Air Force Satellites S3-2 and S3-3 in 1976	148
4.0 DMSP - Electron Precipitation over the Polar Caps	158
 VI. COSMIC RAY TRAJECTORY STUDIES	171
 APPENDIX 1	180
APPENDIX 2	213
PUBLICATIONS	230

LIST OF FIGURES

<u>Figure</u>		<u>Page</u>
I-1	SSJ4 instrument fully assembled	3
I-2	SSJ4 instrument with cover off	4
I-3	SSJ4 electron analyzer assembly	5
I-4	SSJ4 small plates geometry	8
I-5	SSJ4 large plates geometry	9
I-6	Electron analyzer circuit	10
I-7	Ion analyzer circuit	11
I-8	SSJ4 block diagram	14
I-9	9-bit log accumulator	19
I-10	SSJ4 logic	20
I-11	Electron beam energy integration	24
I-12	PHI response	25
II-1.	Energy loss, ΔE (MeV), versus incident proton kinetic energy, E (MeV), for 50 μm , 100 μm , 200 μm and 300 μm thick silicon lithium-drifted detectors	28
II-2.	Schematic of the high energy range (6-10 MeV) head assembly	30
II-3.	Schematic of the sweeping magnet for the high energy range head assembly	32
II-4.	Magnetic field strength (gausses) along the 3 principal axis of the sweeping magnet for the high energy range head assembly	33
II-5.	Energy loss (MeV) versus incoming proton energy (MeV) in the 5 detector configuration of the high energy range head assembly	35
II-6.	Comparison of AEI-7 model spectra with various data set at $L=4$. The III model curve is mainly based on the OVI-19 observations from Vampola (Vette et al., 1978)	39

		<u>Page</u>
II-7.	Energy spectrum of the transmitted bremsstrahlung resulting from the interaction of an electron spectrum of the type HI model (Figure II-6)	40
II-8.	Electronic block diagram for the high energy range spectrometer	43
II-9.	Schematic of the low energy range (1-9 MeV) head assembly	47
II-10.	Energy loss (MeV) versus incoming proton energy (MeV) in the 5 detector configuration of the low energy range head assembly	49
II-11.	Electronic block diagram of the low energy range spectrometer	52
II-12.	Proton omnidirectional flux versus energy for different B/B_0 , at $L=1.50$ (Sawyer and Vette, 1976)	62
III-1.	The diameter distribution of etch pits of protons	95
III-2.	Etch pit diameter (D) as a function of proton energy (E). The parameter on each curve represents etch time.	96
III-3.	Etch pit diameter (D) as a function of bulk material removed from one surface (Vgt)	97
III-4.	Systematic representation of irradiation arrangement	98
III-5.	Normalized track etching rate as a function of residual range for protons, ^3He and ^4He	99
III-6.	Photomicrograph of the mouths of etched tracks of 6-MeV protons	100
III-7.	Photomicrograph of the mouths of etched tracks of 1.5 Mev protons, 70-MeV, ^3He ions and 52-MeV ^4He ions	101
III-8.	A view of long duration exposure facility in orbit	102
III-9	The 12-inch square by 5-inch LDEF box showing the support panel which mounts on the LDEF tray. This occupies 1/6 of a side tray or 1/4 of an end tray	103

	<u>Page</u>
III-10.	The time variation of 55 MeV trapped proton fluxes 104
III-11.	Payload for a balloon flight. The balloon was launched from Eielson AFB, Alaska on 19 June 1979. 105
III-12.	Launching of a balloon from Eielson AFB, Alaska. 106
III-13.	Stopping cosmic ray heavy primary particle in CR-39 107
III-14.	Relativistic cosmic ray heavy primary in CR-39 108
III-15(a).	Track etching rate as a function of residual-range (Events 1 to 25) 109
III-15(b).	Track etching rate as a function of residual-range (Events 26 to 50) 110
III-15(c).	Track etching rate as a function of residual-range (Events 51 to 77) 111
III-16.	Aluminum container for CR-39 detector, CIRRIIS experiment 112
III-17.	Time-altitude history of SKY ANCHOR flight 113
III-18.	Etch rate as a function of residual-range for stopping 210 MeV/N ⁴⁸ Ca ions 114
III-19.	Bulk etching rate as a function of temperature 115
III-20.	Track diameter as a function of etch time (fission fragments) 116
III-21.	Photomicrograph of the mouths of etched tracks of fission fragments and alpha particles from a ²⁵² Cf source 117
III-22.	Bulk etch rate as a function of 1/T (10 ³ K) (Arrhenius plot) 118
III-23.	A precision etching system 119
IV-1.	SSJ3 - small plates geometry/ large plates geometry 123
IV-2.	Complete SSJ3 plate assembly 124
IV-3.	SSJ3 block diagram 127
IV-4.	SSJ3 with analog and digital cards exposed 128

	<u>Page</u>
IV-5. Plate voltage sequence and timing diagram	130
IV-6. Meteosat F2 spacecraft charging monitors - summary for September 1981	134
IV-7. Meteosat F2 spacecraft charging monitors - daily summary for 01 September 1981	135
V-1. Low energy proton data in table form	152
V-2. Typical energy spectra obtained with LEPS on S3-2	153
V-3. Typical energy spectra obtained with P-alpha on S3-2	154
V-4. Typical energy spectra obtained with LEPS on S3-3	155
V-5. Mirroring proton fluxes as measured by satellites 1963-38C, DIAL, 72-1, S3-2, and S3-3 from January 1964 until August 1976	157
V-6. Uniform electron precipitation across the polar cap region	160
V-7. Electron precipitation showing intensity gradient	161
V-8. Electron precipitation with convex distribution	162
V-9. Electron precipitation pattern with large and numerous spikes over a flat continuum	163
V-10. Electron precipitation pattern with large and numerous spikes over a concave continuum	164
V-11. A large PCA event	165
V-12. Typical PCA spectra - day 44	166
V-13. Typical PCA spectra - day 46	167
V-14. Typical PCA spectra - day 47	168
V-15. Electrostatic acceleration of the electron precipitation along geomagnetic field lines - a sampling	169
V-16. Electrostatic acceleration of the electron precipitation along geomagnetic field lines - another sampling	170
VI-1. Frames of reference used in the study on the effects of asymmetric magnetospheric currents on cosmic radiation	176
VI-2. Penumbral structure and cutoff rigidities P_M (main cutoff), P_C (effective cutoff), and P_S (Stormer cutoff) for cosmic ray particles incident from the vertical direction	177

		<u>Page</u>
VI-3.	Illustration of the definition of the asymptotic direction of approach (according to Shea and Smart, 1975)	178
VI-4.	Side and top views of the trajectory within geocentric distances $r \leq 5R_E$ described by a cosmic ray particle with rigidity $P = 4.42$ GV	179

LIST OF TABLES

<u>Table</u>		<u>Page</u>
I-1:	Electrostatic Analyzer (ESA) - SSJ4 Summary of Characteristics	15
II-1.	Channel Boundaries with the Corresponding Energy Loss in each of the Detectors, for the High Energy Range PHA	36
II-2.	Silicon Detector Capacitances of the Detectors to be used in this Spectrometer	37
II-3.	Coincidence Scheme for the High Energy Range	44
II-4.	Channel Boundaries with the Corresponding Energy Loss in each of the Detectors, for the Low Energy Range PHA	50
II-5.	Coincidence Scheme for the Low Energy Range	53
III-1.	Detection Thresholds for Various Track Detectors	81
III-2.	Stack Configuration for CIRRIIS Experiment (CRL258)	87
IV-1.	Mean Energy and Geometrical Factor for Each of 16 Channels	133

SUMMARY

↓

In the areas of communication and surveillance, where there may exist an inability to predict solar particle effects on atmospheric and ionospheric environmental conditions, our research effort has been directed toward the design, development, and construction of energetic particle detection instrumentation for satellite flight. Our instruments measure energetic particle fluxes, discriminate species (electrons, protons, and/or ions), and perform energy analyses; are capable of discovering new scientific knowledge concerning the near-earth space energetic particle environment, and are compatible with Air Force satellite rides. The effort has covered the entire spectrum from design thru construction and integration into the host satellite vehicle.

All instrumentation was adapted to current research needs. New devices such as position-sensitive detectors, microprocessors, and magnetic materials were integrated into current designs to obtain maximum spatial, angular and energy resolution consistent with reliability and delivery schedules. Reports on all aspects of the instrumentation and data formats were prepared for utilization and interpretation in analyses which were performed on the final data.

↑

I. SSJ4 ELECTRON AND ION SPECTROMETER FOR DMSP

1.0 INTRODUCTION

The SSJ4 is a dual electrostatic analyzer which measures both precipitating electron and ion fluxes and replaces its predecessor, the SSJ3, on the DMSP Satellites. Three units have been completed for the F-6, F-7, and F-8 spacecraft.

In the SSJ4, differential energy analysis is performed by two pair of electrostatic analyzers (ESA) in which a time-sequenced variable electrostatic field deflects particles of selected energies toward exit apertures where they are counted by Channeltron Electron Multipliers (CEM). The small ESA's cover energies ranging from 30eV to 1 keV; the larger ones from 1 keV to 30 keV. The accumulation time at each energy level is 95 ms, with both sets of analyzers operating simultaneously. Two complete 20 point spectra are produced each second (one electron and one ion) and the 40 data words are transferred to the satellite on command. Figure I-1 shows the SSJ4 fully assembled; Figure I-2 with the cover off. Figure I-3 shows the electron analyzer assembly.

2.0 INSTRUMENT DESCRIPTION

In this section, five aspects of the instrument are discussed.

2.1 ANALYZERS

The SSJ4 employs four separate electrostatic analyzers of the curved (cylindrical) plate variety. This type analyzer uses a variable potential



Figure I-1

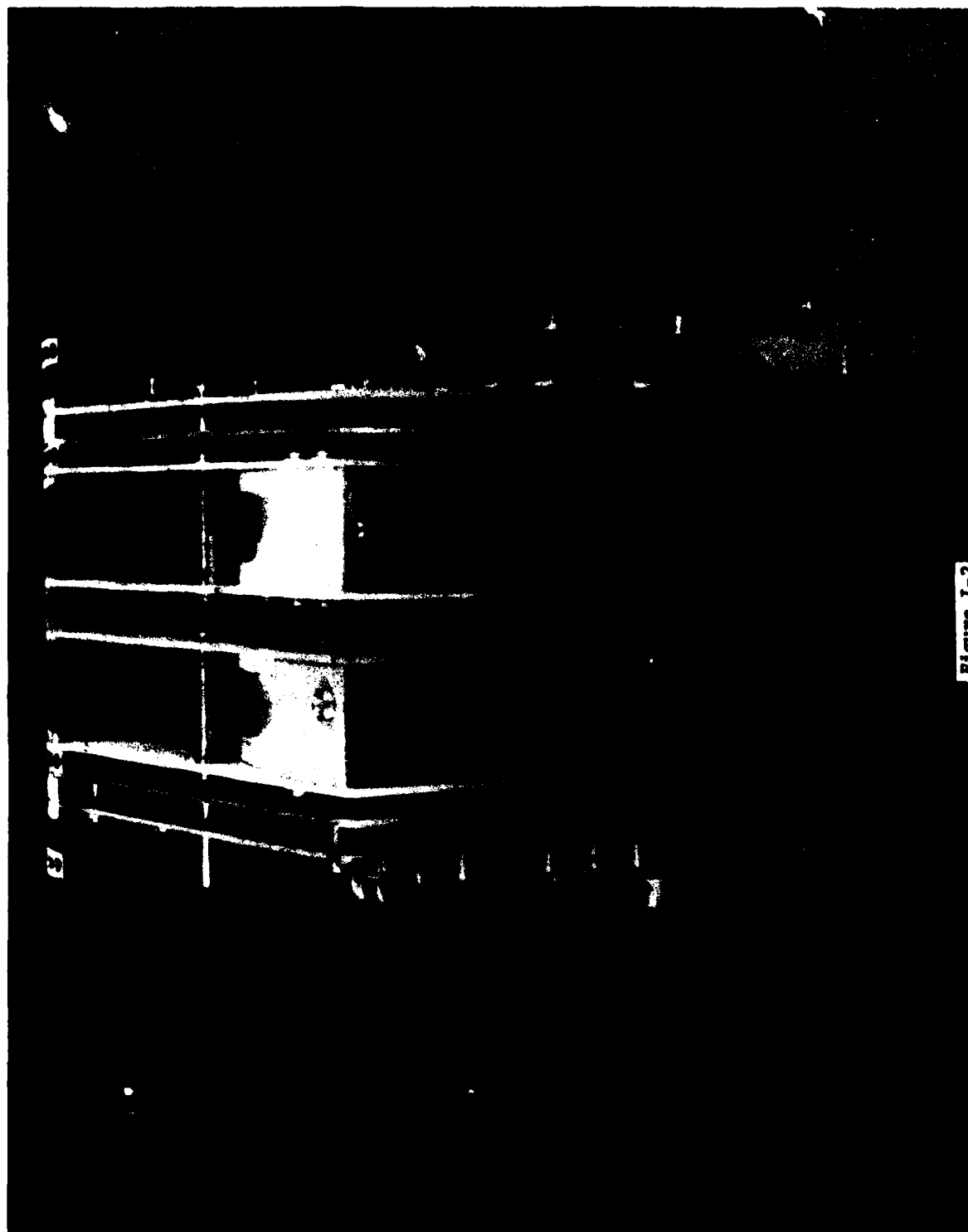


Figure I-2

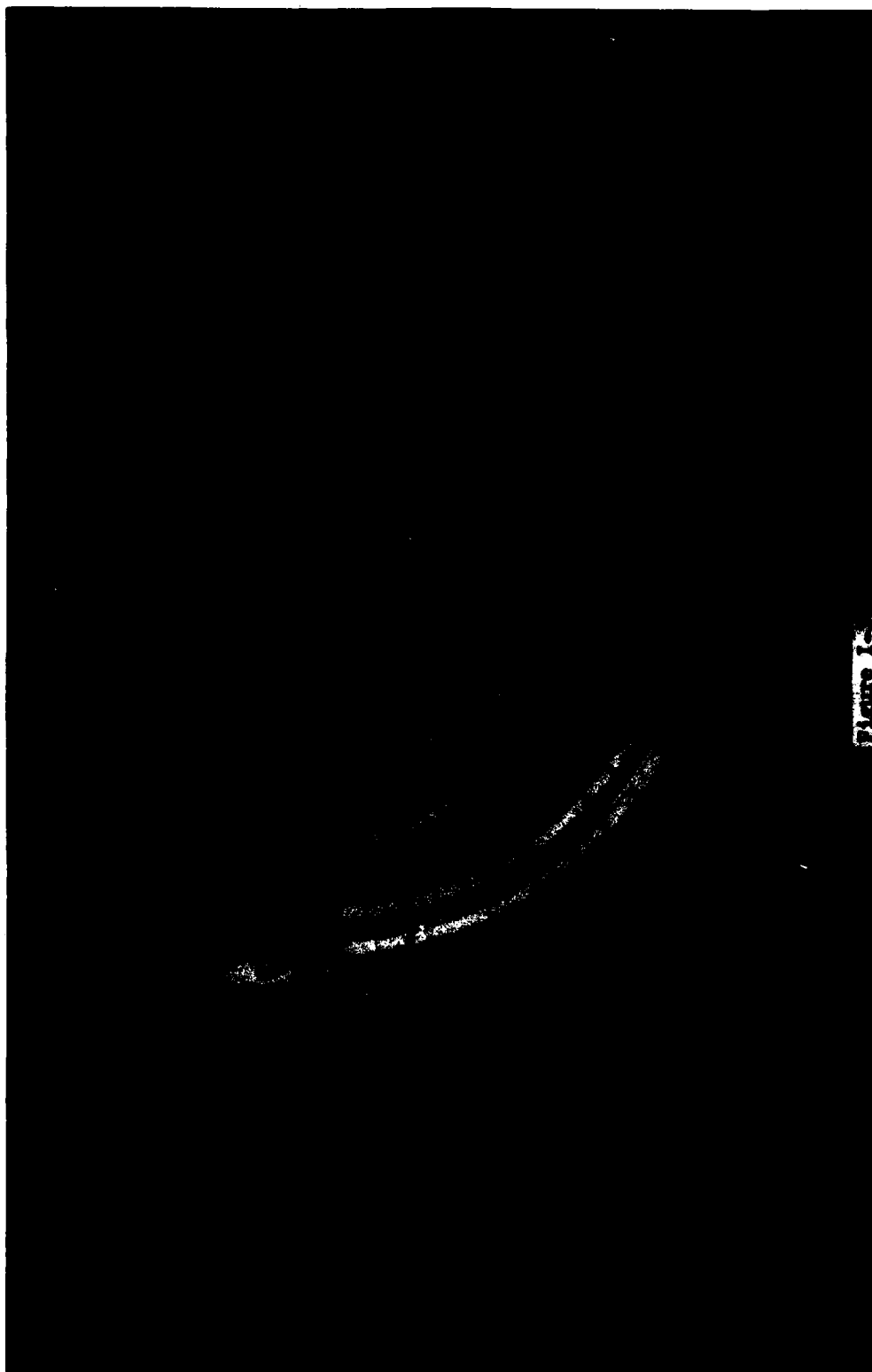


Figure 1.3

difference between two curved plates to effect energy analysis. The collimators and entrance and exit apertures are arranged such that to be counted charged particles must follow a very nearly circular trajectory through the radial electric field between the plates. The center energy in electron volts of singly-charged, non-relativistic particles in such trajectories is given by:

$$E = \frac{RV}{2d}$$

where: V = plate to plate potential in volts

R = mean radius of curvature of plates

d = plate separation ($R_1 - R_2$)

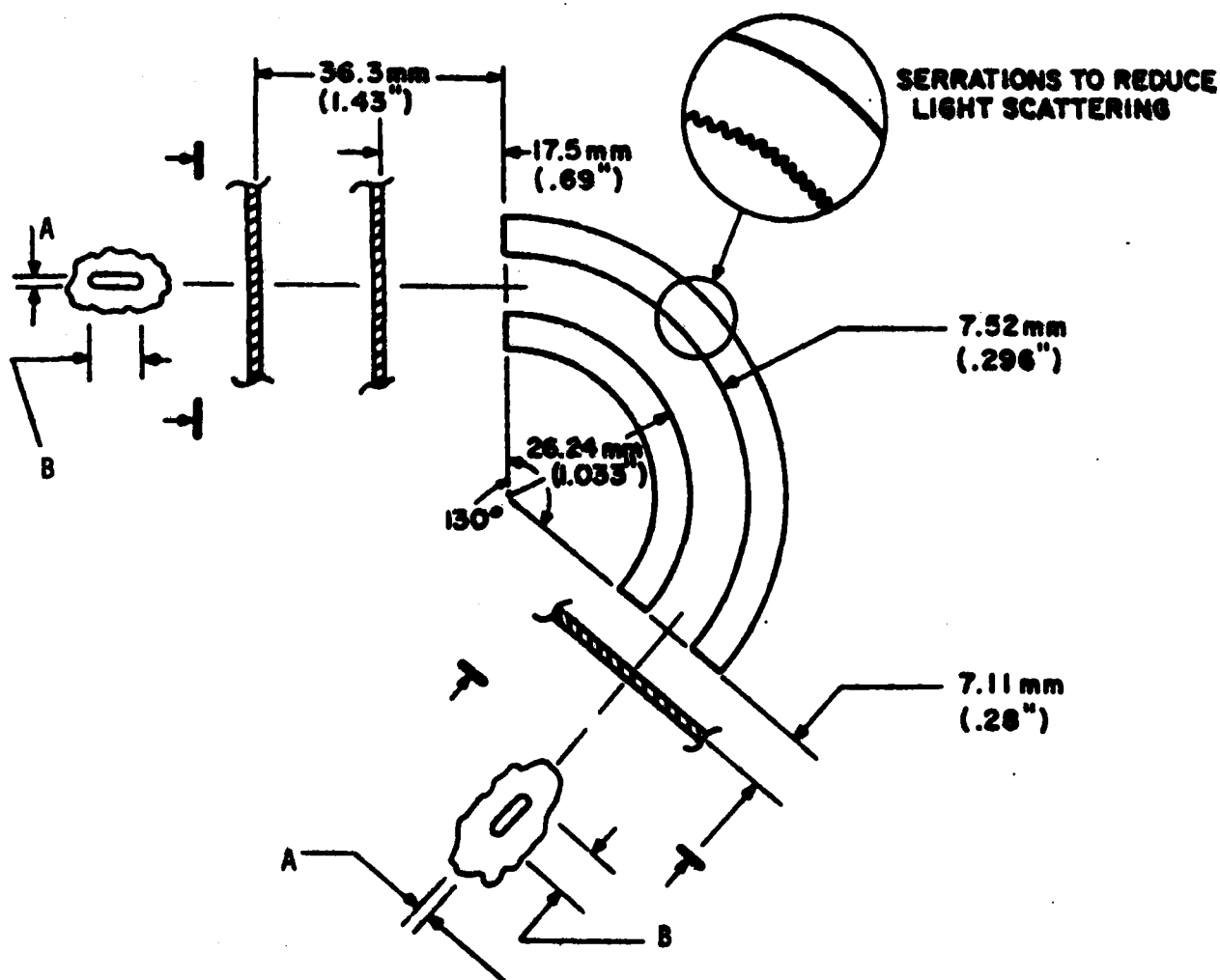
Thus, the energy of particles passing through the exit aperture is directly proportional to the difference in potential between the plates. The constant of proportionality, known as the "analyzer constant" is equal to $\frac{R}{2d}$. The analyzer constants for this instrument are 20 eV/V and 2 eV/V for the high and low energy analyzers respectively. The high energy plates are operated between ± 25 and ± 750 V, covering the energy range from 950 eV to 30 keV. The low energy plates are operated at 1/3 the high energy voltages and cover the range 30 eV to 950 eV.

The balanced \pm configuration creates a zero potential surface midway between the plates. Since this surface passes through the narrow apertures, particles undergo negligible acceleration upon entering and leaving the analyzers.

The plates are aluminum with a sandblasted finish to minimize the amount of solar extreme ultraviolet reaching the Channeltrons, which are sensitive to radiation in this part of the spectrum. Reflections from the small plates are further reduced by closely spaced serrations. The presence of dielectric materials between the plates or in the vicinity of their edges was avoided to prevent charge buildup which could affect the particle trajectories. The low energy geometry is shown in Figure I-4, along with dimensions and a list of the ten energy steps for the small ESA's. Figure I-5 is the large ESA geometry and energy levels.

For both the electron and ion analyzers the front collimators employ four levels of apertures to reject off-axis particles and solar XUV. At the other end of the plates is an exit aperture with a single wire grid which, like the entrance aperture, is normally at ground potential to maintain the symmetry of the electric field. Following this aperture, are a grid and the detector, which are biased differently for the electron and ion analyzers. For electrons, the grid is maintained at -5V to help reject low energy secondary electrons; the front of the channeltron is biased at +95V to provide post-acceleration in order to minimize the effect of the decrease in channeltron efficiency below about 100 eV (Figure I-6). For ions, more post-acceleration is needed, since channeltron efficiency drops off significantly below 1 keV. Thus, the grid and channeltron are both biased at -1 kV (Figure I-7). (The anode of the channeltron is operated at +2 kV to maintain the correct operating voltage.)

SSJ/4 SMALL PLATES GEOMETRY

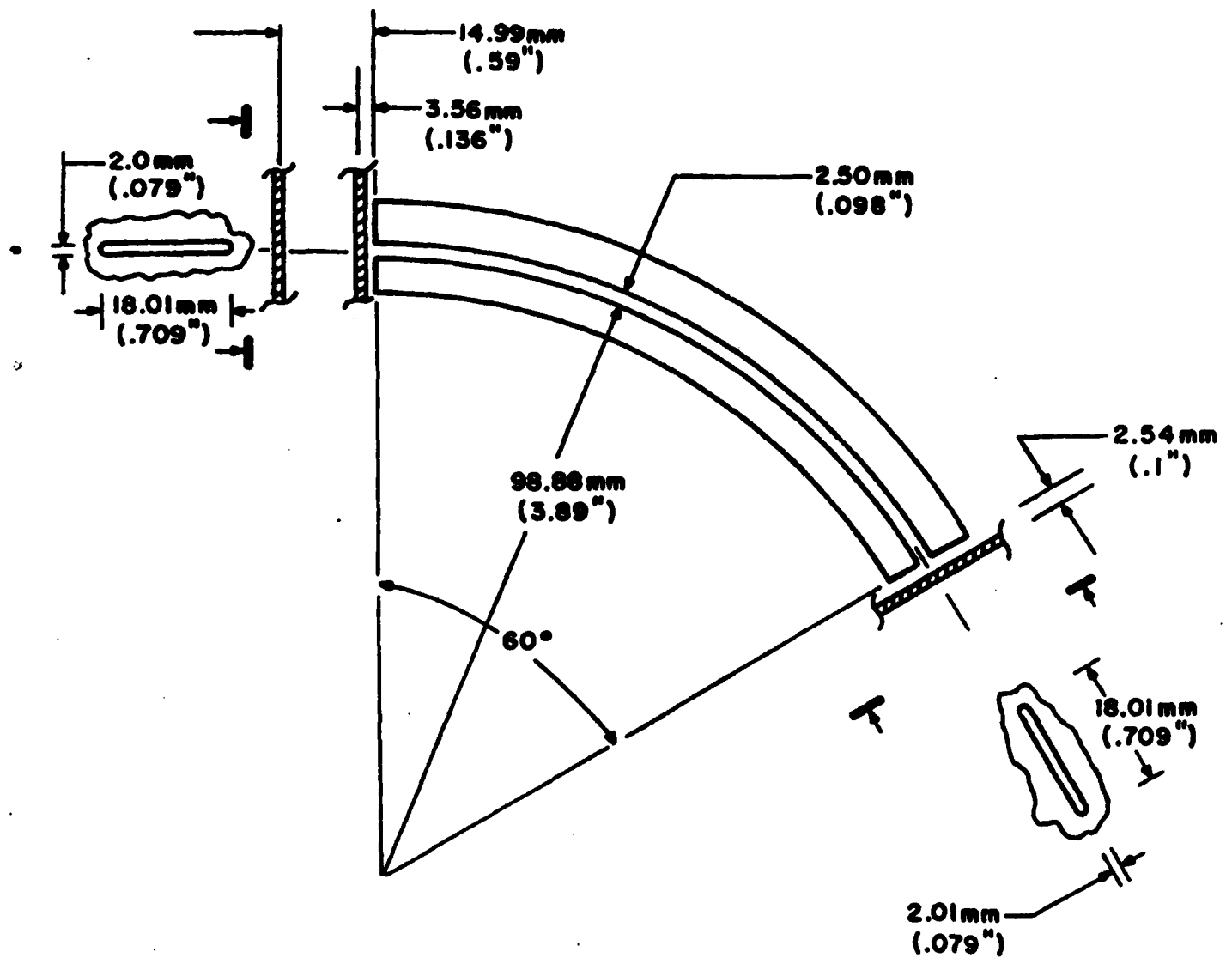


	<u>A</u>	<u>B</u>
Electrons	2.0 mm (.078")	6.00 mm (.238")
Protons	5.08 mm (.20")	16.51 mm (.650")

ENERGIES:	
1.	948 eV
2.	646
3.	440
4.	300
5.	204.4
6.	139.2
7.	94.9
8.	64.6
9.	44.0
10.	30.0

Figure I-4

SSJ/4 LARGE PLATES GEOMETRY



ENERGIES:	
1.	30.00 keV
2.	20.44
3.	13.92
4.	9.48
5.	6.46
6.	4.40
7.	3.00
8.	2.04
9.	1.39
10.	0.948

Figure I-5

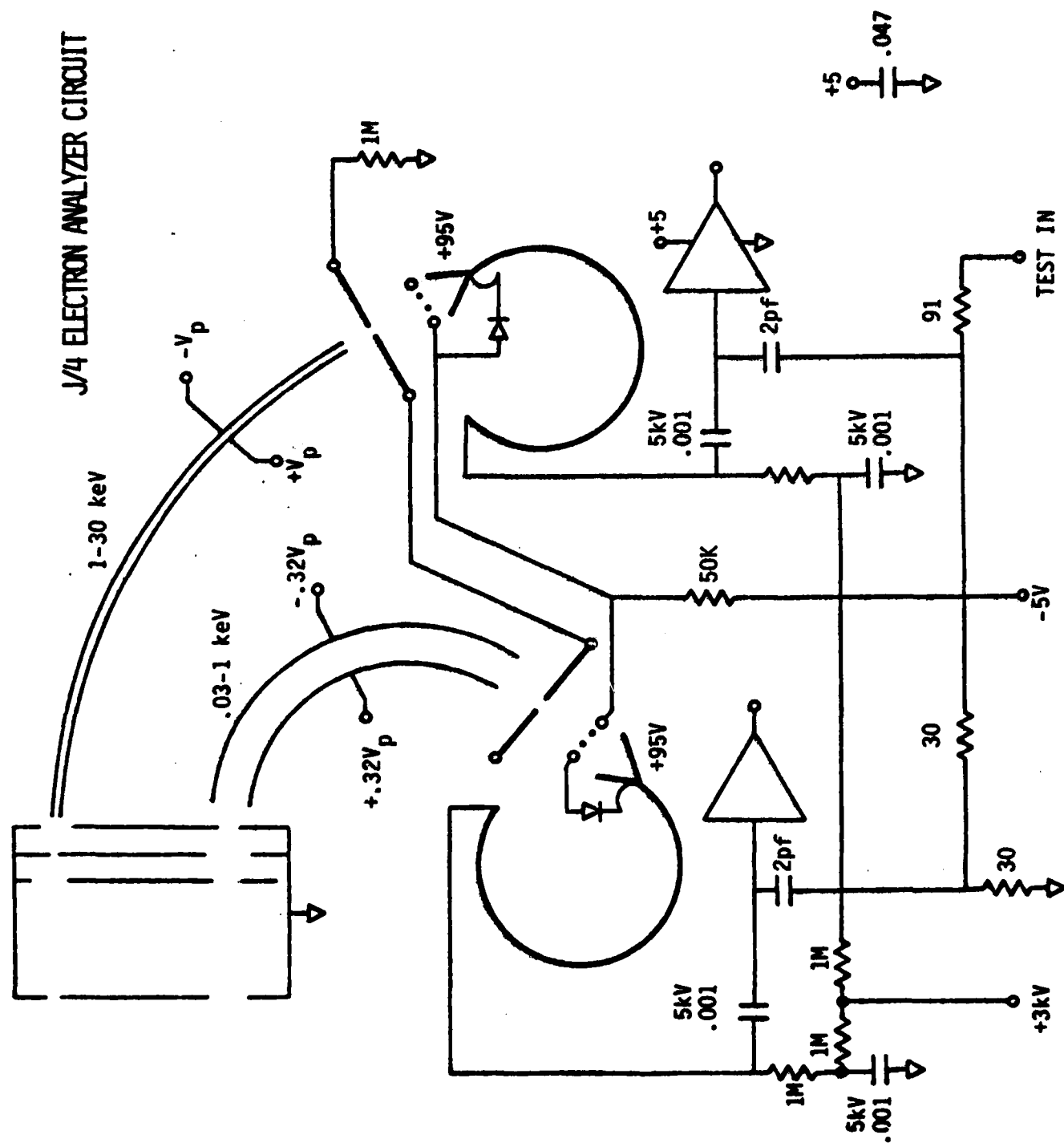


Figure 1-6

J/4 ION ANALYZER CIRCUIT

The schematic diagram illustrates the J/4 Ion Analyzer Circuit, which includes two input channels for 1-30 keV and .03-1 keV. The circuit features a central processing unit with two output channels, IH OUT and IL OUT, and a TEST IN (FROM C BOARD) output. The circuit is powered by a +5V supply and a -1kV supply. The output is labeled TEST IN (FROM C BOARD).

(FROM C BOARD)

2.2 DETECTORS

The detector assembly for each of the four ESA's consists of two channel electron multipliers, or Channeltrons, manufactured by Galileo Electro-Optics of Sturbridge, Mass. Specifically, the large ESA for both the electrons and ions and the small ion ESA use two CEM 4019 (10mm funnels). The small electron ESA uses two CEM 4013 (3mm funnels). These are high gain devices, producing an output charge pulse of $10^7 - 10^8$ electrons about 20 ns in width. The two detectors for each ESA are connected in parallel with a potential difference of 3 kV between their funnels and their anodes.

The Channeltrons used in this instrument have undergone special screening by the manufacturer to minimize the possibility of early failure. These units are expected to have a lifetime exceeding 10^{11} counts which greatly exceeds the predicted total count range for this instrument.

In order to eliminate solar XUV as a limiting factor on the Channeltron lifetime, a solar sensor has been included in the instrument to disable the power supply, and thus Channeltron bias, whenever the sun approaches the fields-of-view of the analyzers.

The instrument is tested and burned-in with Channeltrons in place. For this purpose a clean sorption and ion-pumped vacuum system is used, eliminating the potential problem of gain degradation resulting from exposure to oil vapors found in conventional systems.

The Channeltrons are shock-mounted with Viton spacers inside a hard anodized cylindrical aluminum mount. Care was taken to avoid potentially contaminating materials in the instrument which might cause long-term gain degradation.

2.3 ELECTRONICS

The SSJ4 incorporates a highly refined electronic design which is extremely power and space efficient and of well proven reliability. Figure I-8 is a block diagram. The channeltron outputs are coupled to preamplifier-discriminators which produce C-MOS compatible shaped pulses. These pulses are counted by log accumulators. Timing and control logic steps the energy levels (plate voltages), resets and enables the log accumulators, and loads the data words into serial shift registers. Upon receipt of the shift clock from the spacecraft once per second, the data words are serially shifted out on a single data line. Brief descriptions of the functional clocks follow.

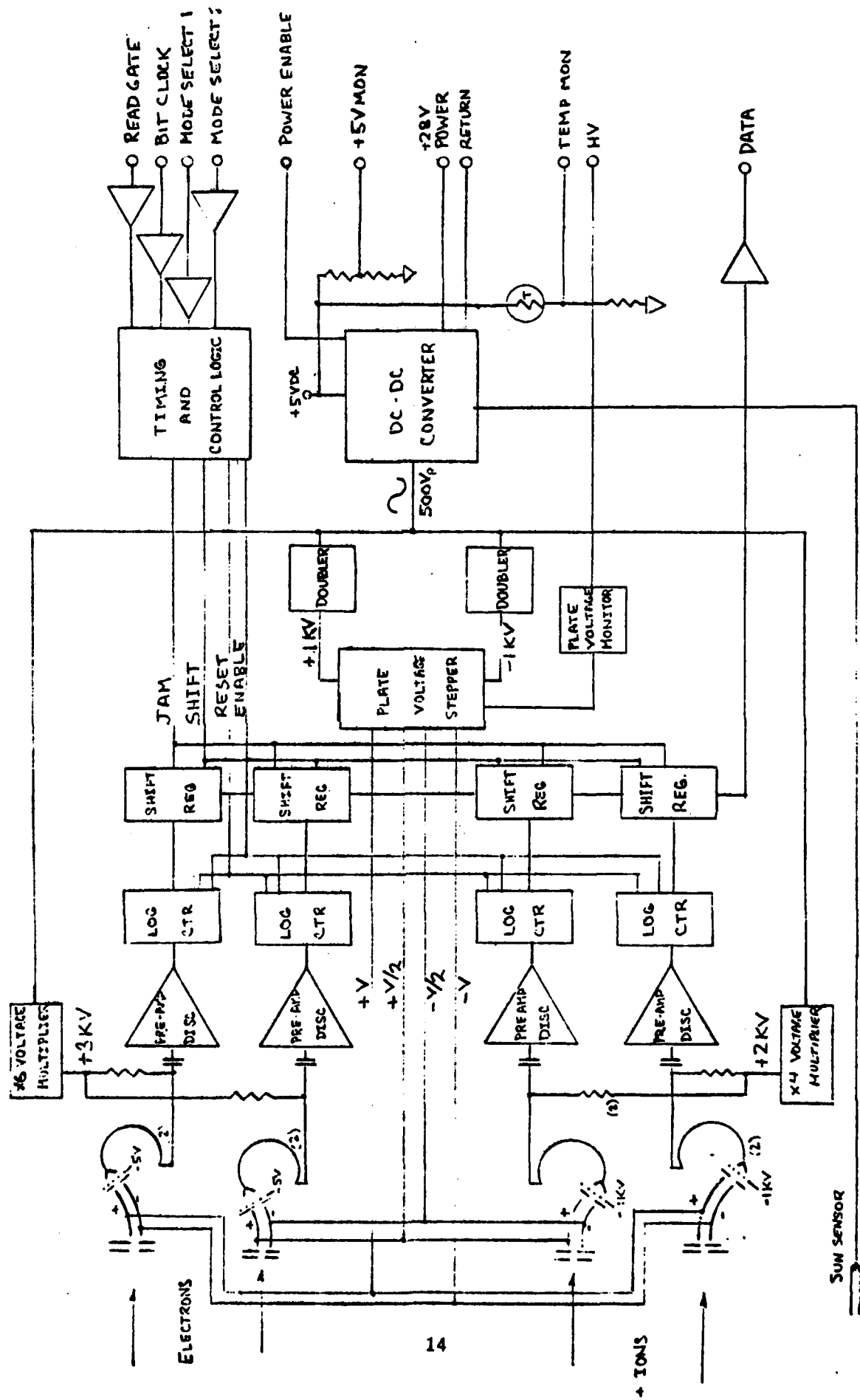
2.3.1 Preamp-Discriminators

These units are charge sensitive and discriminate against pulses below about .5 picocoulomb, an order of magnitude below the lowest expected mean detector output.

An externally accessible test input allows the operation and threshold of these units to be verified during testing.

2.3.2 Log Counters

The log counters produce a 9 bit logarithmic representation of the data count. The five least significant bits comprise the mantissa and the remaining four bits comprise the exponent. The conversion from this representation to actual count is demonstrated in Table I-1. For the SSJ4 instrument, the log accumulator circuit used in SSJ3's was re-designed as a custom hybrid, using high reliability, radiation hardened C-MOS chips. Use of this hybrid enables a high density logic design



SSJ/4 BLOCK DIAGRAM

Figure 1-8

TABLE I-1

**ELECTROSTATIC ANALYZER (ESA)
SSJ4**

Summary of Characteristics

Particles Detected	Electrons, Ions			
Detectors Used	2 Channeltron Electron Multipliers for each of the four sets of ESA plates			
Method of Energy Analysis	Voltage Stepping on ESA plates			
Number of Energy Levels	10 for each set of ESA plates; 20 each for electrons and ions			
Energy Levels	<u>Level #</u>	<u>keV</u>	<u>Level #</u>	<u>eV</u>
	1	30.00	11	948
	2	20.44	12	646
	3	13.92	13	440
	4	9.48	14	300
	5	6.46	15	204.4
	6	4.40	16	139.2
	7	3.00	17	94.9
	8	2.04	18	64.6
	9	1.39	19	44.0
	10	.948	20	30.0
Acceptance Angles - Electrons	Large ESA: 1.6° FWHM across the apertures 8.0° FWHM along the apertures Small ESA: 3.7° FWHM across the apertures 4.8° FWHM along the apertures			
Acceptance Angles - Ions (pending calibration)	Large ESA: 1.6° FWHM across the apertures 8.0° FWHM along the apertures Small ESA: 9.2° FWHM across the apertures 12.0° FWHM along the apertures			
Normalization Constants - Electrons	Large ESA: $1.3 \times 10^{-4} \text{ cm}^2\text{-ster.}$ Small ESA: $4.3 \times 10^{-5} \text{ cm}^2\text{-ster.}$			
Normalization Constants - Ions (pending calibration)	Large ESA: $1.3 \times 10^{-4} \text{ cm}^2\text{-ster.}$ Small ESA: $8.6 \times 10^{-4} \text{ cm}^2\text{-ster.}$			

TABLE I-1 (cont.)

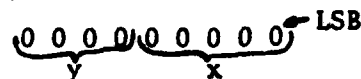
ESA SSJ4 (cont.)

$\Delta E/E$ - Electrons	Large ESA: 4.0% Small ESA: 7.2%
$\Delta E/E$ - Ions (pending calibration)	Large ESA: 4.0% Small ESA: 18.0%
Data Rate	One complete spectrum per second
Accumulation Time at each Energy Level	95 ms.
Digital Data Format	(9 bits per channel) x (40 channels) = 360 Bits

Note: Each 9 bits in every channel are in logarithmic form, the five least significant bits being the mantissa and the remaining four the exponent. This number is converted to decimal form according to the following relationship:

$$\text{Count} = 2^y(x + 32) - 33$$

where



Data Format

Each 9 bit count is designated either EN or IN, where "E" designates electron counts and "I" ions, and "N" is the appropriate energy level. For example, the first 9 bit word out is E1, the 30 keV electron count. The sequence is as shown:

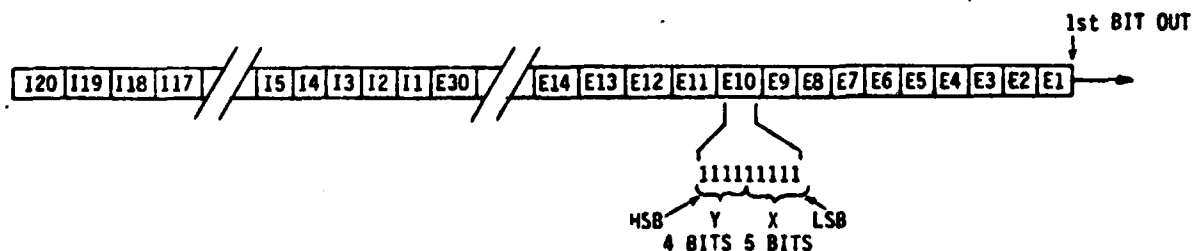


TABLE I-1 (cont.)

ESA SSJ4 (cont.)

Analog Monitors	Plate voltages: 5.0 volts to .25v Power supply : 2.5v Temperature : 2.5 v at room tem.
Size	5.25in x 5.75in x 6.0in
Weight	5.5 lbs
Power Dissipation	28v @ 10.5ma = .3 watts 5v @ 5 μ a normal 5v @ 200 μ a with sun in field of view
External Finish	Electroless nickel over aluminum

and maximizes reliability. These circuits have a capacity of 258,000 counts which is well in excess of the maximum Channeltron output for a 95 ms accumulation time. See Figure I-9.

2.3.3 Control and Data Logic

The SSJ4 logic derives its timing sequence from a spacecraft supplied 10 kHz clock and once per second data shift clock and gate. It generated control signals which, at the end of each 100 ms interval, step the plate voltages and load the contents of the counters into shift registers and reset them. This circuitry consists entirely of high-reliability, radiation-hardened C-MOS logic elements. Figure I-10 is the logic diagram.

2.3.4 Power Converter and Sun Sensor

The SSJ4 package utilizes a 50 kHz sine wave inverter type DC-DC Converter to provide all required power. This supply is built in-house. It supplies six regulated voltage levels: $\pm 5V$, $\pm 1000V$, $+2000V$, and $+3000V$. $+5$ operates all analog and digital circuitry. $\pm 1000V$, which are derived from voltage doublers, supply the plate voltage stepper. $+3000V$, $+2000V$, and $-1000V$ are used to bias the Channeltrons.

A sun sensor is provided to turn the instrument off during periods when the sun is in the field of view. The sensor consists of a photo transistor at the end of a collimator aligned with the analyzer collimators. The photo transistor, through a Schmitt trigger circuit, turns off the power converter. The same circuit is used for on-off control of this instrument by spacecraft command.

2.3.5 Plate Voltage Regulator

A novel feature of the SSJ instruments, and one which enables their

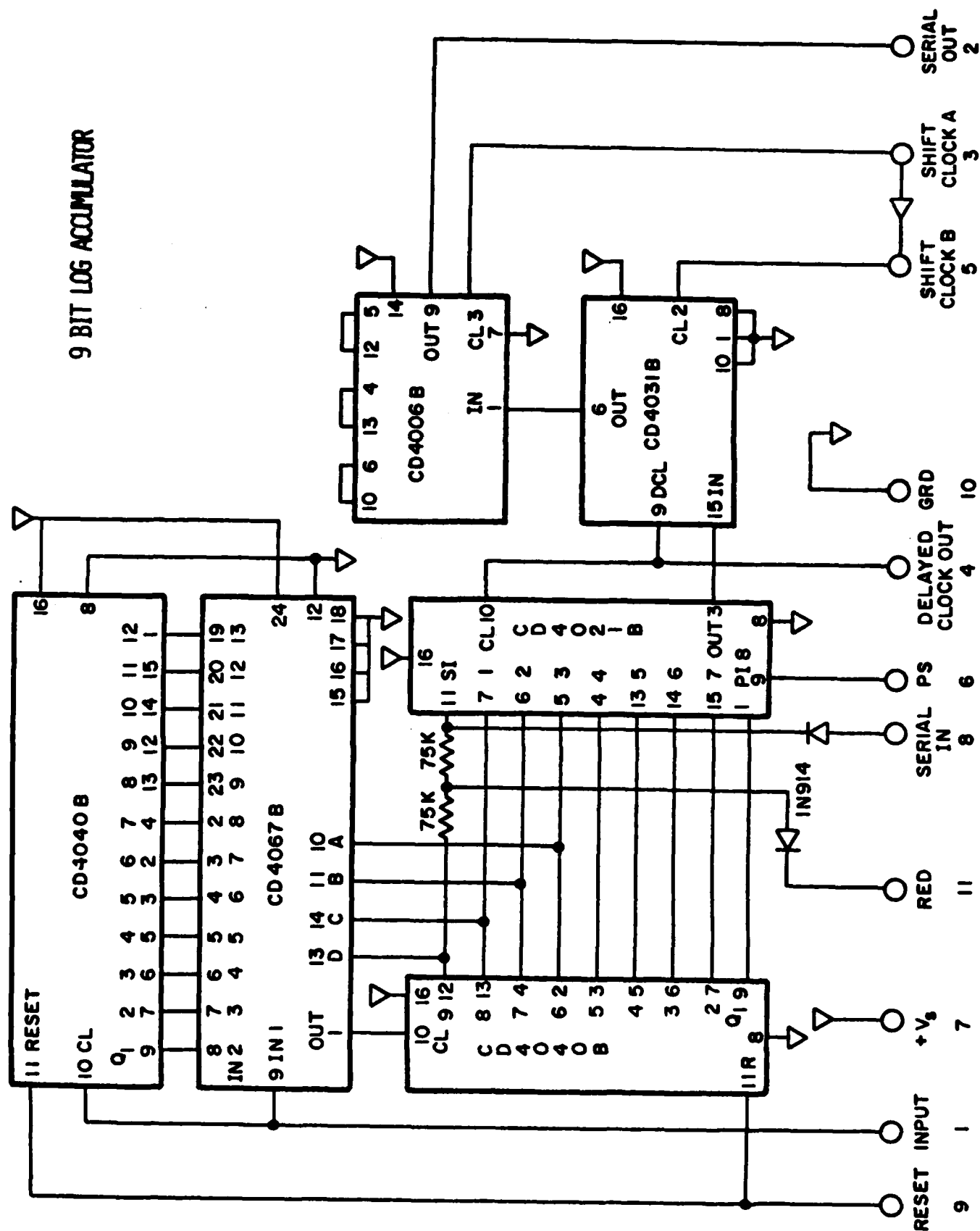
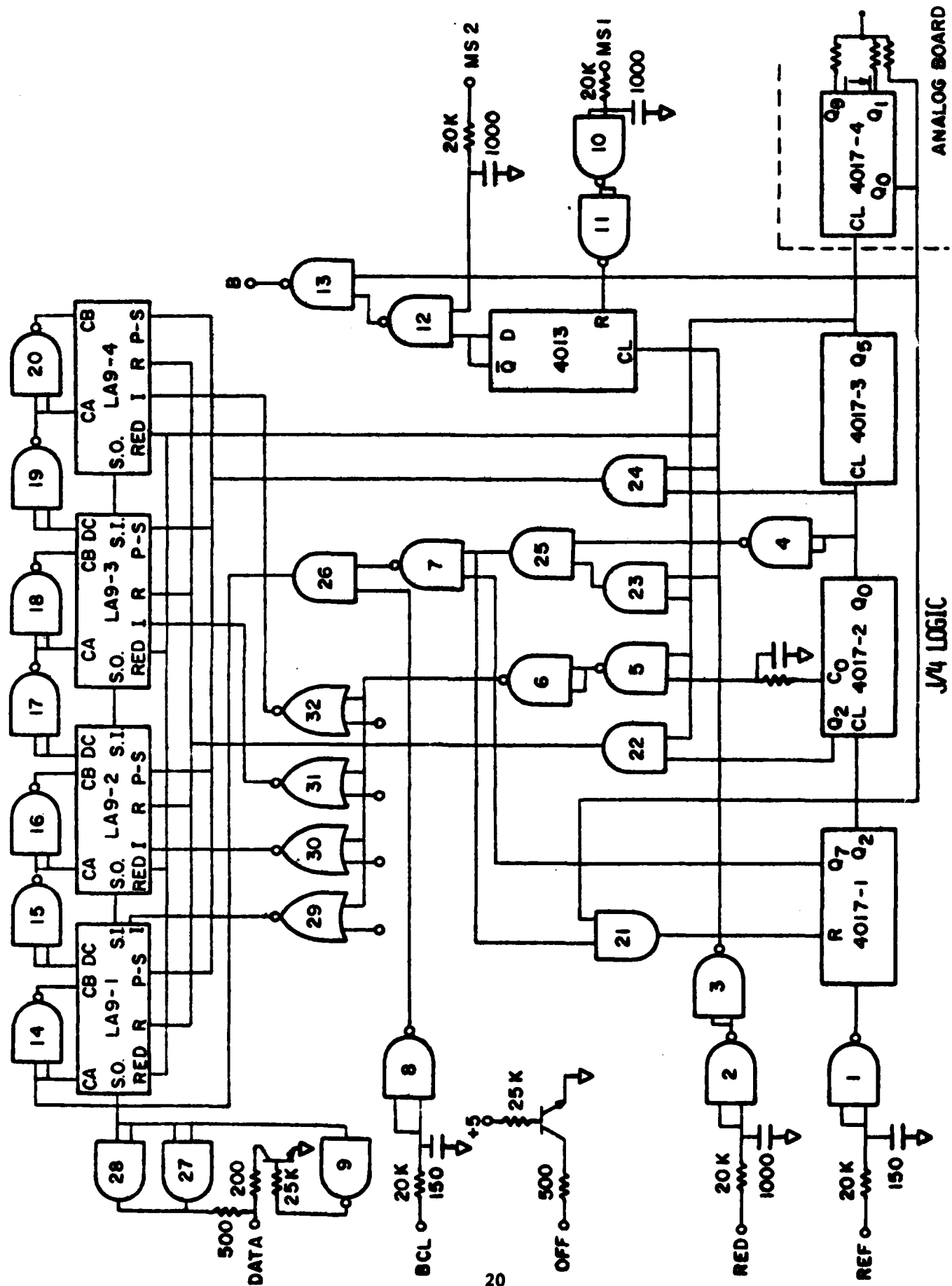


Figure I-9



J/4 LOGIC

Figure I-10

extremely low power consumption and high reliability, is the design of the regulator for the analyzer plate voltages. Basically, it is a high voltage balanced shunt regulator employing a chain of 6 high voltage FET's as the shunt element. Using a single amplifier and the +5 volt power buss as a reference, this circuit provides balanced positive and negative output voltages, ranging from 25 to 750 V, as well as positive and negative outputs at $V_p/3$ to operate the low energy analyzers. A series of precision programming resistors, sequentially placed in the circuit by the C-MOS logic, determine the voltage levels. The voltage settles to within 1% of its final value within 4 ms.

2.3.6 Background Measurement

In order to minimize possible problems in the interpretation of data due to contamination by penetrating particles, two steps have been taken. First, shielding equivalent to about 1/8" of copper has been placed around the Channeltron cones to minimize background counts. Second, two additional commandable operating modes have been provided to enable the inclusion of counts of background only from each analyzer in the data stream. These two modes are:

1. Energy levels 10 and 20 (948eV and 20 eV) are replaced by background counts for both ions and electrons.
2. Background counts replace levels 10 and 20 as in MODE 1, but only on alternate seconds. During the remaining seconds normal, complete spectra are produced.

The background counts are obtained by reducing all analyzer plate voltages to near zero, and re-biasing the ion exit apertures to repel

the low energy ions passed by the analyzers. The biasing of the electron exit apertures does not need to be changed for this purpose.

The choice of operating mode is under ground station control and may be changed in response to particular data requirements. Mode 1 is expected to be most useful. It should be noted that neither background mode significantly compromise the quality of the spectra produced, because of the choice of the spectral points to be sacrificed: level 10 is redundant with 11 and need only be checked on occasion to verify the stability of the detector efficiencies; level 20 (30 eV) is the least reliable point on the spectrum because it is difficult to calibrate, and sensitive to stray electrostatic fields.

2.4 TESTING

The SSJ4 units for F-6, F-7, and F-8 have undergone the same test program as all SSJ3 packages delivered to date. This program includes:

1. Environmental testing of the first unit to qualification levels specified by DMSP.
2. Full electrical testing of each unit.
3. Environmental testing to flight acceptance levels.
4. Additional burn-in at 50°C including full functional testing at periodic intervals.

In addition to these tests, instrument response parameters are verified as indicated in the following section on calibration.

2.5 CALIBRATION

The SSJ4 instruments are quite uniform with respect to plate and aperture geometry and plate voltages, ensuring consistent analyzer characteristics. However, significant variations exist in the characteristics of the channeltron detectors which cause corresponding variations in geometric factor. Primarily for this reason it is important to perform actual beam calibrations on the J/4 units.

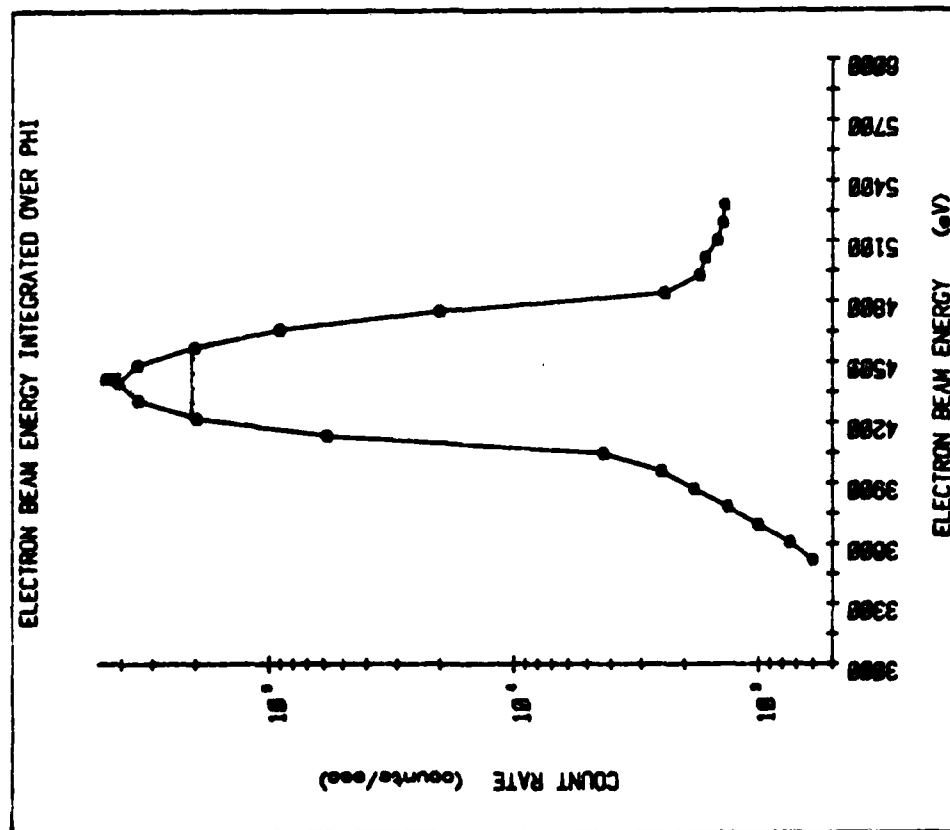
The F-7 unit was calibrated using a facility at the Southwest Research Institute in San Antonio. Because a suitable proton beam was not available, the proton analyzers were calibrated with the same electron beam as the electron analyzers, with plate voltage polarities reversed and post-acceleration voltages adjusted accordingly. Final proton geometric factors were calculated by correcting the values so obtained using published electron and proton efficiency curves for channeltrons. Figures I-11 and I-12 are typical plots produced in this calibration. The geometric factors and angular and energy response curves obtained are unfortunately somewhat uncertain due to uncertainties in the geometry of the beam, which was designed for analyzers with smaller apertures.

The F-6 SSJ4 could not be calibrated because of scheduling constraints.

ELECTRON BEAM ENERGY INTEGRATION

Plot # 4.00
Date Recorded 01261
Date Processed 19-SEP-81
Theta = 4.00

INSTRUMENT: 7c4
Voltage = 110.00



All data points used for these calculations
data integral: 149528488.00

Arithmetic mean calculations

CR: 408329.32
ELECTRON BEAM ENERGY: 4488.96
ELECTRON BEAM ENERGY I: 4227.11
Sensitivity: 48.00

Median calculations

CR: 413218.19
ELECTRON BEAM ENERGY: 4483.88
ELECTRON BEAM ENERGY I: 4228.47
Sensitivity: 48.00

Most probable value calculations

CR: 418229.00
ELECTRON BEAM ENERGY: 4488.00
ELECTRON BEAM ENERGY I: 4229.32
Sensitivity: 48.00

CR/2: 204164.66
FWHM: 348.16
ELECTRON BEAM ENERGY: 4575.27
Resolutions: 8.00

CR/2: 206690.59
FWHM: 345.23
ELECTRON BEAM ENERGY: 4573.78
Resolutions: 8.00

CR/2: 208114.58
FWHM: 343.43
ELECTRON BEAM ENERGY: 4572.75
Resolutions: 8.00

Figure I-11

PHI RESPONSE

Plot # 14.00
 Date Recorded 81281
 Date Processed 18-SEP-81
 Theta = -1.00
 Electron Beam Energy = 4400.00

INSTRUMENT: 7eJ
 Voltage = 110.00

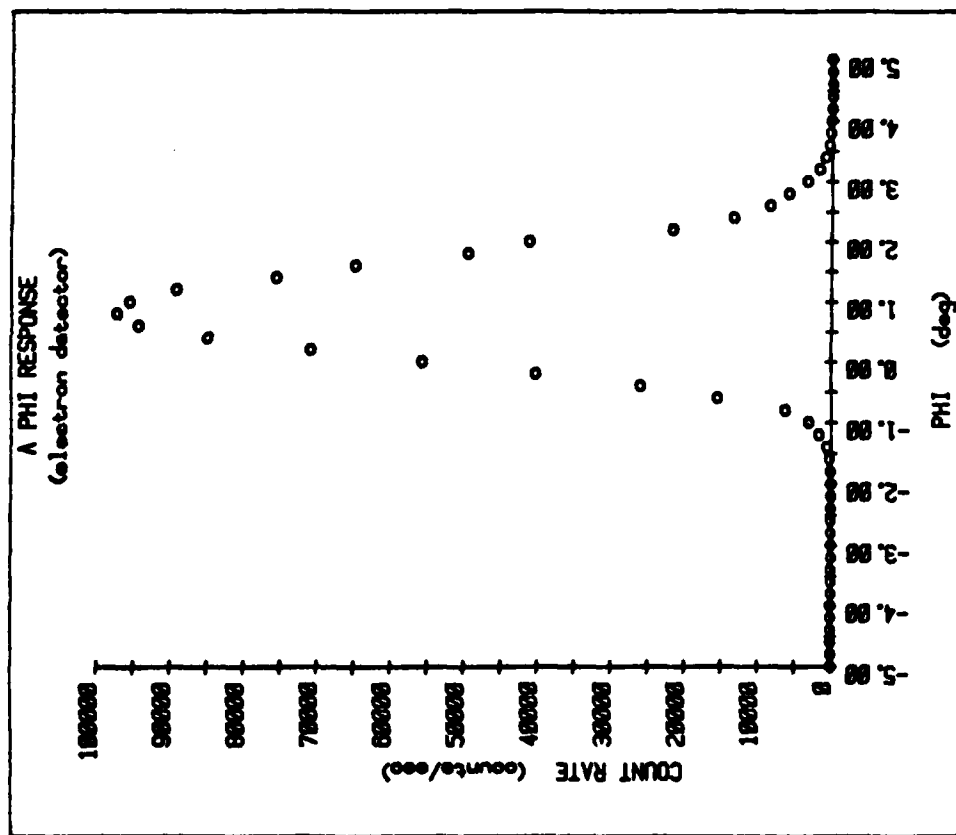


Figure I-12

II. PROTEL

1.0 PHYSICAL PRINCIPLES

Ionizing particles penetrating the depletion region of a solid state detector create hole-electron pairs at a constant rate of approximately one pair/3.5 eV of energy lost by the particle. There exists a well-defined range-energy relationship for proton in silicon, and it is this relationship that we wish to utilize in the proposed instrument.

We can distinguish 2 cases in the interaction of an incoming proton with a solid state detector depending on whether the range of the particle is smaller or greater than the depletion layer of that detector.

In the first case, when the range of the proton is less than the depletion depth of the detector, this proton expends all of its original energy, E_0 , in the depletion region, and the total separated charge is a direct measurement of the particle energy.

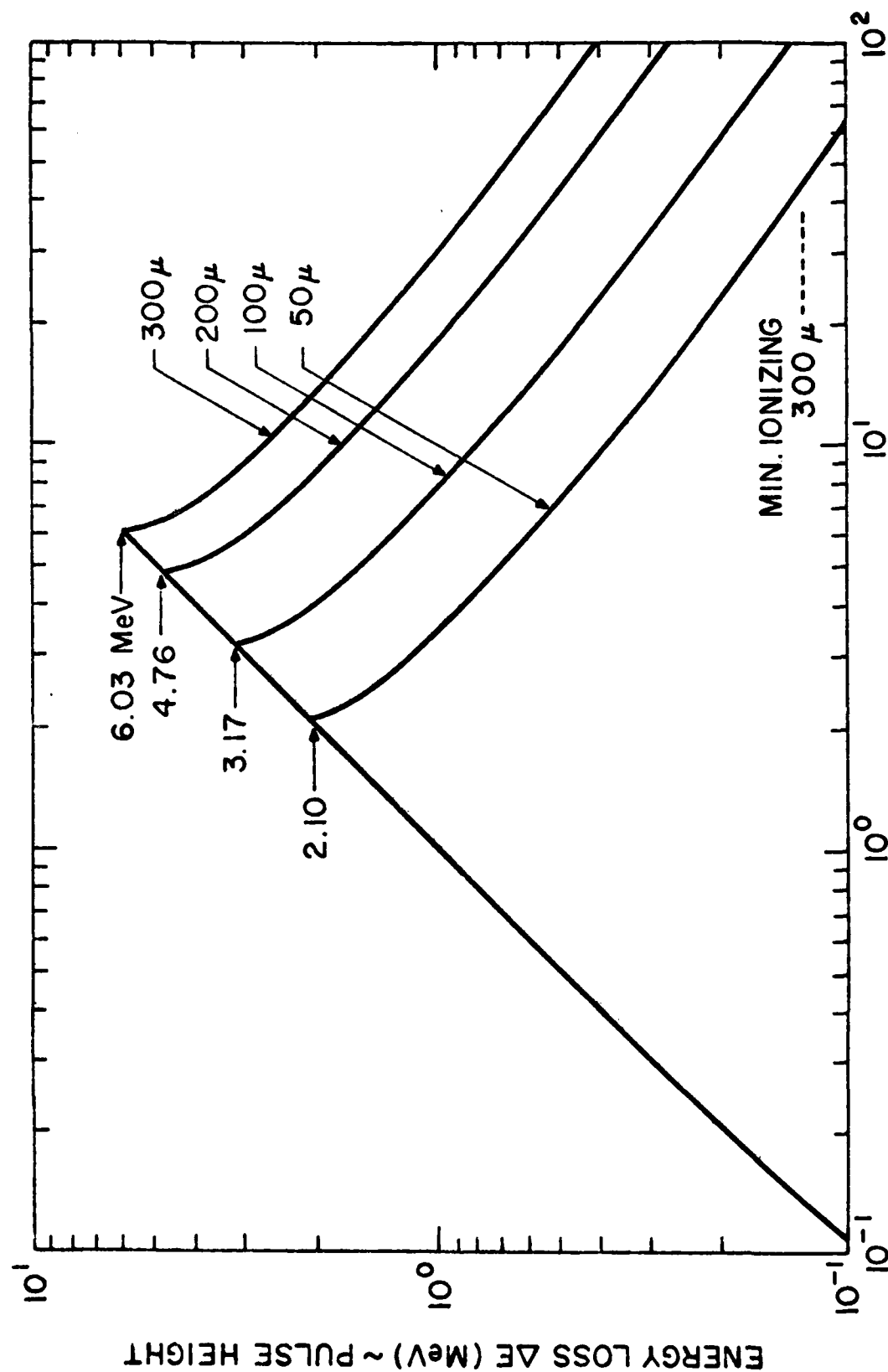
In the second case, the range of the incoming proton is larger than the depletion layer, the amount of energy lost in the detector is a well-defined function of the original energy of the proton. The particle emerges from the back of the detector with an energy $E < E_0$, after having lost $\Delta E = E_0 - E$ in the interaction.

A second detector can be placed immediately following the first one so as to intercept the outgoing particle. If the remaining range of the proton is less than the thickness of the second detector, then the sum of the ionization in these 2 detectors is a direct measurement of the energy of the incoming proton. On the other hand, if the range of the proton still exceeds the depletion depth of that 2nd detector, then the energies lost in the 2 detectors are again an indirect measurement of the original energy of the proton. Furthermore, requiring that these two events be

collected within a very short time interval from one another (called the resolution time of the system) provides a mean for rejecting background events, thus improving the signal/noise of the instrument.

Figure II-1 shows the energy loss, ΔE (MeV) as a function of the incident proton energy, E (MeV) for 4 detectors of different depletion depth. The maximum ranges of protons in each detector are indicated in the figure. Modern silicon detectors have negligible dead layers ("windows"), corresponding to less than few tens of KeV for a 10 MeV proton. The electric field applied to such detector by means of a back-biasing battery assures that hole-electron pairs can be collected without significant recombination occurring. Preamplifiers are made so that output pulse heights are linearly proportional to the amount of separated charges. Pulse height analysis can thus be used to derive spectral information on the incident particle energy.

The proton spectrometer under consideration will measure the trapped proton fluxes in the magnetosphere in the energy range of 1.0 - 100 MeV.



INCIDENT PROTON KINETIC ENERGY E (MeV)

Figure II-1. Energy Loss, ΔE (MeV), versus Incident Proton Kinetic Energy, E (MeV), for 50 μ m, 100 μ m, 200 μ m and 300 μ m Thick Silicon Lithium-Drifted Detectors

2.0 DESCRIPTION OF THE INSTRUMENT

The proposed instrument is made up of 3 distinct parts.

1) Two head assemblies, each covering a different energy range, and each made up of

- a) a collimator,
- b) a sweeping magnet,
- c) a detector assembly,
- d) a passive shield and
- e) an active shield.

2) The associated electronics.

2.1 The High Energy Range (6 - 100 MeV) Head Assembly

Figure II-2 shows the schematics of the head assembly for the high energy part of the total energy range to be covered.

2.1.1 The Collimator

The collimator is made of aluminum, and it has a thickness corresponding to the ranges of protons far in excess of several hundred MeV, when one takes into account the obliquity of the trajectories through the collimator walls necessary if the penetrating particles are to reach the detectors at all. The equivalent range for electrons is substantially larger than that for any electrons trapped in the magnetosphere. The opening half-angle of the collimator is 16.8° , 0.1° larger than the acceptance half-angle, α , of 16.7° which is defined by the entrance and exit apertures in front of the detectors, on either sides of the sweeping magnet. Thus this collimator does not define the geometrical factor of the head assembly, but its function is to collimate to a first order the

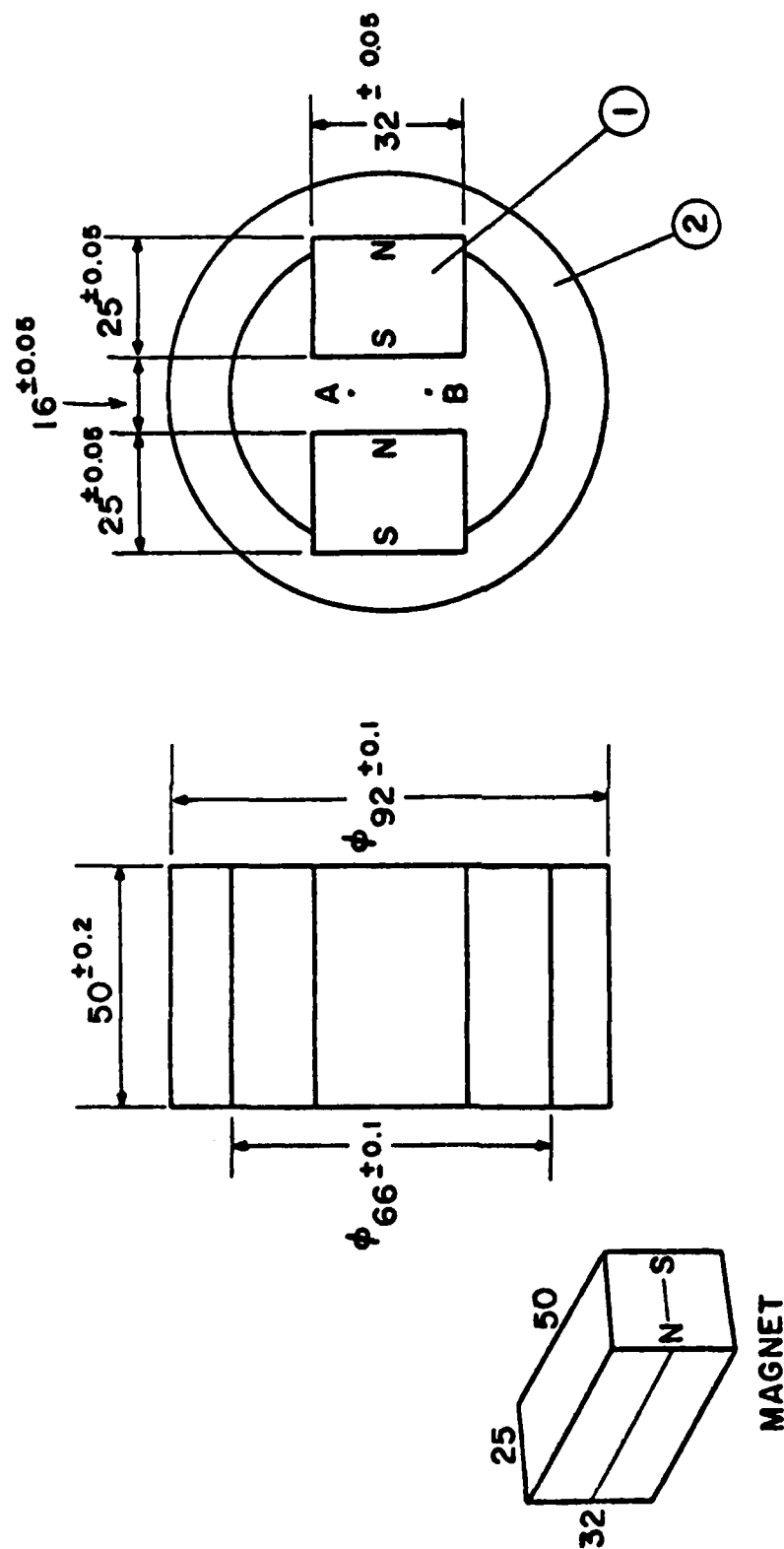
incoming flux of protons, and to eliminate outside of the acceptance cone the proton and electron fluxes. The surfaces of the conical envelope have a saw-tooth pattern machined in it to limit the scattering of particles on this surface and into the entrance aperture.

2.1.2 The Magnet Assembly

The magnet is located between the entrance and exit apertures of the head assembly. Its function is to sweep away from the exit aperture, i.e., from the detectors, the electron fluxes which otherwise would contaminate the proton data. Figure II-3 shows a schematic drawing of the magnet assembly. It consists of the 2 magnet pole pieces and a yoke. The pole pieces are made up of HICOREX-90B while the yoke is made up of CRS1010~1020. Figure II-4 shows the resulting magnetic field along the 3 main axis. Using these data, a computer simulation showed that the minimum electron cut-off energy will be 3.9 MeV for an incoming electron at the maximum angle ($\sim 20^\circ$) with respect to the center axis of the spectrometer, and in the (x,y) plane (see Figure II-4). The electron cut-off will be even greater for incoming particles whose trajectories are contained in a plane making an angle with the (x,y) plane, and/or not intersecting the center of the magnet.

2.1.3 The Detector System

Figure II-2 is a sketch of the detector stack. Six detectors are required. All detectors are of the silicon, lithium-drifted type. They have the following thicknesses: 400 μ m, 500 μ m, 1000 μ m, and 2 x 2000 μ m. This group of detectors is followed by a copper absorber of 1.27 cm, followed by a 6th detector of 2000 μ m depletion depth to be used in anti-coincidence for protons with $E > 100$ MeV, thus defines the upper energy threshold of the spectrometer. Actually this 6th detector can also be



① HICOREX 90B, ② CRS 1010 ~ 1020

AT POINT A AND B, \bar{B} SHOULD BE ≥ 3500 GAUSS

Figure II-3. Schematic of the Sweeping Magnet for the High Energy Range Head Assembly

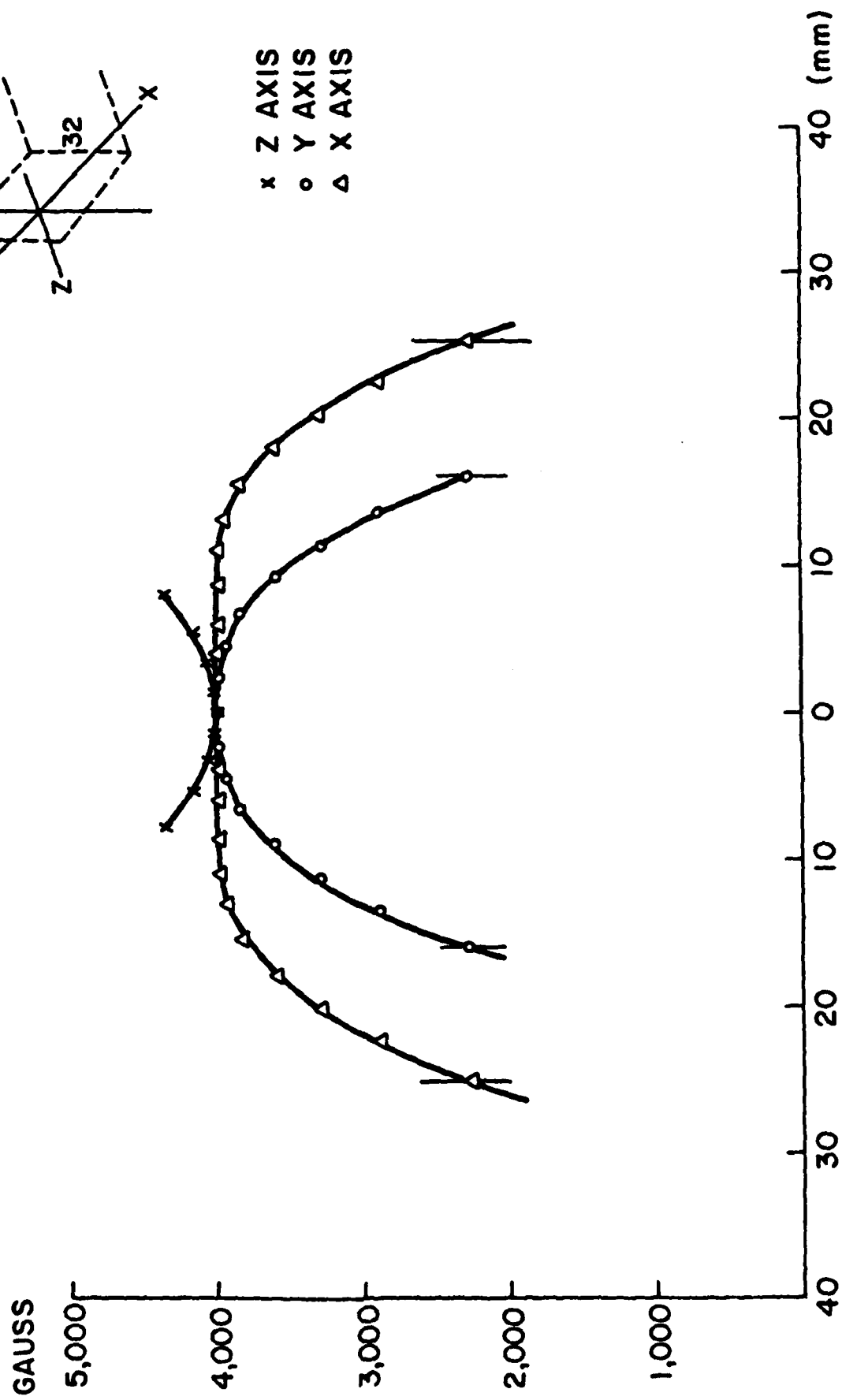


Figure II-4. Magnetic Field Strength (gausses) along the 3 Principal Axis of the Sweeping Magnet for the High Energy Range Head Assembly

used to measure the proton flux from 100 MeV to ~ 300 MeV.

In front of the first detector ($400\mu\text{m}$) is an aluminum absorber of 0.02 cm (54 mg-cm^{-2}) used to absorb low energy proton ($E \lesssim 5\text{ MeV}$).

Figure II-5 shows the energy deposited in each detector of the telescope as a function of the incoming proton energy.

The 6 - 100 MeV range is divided into 15 energy channels. Table II-1 shows the 16 energy channel boundaries with the corresponding energy loss in each of the detectors. Triple and/or quadruple coincidences will be required to ascertain the particle energies. Each detector will have a lower energy threshold of about 1 MeV, which is many sigma's above the energy deposited by a minimum ionizing particle in any of the detectors.

Table II-2 lists the silicon detector capacitance as a function of the thicknesses of the detector which will be used in this instrument. Also listed are the bias required to totally deplete each detector. It should be noted that these bias voltages are the minimum values to totally deplete these detectors, i.e. $|E| = 0\text{ volt/cm}$ right under the aluminum back contact. In practice, the $|E|$ at that point should be $> 0\text{ volt}$, to improve the lifetime of the detectors, i.e. the detector should be over-biased.

The front detector ($400\mu\text{m}$) has a diameter of $2.25 \pm 0.02\text{ cm}$, and precisely define the solid angle of the proton spectrometer. Any event not passing through this well-defined area of the first detector, but interacting with one or more of the following detectors, although possibly losing the right amount of energy in each one of them, will be vetoed out.

HIGH ENERGY RANGE TELESCOPE

Al Absorber : 0.2 mm (54 mg/cm²)

- 1) 400 μ m
- 2) 500 μ m
- 3) 1000 μ m
- 4) 2000 μ m
- 5) 2000 μ m

FOLLOWED BY 1.27cm ABSORBER
(11.31 grams/cm²)

- 6) 2000 μ m

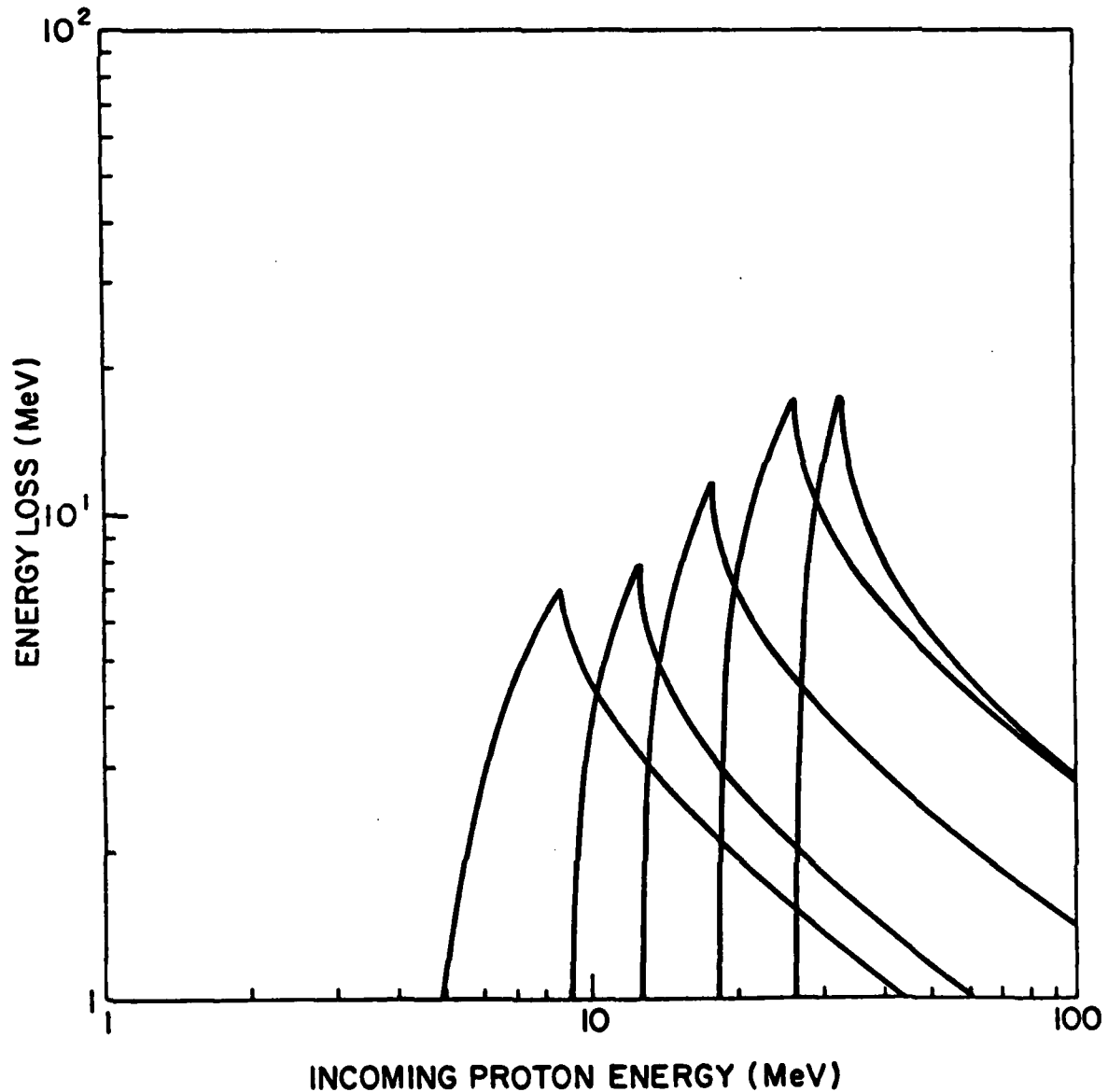


Figure II-5. Energy Loss (MeV) versus Incoming Proton Energy (MeV) in the 5 Detector Configuration of the High Energy Range Head Assembly

TABLE II-1

Channel Boundaries with the Corresponding Energy Loss in Each
of the Detectors, for the High Energy Range PHA

Energy Boundaries (MeV)	Energy Loss (MeV)				
	1st Det.	2nd Det.	3rd Det.	4th Det.	5th Det.
6.0	2.78-4.91	—	—	—	—
7.4	4.91-6.95	—	—	—	—
9.15	6.95-3.80	1.0 -5.48	—	—	—
11.0	3.80-3.12	5.48-7.80	—	—	—
12.7	3.12-2.58	7.80-4.08	1.00- 7.02	—	—
15.0	2.58-2.13	4.08-3.03	7.02-11.73	—	—
18.2	2.13-1.79	3.03-2.43	11.73- 5.94	1.00-10.86	—
22.0	1.79-1.53	2.43-2.02	5.94- 4.54	10.86-16.56	—
26.45	1.53-1.27	2.02-1.65	4.54- 3.52	16.56- 8.47	1.00-17.02
33.12	1.27-1.09	1.65-1.40	3.52- 2.93	8.47- 6.53	17.02- 8.00
40.00	1.09-0.95	1.40-1.21	2.93- 2.49	6.53- 5.34	8.00- 6.00
48.0	0.95-0.84	1.21-1.07	2.49- 2.18	5.34- 4.58	6.00- 4.95
56.0	0.84-0.72	1.07-0.91	2.18- 1.86	4.58- 3.84	4.95- 4.04
68.0	0.72-0.64	0.91-0.87	1.86- 1.63	3.84- 3.34	4.04- 3.46
80.0	0.64-0.54	0.87-0.68	1.63- 1.37	3.34- 2.78	3.46- 2.84
100.0					

TABLE II-2

Silicon Detector Capacitances of the Detectors
to be Used in this Spectrometer

Det. Thicknesses (μm)	Capacitance (pf/mm^2)	Bias Voltages (Volts)
20	5.2	<1.0
50	2.0	2.0
75	1.5	4.5
100	1.0	8.0
400	0.28	120.0
500	0.21	200.0
1000	0.105	780.0
2000	0.054	3000.0

Thus the entrance and exit collimators together with detector 1 define the geometrical properties of the instrument to be:

Angular aperture: 16.7° (half-angle)

Field of view: 0.265 ster

Detection area: 1.77 cm^2

Geometrical factor: $0.12 \text{ cm}^2\text{-ster}$

2.1.4 The Passive Shielding

In order to eliminate penetrating particles (electrons and protons with $E \lesssim 135 \text{ MeV}$), as well as to reduce as much as practically feasible the bremsstrahlung produced by these electrons, require 1.33 cm of copper and 1.2 cm of lead surrounding the detector stack.

The 1.33 cm of copper are sufficient to cut the total flux of high energy electrons encountered in the heart of the outer radiation zone (Figure II-6). This thickness of copper corresponds to the range of 100 MeV protons. However, the high energy electrons will produce large amounts of bremsstrahlung in the same copper shielding (see the section on background estimates). Some of these γ -rays will be transmitted through the copper and will interact with the solid state detectors with a small, but not negligible probability.

With the help of the "Tiger Code" (a computer code developed at Oak Ridge National Laboratory), we have simulated the electron interactions with copper shield.

These calculations have shown that the unwanted bremsstrahlung, can be cut down considerably by using 1.2 cm of lead around the detectors. This added shielding results in ~ 3 orders of magnitude reduction of the bremsstrahlung flux in the 240-360 keV range (see Figure II-7). This

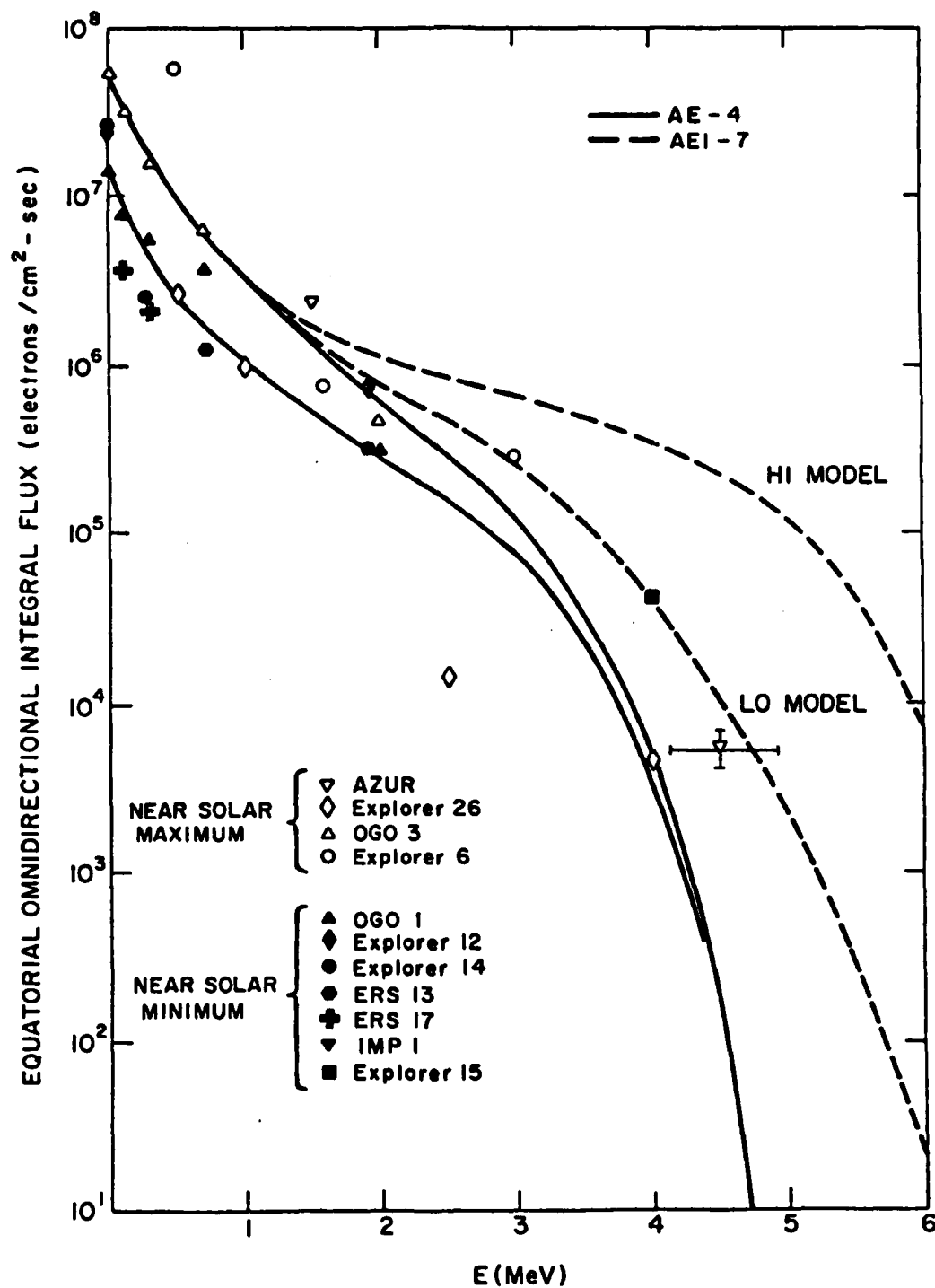


Figure II-6. Comparison of AEI-7 Model Spectra with Various Data Set at L=4. The HI model curve is mainly based on the OVI-19 observations from Vampola (Vette et al., 1978)

ENERGY SPECTRUM OF TRANSMITTED PHOTONS
(NUMBER/MeV NORMALIZED TO ONE INCIDENT PARTICLE)

- ① Brass, 1.33 cm (11.86 gr/cm²)
- ② { Brass, 1.33 cm (11.86 gr/cm²)
Lead, 1.20 cm (13.61 gr/cm²)

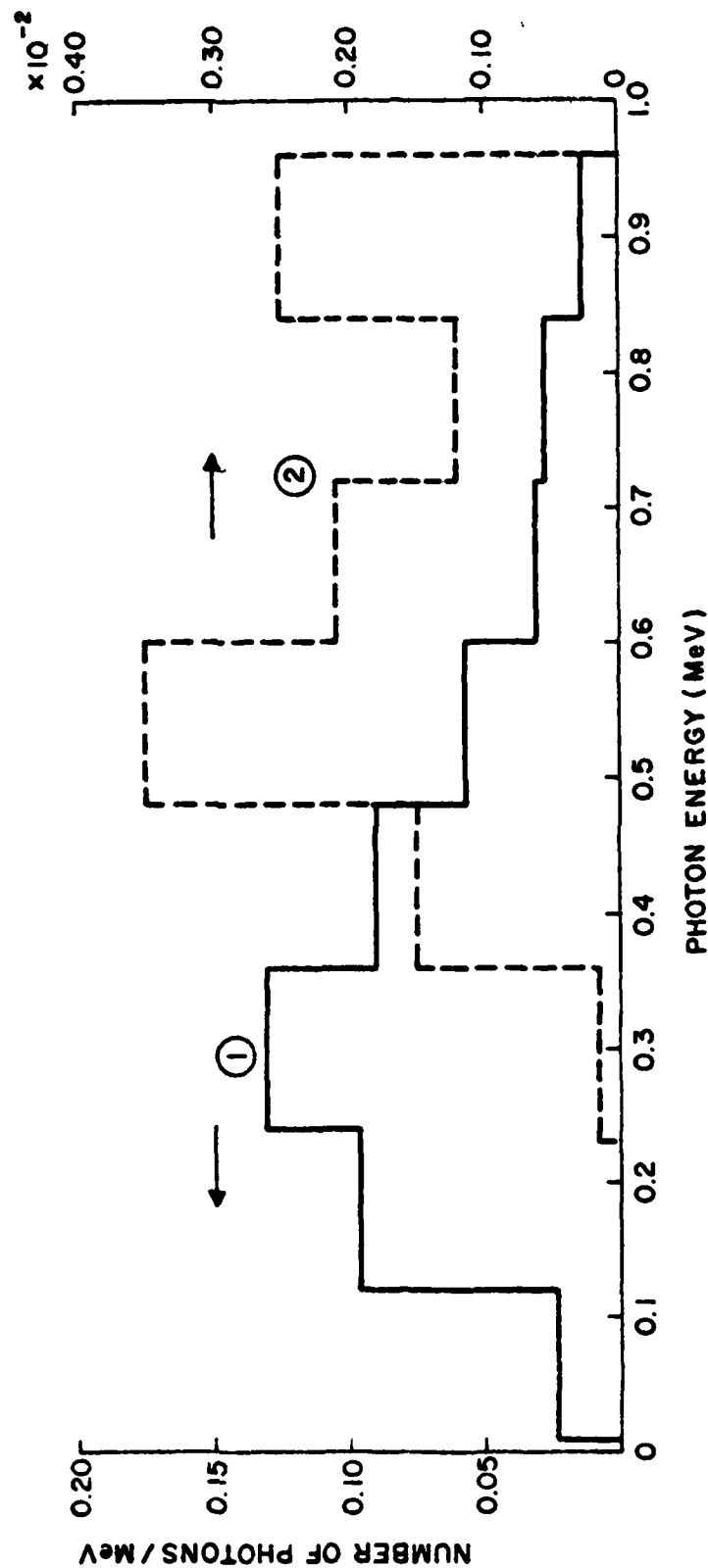


Figure II-7. Energy Spectrum of the Transmitted Bremsstrahlung Resulting from the Interaction of an Electron Spectrum of the Type HI Model (Figure II-6)

added lead shielding further extends the proton range to at least 135 MeV.

2.1.5 The Active Shielding

To further eliminate the unwanted background, especially the protons with $E \gtrsim 135$ MeV, which are present in the inner zone, and could penetrate the total thickness of passive shielding, we rely on an active shielding around the detectors. This active shielding is made up of 5 concentric rings of silicon around the detectors (one ring to each detector). Each ring is etched in the same piece of silicon as its corresponding central detector. Thus, within time resolution of $\Delta\tau \approx 1.-5. \times 10^{-8}$ sec, any event recorded in an outer ring and one or several central detectors will be rejected by the electronics logic.

A 6th detector is located immediately following the stack of 5 detectors of the spectrometer. As mentioned above, its function is to define the upper threshold of the instrument (100 MeV). But it also will veto-out any particle (high energy protons) which, penetrating through the rear of the telescope, would interact with one or more of the detectors, with the proper energies deposited in each of them.

2.1.6 Description of the Electronic Logic

Figure II-8 is a block diagram of the logic for the high energy range (6 - 100 MeV) of the proton telescope. Each of the 5 detectors feeds a standard low noise preamplifier which also shapes the pulse from the incoming proton with the proper time constants, and an amplifier. After the amplifier, the signal is split into two branches, one going to a low level discriminator, the other to the pulse height analyzer.

The output of the low level discriminator goes into a hodoscope where the logic for fast coincidence established the occurrence of a coherent event in several of the detectors. The output of the hodoscope enable the proper PHA for each of the detectors for which a coherent event has been established. For example, if coincident events have been ascertained in detectors 1, 2 and 3, the output gate pulses from the hodoscope enable PHA 1, 2 and 3. Each PHA associated with each detector is a voltage divider, and the voltage level of the incoming pulse is composed to the discrete voltage levels of the divider. The different n-fold coincidence schemes for the high energy range PHA of the spectrometer are shown in Table II-3. For a particular energy channel, the coincidence requirement is read horizontally. In our particular example once it has been established that the incoming event have resulted in one of the 11 voltage intervals in detector 1, one of the 4 voltage intervals in detector 2 and one of the 9 voltage intervals in detector 3, the proper and unique combination of these 3 voltage intervals in coincidence will be stirred through a matrix to the proper counter which will be incremented. This will occur in two cases only in our example: (a5, b5, c5) incrementing the counter for the energy channel #5 (12.7-

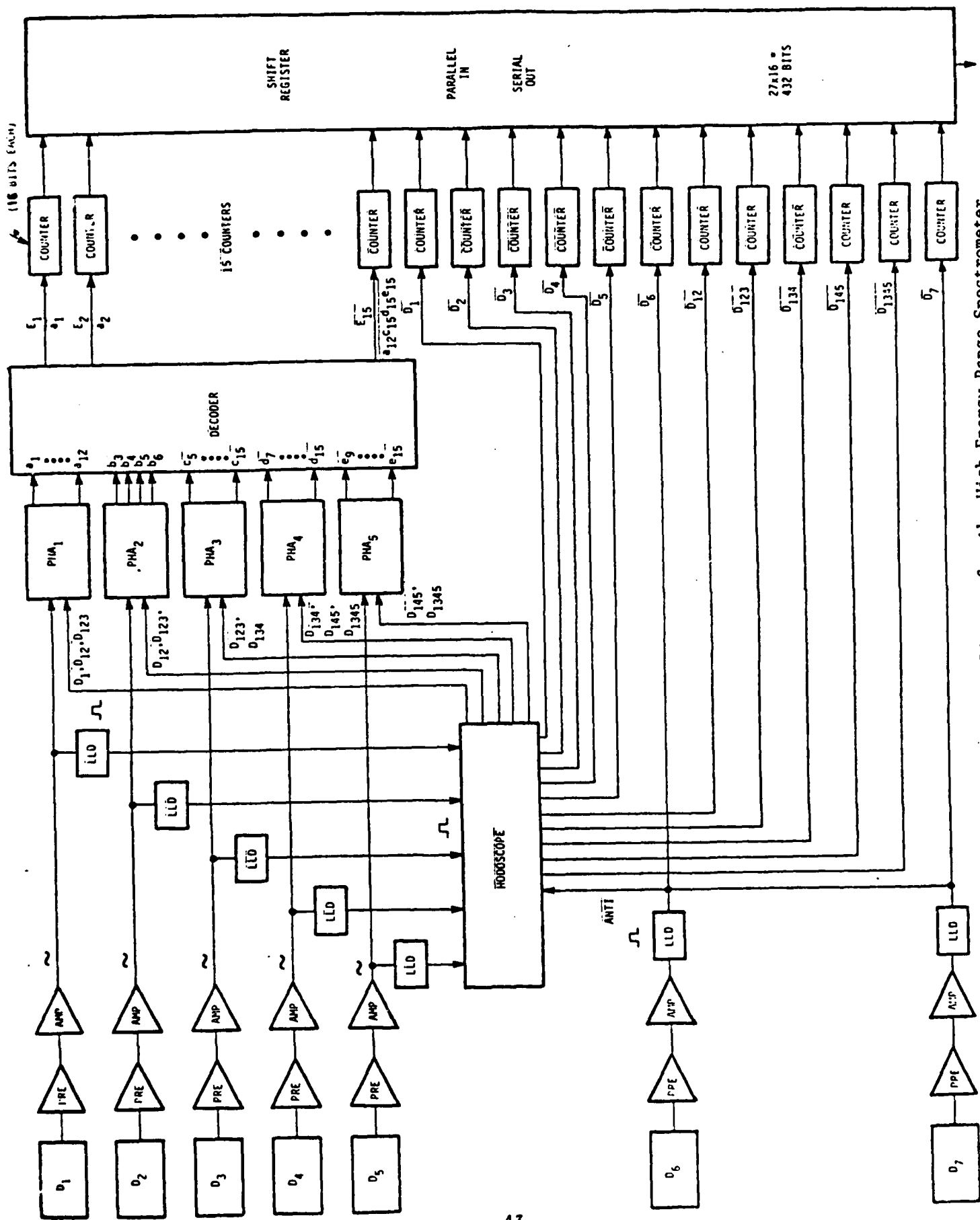


Figure II-8. Electronic Block Diagram for the High Energy Range Spectrometer.

TABLE II-3

Coincidence Scheme for the High Energy Range

6.0					
7.4	a ₁				
9.15	a ₂				
11.0	a ₃	b ₃			
12.7	a ₄	b ₄			
15.0	a ₅	b ₅	c ₅		
18.2	a ₆	b ₆	c ₆		
22.0	a ₇		c ₇	d ₇	
26.45	a ₈		c ₈	d ₈	
33.12	a ₉			d ₉	e ₉
40.00	a ₁₀			d ₁₀	e ₁₀
48.00	a ₁₁		c ₁₁	d ₁₁	e ₁₁
56.00			c ₁₂	d ₁₂	e ₁₂
68.00			c ₁₃	d ₁₃	e ₁₃
80.00			c ₁₄	d ₁₄	e ₁₄
100.00			c ₁₅	d ₁₅	e ₁₅

15.0 MeV) or (a6, b6, c6) i.e., energy channel #6.

Since detector 1 defines the solid angle, in all cases, over the energy range 6 - 100 MeV, a pulse from that detector is required. Up until 40 MeV, where triple coincidence is required whenever possible, the precise energy depositions as shown in Table II-1 are necessary. From 40 MeV to 100 MeV, a trigger of the low level discriminator of detector 1 only is required. The precise energy deposition is established in detectors 3, 4 and 5.

A 6th detector located behind the stack of 5 detectors is used in anti-coincidence with these 5 detectors. If one or more detector are triggered together with this 6th detector, the energy of the particle was greater than 100 MeV, and the analysis of the event will not proceed, i.e. no output gate pulse from the hodoscope to the PHA's will occur. Such an event where several of the 5 detectors are triggered plus the 6th one could occur through a high energy proton penetrating the shielding material from the side or from the rear of the instrument. However, if Detector 1 is triggered in the same time has several of the detectors plus the 6th detector, then we can use the event as a bonified proton event with $E > 100$ MeV. A 7th detector, which is in fact the parallel combination of the 5 rings concentric to the 5 detectors, is used as an anti-coincidence active shield for the stack of detectors. An event in this active shield will immediately veto any gate pulse from the hodoscope.

In order to facilitate the data analysis and trouble shoot any artifact which could exist in the data, the single count rates and the different count rates will also be recorded as will be the count rates from Detector 7, the active shielding.

2.2 The Low Energy Range (1 - 9 MeV) Head Assembly

Figure II-9 shows the schematics of the head assembly for the low energy part of the energy range to be covered.

2.2.1 The Collimator

The collimator is made of aluminum, and considerations in its design are the same as those which went into the design of the High Energy Range head assembly collimator. The opening half-angle, α , of the collimator is 9.64° , again 0.1° larger than the acceptance half-angle, α , of 9.54° which is defined by the entrance and exit apertures in front of the detectors.

2.2.2 The Magnet Assembly

The same magnet design is being considered than for the High Energy Range. Its construction will be realized with similar materials. However, because of the smaller pole gap, the magnetic field will exceed 4000 gauss. The resulting electron energy cut-off will be ~ 4.5 MeV.

2.2.3 The Detector System

Figure II-9 is a sketch of the detector stack. Six detectors are required. All detectors are of the silicon, lithium-drifted type. They have the following thicknesses: 20 μm , 50 μm , 50 μm , 75 μm , and 100 μm . This group of detectors is followed by a thickness of 150 μm of copper, which in turn is followed by the 6th detector of 100 μm thickness.

This 6th detector is used in anti-coincidence with the other detectors, defining the upper energy threshold of the spectrometer at

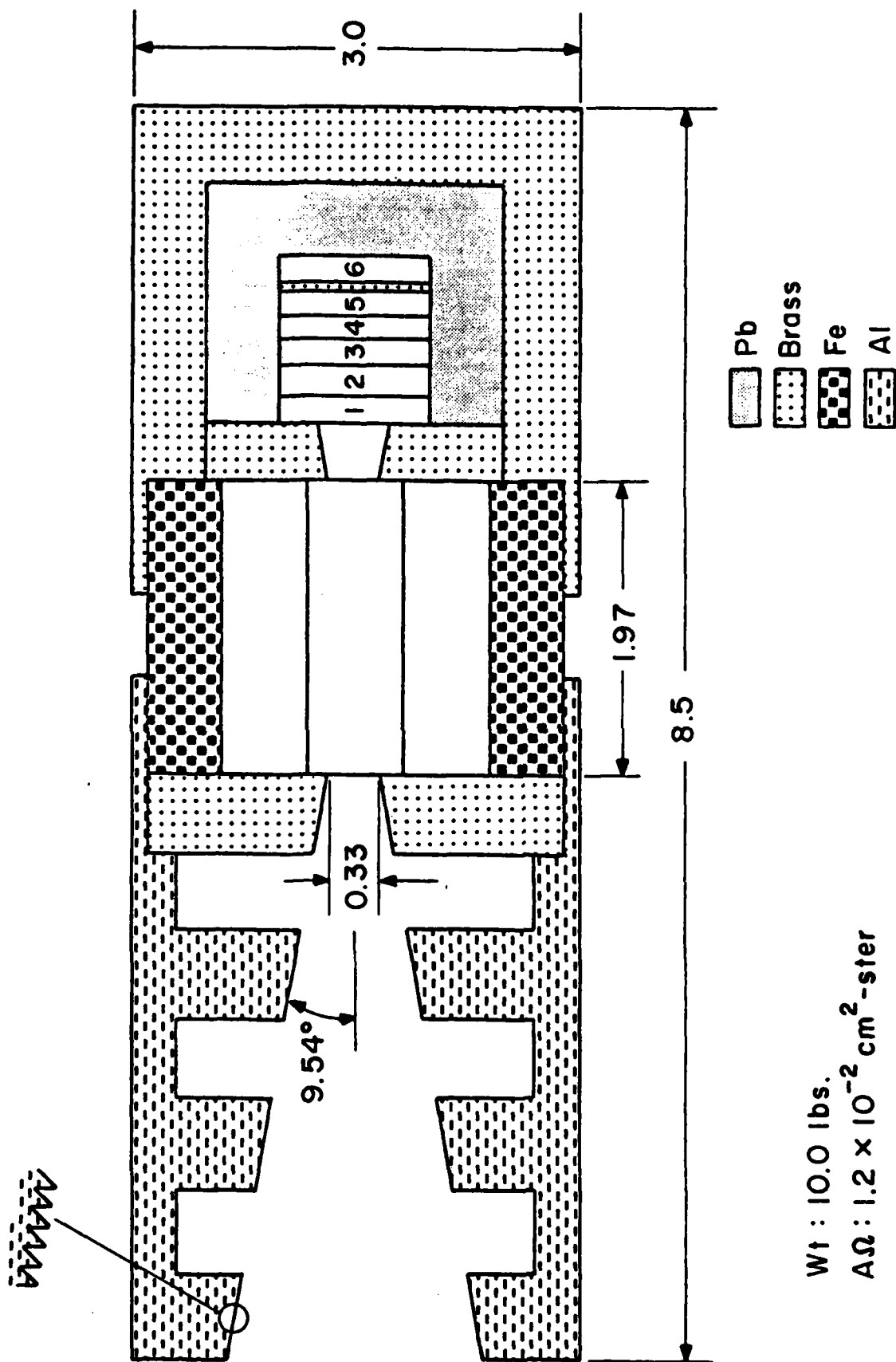


Figure II-9. Schematic of the Low Energy Range (1-9 MeV) Head Assembly

9 MeV.

The front detector is made light-tight by several hundred Angstroms of deposited aluminum.

Figure II-10 shows the energy deposit in each detector of the telescope as a function of the incoming proton energy.

The 1-9 MeV range is divided into 8 energy channels. Table II-4 shows the 8 energy channel boundaries, with the corresponding energy loss in each of the detectors. Triple and/or quadruple coincidences will be required to ascertain the particle energies. Each detector will have a lower energy threshold of 0.250 MeV. A minimum ionizing particle will deposit, on the average, 35 keV in the 100 μ m thick detector. Thus 250 keV lower energy threshold in many sigma's above expected energy loss of a high energy particle.

The front detector (20 μ m) has a diameter of 1.30 ± 0.02 cm, and it defines precisely the solid angle of the proton spectrometer.

The entrance and exit collimators together with detector 1, define the geometrical properties of the instrument to be:

Angular aperture:	9.54° (half-angle)
Field of view:	8.7×10^{-2} ster
Detection area:	0.55 cm ²
Geometrical factor:	1.2×10^{-2} cm ² -ster

2.2.4 The Passive Shielding

The penetrating particles (electrons and protons), as well as a large portion of the bremsstrahlung by the electrons interacting with the S/C and with the shield itself are prevented from reaching the detectors

- 1) 20 μm
- 2) 50 μm
- 3) 50 μm
- 4) 75 μm
- 5) 100 μm

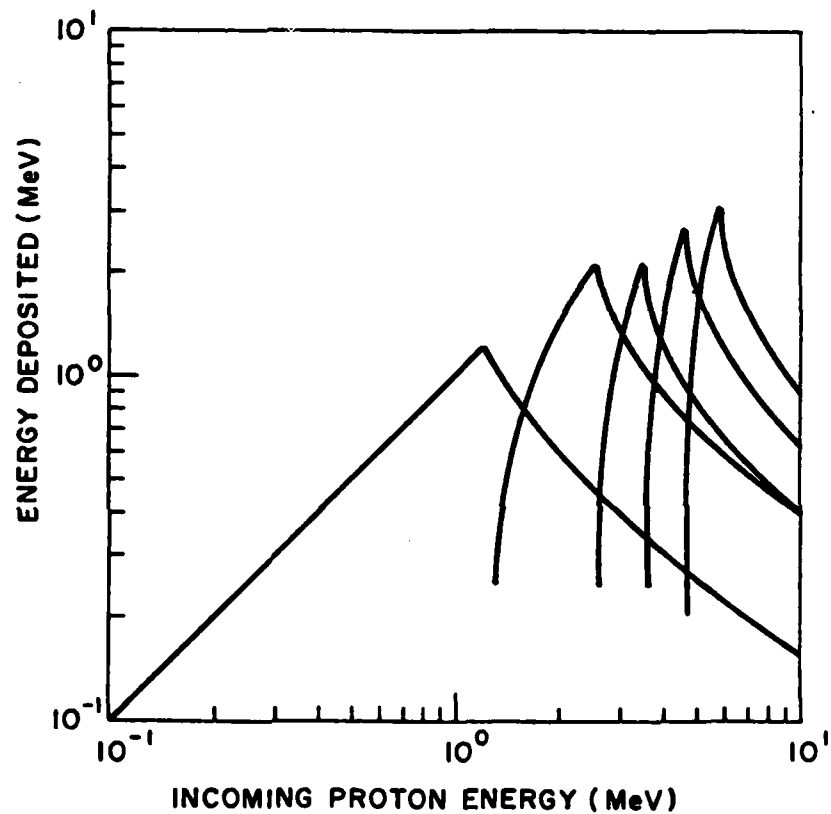


Figure II-10. Energy Loss (MeV) versus Incoming Proton Energy (MeV) in the 5 Detector Configuration of the Low Energy Range Head Assembly

TABLE II-4

Channel Boundaries with the Corresponding Energy Loss in Each
of the Detectors, for the Low Energy Range PHA

Energy Boundaries (MeV)	Energy Loss (MeV)				
	1st Det.	2nd Det.	3rd Det.	4th Det.	5th Det.
1.0	1.05-1.2	—	—	—	—
1.3	1.05-0.80	0.25-0.82	—	—	—
1.6	0.80-0.59	0.82-1.45	—	—	—
2.0	0.59-0.45	1.45-2.10	—	—	—
2.6	0.45-0.34	2.00-1.00	0.25-2.10	—	—
3.5	0.34	1.00-0.76	2.00-0.92	0.25-2.6	—
4.6		0.76	0.92-0.65	2.6 -1.15	0.25-3.1
6.0	0.25	0.42	0.65-0.44	1.15-0.70	2.25-1.00
9.0					

by using 1.33 cm of copper and 1.2 cm of lead around these detectors. The design is similar to that of the High Energy Head Assembly passive shielding.

2.2.5 The Active Shielding

Each of the 5 detectors has a concentric ring on its outside which is used as a live anti-coincidence ring for that detector.

Also the 6th detector will be used to veto-out any particle impinging on the stack of 5 detectors through the rear of the instrument.

2.2.6 Description of the Electronic Logic

Figure II-11 is a block diagram of the logic for the low energy range (1 - 9 MeV) of the proton telescope. This logic is identical to that of the high energy range. Table II-5 shows the different n-fold coincidence requirements for each of the 8 energy channels.

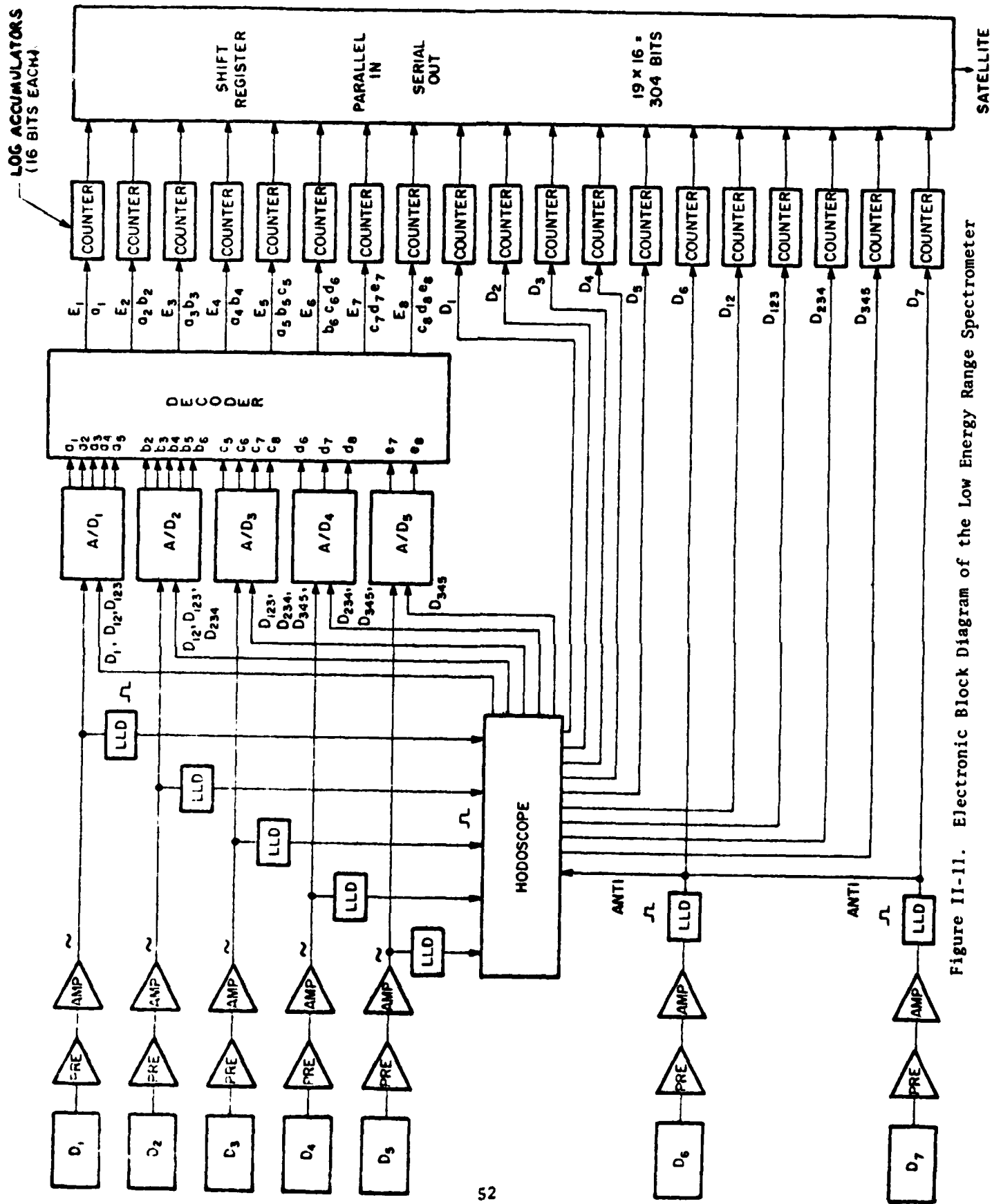


Figure II-11. Electronic Block Diagram of the Low Energy Range Spectrometer

TABLE II-5

Coincidence Scheme for the Low Energy Range

1.0					
	a ₁				
1.3					
	a ₂	b ₂			
1.6					
	a ₃	b ₃			
2.0					
	a ₄	b ₄			
2.6					
	a ₅	b ₅	c ₅		
3.5					
		b ₆	c ₆	d ₆	
4.6	a ₆				
			c ₇	d ₇	e ₇
6.0					
			c ₈	d ₈	e ₈
9.0					

3.0 DISCRIMINATION AGAINST BACKGROUND RADIATION

3.1 Theoretical Considerations

An ideal instrument should analyze only particles of a single known species arriving within a known solid angle about a known direction. Only then can the full physical significance of a measurement be exploited. The instrument must therefore be capable of discriminating very strongly against all other particles - that is, either not detect them, or reject them from analysis. Such other particles constitute a background to the basic desired measurement, and the number of recorded events resulting from them must be a small fraction of the number of recorded events of the desired category.

We may distinguish three classes of such background:

- a. Background arising from particles of the opposite species (e.g. by electrons in a proton spectrometer) which arrive through the entrance aperture.
- b. Background arising from particles of either species (protons or electrons) which are energetic enough to penetrate the shielding about a detector.
- c. Bremsstrahlung background arising from electrons striking the spacecraft and shielding material.

We can derive general approximate expressions for the contribution of each class of background to the measurement. These expressions will be applied in the specific case of the proton spectrometer. The results of such analysis are to be considered as a guide only; actual evaluation of the ability of an instrument to discriminate against background

must await calibration and test procedures.

We consider first background arising from particles of the opposite species which arrive through the entrance aperture. For proton spectrometers using a pulse height analyzer (PHA), a sweeping magnet ahead of the entrance aperture can be utilized to exclude electrons of energies up to several MeV.

Let

$j(E, \Delta E, i)$ be the unidirectional intensity of primary particles of species i ($i = p$ or e for proton or electron respectively) which are detected by an instrument, within an energy channel of width ΔE above E at an arbitrary pitch angle;

$j_B(E_B + E_0, \Delta E_B, i_B)$ be similarly defined for the background radiation;

$P_B(E_B, \Delta E_B, i_B)$ be the probability of detecting a background particle; this depends specifically upon the instrument;

E_0 be the minimum energy required for a background particle to reach a detector;

f_a be the ratio of background to primary radiation

Then

$$f_a = \frac{j_B(E_B + E_0, \Delta E_B, i_B)}{j(E, \Delta E, i)} P_B(E_B, \Delta E_B, i_B) \quad (1)$$

We point out that for spectrometers using PHA from solid state detectors $E_B = E$ and $\Delta E_B = \Delta E$, but this need not be so in the general case. For threshold detectors - i.e., for either or both of ΔE_B and ΔE approaching infinity, the corresponding j is an energy integral omni-directional flux. We may also omit certain symbols in arguments of functions where no

misunderstanding can arise.

P_B can be minimized by electronic techniques, such as by making dE/dx measurements on the incident particle and using this as a basis for acceptance or rejection of a pulse for analysis. In such cases, P_B depends upon statistical fluctuations in the energy deposited by the background particle in a dE/dx detector. P_B may be evaluated in such cases by following the procedures given by Rossi⁴⁹⁾ for determining the probability that more than a certain threshold energy be deposited in a given absorber by a particle of given incident energy. P_B may be further minimized by additional electronic constraints such as many-fold coincidence, or anti-coincidence requirements.

Consider next background arising from particles of either species which are energetic enough to penetrate the shielding about a detector; Let:

A, Ω denote detection areas and solid angles respectively; subscript

B will refer, as before, to background particles;

E_0 be the average energy required to penetrate the shielding over all of space (4π steradians) about a detector;

f_c be the ratio of background counts to primary counts for this case.

Then we have in a single detector:

$$f_c = \frac{A_B \Omega_B}{A \Omega} \frac{j_B(E_B + E_0, \Delta E_B, i_B)}{j(E, \Delta E, i)} P_B(E_B, \Delta E_B, i_B) \quad (2)$$

In form, equation (2) differs from equation (1) by the coefficient involving the ratio of geometrical factors; this coefficient may be as large as 10^3 . On the other hand, the ratios of j 's will be much smaller,

since E_0 will be generally very large, of the order of 135 MeV for protons, and ~ 40 MeV for electrons. This term will thus compare, for example, fluxes of 135 MeV protons with fluxes of a few MeV protons ; this ratio will be small because of the steepness of proton spectra in the magnetosphere, except in the inner zone where the proton spectrum is known to be constant until $\sim E = 400$ MeV.

In the detectors where two-fold coincidence requirements are further imposed in order to analyze a particle, for coherent events (caused by scattering of the particle detected in one of a coincidence pair into the other), equation (2) is further modified by a geometrical factor g_{12} representing the probability that the scattered particle will scatter into the second detector of the coincidence pair, and by a factor analogous to P_B , call it P_{B2} , representing the probability that the particle will be detected in the second detector. Since a particle may also scatter from the second to the first, we thus have

$$f_c^{\text{coh}} = f_{c1} g_{12} P_{B2} (E_{B2}, \Delta E_{B2}) + f_{c2} g_{21} P_{B1} (E_{B1}, \Delta E_{B1}) \quad (3)$$

where subscripts 1 and 2 refer to detectors.

For incoherent events, i.e., accidental coincidences, the approximate expression for the ratio f_c^{acc} of background to primary counts is given by

$$f_c^{\text{acc}} = \frac{R_1 R_{c2} + R_2 R_{c1}}{A \Omega j(E, \Delta E)} 2\tau \quad (4)$$

where τ is the coincidence circuitry resolving time (about $2-5 \times 10^{-8}$ sec for the instruments proposed) and the R 's are singles counting rates in the logic of each detector. The absence of a c-subscript indicates a

total rate, not just due to the background particle alone being considered. The numerator of equation (4) is derived from the well known expression for accidental counting rates.

We finally consider bremsstrahlung background produced in the spacecraft. This is the most difficult type of background to deal with quantitatively, but we shall strive to derive an upper limit. A bremsstrahlung photon must undergo a Compton or photoelectric process in order to be detected at the energies of importance to us. We next note from geometrical considerations that bremsstrahlung production can be considered as all arising in shielding of the appropriate thickness (in g/cm^2) immediately surrounding a detector, and that the effective area for determining the number of electrons generating the bremsstrahlung is the projected area of the detector averaged over solid angle. Let:

$P_\gamma(E, E_\gamma) dE_\gamma$ be the probability that an electron of energy E produces a bremsstrahlung photon within the energy interval dE_γ about energy E_γ ;

Z be the atomic number of the shielding;

Then we will approximate:

$$P(E, E_\gamma) dE_\gamma \approx 10^{-3} Z dE_\gamma \quad (5)$$

This amounts to assuming a flat thick target bremsstrahlung spectrum.²⁴⁾

Equation (5) underestimates the number of low energy photons, but many of these would be absorbed within the shielding anyway. Since the equation also over-estimates the number of high energy photons, the approximation is probably on the safe side. The total number of such bremsstrahlung photons produced by electrons of all energies between E_γ and E_0 which could (in the absence of absorption)

impinge upon a detector is then approximately

$$10^{-3} Z \cdot 4\pi[j_B(E_\gamma) - j_B(E_0)] A_B dE_\gamma \quad (6)$$

or

$$10^{-3} Z \cdot A_B j_B(E_\gamma) dE_\gamma \text{ sec}^{-1} \quad (7)$$

where we have neglected the term $j_B(E_0)$. Now let:

$\mu_S(E_\gamma)$, $\mu_D(E_\gamma)$ be linear absorption coefficients for photons of energy E_γ in the shielding and detector respectively;
 x_S , x_D be characteristic thicknesses of shielding and detector respectively.

Then approximating the energy of a Compton recoil electron by the incident photon energy, a fair approximation at energies above 1 MeV, somewhat worse at lower energies,¹²⁾ replacing γ subscripts by B to indicate that charged particles causing background are now involved, we approximate the differential background spectrum of electrons from bremsstrahlung interactions in the detector by:

$$10^{-3} Z \cdot A_B \exp[-\mu_S(E_B)x_S] \exp[-\mu_D(E_B)x_D] j_B(E_B)\Delta E_B \text{ sec}^{-1} \quad (8)$$

Thus, where:

f_b is the ratio of background counts arising from bremsstrahlung to primary counts, we have in a single detector:

$$f_b \approx \frac{10^{-3} Z \cdot A_B \exp(-\mu_S x_S) \exp(-\mu_D x_D) j_B(E_B)\Delta E_B}{A\Omega j(E, \Delta E_B)} P_B(E_B, \Delta E_B) \quad (9)$$

In detectors where two-fold coincidence requirements are further imposed, we obtain modified expressions for f_b , which we denote by f_b^{coh} and f_b^{acc} in complete analogy to equations (3) and (4):

$$f_b^{\text{coh}} \approx f_{b1} g_{12} P_{B2}(E_{B2}, \Delta E_{B2}) + f_{b2} g_{21} P_{B1}(E_{B1}, \Delta E_{B1}) \quad (10)$$

and

$$f_b^{\text{acc}} = \frac{(R_1 R_{b2} + R_2 R_{b1}) 2\tau}{A\Omega j(E, \Delta E)} \quad (11)$$

A final word about notation: the various f functions used may be followed by arguments to further classify the function.

As pointed out, such analysis is to be accepted as suggestive only. Actual evaluation of the ability of an instrument to discriminate against background must await full calibration and testing.

We should finally mention that any background that arises from radiation which penetrates shielding, and which is therefore fairly independent of the instrument's orientation, can be measured rather accurately by observing counting rates when the instrument's detection vector lies outside the pitch angle cutoff, i.e., within the loss cone. At such times, the counting rate due to primary particles will be zero, and any counts observed will thus be due to such background alone. Thus this measured background can be subtracted from the total counts observed at an arbitrary pitch angle to obtain a true primary particle count rate.

In our estimate of the background counting rates due to the different sources which have been identified, we evaluate these different backgrounds in regions of space where the ratios of the intensity of the particular background source to the primary radiation is maximum. Thus,

when calculating background counting rates due to high energy electrons, we chose the region of space at $L \approx 4.0$ (Figure II-6). When concerned with penetrating high energy protons, we consider $L \approx 1.15 - 1.50$, where the proton energy flux spectrum is constant, or nearly constant, in intensity up to several hundred of MeV (Figure II-12).

3.2 Background Estimates for the High Energy Range Head Assembly

Consider first for Equation (1), the fraction of analyzed events due to high energy electrons entering the aperture proper. We have

$$J_B (4 \text{ MeV}, \infty, e) \approx 3.5 \times 10^4 \text{ el/cm}^2 \cdot \text{sec}$$

$$J (6 \text{ MeV}, \infty, p) \approx 3.5 \text{ p/cm}^2 \cdot \text{sec}$$

J_B 's and J 's are omnidirectional fluxes. E_0 is chosen as 4 MeV since all of the electrons with lower energies will be swept away from the exit aperture, immediately in front of the detectors, by the sweeping magnet. The G-factor for protons is $0.12 \text{ cm}^2\text{-ster}$. For electrons, the G-factor is not a constant but varies with the energy of the electrons, only having the value of $0.12 \text{ cm}^2\text{-ster}$ for particles hardly affected by the magnetic field, i.e. for $E_e \gg 4 \text{ MeV}$. However, to be conservative in our estimates, we take $G = 0.12 \text{ cm}^2\text{-ster}$, independent of energy. Thus,

$$f_a \approx 10^4 P_B(e)$$

We first calculate the probability of interaction, $P_B(e)$, with only the 1st detection (400 μm depletion depth). We consider a 4 MeV electron which will deposit amounts of energy in excess of critical energy thresholds, i.e., 0.54, 1.0 and 2.78 MeV. These probabilities are: $P_B (E > 0.54 \text{ MeV}) \approx 10^{-2}$, $P_B (E > 1.0 \text{ MeV}) \approx 1.2 \times 10^{-3}$ and

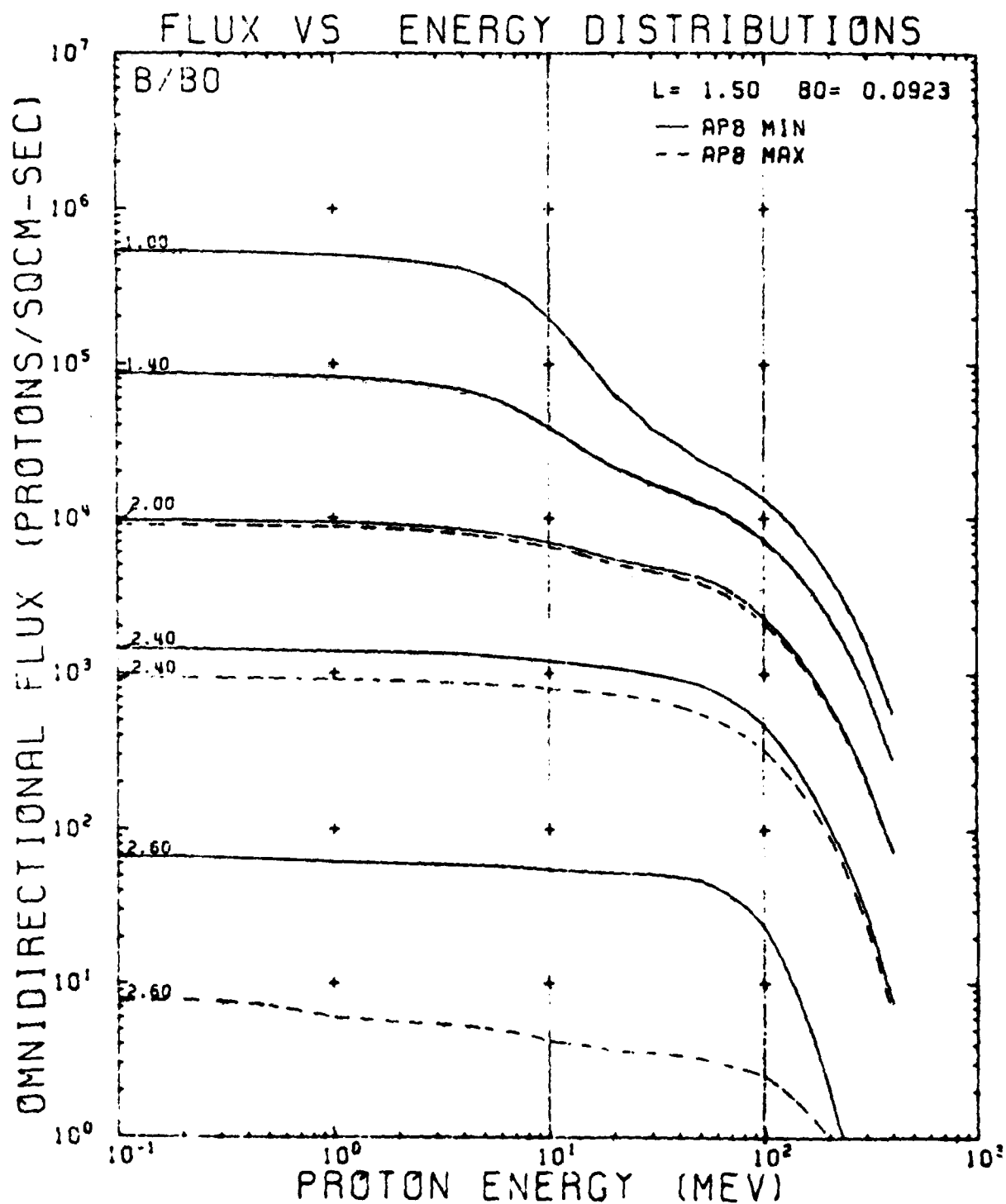


Figure II-12. Proton Omnidirectional Flux versus Energy for Different B/B_0 , at $L=1.50$ (Sawyer and Vette, 1976)

$P_B (E > 2.78 \text{ MeV}) \approx 0.0$. These energies are chosen according to Table II-1, for reasons which will soon become evident.

Events which deposit more than 0.54 MeV in that detector will fire the low level discriminator. Thus, in this case

$$f_a \approx 10^2.$$

However, when one adds the energy requirements for a genuine proton event which does not require any other interaction with any of the other detectors ($6.0 \lesssim E_p \lesssim 9.3 \text{ MeV}$), and therefore must lose 2.78 - 6.95 MeV in that 1st detector,

$$f_a \approx 0.0$$

since $P_B(e)$ approaches 0.

Thus we see that electrons with $E_e > 4 \text{ MeV}$ will not contribute background counts in the first 2 channels of the high energy range spectrometer. It should further be noted that the expected counting rate of 4 MeV electrons is $\lesssim 3.3 \times 10^2 \text{ el/sec}$, and should not produce any pile-up problem in the detector. The electronic shaping time-constants are such as to allow for total counting rates $\sim 10^5 \text{ cts/sec}$.

The probabilities, $P_B(e)$, increase as an electron penetrates the stack of detectors due to the decreasing energy loss of the particle as well as the increasing thicknesses of the detectors. However, the additional constraints in the form of coincidence requirements between coherent events and the energy deposition requirements will further reduce the total $P_B(e)$ for a particular energy channel. For example in the 9.15 - 12.7 MeV range we require that a proton should deposit

3.12 - 6.95 MeV and 1.0 - 7.8 MeV in the 1st and 2nd detectors, respectively. The probability that a 4 MeV electron will deposit that is $< 1.4 \times 10^{-6}$, since $g_{12} \approx 1.0$ (Eq. 3), but this probability calculation does not take into account the low probability that the electron will scatter after the 2nd detector in such a way not to be detected by the remaining 3rd-5th detectors. Also, one should note that the 2nd term in Equation (3) can be neglected because g_{21} is less than 1% for $E_e > 4$ MeV.

In the energy range 12.7 - 100 MeV, where triple coincidence is required, the probability of a 4 MeV electron producing the required coincidences and deposit $E \gtrsim 1$ MeV vary from $P_B(e) \approx 2.0 \times 10^{-7}$ to $P_B(e) \approx 6.25 \times 10^{-4}$. Again the added well-defined energy deposition requirements further reduce these probabilities by order-of-magnitudes.

Thus, we see from these calculations that the background in the instrument due to electrons with $E_e \gtrsim 4$ MeV entering through the front aperture will be of no concern in the data analysis.

We have not attempted to calculate the background counting rate due to electrons with $E_e < 4$ MeV, which are deflected by the magnet, and which after multiple scattering will find their way into the detectors. Since multiple-scattering is required, this is second or higher-order process which, when coupled to the small solid angle subtended by the detector stack, will result in a negligible contribution to the total counting rate.

Next, we calculate the background due to high energy particles which penetrate the shieldings, leading to f_c .

Electrons will not be able to penetrate the massive passive shielding (1.33 cm brass and 1.20 cm lead thicknesses), and to directly interact

with the detectors, i.e. $P_B(e) = 0$. However these high energy electrons will produce a bremsstrahlung spectrum in this same brass shielding. This source of background will be treated below.

Protons penetrating through the shield, perpendicularly (or nearly) to the length of the cylinder made up of the detector stack, will be anti-coincided by the live shielding, i.e. the ring concentric to each detector. Thus, again $P_B(p) \approx 0$.

Only high energy protons which are incident on the shielding material at an appropriate angle will, after losing energy in that shielding, interact with the detectors.

First, we calculate the counting rate in the first detector alone. We can think of this counting rate being produced by the flux of high energy protons which lose all their energies in the shield minus ~ 7 MeV. In that case they will be stopped in the 1st detector as would 6 - 9.15 MeV protons entering through the front aperture. We estimate that

$$A_B \Omega_B \approx \pi \text{ cm}^2\text{-ster}$$

Using

$$J_B (135 \text{ MeV}, \infty, p) \approx 8 \times 10^3 \text{ p/cm}^2\text{-sec}$$

$$J (6 \text{ MeV}, \infty, p) \approx 3.0 \times 10^5 \text{ p/cm}^2\text{-sec}$$

since $A\Omega = 0.12 \text{ cm}^2\text{-ster}$, we obtain

$$f_C(p) \approx 0.70 P_B(p)$$

and since $P_B(p) = 1$, then

$$f_C(p) \approx 0.70 P_B(p)$$

However our assumption that all of the high energy protons penetrating the outer shield lose precisely all of their energy minus the

energy required to trigger the first detector alone is rather unrealistic. Rather we start with a proton spectrum, incident on the shield at a wide range of angles, thus resulting in a continuum spectrum of protons striking the detectors. Thus this calculated $f_c(p)$ is a "worst case" upper limit. Furthermore at other $L > 1.5$ values, the proton energy spectrum becomes softer very fast. For example, at $L = 2.0$, and at the equator,

$$J_B (135 \text{ MeV}, \infty, p) \approx 1.4 \times 10^2 \text{ p/cm}^2\text{-sec}$$

$$J (6 \text{ MeV}, \infty, p) \approx 1.0 \times 10^6 \text{ p/cm}^2\text{-sec}$$

and

$$f_c(p) \approx 4 \times 10^{-3} P_B(p) \approx 4 \times 10^{-3}.$$

Similar calculations for the energy range 9.15-12.7 MeV can be carried out. If we first look at the count rate in the low level discriminator produced by the penetrating protons with $E_p > 135 \text{ MeV}$, we obtain, using $A_B \Omega_B \approx \pi \text{ cm}^2\text{-ster}$, and

$$J_B (135 \text{ MeV}, \infty, p) \approx 8 \times 10^3 \text{ p/cm}^2\text{-sec}$$

$$J (10 \text{ MeV}, \infty, p) \approx 2 \times 10^5 \text{ p/cm}^2\text{-sec}$$

$$f_c(p) \approx 1.0 P_B(p)$$

and since $P_B(p) \approx 1$,

$$f_c(p) \approx 1.0.$$

Again, our assumption is that all of the penetrating protons, will lose enough energy in the shield such as to have the precise energy remaining to trigger the one-shot in the first and second detectors. If

one adds the energy requirements in the first two detectors, one sees that most likely $f_c(p)$ will be reduced by several order-of-magnitudes.

We thus expect that the penetrating high energy protons will not be a problem even at low L values where the fluxes are most intense.

Finally, let us examine the detector background due to bremsstrahlung resulting from the interaction of the high energy electrons with the S/C and the shielding material of the telescope. We will neglect the bremsstrahlung produced in the S/C ($Z \approx 14$), and instead assume that all of the electrons strike the brass shielding ($Z = 29$).

Using the "Tiger" code developed at the Oak Ridge National Observatory, and the electron spectrum shown in Figure II-6, we have calculated the resulting transmitted bremsstrahlung energy spectrum and angular distribution. Figure II-7 shows the resulting γ -ray spectrum up to 1 MeV. The minimum energy a photon should have in order to trigger the one-shot is 1 MeV (except for the 1st detector where 0.54 MeV is needed). The calculations show that

$$\begin{aligned} J_B (1 \text{ MeV}, \infty, \gamma) &\approx (3.3 \times 10^{-5} \gamma/e) (3 \times 10^6 \text{ e/cm}^2\text{-sec}) \\ &\approx 1.0 \times 10^2 \gamma/\text{cm}^2\text{-sec.} \end{aligned}$$

Furthermore,

$$J (6 \text{ MeV}, \infty, p) \approx 3.5 \text{ p/cm}^2\text{-sec.}$$

We estimate the effective area for interaction of the electrons with the shielding at $\sim 75 \text{ cm}^2$,

$$J_B (1 \text{ MeV}, \infty, \gamma) \approx 2.36 \times 10^4 \gamma/\text{sec.}$$

The $A_A \Omega_A \approx \pi^2 \text{ cm}^2\text{-ster}$. Therefore,

$$f_b(\gamma) = 5.52 \times 10^5 P_B(\gamma)$$

Given that the photoelectric (μ/ρ) for silicon at 1 MeV is $0.002 \text{ cm}^2/\text{gr}$, we can calculate $P_B(\gamma)$. The average thickness of the 1st detector is $\sim 0.52 \text{ cm}$. Thus

$$\begin{aligned} P_B(\gamma) &= (1 - \exp(-0.002 \times 2.33 \times 0.52)) \\ &= 2.34 \times 10^{-3} \end{aligned}$$

and

$$f_b(\gamma) = 1.29 \times 10^3$$

This number is very large indeed, but the underlying assumptions made in the calculations are too simpleminded. First we should take into account the angular distribution of the γ -rays. Most of the intensity comes out in a cone of $\frac{1}{2}$ angle $\approx 20^\circ$. Thus J_B would be reduced to $\sim 6.3 \times 10^3 \text{ } \gamma/\text{sec}$, and the geometrical factor becomes $0.45 \pi \text{ cm}^2\text{-ster}$. Since $P_B(\gamma)$ will not change appreciably we have

$$f_b(\gamma) \approx 50.$$

This number is still quite high and would still exclude a measurement in the 1st detector alone. We must consider now the energy requirements set for the measurement of 6-9 MeV protons. The energy threshold equals 2.8 MeV. Thus

$$J_B(2.8 \text{ MeV}, \infty, \gamma) \approx 30 \text{ } \gamma/\text{cm}^2\text{-sec}$$

or

$$J_B(2.8 \text{ MeV}, \infty, \gamma) \approx 1.9 \times 10^3 \text{ } \gamma/\text{sec}$$

The (μ/ρ) at 2.8 MeV should be $\sim 1/10$ the value at 1 MeV, or 2.0×10^{-4} .
Thus $P_B(\gamma) = 3.0 \times 10^{-4}$ and

$$f_b(\gamma) = 1.9.$$

This number is still too large for a proper measurement to be performed in the 6-9 MeV range. However, we have further neglected the scattering of γ -rays into the other detector(s), which would result in the event in the 1st detector to be anti-coincided. Also the efficiency of the anti-coincidence ring surrounding each detector has not been considered. Thus we would expect the calculated $f_b(\gamma)$ to be reduced appreciably, may be by one or two orders of magnitude.

Thus, from the above estimates, we can conclude that there should be no background problems in the proposed instrument. However definite conclusions must await final instrument testing at accelerators.

3.3 Background Estimates for the Low Energy Range Head Assembly

We now consider in a similar approach the background expected in the head assembly measuring the proton spectrum in the 1-9 MeV energy range.

First, consider the electrons which penetrate the front aperture.

$$J_B(5 \text{ MeV}, \infty, e) \approx 2.0 \times 10^3 \text{ el/cm}^2\text{-sec}$$

$$J(1 \text{ MeV}, \infty, p) \approx 3.0 \times 10^6 \text{ p/cm}^2\text{-sec.}$$

E_0 is chosen as 5 MeV since all of the electrons with lower energies will be swept away from the exit aperture. Thus

$$f_a(e) \approx 0.6 \times 10^{-3} P_B(e)$$

Since $P_B(e)$ is very small ($\ll 10^{-3}$),

$$f_a(e) \approx 0.$$

The background due to penetrating protons is now being considered. A high energy proton ($E_p > 135$ MeV). If we make the simple-minded assumption that all these protons lose all of their energy in the passive shield minus 1 - 1.2 MeV needed to trigger the 1st detector, we have

$$J_B (135 \text{ MeV}, \infty, p) \approx 8 \times 10^3 \text{ p/cm}^2\text{-sec}$$

$$J (1 \text{ MeV}, \infty, p) \approx 5 \times 10^5 \text{ p/cm}^2\text{-sec}$$

Since $A_B \Omega_B \approx 0.4\pi \text{ cm}^2\text{-ster}$ and $A\Omega = 1.2 \times 10^{-2}$, we have

$$f_c(p) \approx 1.7 P_B(p).$$

The above assumption that each penetrating proton loses all of its energy minus the 1 - 1.2 MeV needed for the 1st detector, is obviously quite unrealistic. We would expect that the actual penetrating proton flux which fulfill these assumptions to be several order-of-magnitudes smaller.

Concerning the measurement at higher energies which require coherent events in 2 or 3 detectors, let us consider a high energy proton which would penetrate through the shielding material (collimator, magnet, etc.) and having (6-9 MeV) remaining energy, would trigger the 1st and last detectors. $A_B \Omega_B$ for that case $\approx 5 \times 10^{-2}$

$$J_B (135 \text{ MeV}, \infty, p) \approx 8 \times 10^3 \text{ p/cm}^2\text{-sec}$$

$$J (6 \text{ MeV}, \infty, p) \approx 3 \times 10^5 \text{ p/cm}^2\text{-sec}$$

and

$$f_c(p) \approx 0.11 P_B(p).$$

Again since a small fraction of the protons with $\langle E_p \rangle > 135$ MeV will have just 6 - 10 MeV left after passage through the outer shield of the spectrometer, we expect $f_c(p)$ to be several order-of-magnitudes less than that calculated above.

Finally we consider the bremsstrahlung background induced counts. The lower energy threshold in each detector is 0.25 MeV. From our calculations with the "Tiger" computer program, we get:

$$\begin{aligned} J_B(0.25 \text{ MeV}, 2 \text{ MeV}, \gamma) &\approx (4 \times 10^{-3} \gamma/e)(10^7 \text{ e/cm}^2\text{-sec}) \\ &= 4 \times 10^4 \gamma/\text{cm}^2\text{-sec} \end{aligned}$$

$$\text{or } J_B(0.25 \text{ MeV}, 2 \text{ MeV}, \gamma) = 5 \times 10^6 \gamma/\text{sec}$$

$$\text{and } J(1 \text{ MeV}, \infty, p) \approx 3 \times 10^6 \text{ p/cm}^2\text{-sec}$$

Since $A_A \Omega_A \approx .35\pi$

$$f_b(\gamma) \approx 154 P_B(\gamma)$$

$$P_B(\gamma) = (1 - \exp(-0.04 \times 2.33 \times .6)) = 5.4 \times 10^{-2}$$

and

$$f_b(\gamma) = 8.3$$

When the energy requirements are imposed on the 1st detector (1-1.2 MeV)

$$J_B(1 \text{ MeV}, 0.2 \text{ MeV}, \gamma) \approx (2.7 \times 10^{-4} \gamma/e)(3 \times 10^6 \text{ e/cm}^2\text{-sec}) \approx 810$$

or

$$J_B(\text{total}) \approx 1 \times 10^5 \gamma/\text{sec}$$

$$f_b(\gamma) \approx 3.1 P_B(\gamma)$$

And since

$$P_B(\gamma) = (1 - \exp(-0.002 \times 2.33 \times .6)) = 2.8 \times 10^{-3}$$

we have

$$f_b(\gamma) = 9 \times 10^{-3}$$

The above calculations show that no background problem should exist in the measurements of protons in the 1-9 MeV range. Again we should await for the testing of the actual detector using particle accelerators to fully appreciate the efficiency of the design as far as background is concerned.

4.0 CALIBRATION

Preliminary alignment and calibration of this proton spectrometer involves setting amplifier gains, discriminator thresholds, and voltage dividers defining the lower and upper level of the different energy channels.

Complete final calibration of this spectrometer involves

- a) measurement of the geometrical factor;
- b) calibration of the energy scale, i.e., determining upper lower energy limits for each channel and the "sharpness" of each;
- c) calibration of the counting logic;
- d) calibration of the voltage monitor circuits;
- e) determination of the electron energy cut-off by the magnet;
- f) investigation of the susceptibility of the spectrometer to penetrating high energy protons.
- g) investigation of the susceptibility of the spectrometer to bremsstrahlung.

For the preliminary alignment, we will use an Am^{241} source which emits 5.5 MeV α . For the low energy range we will trim the different gains of the preamplifiers and amplifiers so as to yield ~ 2.75 volts for the 5.5 MeV, α -particle energy, or 0.5 MeV/volt. The 8-channel voltage dividers can then all be set to define very nearly the upper level energy values desired, by linear interpolation. This interpolation can actually be verified using a pulser whose rise and fall times have been adjusted to match the pulse shape at the preamp output resulting from the Am^{241} α -particle interaction with the detector. The same procedure will be followed for the high energy range, with

the output of the amplifiers set to ~ 20 MeV/volt.

Two proton accelerators will be required for the calibration of this instrument. In the 1-10 MeV energy range, a Van de Graaf accelerator will be used. In the 10-100 MeV energy range, we will use an accelerator such as the Harvard synchro-cyclotron. The geometrical factor can best be determined at high energy from the plots of count rate versus angle with respect to a unidirectional beam covering the whole area of the entrance aperture. A scattering foil will be required to reduce the beam intensity sufficiently to prevent saturation. The unscattered beam current will be monitored for normalization of data. For the low and high energy range no vacuum is needed. The instrument heads can be placed on a goniometer in air, since a beam of ~ 8 MeV and ~ 100 MeV can be used.

The usual technique of calibrated absorbers in the beam to degrade the energy of the particles extracted from the accelerators will be used to calibrate the energy scale. Fine control on the energy of the particles penetrating the absorbers will be achieved by rotating one absorber through known angles. Calibration accuracy thus depends upon the accuracy of range energy tables, such as the Lawrence Radiation Laboratory Tables which are good to a few percent. Calibration data obtained directly will thus be the count rate in each channel as a function of interposed absorber thicknesses (in g/cm^2). With a known incident energy, the residual energy (the energy incident upon the detectors) can thus be calculated accurately.

To determine the electron energy cut-off of the sweeping magnets, we will use an electron accelerator such as the LINAC at AFGL. The electron

beam, at an energy above the expected energy cut-off will be made to impinge on the aperture, and the counting rate in the instrument will be monitored. Known thicknesses of absorber will be placed in front of the instrument aperture in order to degrade the electron beam until no counts are recorded in the instrument thus determining the energy cut-off. The beam will be constantly monitored to normalize the count rates in the detectors.

The susceptibility of the spectrometer to penetrating high energy protons will be carefully investigated using high energy accelerators. The minimum energy need is ~ 135 MeV, which is the expected cut-off of the passive shielding. Higher energies will be needed, up to 200 MeV if possible. The instrument will be placed, in air, on a goniometer and the counting rates due to penetrating high energy protons recorded as a function of angle for a given energy. The energy spanned should be from slightly below the expected energy cut-off at ~ 135 MeV to 200-300 MeV.

High energy electrons (1-6 MeV) are not expected to penetrate the the passive shielding but the bremsstrahlung they produce should also be carefully investigated. We will use the electron beam of the LINAC, at 3, 4 or 5 MeV, to bombard the spectrometer head outside the aperture. The head assembly will be mounted in air, on a goniometer, and the susceptibility of the detectors to γ -rays will be investigated as a function of angle and energy.

Both, in the cases of the penetrating high energy protons and electron bremsstrahlung, the efficiency of the silicon rings, the live anti-coincidence shell surrounding each detector, will be ascertained by switching on and off the anti-coincidence circuitry. This test should be performed also at different angles of incidence of the beam, and different energies.

III. SOLID STATE NUCLEAR TRACK DETECTORS

1.0 EXPERIMENTS AT BROOKHAVEN NATIONAL LABORATORY

A new polymer track detector based on monomer ALLYL DIGLYCOL CARBONATE, which goes by the commercial name of CR-39, has been developed to measure the composition, flux and energy spectra of trapped particle, using Long Duration Exposure Facility of NASA.

In recent years solid state nuclear track detectors have found widespread applications. Track etching technique has been successfully employed in many insulating materials for detection and identification of charged particles, e.g. in the study of heavy primary cosmic rays, the search for super heavy elements and exotic particles, recording of fission fragments and innumerable applications in radiation dosimetry. Early in the past decade cellulose nitrate was recognized as the most sensitive of all track detectors and so has been used as a detector to record protons. However, cellulose nitrate suffers from being inhomogeneous and anisotropic with regard to its physical characteristics. These defects reveal themselves in non-geometrical track profiles, differences in sensitivity in a given sheet, and varying bulk etch rate.

CR-39 is a very useful addition to the range of plastic track detectors that are available for studies relating to primary cosmic rays, radiation dosimetry and other applications. The thermoset plastic sheet cast from CR-39 monomer has been found to have a unique sensitivity and resolution in recording of nuclear particles. This material was found to have a lower detection threshold ($Z/\beta = 7$) than cellulose nitrate ($Z/\beta = 30$) and a smaller variation of response ($\approx 1\%$) to particles of a given ionization rate than Lexan polycarbonate ($\approx 3-8\%$). CR-39 is an ideal detector for this experiment because very low energy protons are registered. The track etching rate is only slightly greater than bulk etch rate for protons, and hence normally incident protons are registered.

The samples of CR-39 which we have used for experiments at Brookhaven Laboratory were obtained from Polytech Inc., Owensville, Missouri. The sheets (1500 μm thick) were cast from monomer allyl diglycol carbonate manufactured by Pittsburgh Plate Glass Co. Samples of size $(2.5 \times 2.5) \text{ cm}^2$ were exposed to a beam of protons from the van de Graff generator at Brookhaven National Laboratory.

The beam was tuned to four different energies, viz., 1.5 MeV, 2.2 MeV, 3.2 MeV and 4.3 MeV. The corresponding fluences were: 2.8×10^5 particles/cm², 0.44×10^6 particles/cm², 0.67×10^6 particles/cm² and 0.91×10^6 particles/cm². All irradiations were carried out in such a manner their particles are nearly normally incident to the surface of the plastic sheet.

After irradiation the samples were etched in a solution of 6.25 N sodium hydroxide solution at 50°C in four different batches for 7 h, 17 h, 30 h and 48 h. After etching, measurements were made on track profiles due to protons using a KORISTKA R₄ microscope. In Figure III-1 are shown the distribution of track diameters for protons from samples etched for 30 h for all incident energies. The distribution clearly show an excellent energy resolution for protons of different energies. Figure III-2 shows etch pit diameter as a function of proton energy. The samples etched for 48 h show a maximum slope, thereby indicating a better resolution. In earlier investigations it has been recognized that measurements of track diameter as a function of the amount of bulk material removed can be used for identification of nuclear particles. This method is applicable for particle tracks which lie in the region of detection limit such as protons where the track diameter is a more sensitive function of ionization rate than track length. In principle the method should work for particles incident at arbitrary angles on a solid surface, but in practice it is much simpler if the detector can be positioned such that particles are nearly normally incident. The amount of bulk material removed is defined as

$$h = \int_0^t Vg \, dt$$

where Vg is the bulk etch rate. In order to determine the value of Vg for CR-39, small areas of detectors were irradiated in vacuum with fission fragments from ²⁵²Cf source and then etched for a definite period of time. The bulk etch rate is given by

$$Vg = D/2t$$

where D is the diameter of fission fragment tracks and t is the etch time and finally h is given by Vgt . Figure III-3 shows etch pit diameters as a function of amount of bulk material removed from one surface for various etch times and for all incident energies. We developed a computer code to describe the diameter evolution of proton tracks as a function of amount of bulk material removed. The theoretical curves in Figure III-3 were obtained using this computer code.

From these irradiations at Brookhaven National Laboratory, we conclude that, a) CR-39 track detector registers protons up to 4.3 MeV, b) the detection efficiency at these energies is close to 100%, c) the diameter distributions clearly show an excellent energy resolution for protons of different energies and, d) the etch pit diameter as a function of amount of bulk material removed from one surface for various etch times and for all incident energies was obtained.

2.0 EXPERIMENTS AT NASA-LEWIS RESEARCH CENTER

The sheets of CR-39 which we have used in this investigation were obtained from PERSHORE MOULDINGS, Ltd., England. We have for the first time employed this detector for the detection of 6-MeV and 10-MeV protons, 70 MeV ^3He ions, and 52-MeV ^4He ions and have obtained a smooth variation of normalized track etching rate as a function of residual range. Our results also indicate that CR-39 will register perpendicularly-incident particles with a value of Z/β as low as 7.

The irradiation arrangement at the NASA-Lewis Research Center's Cyclotron is shown schematically in Figure III-4. This drawing shows the pertinent part of the beam line where bending and focusing magnets are adjusted to produce a 10 mm beam spot upon a 2.5 μm tantalum foil. This foil is centered in a 0.1 m diameter beam duct at a position immediately in front of 6 m shielding wall. Small angle scattering in the foil produces a uniform flux distribution over a 75 mm diameter circle located at the far side of the shield wall. A measurement of the induced radioactivity at this position showed that the particle flux varies less than $\pm 5\%$. The inset in Figure III-4 shows the 75 mm diameter end plate onto which the CR-39 sheets were affixed with double-face adhesive tape. A gold surface barrier detector was mounted to a BNC feed-trough connector. The detector was used to monitor the number of particles passing through the 3 mm diameter tantalum collimator located immediately in front of the detector. Because of the uniformity of the particle distribution, the total number of detector pulses in an irradiation was used to determine the particle fluence of the CR-39 sheet.

After mounting the CR-39 sheets, the end plate was held against the "O" ring at the end of the beam duct and the roughing valve V opened to remove most of the air. The atmospheric pressure holds the end plate in position and the gate valve was opened to place the sheets in the high vacuum of the beam duct. Following the above procedure, three stacks of CR-39 sheets were exposed to 6 and 10-MeV protons, 70-MeV ^3He ions and 54-MeV ^4He ions. For proton and ^4He irradiations, sheets of thin CR-39 (each 100 μm thick) were used, while for ^3He

exposure sheets of thick CR-39 (each 500 μm thick) were employed. In all these irradiations the beam was normally incident to the surface of the detector.

The stacks exposed to protons, ^3He ions and ^4He ions were etched for 74, 49.5 and 47 h respectively in a solution of 6.25 N sodium hydroxide solution at 50°C. Precision measurements were made on the surface diameter of tracks due to protons, ^3He ions and ^4He ions in all sheets. The measurements were made with a Koristka R4 microscope using a X80 Zeiss dry objective and X10 widefield American optical eyepiece. It should be pointed out that no attempt was made to follow individual tracks into various sheets. Rather, a large sample of tracks was measured on each surface of the detector and the mean diameter was computed. The track etching rate was estimated using the relation:

$$\frac{V_T}{V_g} = \frac{h^2 + r^2}{h^2 - r^2}$$

where V_T is the track etching rate, V_g is the bulk etching rate, r is the surface radius, and h ($= V_g t$) is the amount of bulk material removed from one surface during an etching time t . The particle's residual range is determined by adding the thickness of each sheet from the stopping point to the top of the stack taking into account the surface layer removed during etching. The residual ranges of 10-MeV protons, 70-MeV ^3He and 52-MeV ^4He were compared with our range-energy tables and found to be in good agreement. For each value of track etching rate, an appropriate value of residual range was assigned to obtain an experimental point on an etching rate versus residual-range curve. Figure III-5 shows the variation of normalized track etching rate as a function of residual range. The experimental data have been fitted with the function:

$$V = \frac{V_T}{V_g} = A J^{1/2}$$

where

$$J = (Z_{\text{eff}}^2 \beta^{-2}) [K + \ln \beta^2 \gamma^2 - \beta^2]$$

The effective charge, Z_{eff} , of an ion of atomic number Z and with a velocity β can be expressed as

$$Z_{\text{eff}} = Z[1 - \exp(-130Z^{-2/3})]$$

A and n are constants. Assuming $K = 20$, the data have been fitted with the function. Our results suggest that the response of CR-39 to protons can be represented as a function of $V = 0.801 J^{0.036}$, while $V = 0.516 J^{0.112}$ for the ^3He and ^4He .

In Table III-1 are presented the detection thresholds for various track detectors. A value of $Z/\beta = 7$ for CR-39 plastic makes it an excellent detector to study the charge composition of heavy cosmic rays over a wide range of Z . Also, a comparison was made between track densities due to protons, ^3He ions and ^4He ions in CR-39 sheets and the counts given by the silicon detector, and it was found that the registration efficiencies were close to 100%. Figure III-6 shows the photomicrograph of mouths of etched tracks of 6-MeV protons. In Figure III-7 are shown photomicrographs of mouths of etched tracks of 1.5-MeV protons, 70-MeV ^3He and 52-MeV ^4He ions.

TABLE III-1
Detection Thresholds for Various Track Detectors

	Lexan Polycarbonate	Cellulose Nitrate	CR-39
Z/β	60	32	7

From these irradiations at NASA-Lewis Research Center, we conclude that a CR-39 track detector registers 10-MeV protons, 70-MeV ^3He and 52-MeV ^4He . The detection efficiencies for these particles in these energy bands is close to 100%. CR-39 will register tracks of perpendicularly-incident particles with Z/β as low as 7. Our results also indicate that clear discrimination would be possible between isotopes ^3He and ^4He .

3.0 LONG DURATION EXPOSURE FACILITY (LDEF)

The Long Duration Exposure Facility of NASA will be placed in a 450-km circular, 30° inclination orbit around December 1983 by the space shuttle and recovered approximately twelve months later. The facility consists of a twelve-sided cylinder (Figure III-8) 30 feet long by 14 feet in diameter. Each side consists of six trays of experiments and each end has eight trays. This experiment will occupy one-sixth of a tray on three sides and one-fourth of a tray on the earth side. Appropriate mounting panels allow four equal boxes 12 inches square by 5 inches to be used as shown in Figure III-9.

LDEF will be gravity gradient stabilized and carefully placed so that total stabilization will occur through most of the twelve months. Under these conditions the orbital exposure to trapped protons in the south Atlantic is closely approximate to those which prevailed on Air Force satellites during the 1960's. During this period a study of trapped proton fluxes was carried resulting in the long-time history of 55 MeV protons shown in Figure III-10. Measurements on lower energy protons were not possible because of fixed absorber over the nuclear emulsions used in that study. The only emulsion measurement of very low energy proton fluxes was made on a single rocket flight, the NERV study which showed virtually no low energy protons in the inner radiation belt. The most reliable measurements of low energy proton flux in this region was obtained by a four-month average of data taken by the particle identifier instrument in 1972-73. Because of the small solid angle area factor of this counter there were no counts at all in the 5 to 7 MeV channel and only a few counts in the 7 to 11 MeV channel. Only the highest energy channel shows sufficient statistics for a good proton flux determination. Because of the large number of high energy protons which penetrate this instrument during the flight, it is also possible that the low energy proton counts are background and the true intensities are lower.

This experiment will consist of a group of CR-39 plastic track detectors arranged to look into the trapped proton mirror planes at various L values. CR-39 is a very suitable detector for this

experiment because: a) protons up to 10 MeV are clearly detectable and easy to count, b) the track etch rate is only slightly greater than bulk etch rate for protons, so only normally incident protons are registered, c) this makes CR-39 a narrow angle, large-area detector with low background and, d) it would be possible to discriminate protons and trapped heavy ions.

The stack holders for this experiment have been designed at AFGL. All the stacks would be completed by October 1982 to mount on LDEF trays.

4.0 COSMIC RAY EXPOSURE I

A study of the relative abundances and energy spectra of heavy cosmic rays and isotopic composition in the region of Fe peak can yield significant information concerning the origin, acceleration and interstellar propagation. The relative abundances of the Fe isotopes measured near Earth are of great astrophysical significance since isotopic composition of heavy cosmic ray nuclei is almost independent of the models of propagation and acceleration and such studies would lead to a better understanding of the nuclear processes in the source regions. In recent years solid state nuclear track detectors have been employed extensively to study heavy primary cosmic rays. Also it has been demonstrated that, at present, plastic track detectors present the best possibility of obtaining isotopic composition of heavy cosmic rays. In addition they have necessary large geometric factors for those heavy particles and a continuous sensitivity for the duration of an extended exposure. In the light of this, we designed a 1 m^2 passive detector array for exposure to cosmic radiation. Included in the array is a new type of nuclear track recording plastic, a polymer made from the monomer allyl diglycol carbonate (commercially known as CR-39).

A determination of the cosmic ray iron flux at this time is essential to an understanding of anomalies which have occurred in electronic computer memory elements on various satellites. Current accelerator studies of these anomalies indicate that energetic iron nuclei are capable of tripping microelectronic memories. Results from this study will also be used to evaluate the background buildup in CR-39 track detector from cosmic radiation.

The stack was built as a set of nine modules where a module is essentially an aluminum box with dimensions (30x30x12) cm. We adopted three types of stack assembly for these modules; one consisting of 'pure' CR-39, the next one, a composite assembly of CR-39 with three layers of 600 micron thick C5 emulsions at appropriate depth in the stack and, the last one consisting of CR-39 and Lexan polycarbonate plastic. The detector was exposed to the cosmic radiation aboard a balloon launched from Eielson Air Force Base, Alaska on June 19, 1977.

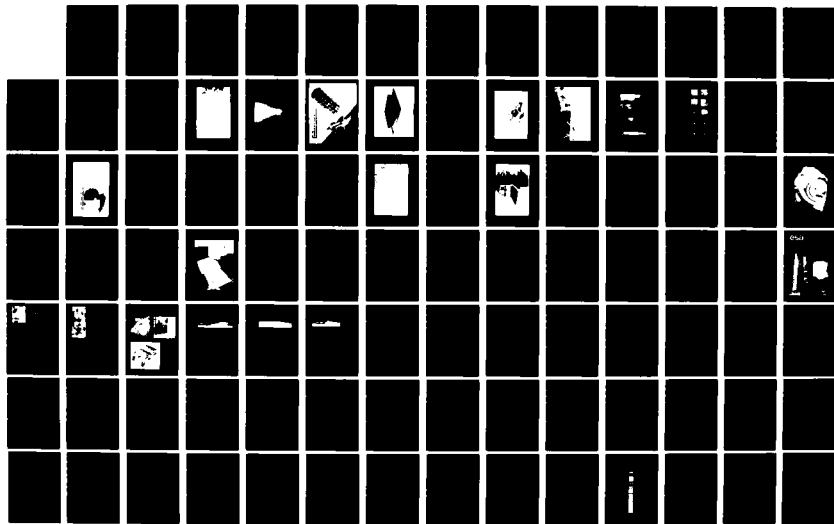
AD-A121 994

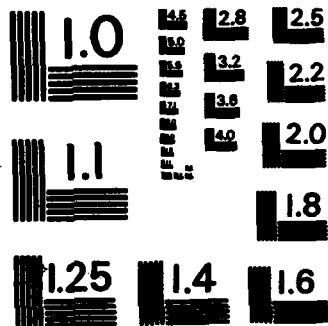
STUDY AND ANALYZE ENERGETIC PARTICLE AND MAGNETIC
ACTIVITY DATA(U) EMMANUEL COLL BOSTON MASS PHYSICS
RESEARCH DIV L GENTILE ET AL. JUN 82 AFGL-TR-82-0217
F19628-79-C-0102 F/G 3/2

2/4

UNCLASSIFIED

NL





MICROCOPY RESOLUTION TEST CHART
NATIONAL BUREAU OF STANDARDS-1963-A

A squib was fired to allow a spring loaded sliding plate to shift to a new position. This operation was successful and cosmic ray particles which penetrated at float altitude to the main stack below can be separated from particles which penetrated during the ascent phase. An attempt to stabilize and orient the payload utilizing a biaxial magnetometer combined with an electrical rotator was unsuccessful. The failure to orient the payload in a stable position would prevent us from determining the true direction of each cosmic ray particle and trace it backwards through the Earth's magnetic field utilizing a computer tracing program. The flight duration at float altitude and average ceiling were 3 hours 30 min and 3 g/cm^2 respectively. Figure III-11 shows the balloon payload while Figure III-12 shows the launching of the payload from Eielson AFB, Alaska.

Sheets of CR-39 from one of the modules have been etched in a solution of 6.25 N sodium hydroxide solution at 50°C for 120 hours. The etching was carried out in a precisely controlled bath that is stable to $\pm 0.0^\circ\text{C}$. Optical scanning of CR-39 sheets was performed using an Olympus Sz-3 stereo microscope. The top twenty-five sheets have been scanned for stopping and relativistic cosmic ray nuclei. In this scanning 200 stopping particles and several relativistic primaries were detected. The relativistic nuclei passed completely through the entire stack of thickness 14 gm/cm^2 with no diminution in ionization. Figures III-13 and III-14 show the photomicrographs of a stopping heavy primary and a relativistic heavy primary respectively.

Optical measurements were carried out on a sample of 77 stopping particles. The track etching rate and residual range was computed for each event. The track etching rate was obtained for each event from several measurements. Figure III-15(a) through III-15(c) show track etching rate as a function of residual range. Two features stand out very clearly in these figures; i) a smooth variation of track etching rate with range is indicated for individual particles, ii) in the high etch rate region there is no evidence of saturation of etch rate, which is in excellent agreement with the results of other investigations. Furthermore, the Fe peak stands out very clearly in all these figures. Work is in progress to estimate the charge for these particles.

5.0 PASSIVE ENERGETIC PARTICLE DETECTOR EXPERIMENT WITH CIRRIIS ON AN EARLY SPACE SHUTTLE MISSION (CRL 258)

A composite stack consisting of CR-39 and emulsions with lead degrader will be exposed to the space on board the space shuttle. Data on energetic particles capable of causing false signals in the "CIRRIIS" instrument will be compiled after recovery. In addition, the flux and energy spectra of major species of the energetic particles, namely, high energy cosmic ray nuclei, will be obtained for the space shuttle orbit and correlated with the expected fluxes when geomagnetic cut-offs are included. The package will be mounted with the upper face exposed to free space when the space shuttle "bay doors" are opened.

For this experiment, the stack holder is essentially a cylindrical aluminum box with 13.5" inner diameter. Figure III-16 shows the container for CR-39 track detector for this experiment. The fabrication of the container was carried out by AFGL. All the details regarding outgassing properties and self-ignition temperature pertaining to CR-39 were obtained from Pittsburgh Plate Glass Co. Similar data for nuclear emulsions was supplied by Dr. R. Silberberg of Naval Research Laboratories, Washington, D.C. However, the outgassing from nuclear emulsions (mostly water vapor) is far above the acceptable limits and hence it was decided to use only CR-39 with lead degrader as flight material. Figure III-16 shows the stack configuration for CIRRIIS experiment. The container was filled with the flight material and then tested for structural integrity. Tests on vacuum and random vibration test on the container was carried out at AFGL. The final stack assembly for this experiment was completed during the third week of December 1981. The stack consists of CR-39 track detector with lead as degrader as flight material. The final stack configuration is given in Table III-2. The container was delivered to AFGL in December 1981.

TABLE III-2

Stack Configuration for CIRRIIS Experiment (CRL 258)

TOP

<u>Number of Sheets</u>	<u>Material</u>
17	CR-39
1	LEAD
20	CR-39
1	LEAD
20	CR-39
1	LEAD
20	CR-39
1	LEAD
20	CR-39
1	LEAD
20	CR-39
1	LEAD
20	CR-39
1	LEAD
20	CR-39
1	LEAD
20	CR-39
1	LEAD
40	CR-39

BOTTOM

6.0 COSMIC RAY EXPOSURE II (SKY ANCHOR XIII)

A balloon-borne experiment consisting of two square feet detector array with CR-39 track detector has been designed in order to obtain charge and energy spectra of high energy heavy primary cosmic rays. The detector was exposed to cosmic radiation aboard a balloon, Sky Anchor XIII Flight, launched from Greenville, N.C. in September 1981. The flight duration at float altitude and average ceiling were 43 hours and 5.8 g/cm^2 . The package was recovered within a few hours after termination and all materials were in perfect condition. Figure III-17 shows the time-altitude history of Sky Anchor XIII Flight,

7.0 HEAVY ION EXPERIMENTS AT BEVALAC

To calibrate CR-39 plastic track detectors, we exposed several stacks to beams of 210 MeV/N ^{48}Ca ions and 300 MeV/N ^{20}Ne ions. Beam dip angles of 45° , 60° and 90° were used for these stacks and a beam intensity (defocused) of about 10^2 cm^{-2} was employed. One of the stacks exposed to 210 MeV/N ^{48}Ca was etched. A sample of 100 particles were measured for track etching rate and residual range. Our results suggest that the response of CR-39 to 210 MeV/N ^{48}Ca ions can be represented as a function

$$V_T \propto \frac{Z_{\text{eff}}^5}{\beta^5}$$

Figure III-18 shows the etching rate as a function of residual range for these ions.

A stack exposed to 300 MeV/N ^{20}Ne ions was etched. A sample of 40 events were measured. The results from these experiments will be communicated for publication soon.

8.0 MEASUREMENTS OF BULK ETCH RATE (V_g)

A knowledge of bulk etch rates at different temperatures for solid state track detectors is of considerable importance. During the etching of particle tracks to full extent by chemical etchants, a portion of the track near the surface is dissolved out by the etchant, necessitating a correction to the measured residual range, the magnitude of which depends on the bulk etch rate.

Bulk etch rate, although apparently simple to measure, is difficult to obtain with any great accuracy. The conventional method of measuring the bulk etch rate is simple to measure the thickness of a sheet of a plastic before and after etching, the difference being twice V_g . The thickness measurements may be made either by an optical microscope or by using a dial gauge. A thickness measuring device such as dial gauge is convenient for this purpose, but one must make sure that the same position of plastic sheet is always measured.

Another simple method of estimating V_g is to use the mass loss during etch. The change in weight with etching of a piece of plastic, together with density and the area of the piece, give a value of the etch rate. The main disadvantage of this method is the following. Surface charge on plastic film is very common and hence great care must be taken to obtain an accurate weight for the sample. The plastics may have absorbed some water during etching (this is very pronounced in the case of CR-39) and this introduces considerable uncertainty in obtaining an accurate weight for the sample.

The bulk etch rate can be determined from the mouth opening of tracks. In such case, the cone angle of the etch pit whose mouth opening is to be measured must be nearly zero. An illustration of this, consider a track at normal incidence ($\theta_{dip} = 90^\circ$). The diameter (D) of the etch pit at the surface is given by

$$D = (V_T - V_g) \tan \alpha/2$$

where $\sin \alpha/2 = V_g/V_T$, T is the etch time, V_T is the etching rate and α is the cone angle of the etch pit. In the limit of zero cone angle, the

diameter is given by

$$\lim_{\alpha \rightarrow 0} D = 2V_g T$$

$$\text{or } V_g = D/2T$$

In our investigations this method is being used to determine bulk etch rate for CR-39 plastic detectors. Small areas of detectors were irradiated in vacuum with fission fragments for a ^{252}Cf source and then etched for a definite period of time. The bulk etching rate is determined from the above relation. Figure III-19 shows V_g as a function of temperature. The V_g for CR-39 increases very rapidly above 60°C and thus it is very important that the etching temperature should be maintained very accurately to avoid large fluctuation in bulk etching rate. Figure III-20 shows track diameter as a function of etch time. The track diameter varies linearly with etch time which implies a uniform sensitivity of CR-39. Figure III-21 shows a photomicrograph of fission fragments and alpha particle tracks in CR-39 from a ^{252}Cf source.

The bulk etching process can be discussed in terms of the theory of activated complexes for chemical reactions. The reactants and products in the etching process are separated by a potential barrier, a state defined as the activated complex. A dynamic equilibrium exists whereby reactants pass over the barrier at a fixed rate to the final state, namely the products. The rate of passing through the activated complex state is analogous to the bulk etching rate of the material in the etchant. The rate is proportional to the change in free energy between the initial and final state for this reaction. Thus, the bulk etch rate (V_g) is given by

$$V_g = V_0 e^{-\Delta f/kT}$$

where V_0 is a constant, Δf is the change in the free energy per molecule between the final and initial states, k is Boltzmann's constant, and T is the temperature ($^\circ\text{K}$). The logarithm of both sides yields

$$\ln V_g = \ln V_0 - \Delta f/kT$$

This is the well-known Arrhenius law that represents many chemical reactions. Plotting $\ln V_g$ versus $1/T$ yields a straight line whose slope is $-\Delta f/k$. Figure III-22 shows the Arrhenius plot and our results are compared with the results of other investigators.

9.0 RANGE ENERGY PARAMETERS

A computer program has been developed for heavy ion range-energy in CR-39 track detector. A number of parameters that are of interest in the analysis of heavy ion tracks in the detector have been computed. The parameters are: residual range (R), velocity ($\beta = v/c$), kinetic energy per nucleon ($E/\text{nucleon}$), effective charge (Z_{eff}) and energy loss (dE/dx). The computation has been performed for isotopes of interest in cosmic ray work with charges in the region $2 \leq Z \leq 30$ and for the residual range, $R \leq 30$ cm. The residual ranges of 6-MeV protons, 10-MeV protons, 70-MeV ^3He , 52-MeV ^4He , 300 MeV/N ^{20}Ne and 210 MeV/N ^{48}Ca were compared with these range-energy tables and found to be in good agreement.

10.0 TECHNICAL DEVELOPMENTS

Three precisely controlled etch baths (12 liters, 28 liters and 220 liters) have been built that are stable to $\pm 0.01^{\circ}\text{C}/\text{day}$. The etchant is contained in a plastic tank which is surrounded by 2 cm of polyurethane foam and an outer tank made by plywood. A stainless steel stirrer, driven by a small motor is used to stir the etchant continuously. The etchant is heated from outside the plastic tank (instead of quartz immersion heater) by employing two 50 W heating mats made of flexible silicone rubber. The resistance wire in the mat is made by spiralling fine nickel alloy wire around a glass string. The etchant is maintained at a set-point temperature by means of a thermoregulator (Forma Scientific Co.). For temperature control, the thermoregulator is combined with a Versa Therm Electronic Temperature Control Relay (Cole-Parmer). The solid state relay has a transistorized voltage amplifier; its response time is in milliseconds. Heating or cooling procedures and temperature maintenance can be controlled reliably and consistently to remarkable fine tolerances by this system. Figure III-23 shows a 220 liters precision etching system.

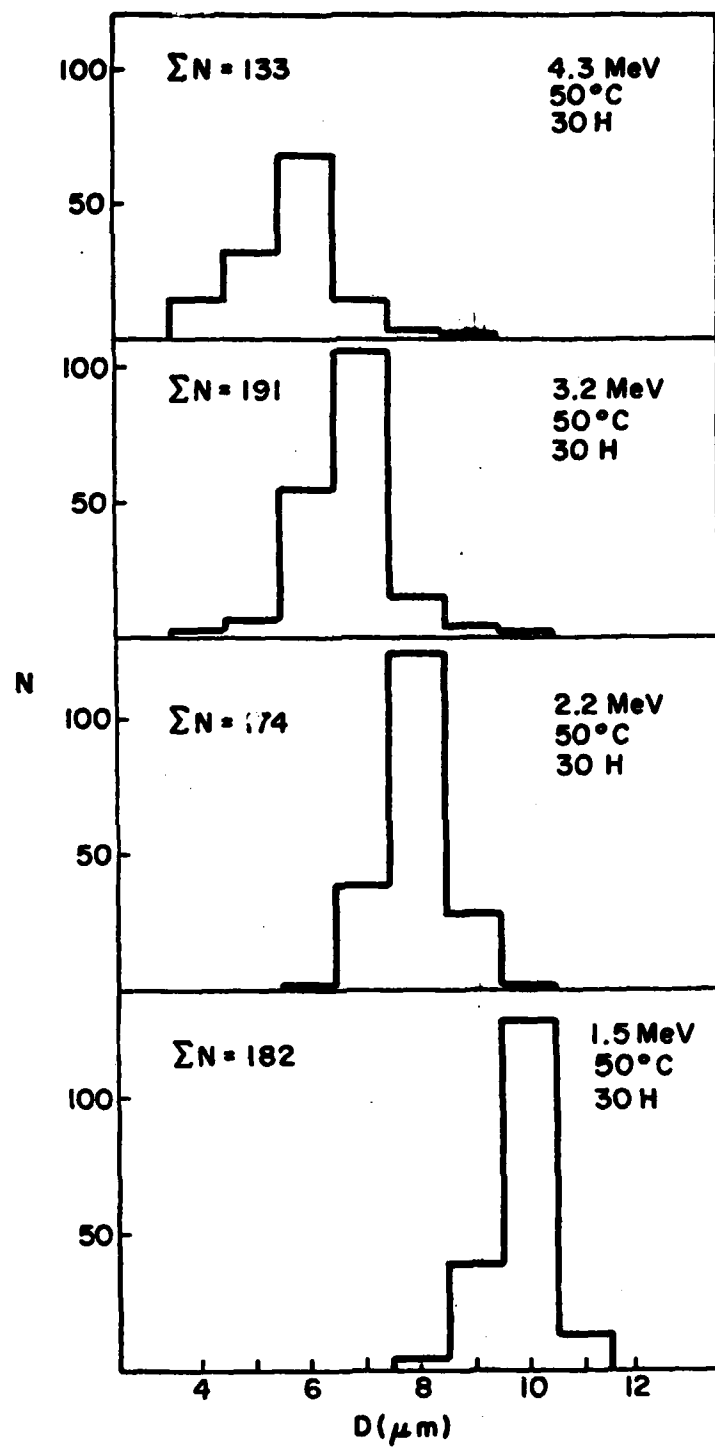


Figure III-1

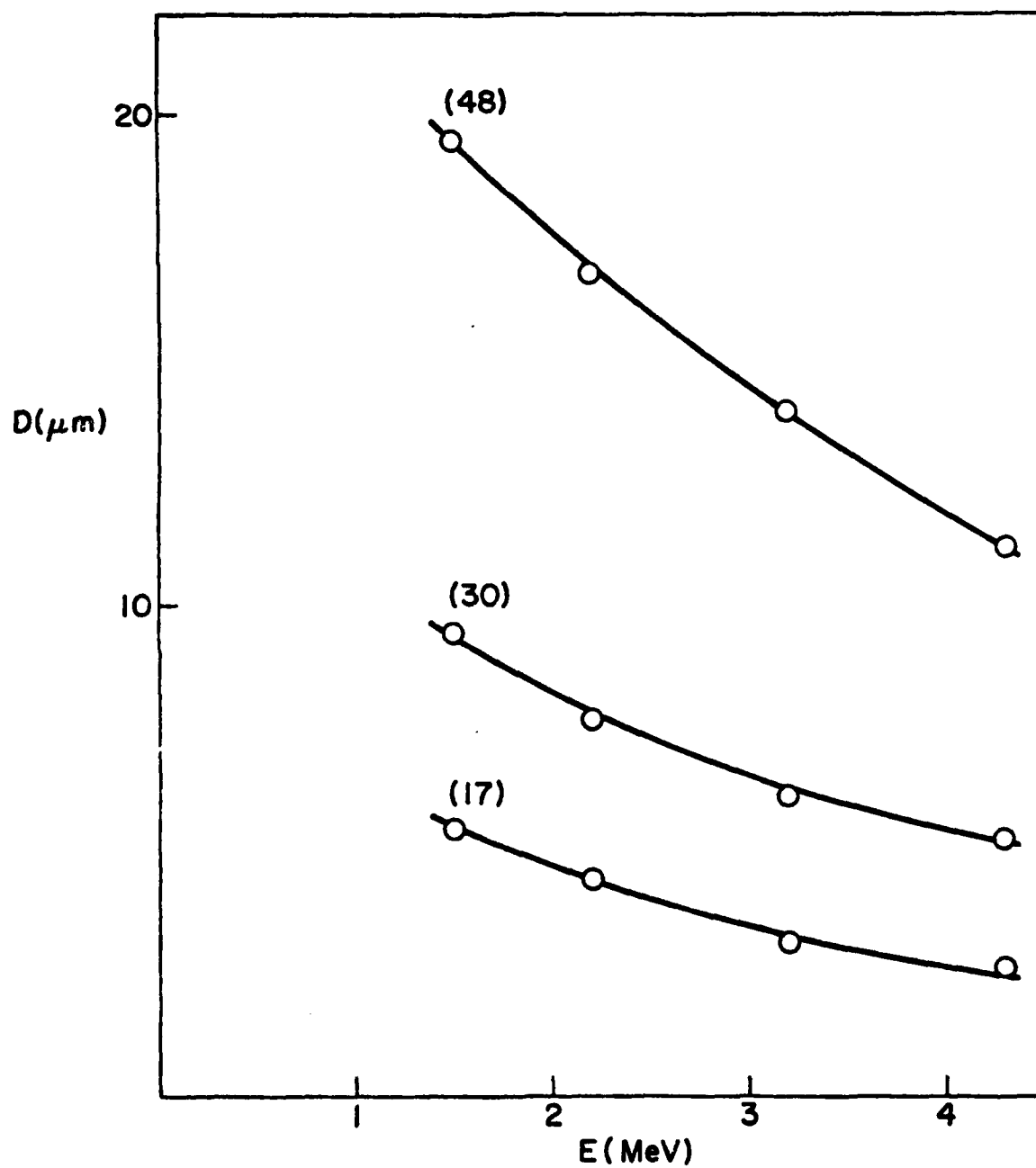


Figure III-2

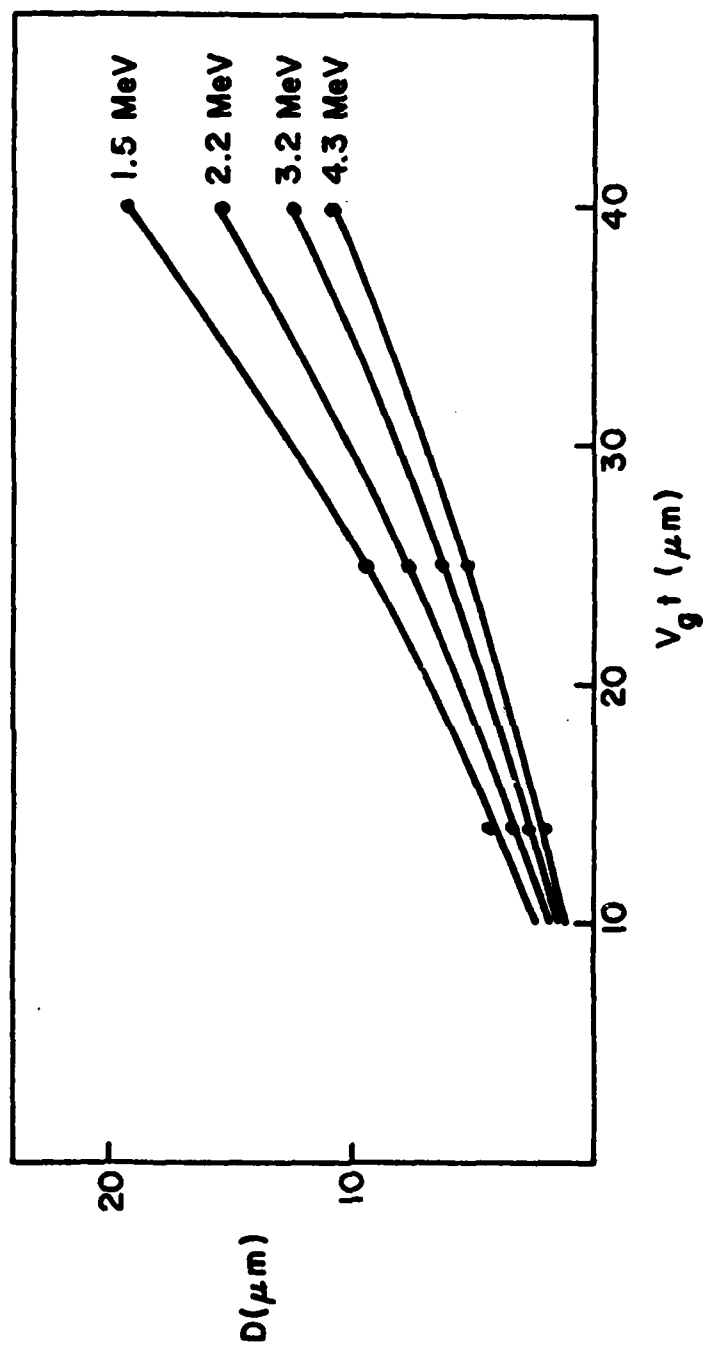


Figure III-3

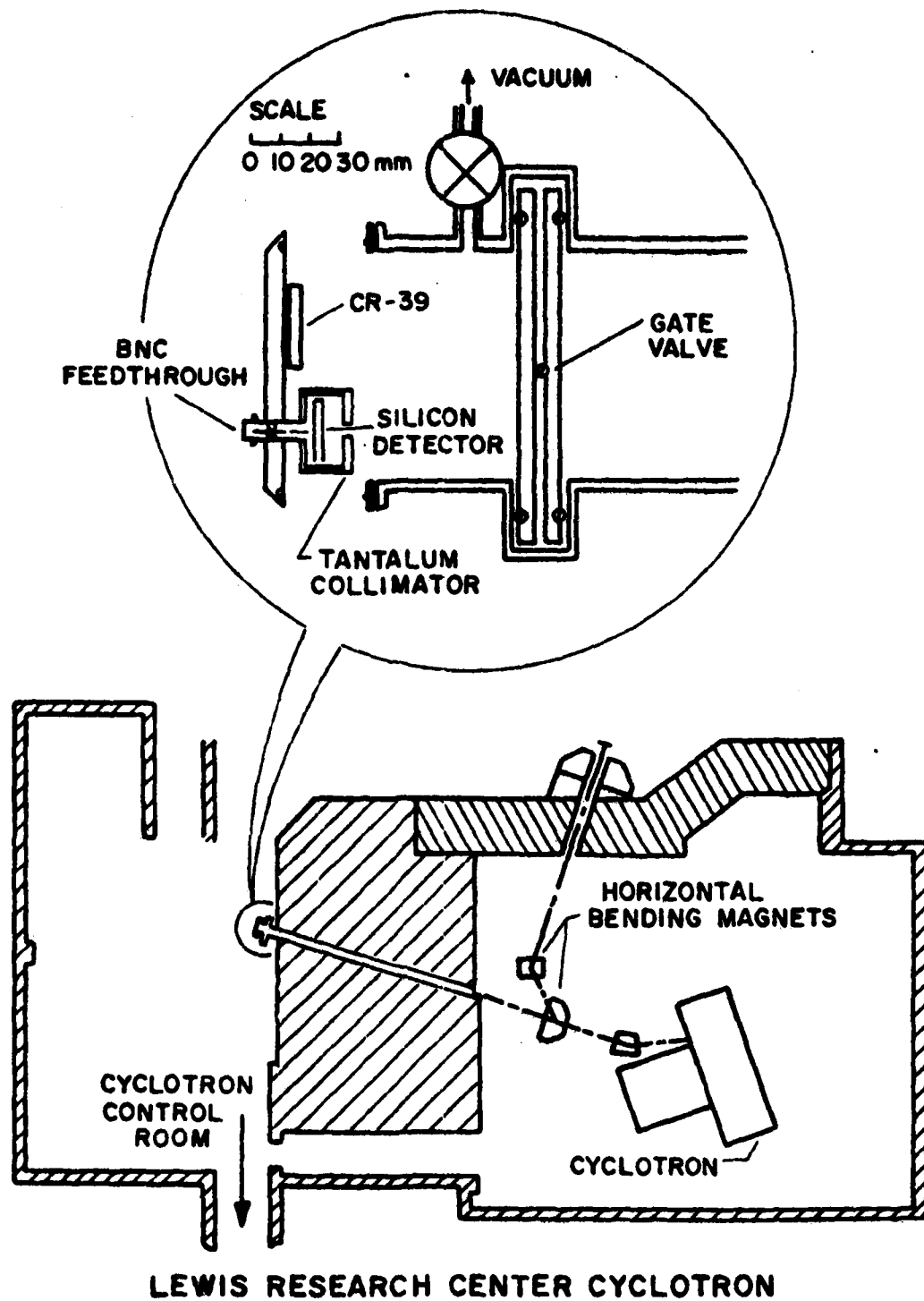


Figure III-4

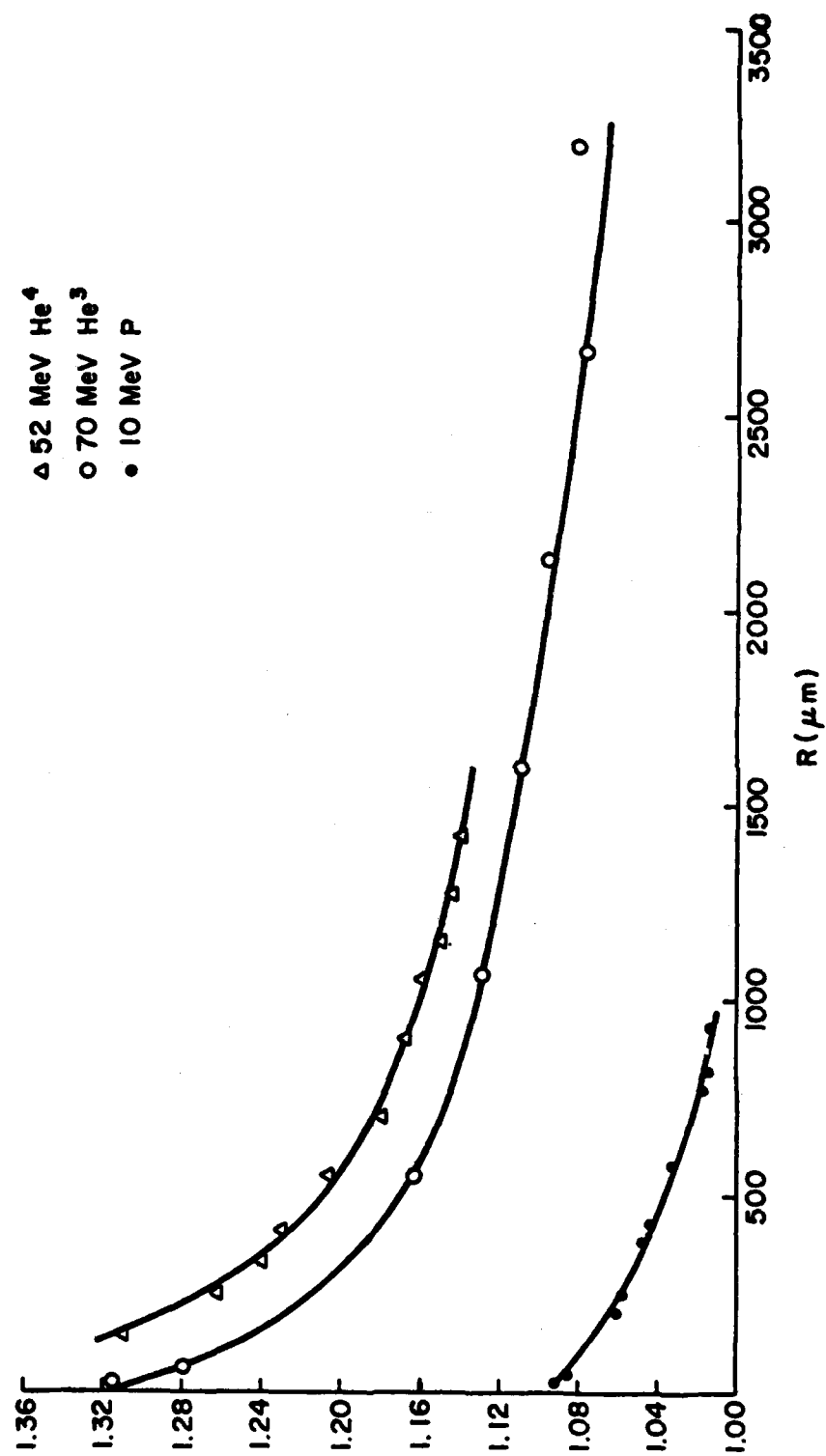


Figure III-5

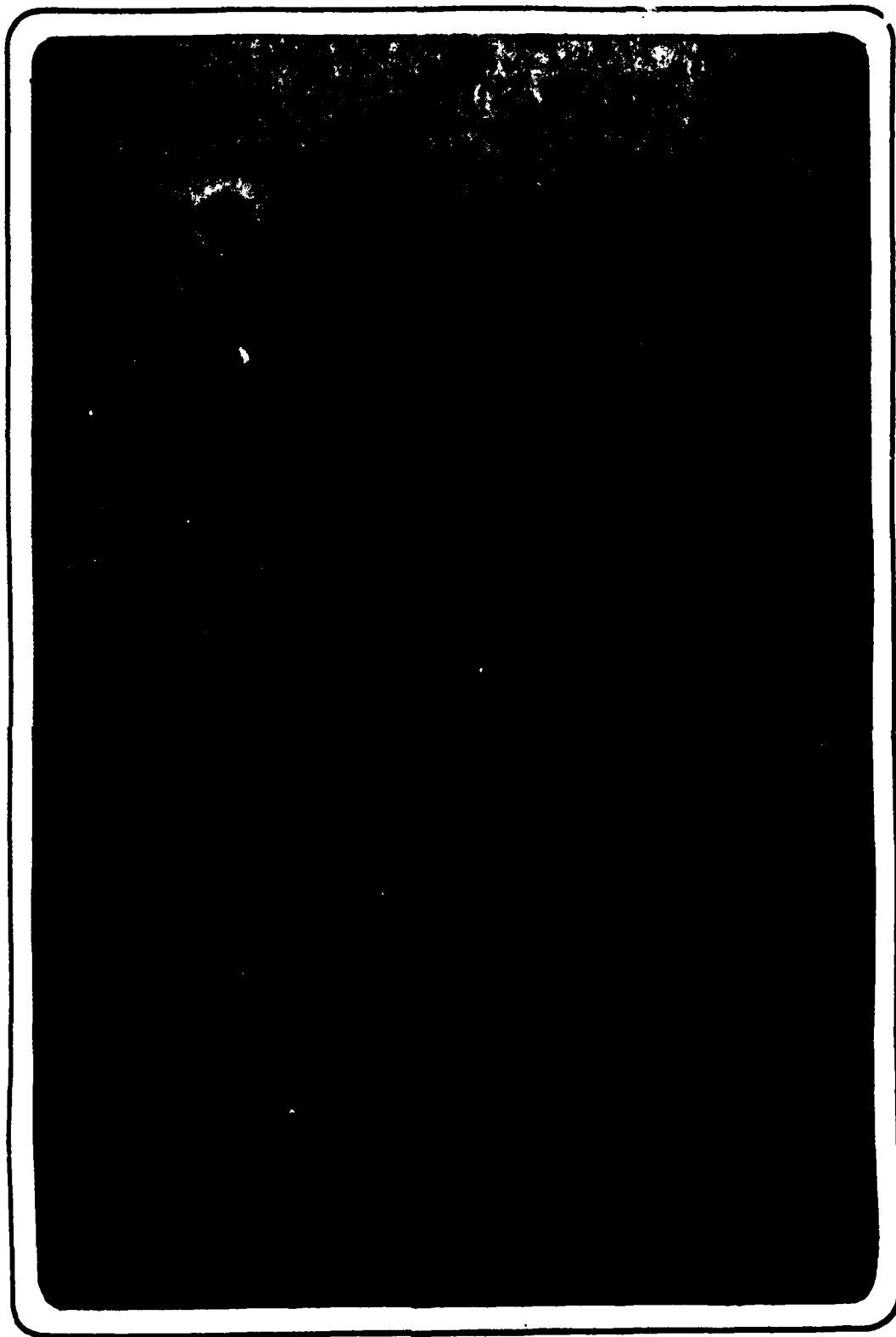
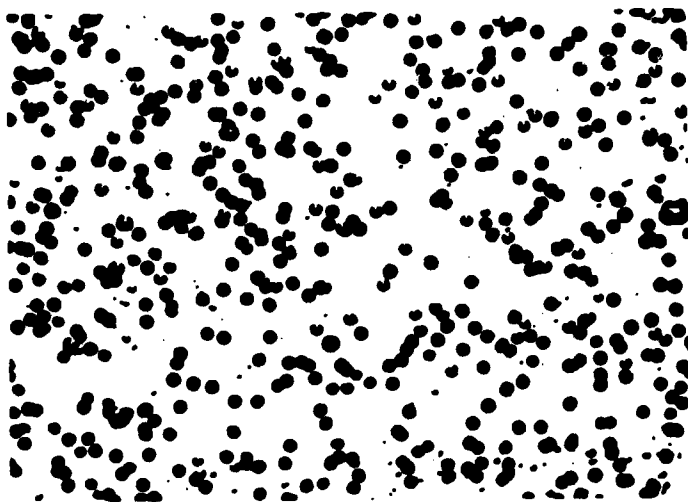
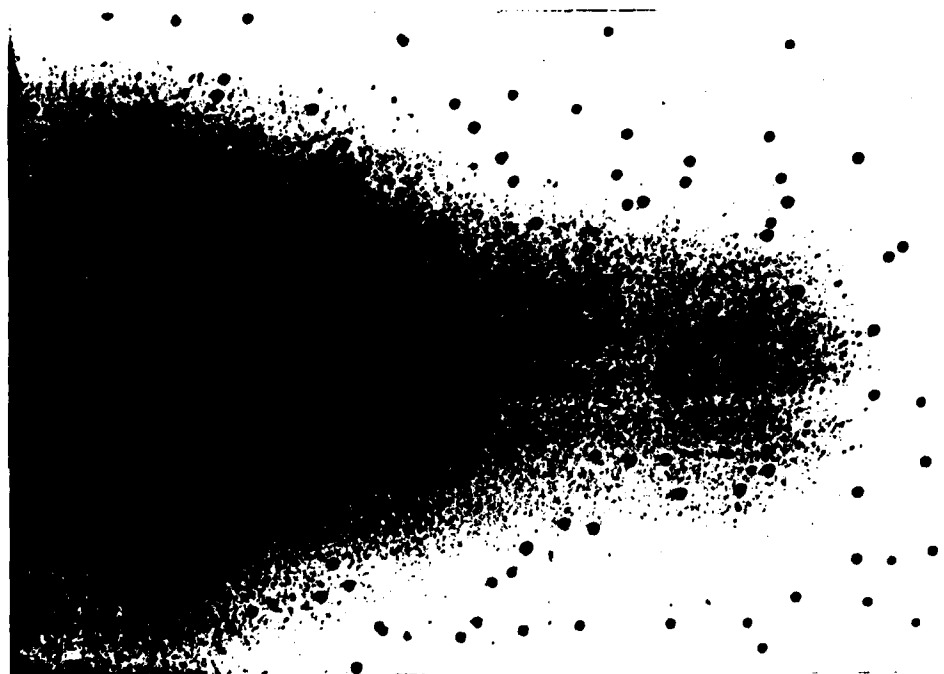


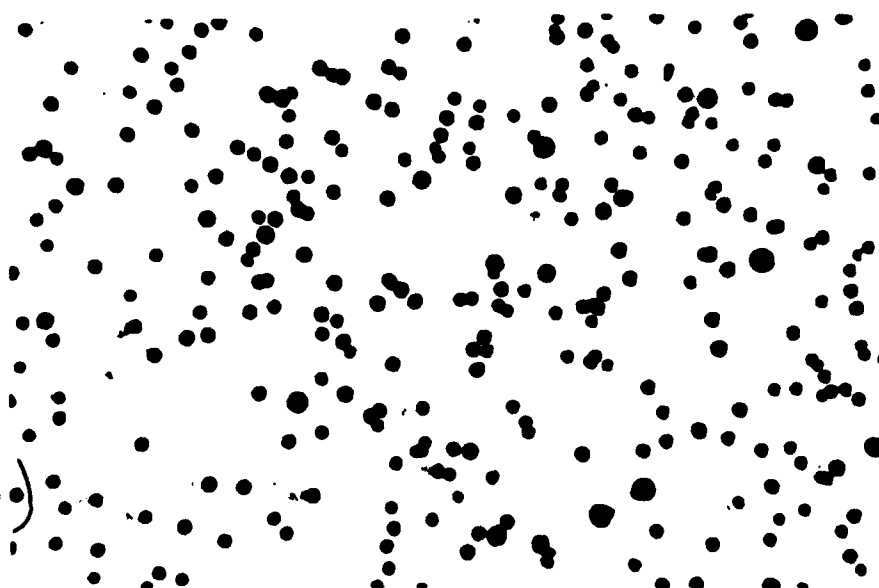
Figure III-6
100



1.5 MeV Protons



70 MeV ^3He



52 MeV ^4He

Figure III-7

LONG DURATION EXPOSURE FACILITY

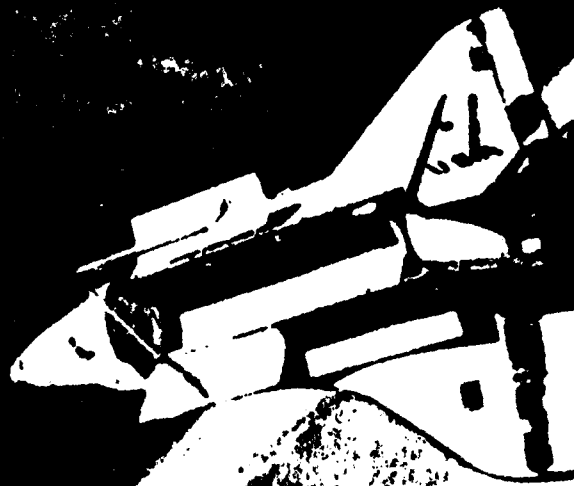
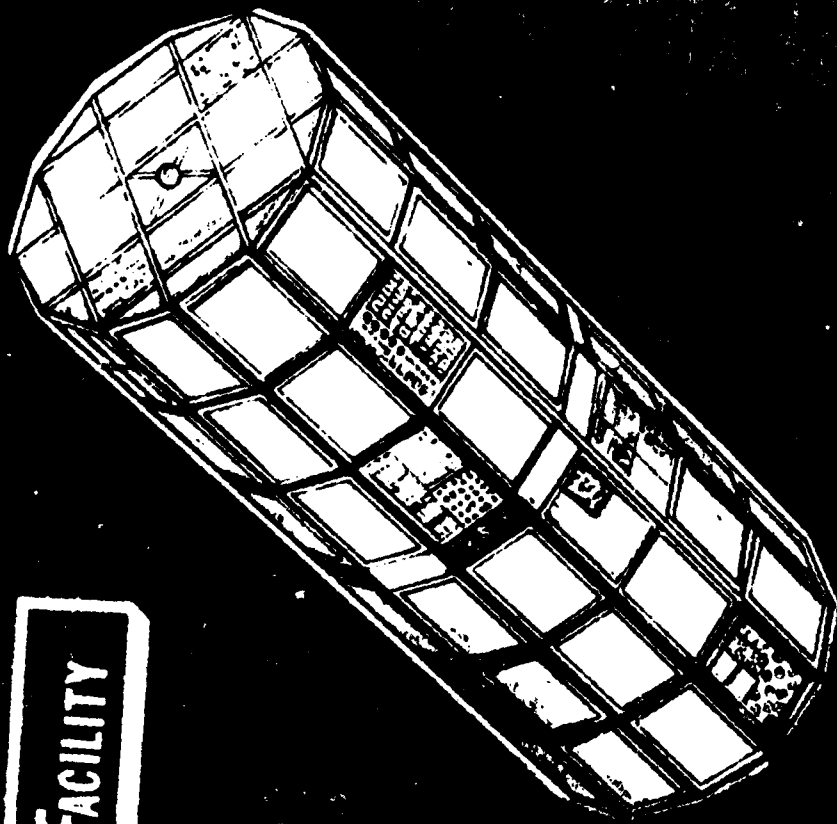


Figure III-8

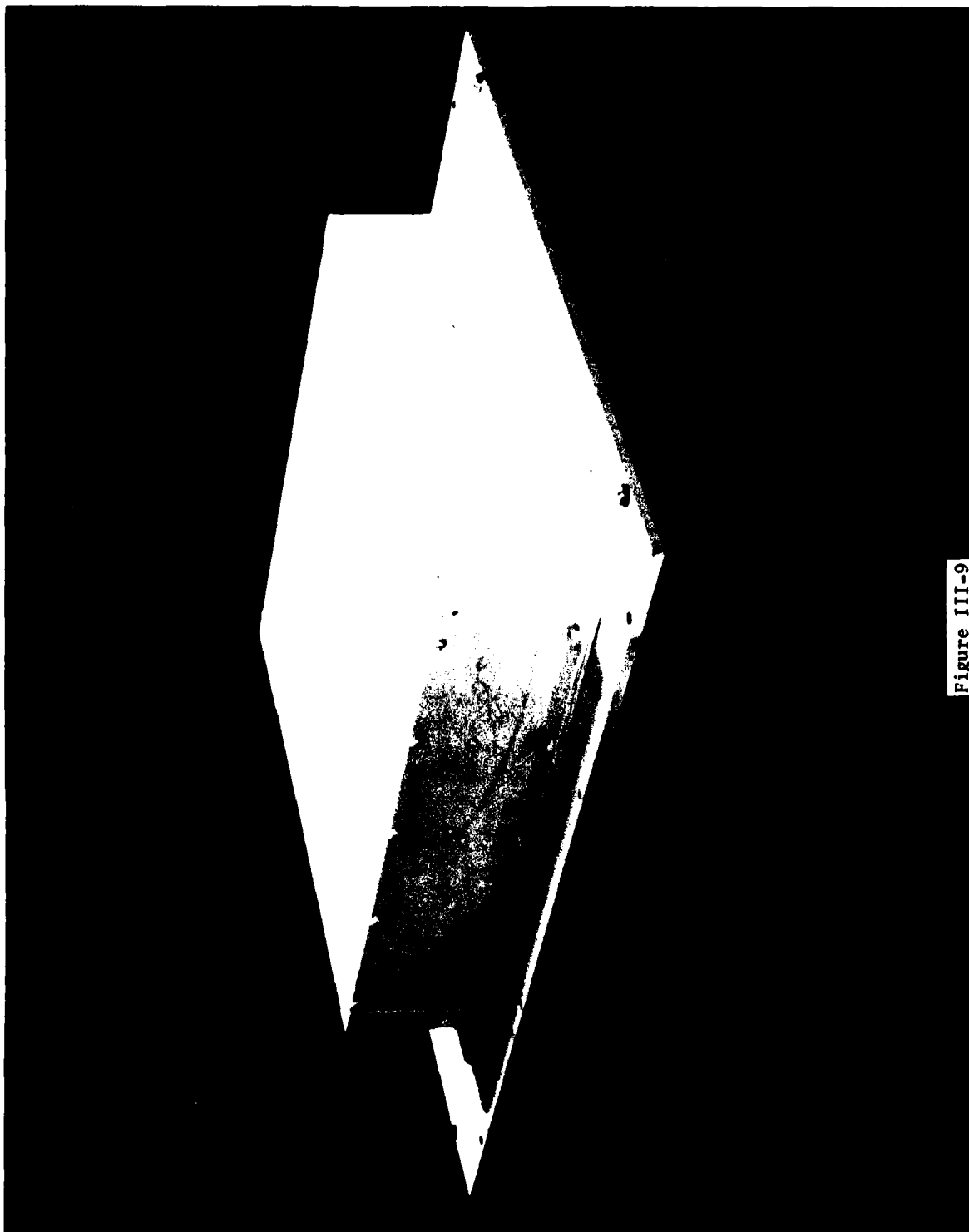


Figure III-9

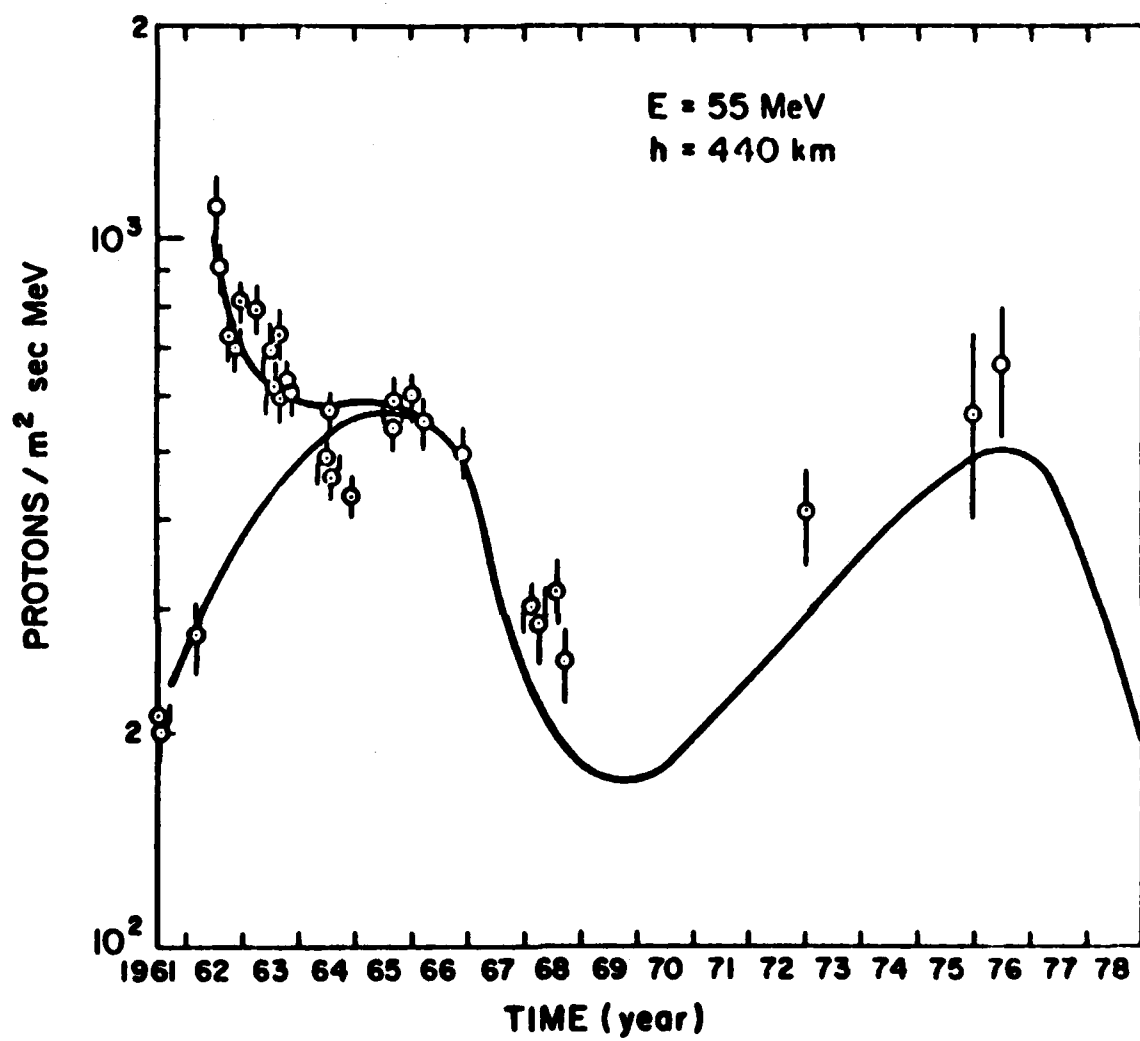


Figure III-10



Figure III-11



Figure III-12

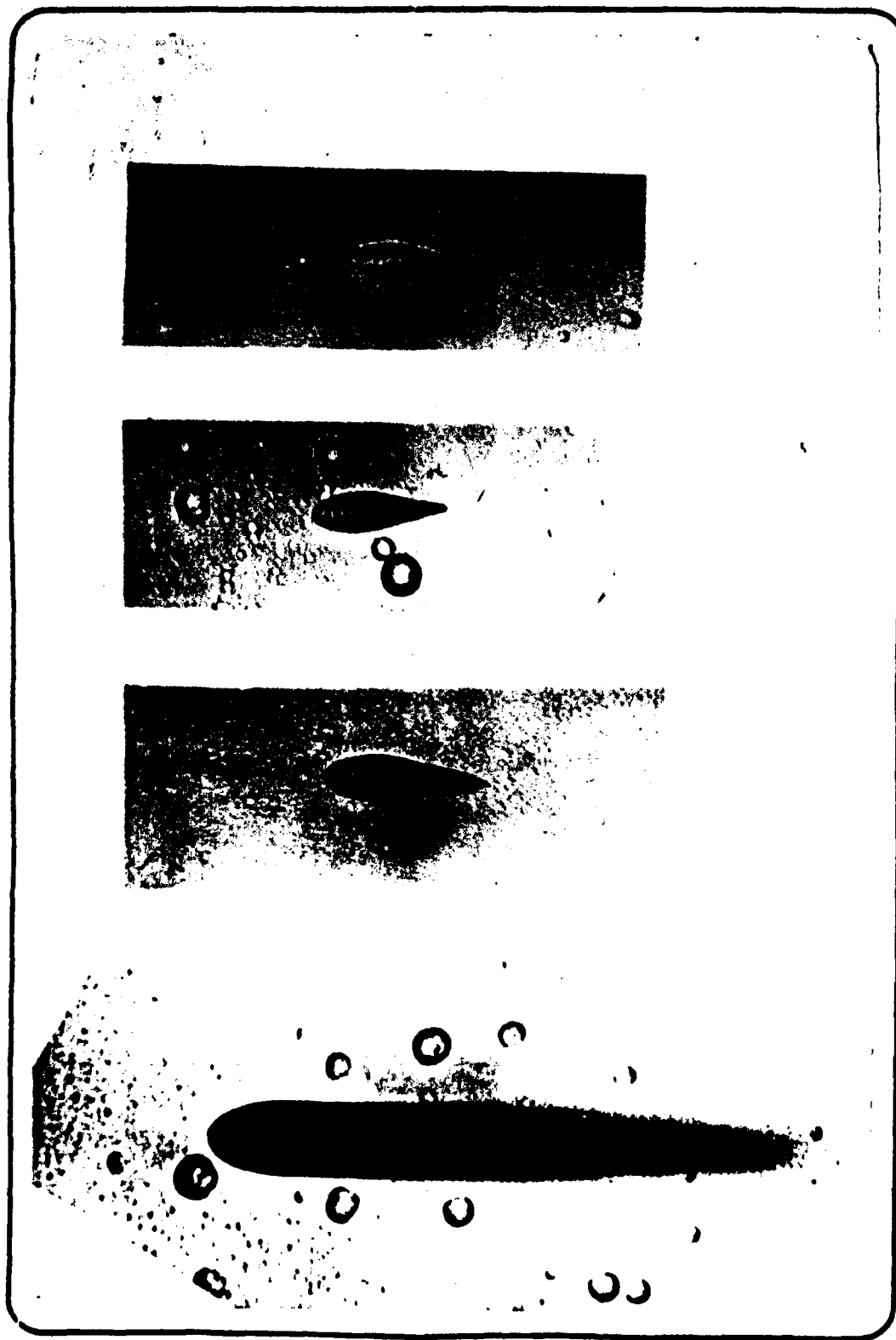
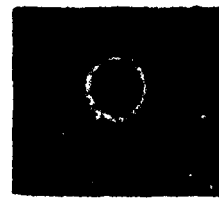


Figure III-13
107

Sheet No. 74



T



B

52



T



B

32

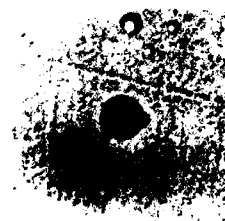


T

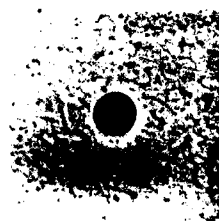


B

11

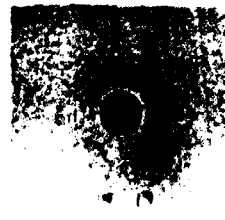


T

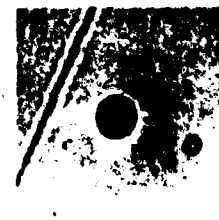


B

1



T



B

Figure III-14
108

AFGL BALLOON FLIGHT (JNE 79)
POLYTEX CR-39 (1.5 MM SHEETS)

.D

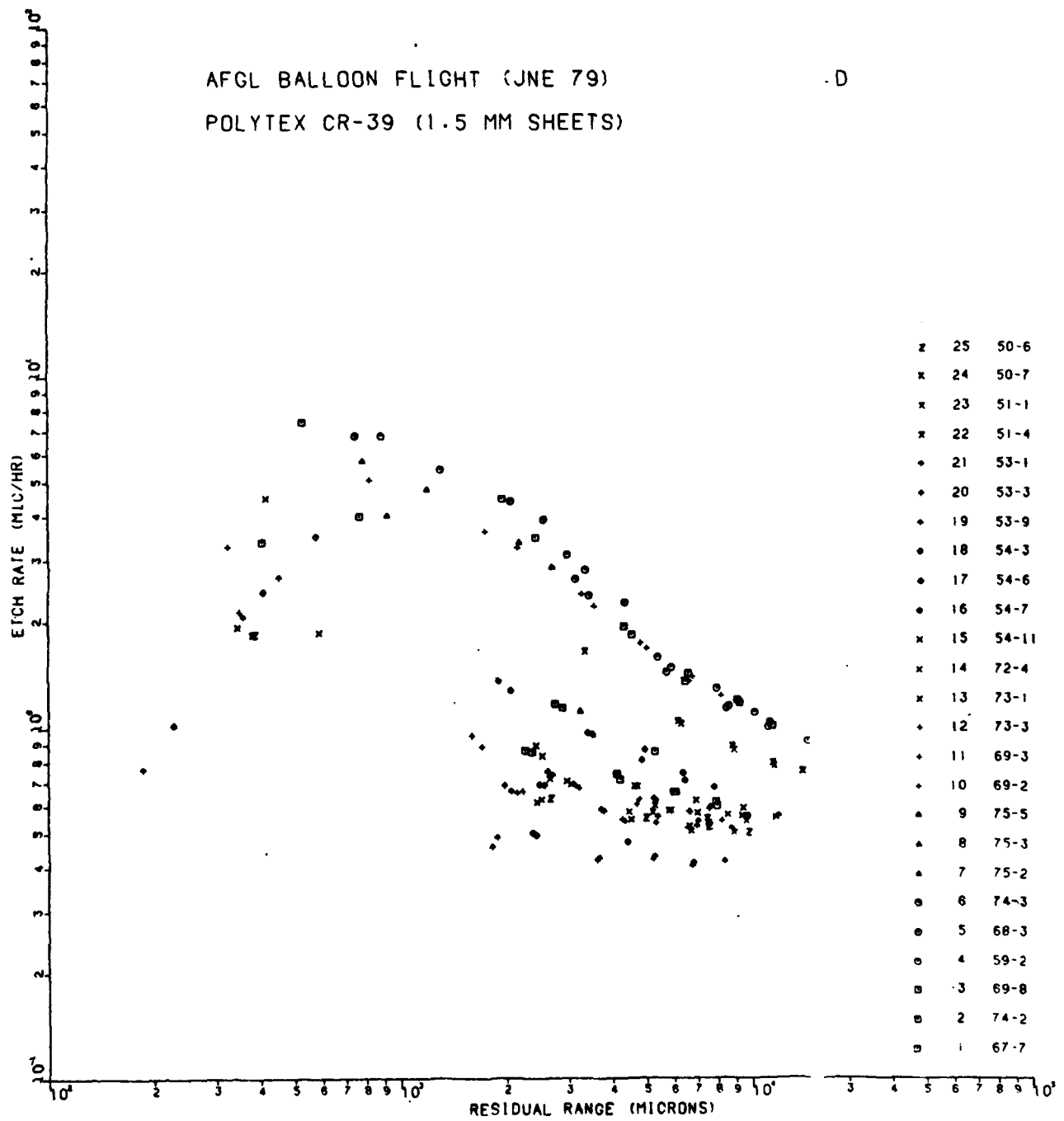


Figure III-15(a)

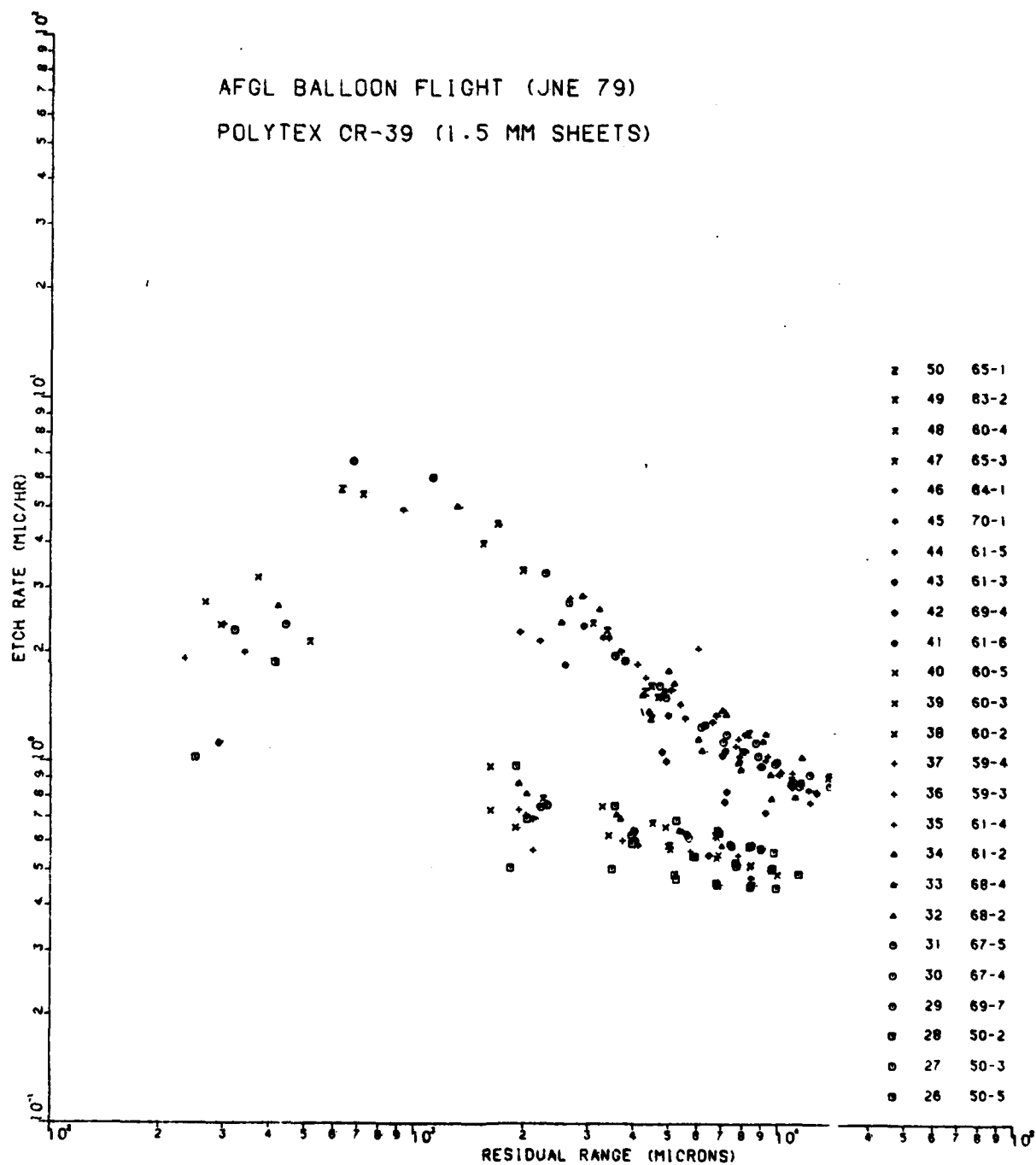


Figure III-15(b)

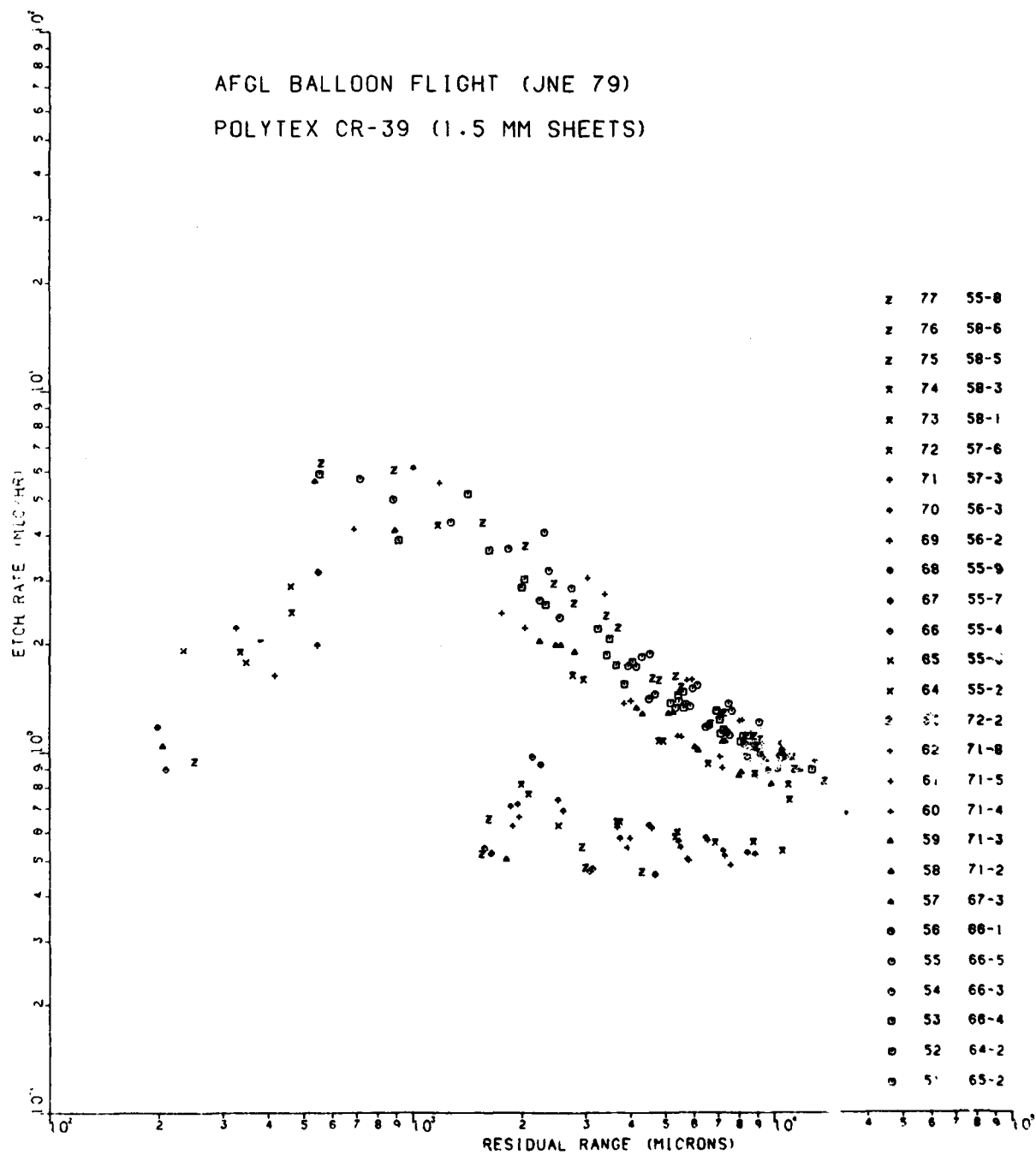


Figure III-15(c)

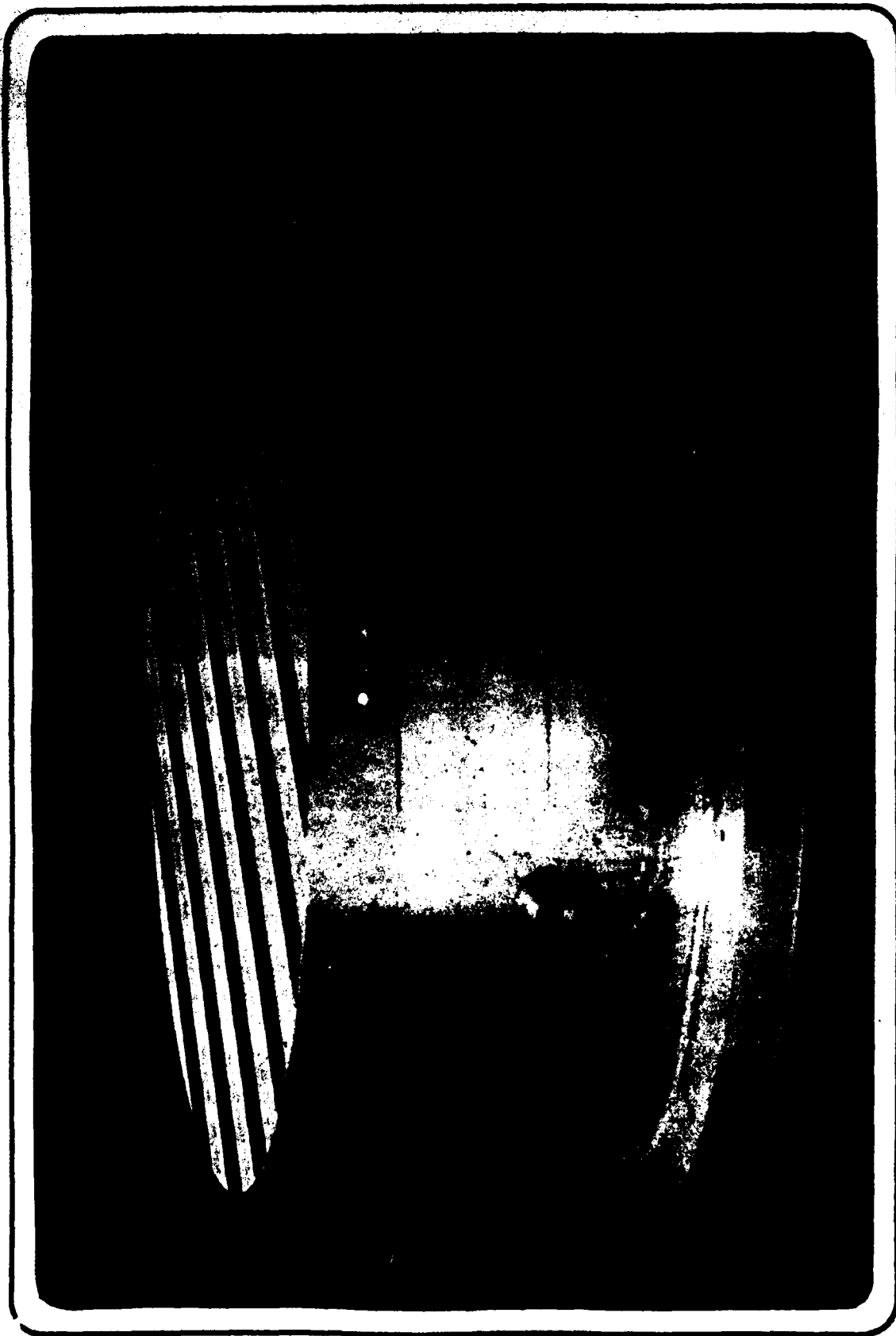


Figure III-16

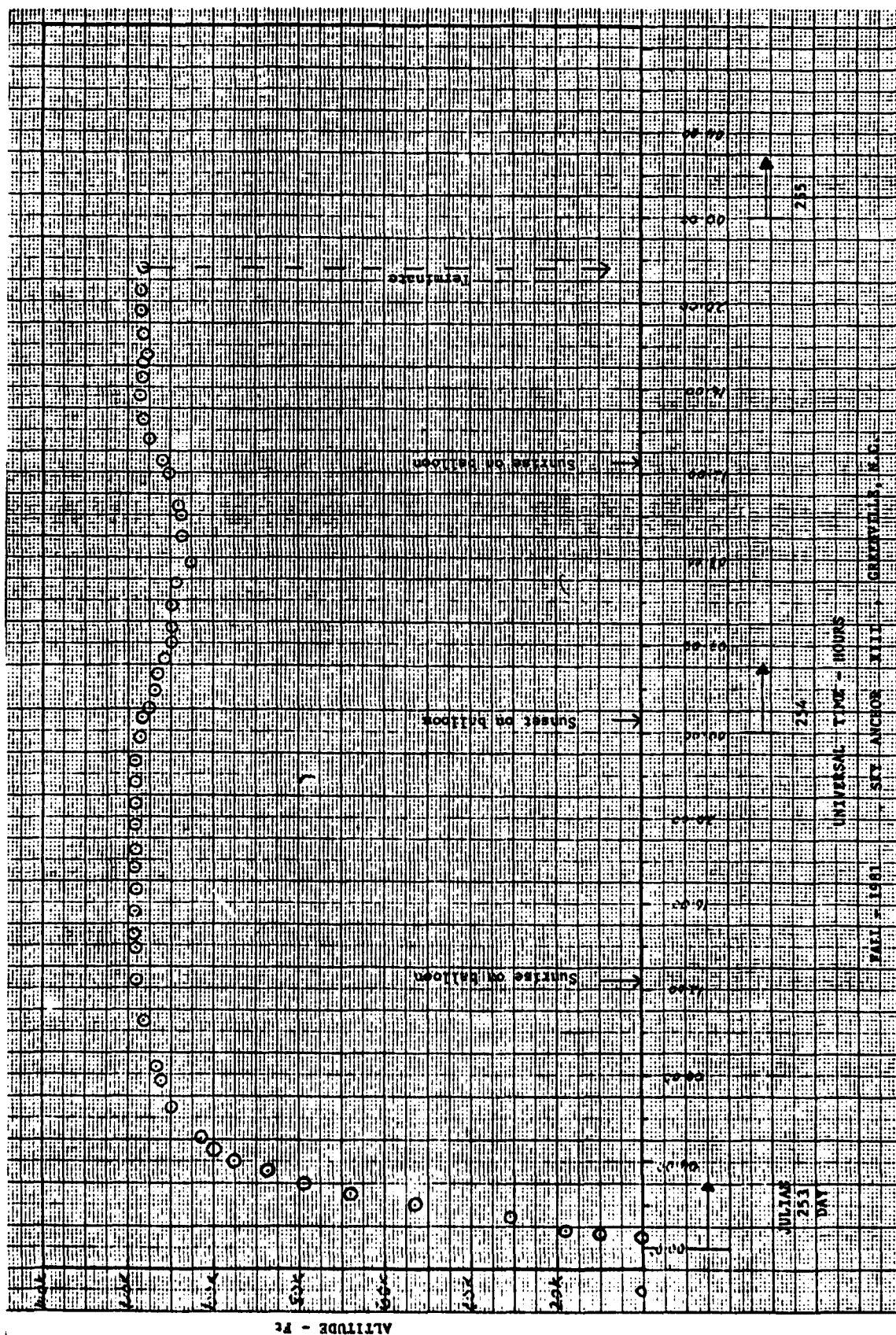


Figure III-17

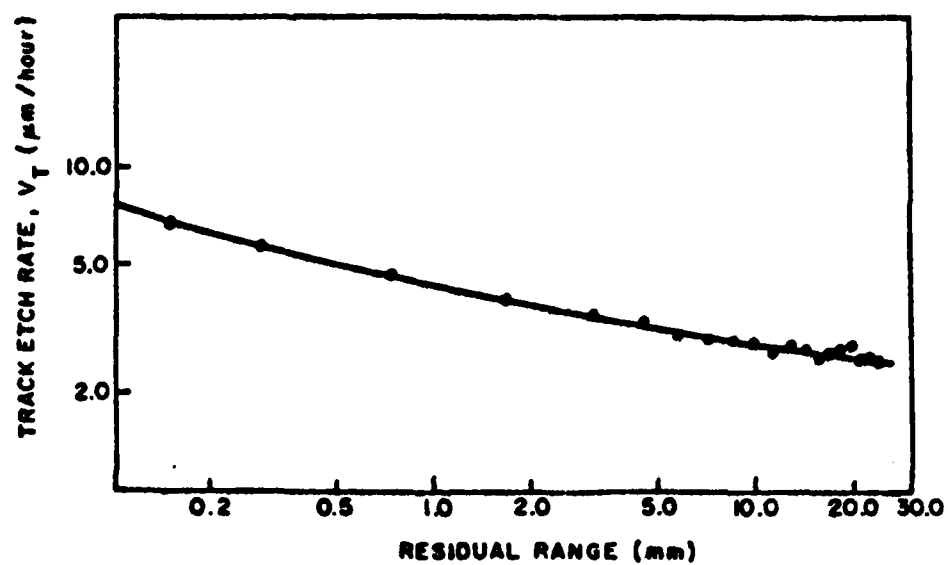


Figure III-18

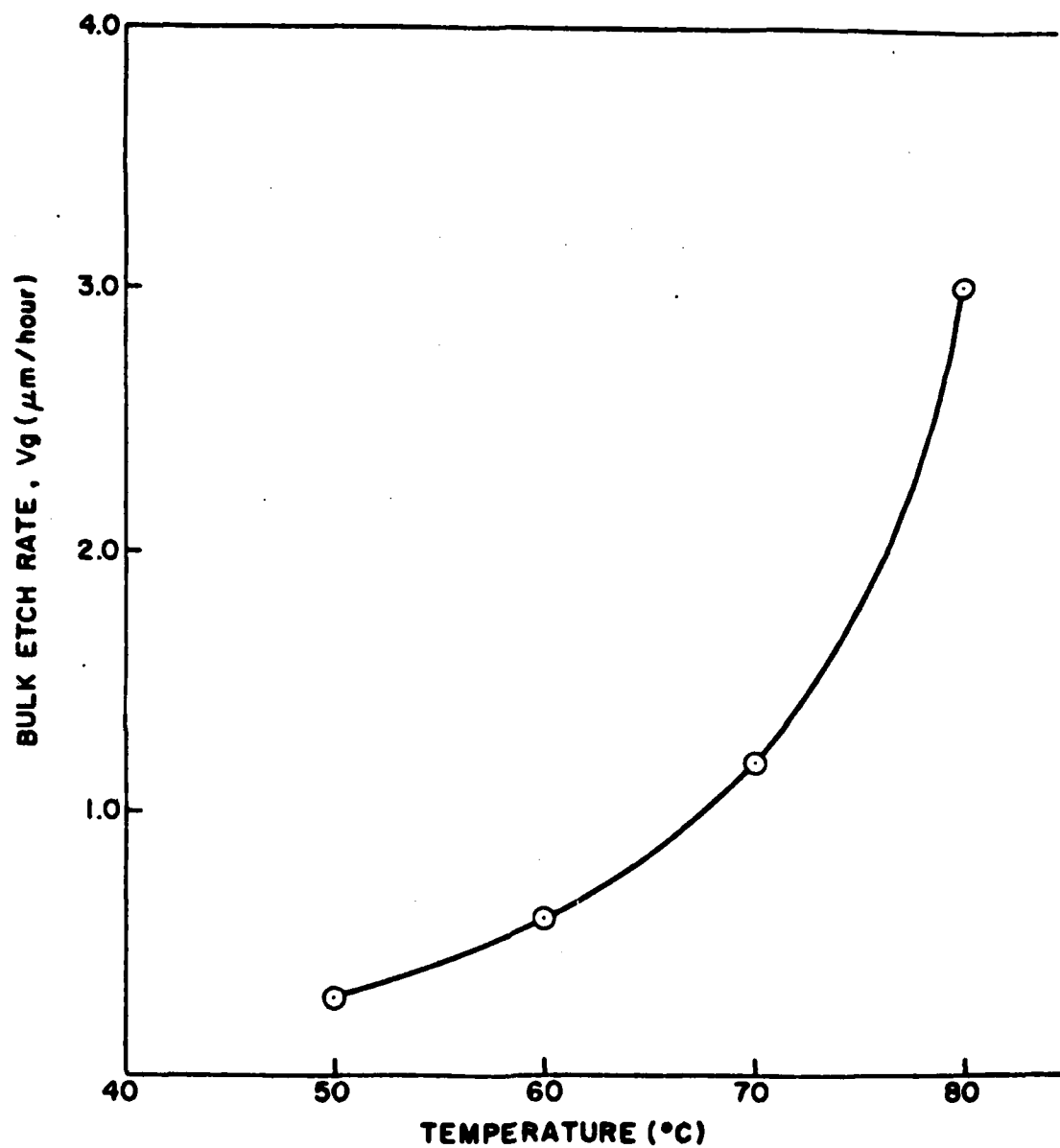


Figure III-19

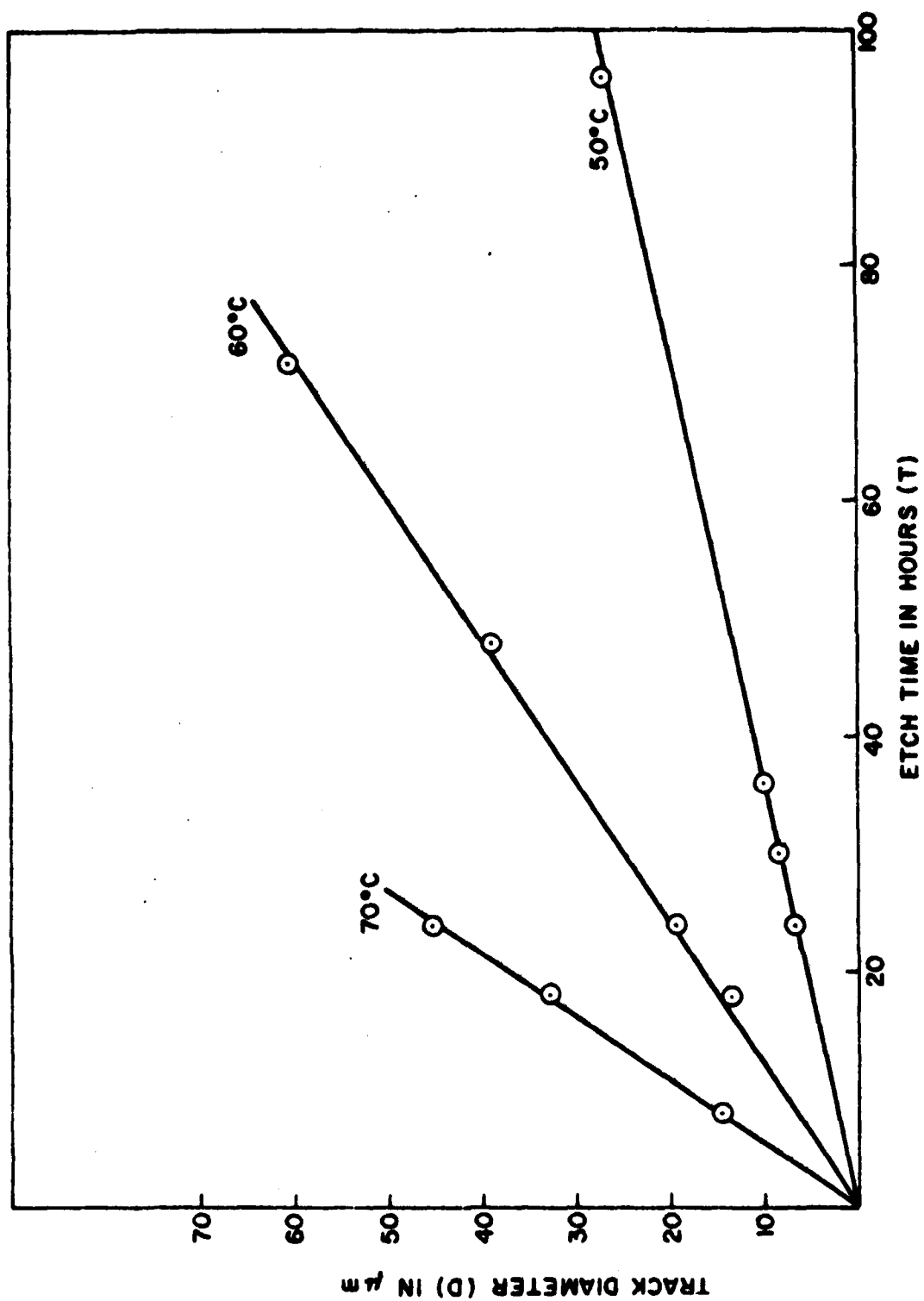


Figure III-20

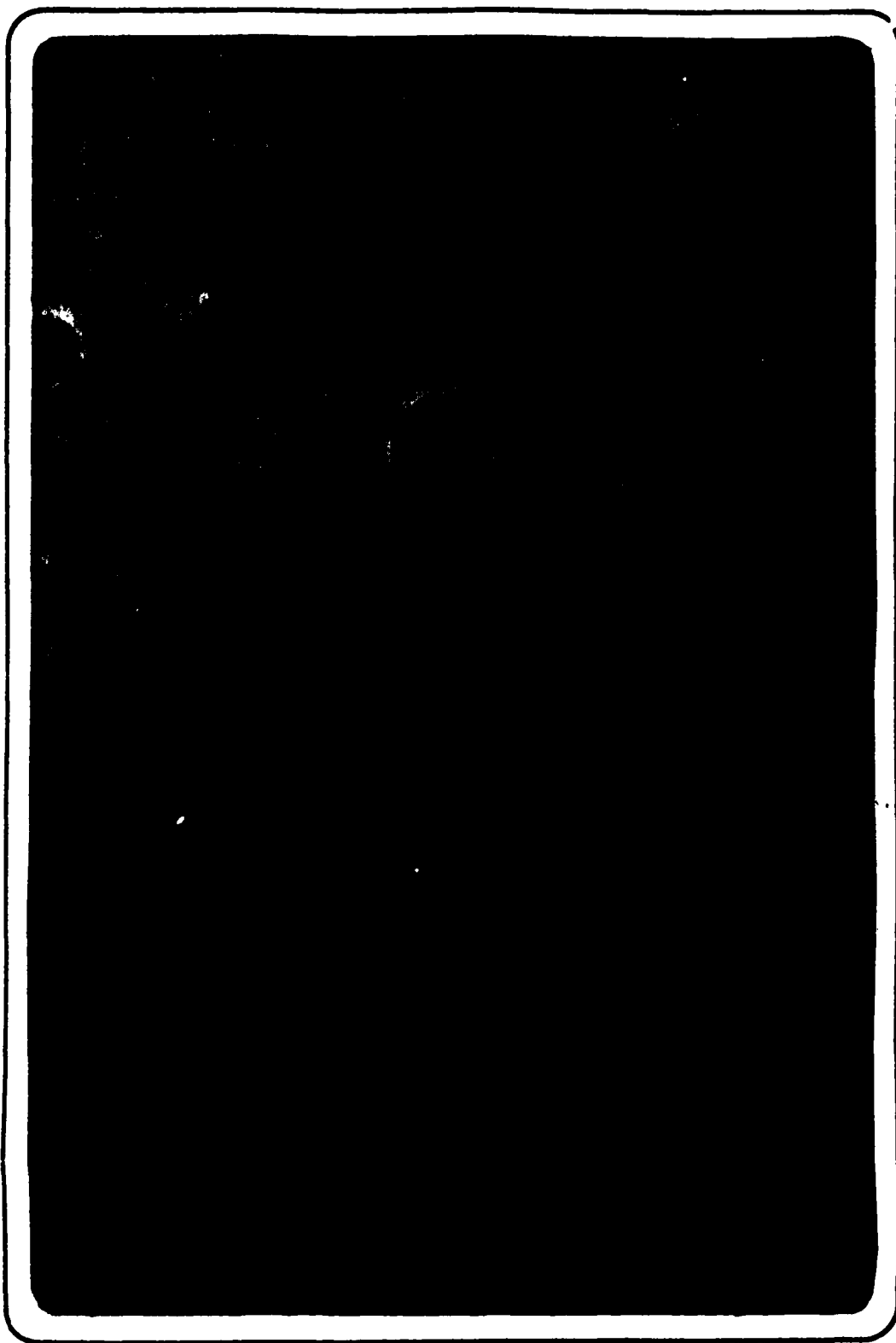


Figure III-21

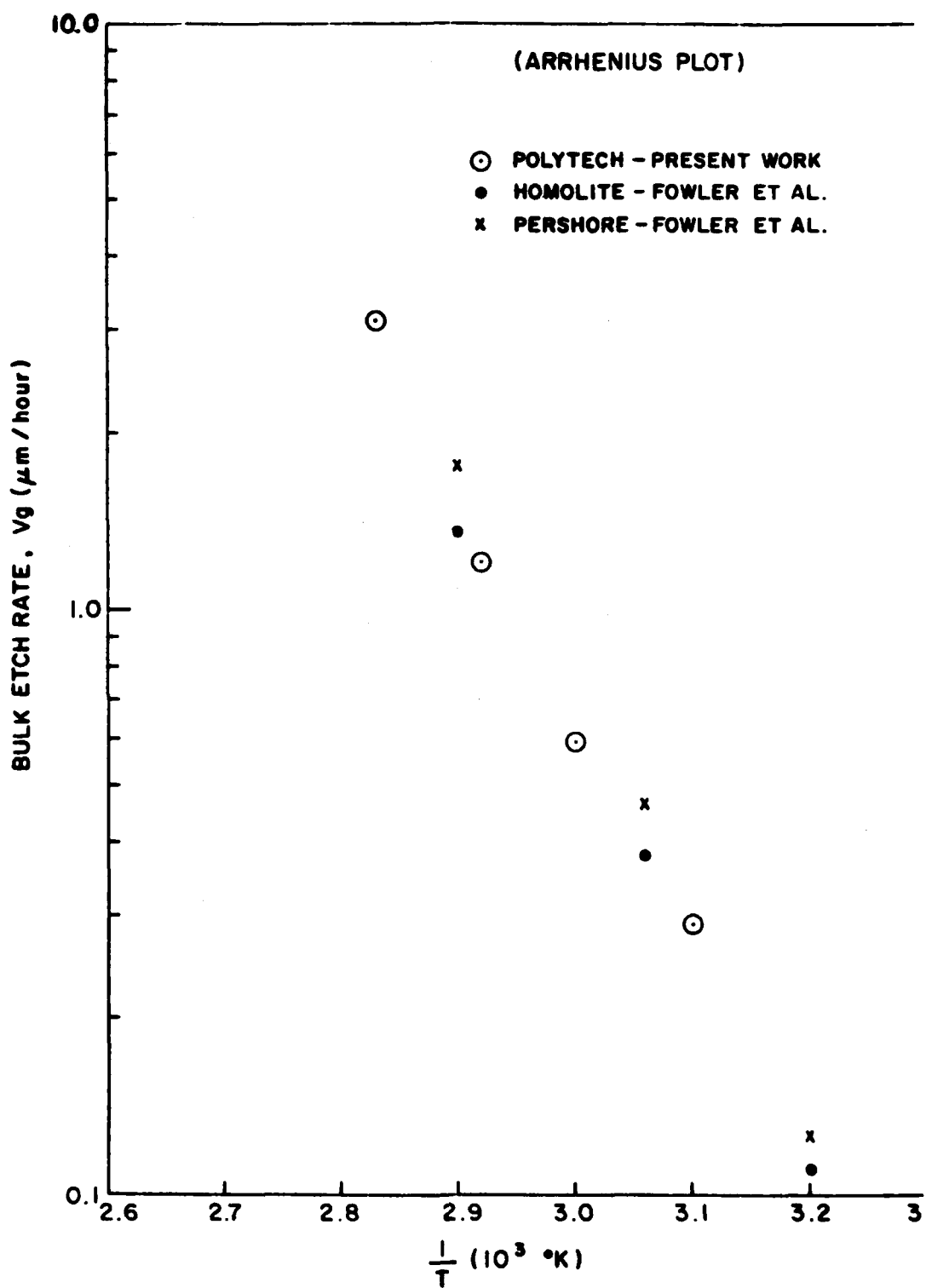


Figure III-22

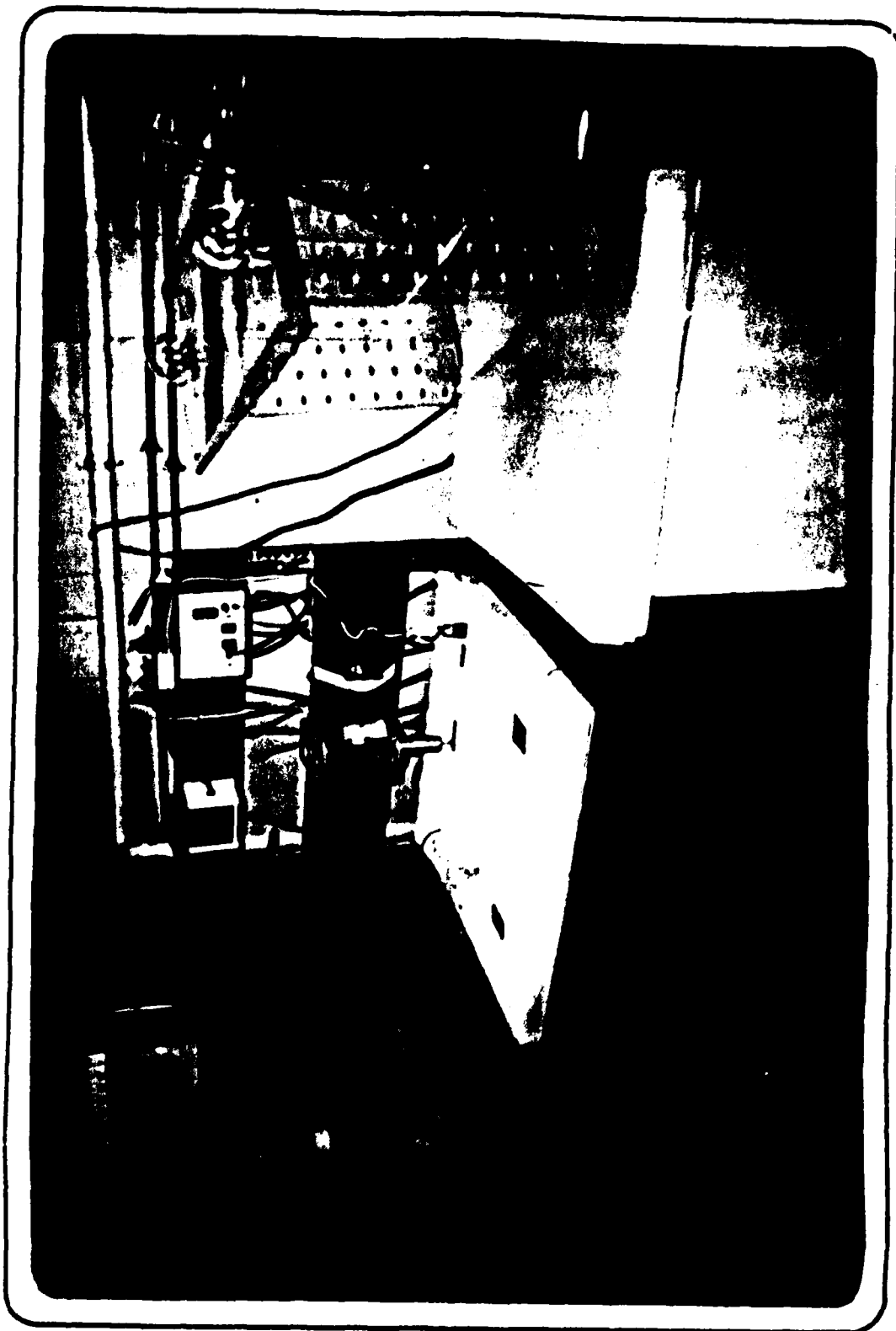


Figure III-23

IV. THE PLASMA EXPERIMENT ON BOARD METEOSAT-F2

1.0 INTRODUCTION

The electric potentials of synchronous satellites are known to vary according to the geomagnetic substorm environment which charges the spacecrafts negatively. The excess charges build up on different parts of a satellite leading to eventual breakdowns between two or more regions on the surface of the vehicle.

The European geosynchronous satellite METEOSAT-F1 suffered from such spacecraft charging phenomenon. The spacecraft did not suffer any permanent damage, but the charging resulted in loss of data. Wrenn et al. suggested to the European Space Agency that diagnostic instrumentation should be carried on-board the next satellite of the series, METEOSAT-F2. For that purpose, this vehicle was equipped with an internal antenna sensitive to certain electric transients resulting from electric discharges, and with an electrostatic analyzer to monitor the plasma environment in the 50 eV - 20 keV energy range.

The Physics Research Division at Emmanuel College, through the U.S. Air Force Geophysics Laboratory, provided the electrostatic analyzer for the plasma measurements. This report describes this instrument and presents preliminary data obtained during the first month of operation.

2.0 THE SPACECRAFT

METEOSAT-F2 was launched into a geosynchronous orbit on June 19, 1981. After about one month of programmed drift and maneuvers, the S/C reached its final position on July 21, at 0 degree of longitude. The satellite is spin stabilized at 100 rpm, with its spin axis roughly parallel to the earth's spin axis.

The first of the two instruments, the Electrostatic Event Monitor (EEM) was turned on a few days after launch, on June 21. The Electrostatic Spectrometer (SSJ 3) was commissioned on July 28, 1981. Quick look data taken with this instrument between July 28-31 showed that it was performing nominally. Production data up to this day indicate that the SSJ/3 is performing flawlessly.

3.0 THE ELECTROSTATIC ANALYZER (SSJ3)

3.1 Physical Principle

This instrument uses an electric field established between metallic plates in the shape of concentric cylindrical segments to effect the energy analysis. Let R_1 and R_0 be the radii of curvature of the inner and outer plates respectively, to which electric potentials of $+V$ and $-V$ are applied. Using Gauss' theorem and the definition of potential, we calculate the electric field E between the plates to be

$$E = \frac{1}{r \ln(R_0/R_1)} V \quad (R_1 \leq r \leq R_0)$$

where fringing of the electric field has been neglected. To a first order approximation, the trajectories of non-relativistic particles entering the set of plates are arcs of circles concentric with the plates. The energy E (expressed in electron volts) of a non-relativistic particle of charge q with a circular trajectory of radius r is then related to V by

$$E = \frac{V}{2 \ln(R_0/R_1)} \text{ (ev)}$$

which to a good level of accuracy, for $R_0 - R_1 \ll R_1$ can be reduced after expansion of the \ln formation to

$$E \approx \frac{\bar{V}R}{2\delta}$$

where the mean radius $\bar{R} = 2R_0R_1/R_1 + R_0$, and $\delta = R_0 - R_1$.

The formula above thus indicates a linear relationship between the electric potential applied to the plates and an average energy of the particles which will be transmitted through the field, from an entrance aperture at one end of the cylindrical segments to the exit aperture at the other end.

The proportionality constant, known as the analyzer constant, is low to $\bar{R}/2\delta$ and is equal to 1.96 eV/V and 20.0 eV/V for the low and high energy analyzers respectively.

It can be shown that the energy resolution, $\Delta E/E$, of the instrument is to a good approximation equal to δ'/\bar{R} , where δ' is the width of the entrance aperture. The angular aperture of the system is approximately δ'/R radians (FWHM) in the plane of the trajectory. This instrument may be used for the analysis of either electrons or protons by the choice of the polarities of the applied potentials. Discrimination between protons and electrons is thus inherently excellent.

3.2 Physical Description

The SSJ3 consist of 2 sets of plates, one set for each of the 2 energy ranges (51 - 1045 eV and 1.06 - 20 keV respectively). Schematics of the small plates geometry (low energy range), and large plates geometry (high energy range) are shown in Figure IV-1.

The plates are made of aluminum with a sand-blasted finish to minimize the amount of XUV reaching the channeltrons (see "Detectors" below) which are extremely sensitive at these wavelengths. Further reduction of the XUV scattering from the small plates is achieved through closely spaced serrations on the plate inner surfaces.

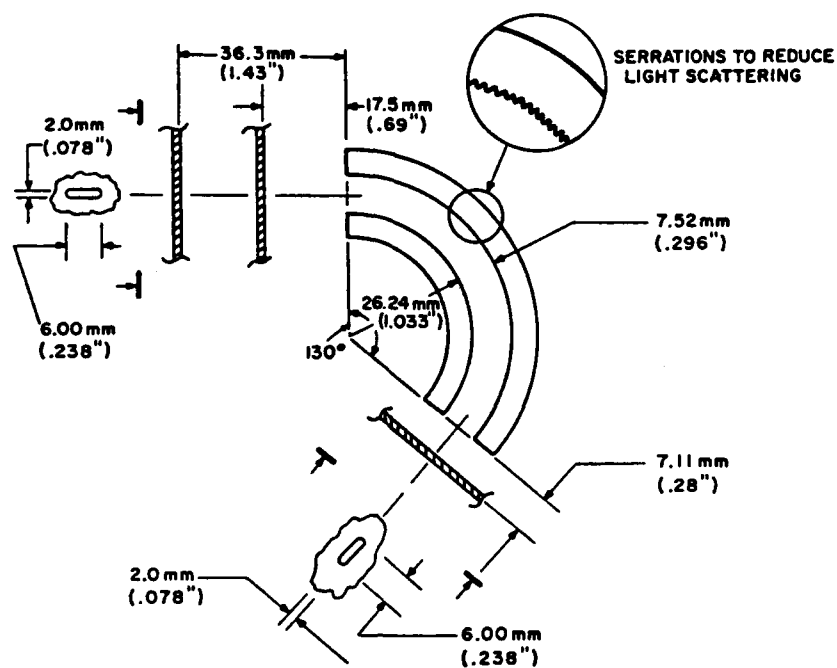
Dielectric materials between the plates and in the vicinity of their edges were carefully avoided to prevent charge buildup in these areas which in turn would affect the electron trajectories.

Figure IV-2 shows a picture of the complete SSJ3 plate assembly together with the collimation system and the channeltrons in their housing.

The operating voltages are between ± 25 V and ± 500 V and ± 12.5 V and ± 250 V for the high and low energy analyzers. The use of a balanced \pm (volts) configuration results in a zero potential surface midway between the plates. Since this surface passes through the narrow apertures, electrons undergo negligible acceleration upon entering and leaving the analyzer.

The field-of-view of the spectrometer is oriented at 45 degrees

SSJ3 - SMALL PLATES GEOMETRY



SSJ3 - LARGE PLATES GEOMETRY

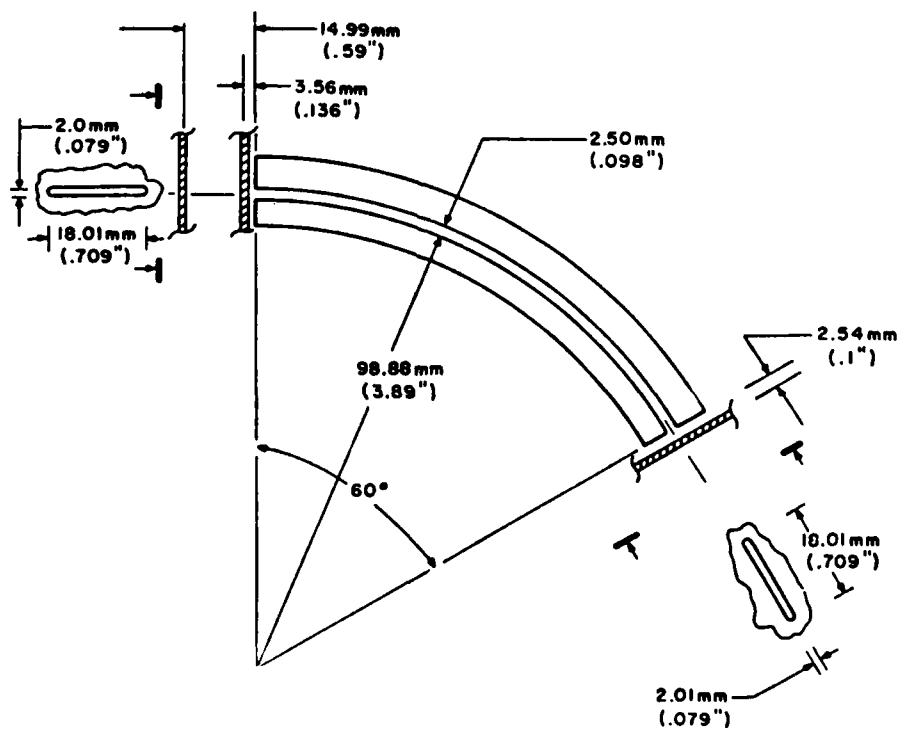


Figure IV-1



Figure IV-2

with respect to the spin axis of the satellite. Thus the electron pitch angles sampled are between 30 and 60 degrees under quiescent magnetic conditions.

The integration time for each of the 16 channels (8 channels in the "high" and "low" energy range) is 12.583 seconds. Since the spectrometer records the electron fluxes in 2 energy channels (one in the "high" and one in the "low" energy range) simultaneously, a complete sixteen point spectrum is obtained in 100.7 seconds.

3.3 The Detectors

Immediately following the exit aperture of each set of plates are a pair of Channeltron Electron Multipliers*. The high energy range uses two CEM 4019-C/WL-SC (10 mm funnel), while the low energy range uses two CEM 4013-C/WL-SC (3 mm funnel). Each device has a gain of $\sim 10^7$ - 10^8 . The anodes of the Channeltrons operate at +3 kV and their funnels are at ground potential. The critical dose for each Channeltron is in excess of 10^{11} counts.

Special care was taken to avoid potentially contaminating materials in the instrument which may have resulted in a long-term gain degradation of the detectors.

*Galileo Electro-Optics, Sturbridge, MA

4.0 THE ELECTRONICS

Figure IV-3 is a block diagram of the instrument. The Channeltron outputs from each ESA are capacitively coupled to a preamplifier-discriminator. These units produce logic-compatible outputs which are counted by log accumulators. Timing and control logic steps the energy levels, resets and enables the log accumulators, and loads the data words into the shift registers. Upon receipt of a gate pulse from the spacecraft, the data word in the corresponding shift register is serially shifted out on a data line. Figure IV-4 shows the SSJ3 with its analog and digital cards exposed. Brief descriptions of the functional blocks follow.

4.1 The Preamplifiers

The preamplifiers used in this instrument are of the charge sensitive type and have an inherent discrimination level of about .5 picocoulomb, corresponding to an electron gain of 3×10^6 . They include pulse forming circuitry which produces CMOS-compatible output pulses about 0.5 μ s in duration.

An externally accessible test input is provided to verify operation of the preamps, counters, and logic. This input couples an external pulse generator through a 2 pf capacitor to the preamp inputs. A fast-rising pulse of about .5 volt amplitude transfers enough charge into the preamps to produce output pulses.

4.2 The Logarithmic Counters

The electron count from each analyzer is accumulated in a log counter following the preamp. These units produce an 11-bit logarithmic representation of the actual count. The seven least significant bits represent the mantissa and are the contents of a 7-bit binary counter. The remaining four bits, the exponent, represent the final prescale factor by which the input to the 7-bit counter is divided. The unit operates as follows: Initially, the 7-bit counter counts all incoming pulses, up to a count of 128, or 0000000; at this point the input begins to be divided by two, so that only alternate pulses increment

SSJ3 BLOCK DIAGRAM

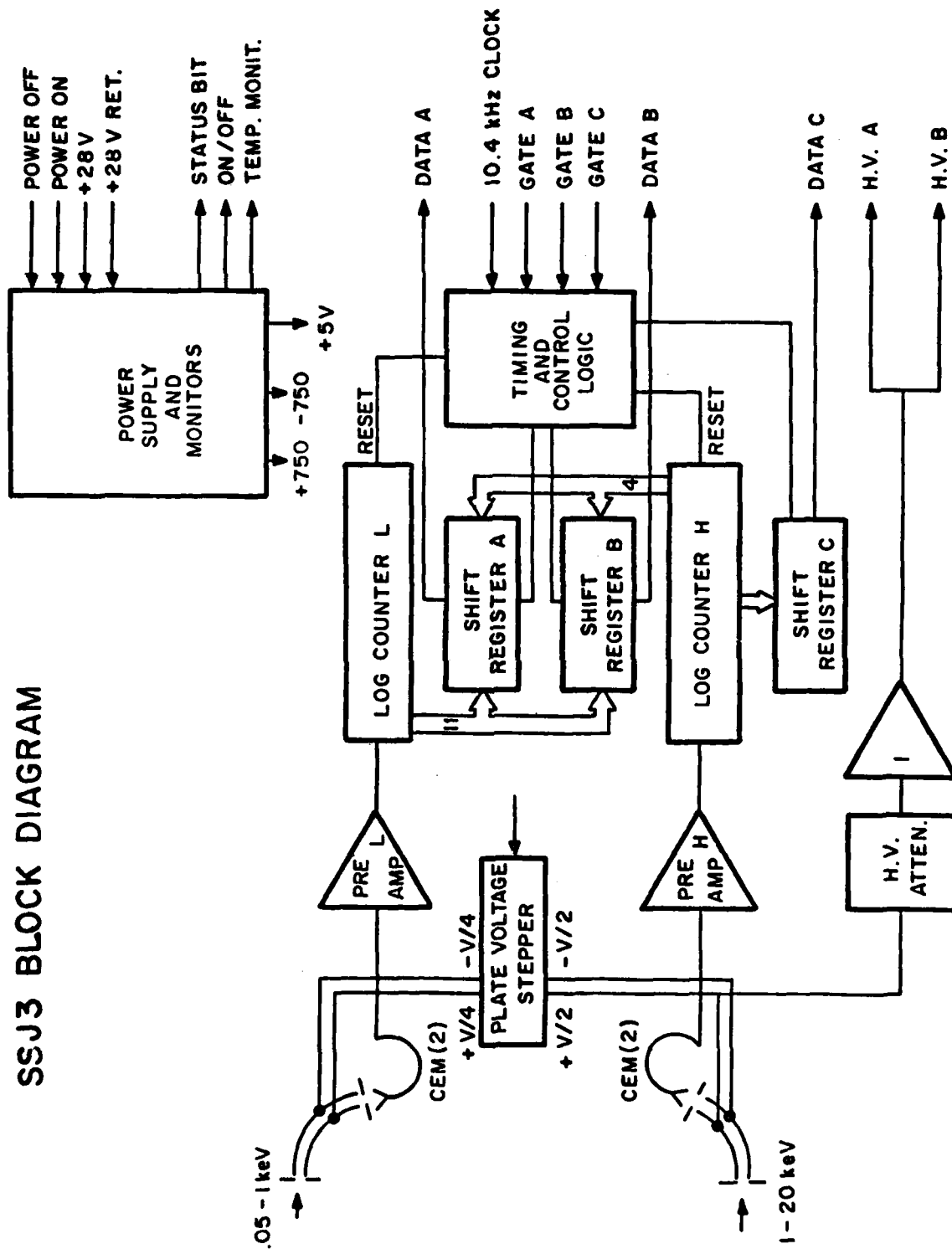


Figure IV-3

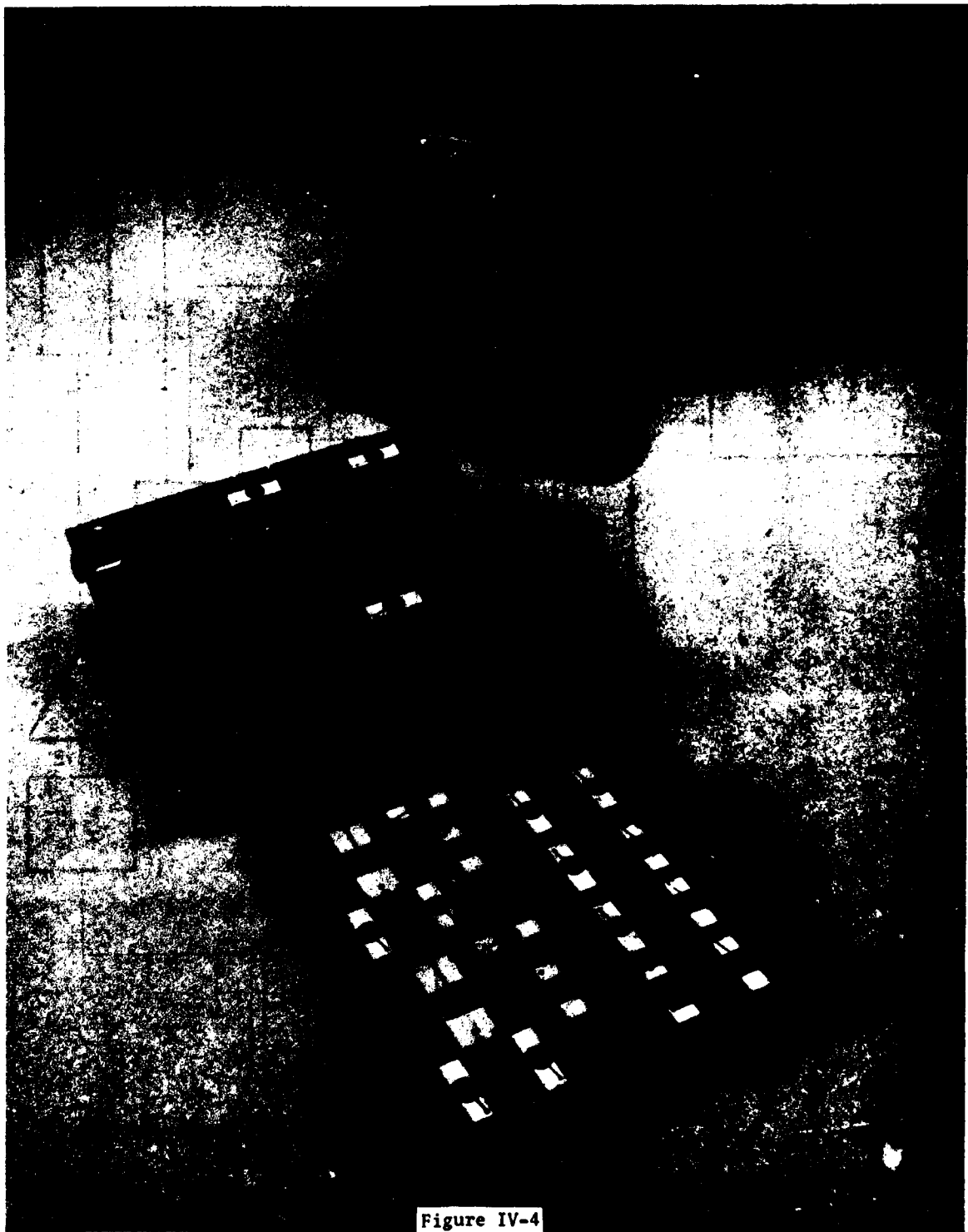
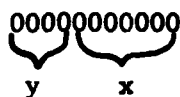


Figure IV-4

the counter. When the counter again reaches the 0000000 state, the pre-scale factor doubles, up to a maximum value of 2^{15} . The actual count represented by the 11-bit word is given by:

$$\text{COUNT} = 2^y(x + 128) - 129.$$



The value 129 rather than 128 appears here because a 1 count is preset into each log accumulator at the beginning of every data interval to aid in readout verification. This count must be subtracted to get actual count.

The maximum capacity of these accumulators is 8,355,711 counts, which is well in excess of the maximum expected count for the 12.5 seconds integration time period.

4.3 The Control Logic and Data Output

To establish timing for plate voltage stepping and data accumulation the control logic section uses two of three gate pulses provided by the spacecraft (see Fig. IV-5). These pulses, which read out data words A and B, are spaced 12.5 sec, of 1/2 data frame apart, to simplify instrument timing. At each occurrence of pulse A or B, the plate voltage is stepped, and the log counters are disabled and their contents latched into shift registers. Then the contents of the corresponding 16-bit shift register, either A or B, is transferred across the interface. Since 16 bits are not adequate to read out the two 11-bit counts (plus sync bits), the 7-bit mantissas of the high energy counts are stored in a third shift register and read out by Gate C later in the frame.

In each 25 second data frame, 4 counts, representing four energies, are read out, producing a complete 16 point spectrum in 100 seconds.

All logic elements in the SSJ3 are C-MOS. Radiation hardened devices were used where possible.

PLATE VOLTAGE SEQUENCE AND TIMING DIAGRAM

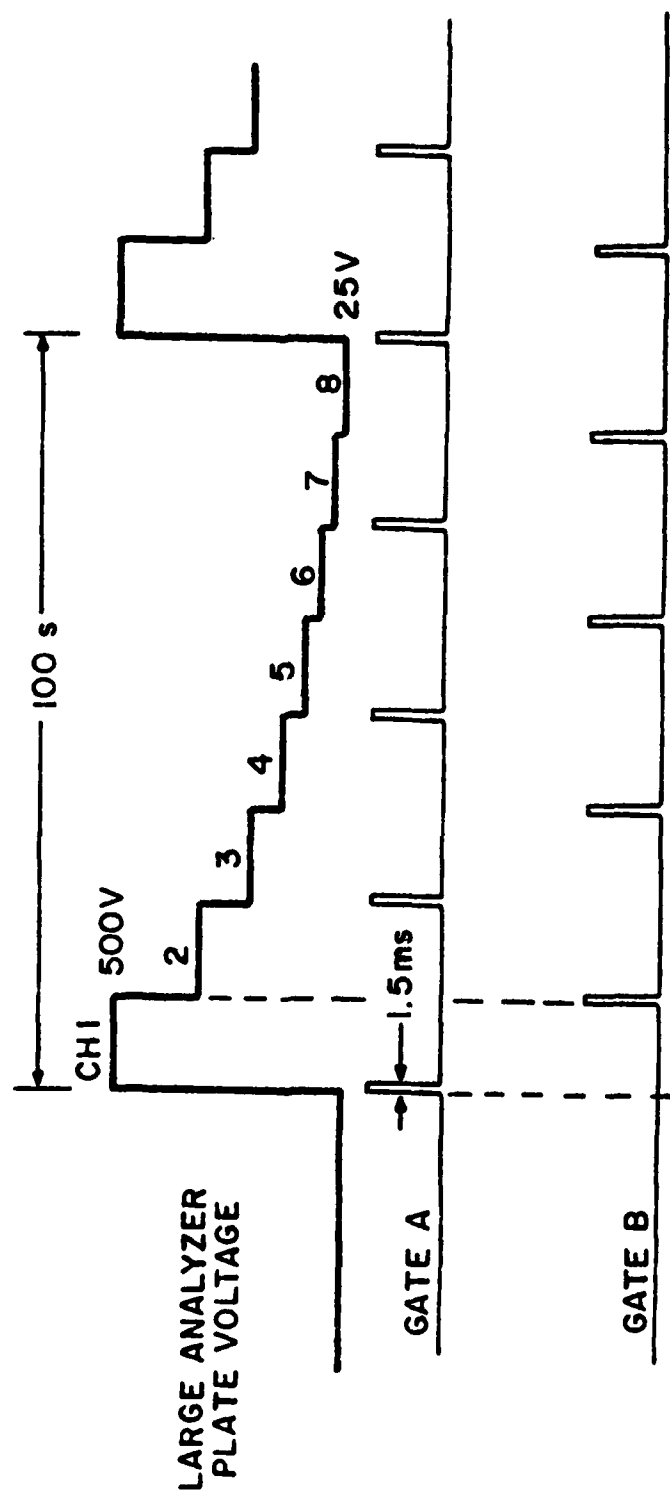


Figure IV-5

4.4 The Power Supply

The SSJ3 package utilizes a 50 kHz sine wave inverter type DC-DC Converter to provide all required power. This supply is built in-house. It supplies four regulated voltage levels: +5 V; ± 750 V; and +3000 V. +5 V operates all analog and digital circuitry. ± 750 , which are derived from voltage doublers, supply the plate stepper. +3000 V is the bias voltage for the Channeltrons.

4.5 The High Voltage Stepping Circuit

The plate voltages are controlled by a shunt regulator using a chain of 4 high voltage field effect transistors as the shunt element. Employing only a single reference and error amplifier, this circuit produces balanced positive and negative outputs. The voltage levels are determined by fixed programming resistors which feed known currents into the error amplifier. These resistors are sequentially placed in the circuit by a Johnson-type C-MOS counter.

The settling time for this circuit is about 3 ms for the negative-going steps. This represents a negligible dead time for the instrument. Figure IV-5 is the wave form at the inner high energy plate.

5.0 THE DATA

Table IV-1 lists the mean energy (in eV) of each of the 16 energy channels together with the corresponding geometrical factor ($\text{cm}^2\text{-ster-eV}$). The energy resolution for each channel is $\sim 10\%$, and the acceptance angles of the low energy and high energy analyzer are 3.7×4.6 degrees (FWHM) and 1.9×9.6 degrees respectively.

Because of a tight schedule for the delivery of the SSJ3, only a preliminary calibration was performed on the instrument. The parameters shown in Table IV-1 were obtained for 2 other similar instruments flown in connection with the Defense Meteorological Satellite Program (DMSP) of the U.S. Air Force. These instruments were calibrated using an electron system at Rice Institute in Houston, Texas. Our experience has shown that there is a remarkable consistency from instrument to instrument in the mean energies and normalization constants. Thus, we estimate the certainties in the energies to be of the order of $\pm 4\%$, and that of the normalization constants $\pm 10\%$ approximately.

5.1 Presentation of the Data

The SSJ3 electron data are written onto magnetic tapes at ESOC, and sent monthly to Mullard Space Science Laboratory (MSSL) and to Emmanuel College for processing.

MSSL presents the data in the output format shown in Figures IV-6 (daily summaries) and IV-7 (monthly summaries).

The Daily Summaries - The daily summaries are presented according to the following format. The channels are interpreted over 12 formats (5 min 02 sec) giving 286 points in 24-hour period. Note that UT and local time are identical for METEOSAT-F2.

1. High Energy Spectrum (HI) - For each of the 8 energy channels ($i = 9$ to 16), the electron intensity ($\text{cm}^{-2}\text{-sr}^{-1}\text{-s}^{-1}\text{-eV}^{-1}$)

$$J(i) = C(i)/N(i)/T$$

where $C(i)$ is the accumulated number of counts in the time T
($T = 37.5$ sec).

TABLE IV-1

Channel Number	Center Energy (eV)	Normalization Constant (cm ² -ster-eV)
1	49	1.72 x 10 ⁻³
2	75	3.53 "
3	116	5.65 "
4	177	8.42 "
5	274	1.30 x 10 ⁻²
6	418	2.00 "
7	664	3.17 "
8	990	4.74 "
9	984	1.09 x 10 ⁻¹
10	1508	1.50 "
11	2316	2.02 "
12	3540	2.82 "
13	5480	3.75 "
14	8360	5.03 "
15	12880	6.67 "
16	19800	8.25 "

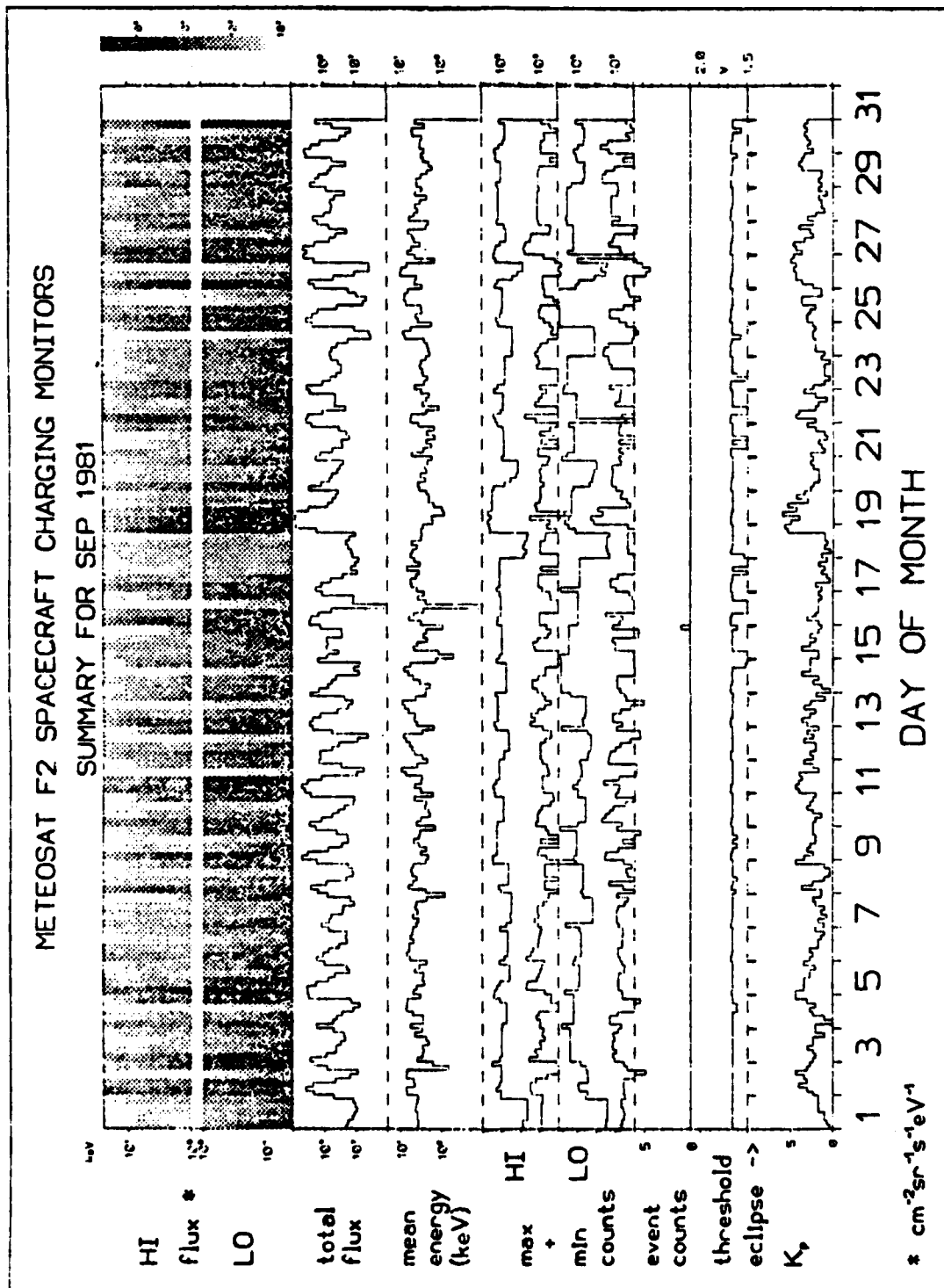


Figure IV-6

METEOSAT F2 SPACECRAFT CHARGING MONITORS
DAILY SUMMARY FOR DAY 244 (1 SEP) 1981

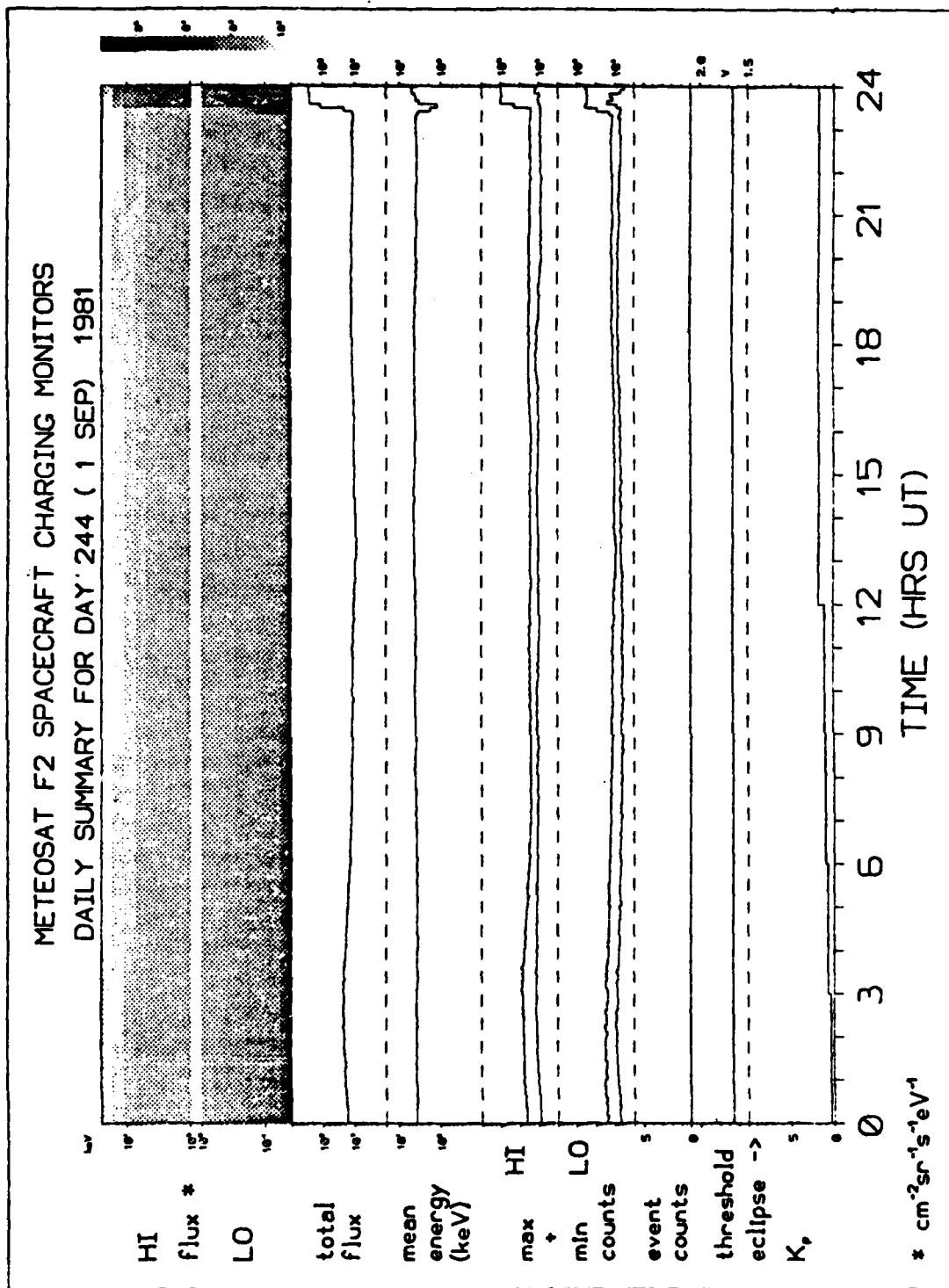


Figure IV-7

Successive pairs of fluxes are then averaged and grey-scaled logarithmically for the display within the range of 10^2 (white) to 10^6 (black) $\text{cm}^{-2}\text{-sr}^{-1}\text{-s}^{-1}\text{-eV}^{-1}$.

2. Low Energy Spectrum (LO) - The same procedure as for the High Energy Spectrum is followed for the 8 energy channels ($i = 1$ to 8) of the low energy detector.

3. Total Flux - The total number flux ($\text{cm}^{-2}\text{-sr}^{-1}\text{-s}^{-1}$) for the 16 energy channels is calculated according to the following summation

$$\Sigma NF = \frac{1}{2} \Sigma [J(i) + J(i+1)][E(i+1) - E(i)] \quad i = 1, 7 + 1 = 9, 15$$

giving the total number flux which varies between 10^6 and 10^9 .

4. Mean Energy - A mean energy ($\text{eV}\text{-cm}^{-2}\text{-sr}^{-1}\text{-s}^{-1}$) for the electron spectrum is then calculated according to the summation

$$ME = \frac{1}{2} \Sigma [J(i)E(i) + J(i+1)E(i+1)] [E(i+1) - E(i)] \quad i = 1, 7 \text{ and } 9, 15$$

This mean energy is plotted between 0.1 and 20 keV.

5. Maximum and Minimum Counts for the High Energy Detector (HI max + min) - For each integration period the maximum and minimum values of $12.5 \cdot C(i)/T(i)$ with $i = 9, 16$ are determined and plotted between the limits 10^2 and 10^6 .

6. Maximum and Minimum Counts for the Low Energy Detector (LO max + min) - Same as 5, but with $i = 1, 8$.

7. EEM Discharge Event Counter - Every 12.5 seconds a read out of the event counter gives the number of times that the threshold has been exceeded. The accumulation of this counter over 24 hours with a point plotted every 5 minutes on a scale of 0 to 5. Whenever the count exceeds 5 then 5 is subtracted. Note that the count is not integer due to the analogue nature of the output.

8. EEM Threshold Voltage - The average threshold voltage during each 5 minute period is plotted on a scale from 1.5 to 2.0 volts.

9. Eclipse Flat - On days when the spacecraft enters the shadow of the Earth a hatched panel indicates the eclipse time.

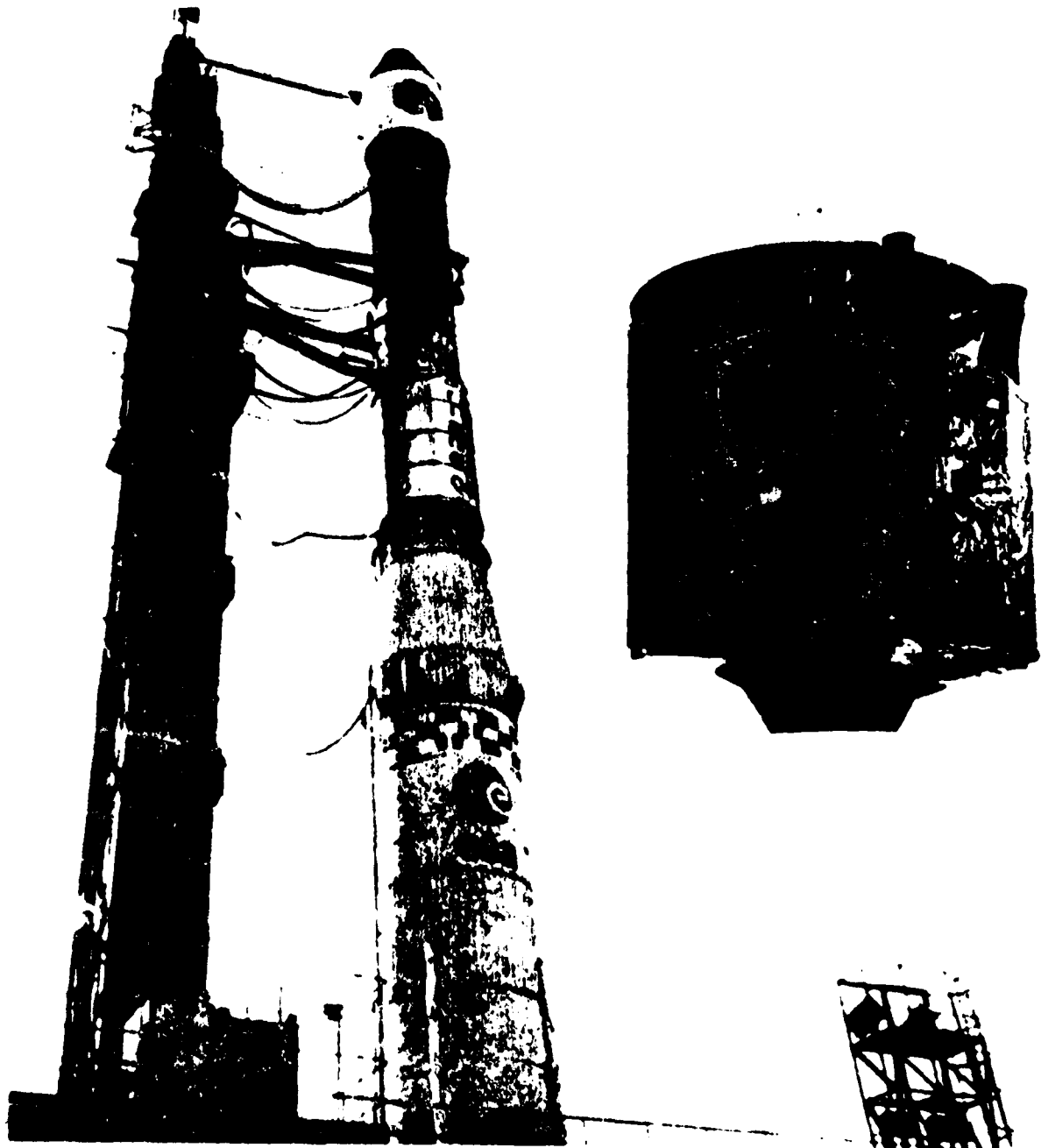
10. Geomagnetic Index Kp - The three hour planetary index is calculated from the magnetic field excursions measured at eleven stations spread around the Earth. It is plotted on a scale from 0 to 9. (Note 2₋ = 1.7, 2₊ = 2.3)

The Monthly Summaries - Data for a whole month is plotted using the same format as the daily summaries but using a basic integration period of 432 formats instead of 12 formats (3 hours). Although the grey-scaled panels are of limited value, the total flux curve does give a good monitoring of the long term changes in the diurnal variation and their association with Kp.

esa bulletin

number 29

february 1982





First Results from Meteosat-2 Discharge Experiments

A.D. Johnstone & G.L. Wrenn, Mullard Space Science Laboratory, University College London

A. Huber, Emmanuel College, Boston, USA

D. Hoge, Meteosat Satellite Manager, ESA, Toulouse, France

Many operational spacecraft have proved susceptible to unexpected status changes or anomalies and these have often been attributed to the consequences of surface charging. During its four years of operation Meteosat-1 suffered from 150 irregularities which, although not damaging, have led to a certain loss of data. Since there was a clear correlation between occurrence of anomalies and periods of geomagnetic activity, two new instruments were included on Meteosat-2 to see if anomalies are caused by discharges resulting from magnetospheric electron fluxes.

Spacecraft charging phenomena

Irradiation tests on the Meteosat prototype spacecraft and numerous spare components after Meteosat-1's launch showed that the anomalies could be triggered by arcing from high potentials generated by the impact of charged-particle fluxes, but these investigations posed more questions than they answered. The Meteosat-2 flight model had already been built by this time, but two actions were undertaken with a view to finding a solution. The electromagnetic cleanliness of the Meteosat-2 spacecraft was improved by changing critical interfaces and by grounding the outer thermal shields to reduce the susceptibility to charging. In addition, two new instruments were included in the payload so that data on the plasma environment and internal-discharge transients would be available if the anomalies were not eliminated.

After four months in orbit and only two such status changes, it does appear that the immunity of Meteosat-2 to the charging hazard has been significantly improved, but the problem has not been completely suppressed. The question now is, do the special on-board monitors give a plausible explanation of what is happening?

The Meteosat-1 anomalies

Meteosat-1, launched in November 1977, was fully operational for its first two years in orbit. Since then, a reduced mission has been performed as a result of a malfunction in the satellite's overload protection system. Soon after Meteosat-1 operations began, it became evident that

anomalous status changes were occurring occasionally within a few sensitive command interfaces, and there was evidence of a correlation with geomagnetic index. Ground simulations gave somewhat contradictory results, and could not provide a model for the mechanism that was leading to the anomalies. Most anomalies were observed during the period of full operations, but status changes have been observed even in the reduced mode.

The Meteosat-2 anomalies

Meteosat-2, launched on 19 June 1981, has shown only a small number of anomalies compared with Meteosat-1 and only two might be attributed to spacecraft charging – on days 251 and 271 (8 and 28 September). A major peak in the Fredericksburg geomagnetic index (Fig. 2) occurred on day 206 (113), and a second one on day 235 (48), but September was in fact a quiet month. Significantly, no anomaly occurred near either of these increases in geomagnetic activity.

The Meteosat-2 charging instruments

In addition to its normal payload Meteosat-2 is carrying three special 'experiments'. One, suggested and incorporated by ESTEC Power Systems & Electronics Section, and involving a Hexfet power transistor, was conceived as a technology demonstration. So far no changes in its parameters have been detected. The other two experiments are designed to seek a correlation between the environment of the spacecraft and the electromagnetic interference within it. Energetic electrons in the neighbourhood



Figure 1 Meteorat-2 being readied for launch on 19 June 1981, together with the Indian experimental communications satellite 'Apple' and the Ariane technological capsule (CAT)

of the spacecraft are being monitored by an electron spectrometer (SSJ/3, Fig. 3a) built by Emmanuel College, Boston. The electrical environment inside the spacecraft is being studied with an electrostatic event monitor (the EEM, Fig. 4), again developed and built by ESTEC Power Systems & Electronics Section.

The Electron Spectrometer (SSJ/3)

This instrument has been designed to count precipitating electrons in the energy range 50 eV–20 keV. The energy analysis is performed by a pair of electrostatic analysers employing a time-sequenced deflecting electrostatic field. Electrons entering the input aperture must have a certain energy to pass the deflecting electrostatic field of the curved plates and reach the exit aperture; this energy is proportional to the plate voltage.

Figure 2 Record of the Fredericksburg geomagnetic index (A-index) on days 170 to 300 of 1981

At the exit aperture, channeltron electron multipliers are used as detectors to provide the counting signals for the registers. The instrument provides a total of 16 energy-level counts, between 50 eV and 20 keV, by stepping the plate voltages of a low- and a high-energy channel sequentially twice per format. The output data are provided in a set of three, 16-bit data words containing four counts. Reduction of these data into 16-point energy spectra and production of suitable displays required a special processing arrangement.

Although the SSJ/3 instrument is fairly small and has a very low power consumption, it was quite difficult to incorporate on Meteorat-2 because the satellite was already in a very advanced state of integration. Two particular problems were:

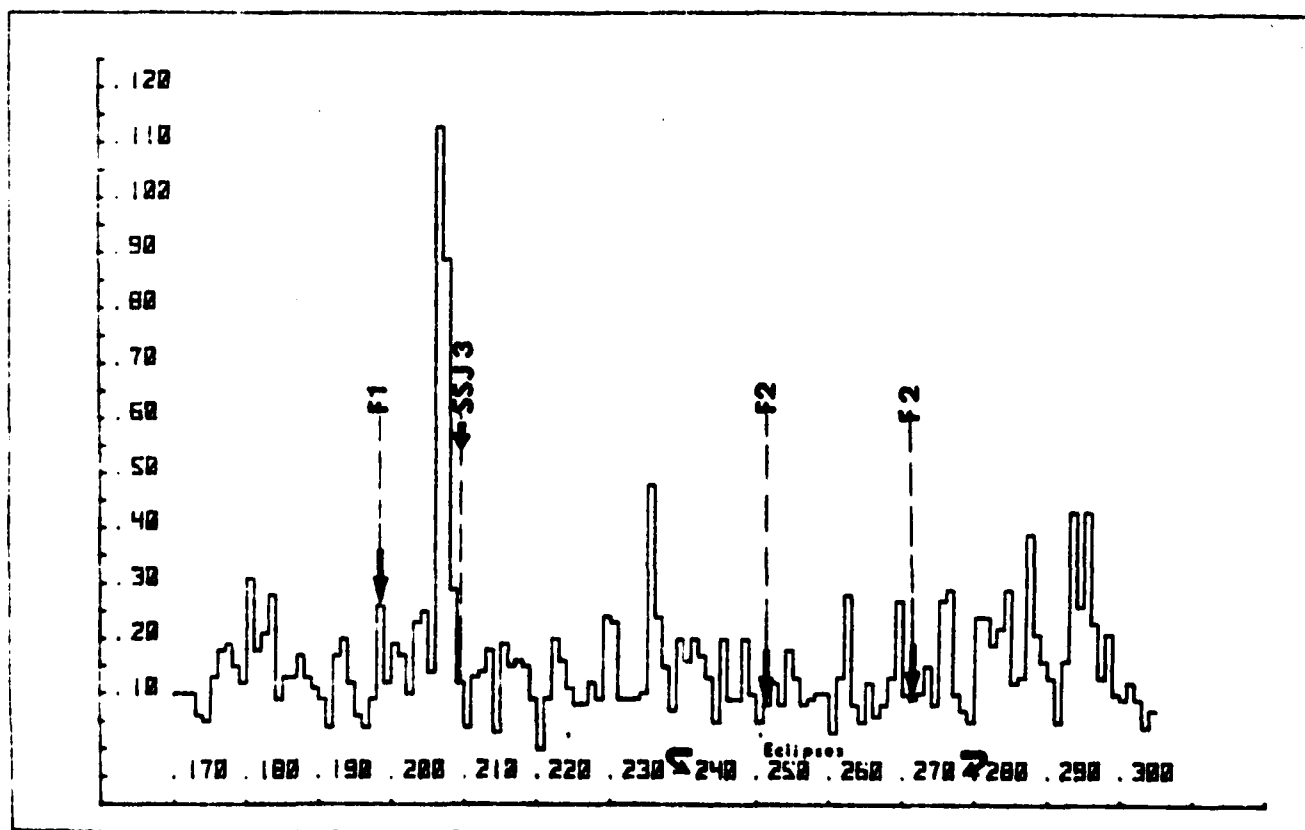
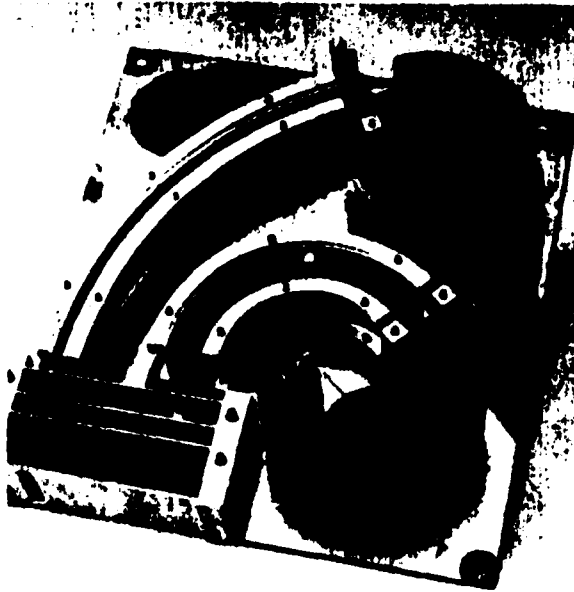


Figure 3 - The Electron Spectrometer (SSJ3) for Meteosat-2 provided by Emmanuel College, Boston

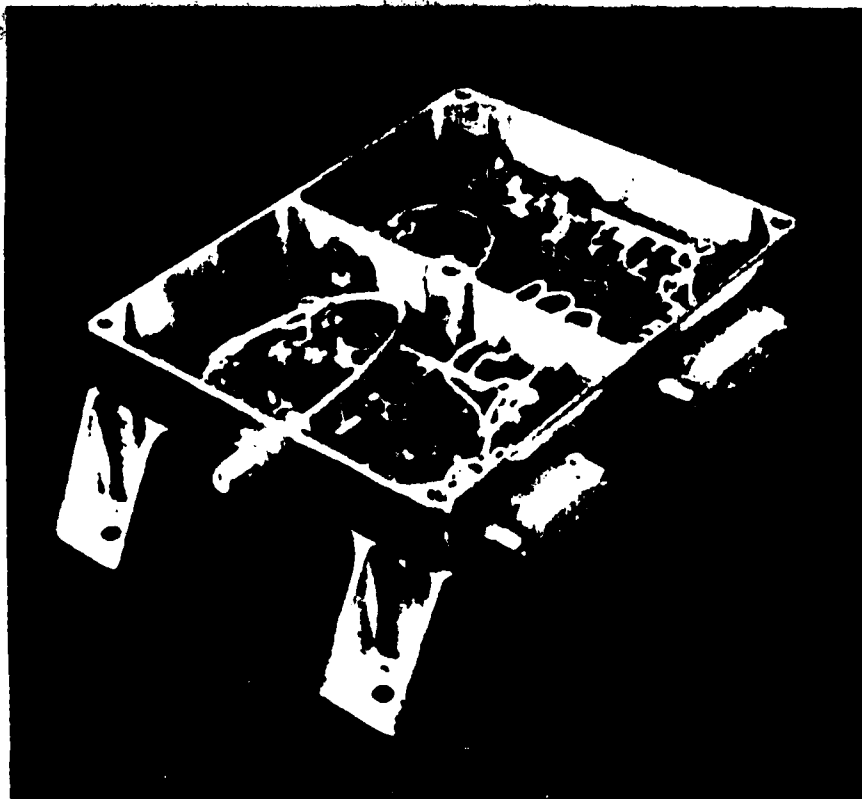
Figure 4 - The Electrostatic Event Monitor (EEM) for Meteosat-2 provided by ESTEC Power Systems & Electronics Section



a



b



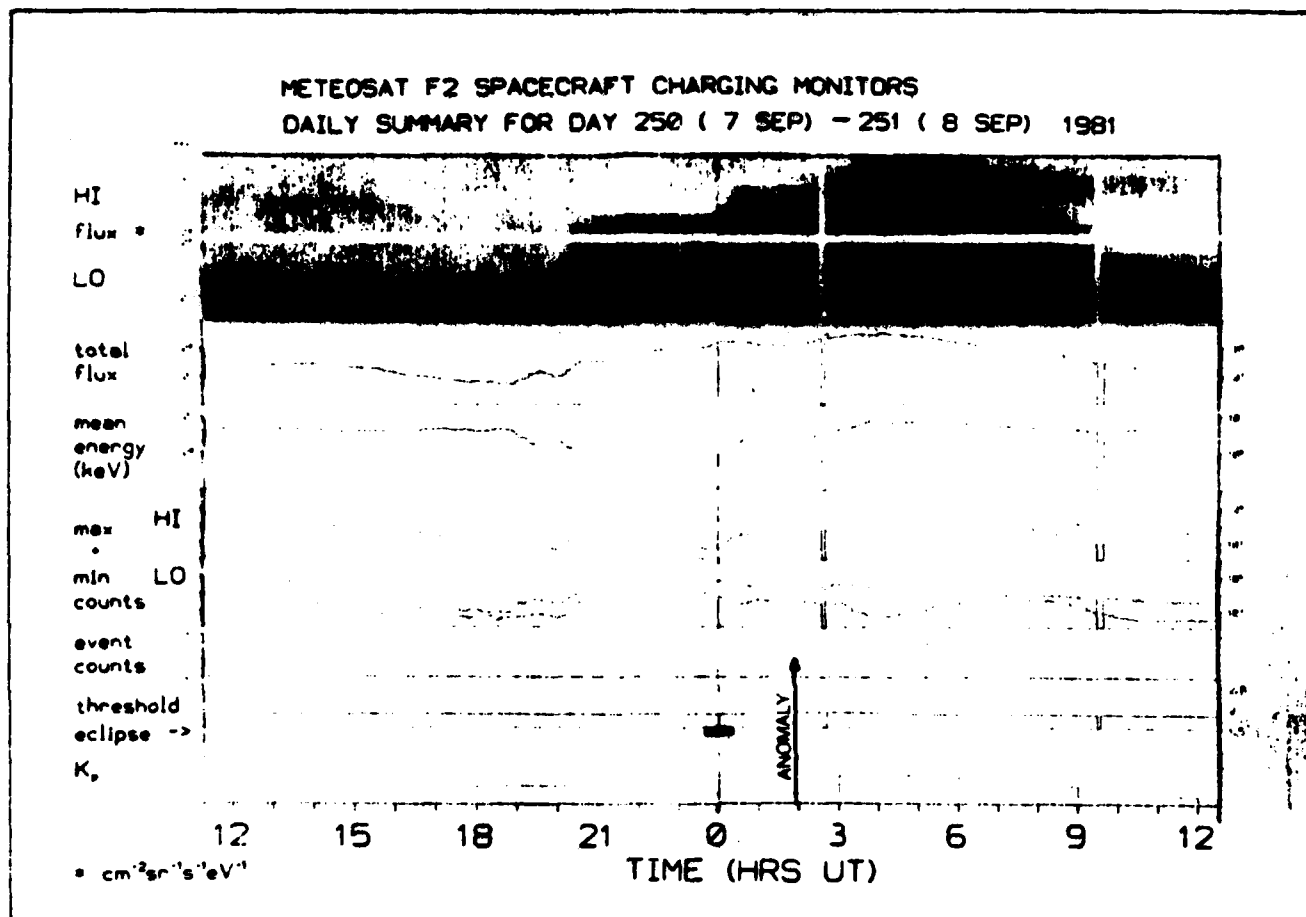
- to find a location for the instrument where its apertures could look into space, but not at the Sun
- to adapt the instrument's data to the 8-bit standard, as it had originally been developed for a 9-bit format

Fortunately, the Meteosat solar panels contain cut-outs to make them interchangeable and one of these openings could be used as a window for the experiment. The latter had to be tilted at 4.9° to avoid direct sunlight falling on the apertures (see Fig 3b). The second problem was solved by the experimenter

The Electrostatic Event Monitor (EEM)
The Electrostatic Event Monitor measures the signal from a probe mounted inside the spacecraft. For each telemetry format of 25 s duration, a signal processor provides a record of

- noise threshold level
- events exceeding this threshold (number, total time, highest peak amplitude)

Figure 5 - Daily summary of SSJ/3 and EEM instrument data for 7/8 September 1981 (day 251) showing the first Meteosat-2 charging anomaly at 01.56 UT



The instrument itself, which uses analogue circuitry for simplicity of design is small, light and employs a flexible antenna. Its installation on the spacecraft therefore caused no major problems. Its data are processed together with the data from the SSJ/3 instrument.

Initial measurements

The data from the charging experiments are being processed at Mullard Space Science Laboratory to give daily summary plots in the form of Figure 5. Five-minute integrations are carried out for the SSJ/3 and EEM outputs to compose the following data panels:

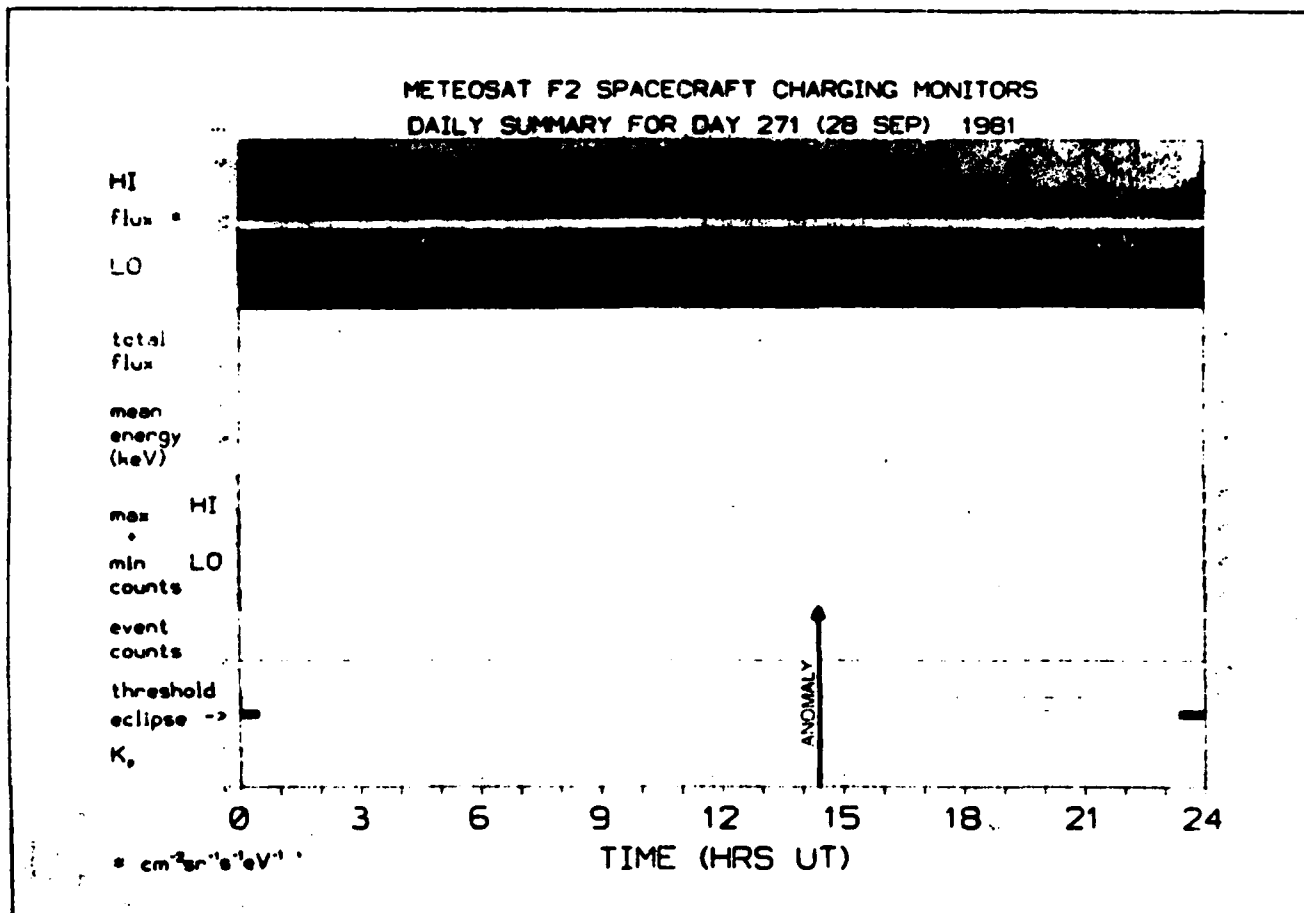
1. Differential number flux ($\text{cm}^{-2} \text{sr}^{-1} \text{s}^{-1} \text{eV}^{-1}$) of electrons for the 16 energy bins, grey-scaled logarithmically as the inset key
2. Total number flux ($\text{cm}^{-2} \text{sr}^{-1} \text{s}^{-1}$) of the electrons. This is proportional to the electric current carried by the electrons to the spacecraft
3. Mean energy (keV) of the detected electrons. This is a measure of the potential to which the electron flux could charge the spacecraft
4. Maximum and minimum counts per 12.5 s sampling period, registered by the High-energy detector
5. Maximum and minimum counts registered by the Low-energy detector
6. Accumulated number of EEM events detected
7. Threshold voltage for the event detection
8. A bar indicates periods of satellite eclipse
9. Three-hour Kp index appended to monitor geomagnetic activity

Kp is derived from the variations in the magnetic field measured at eleven stations around the world; it has a value from 0 to 9. In contrast, the Fredericksburg A index, referred to earlier, is a 24 h integration of variations recorded at a single subauroral station.

Figure 5 is composed of two daily summaries of SSJ/3 and EEM data, centred at midnight, covering the first charging anomaly at 01.56 UT on 8 September, whilst Figure 6 shows data for 28 September, covering the time of the second anomaly at 14.23 UT.

These data permit a number of immediate

Figure 6 -- Daily summary of SSJ/3 and EEM instrument data for 28 September 1981 (day 271) showing the second Meteosat-2 charging anomaly at 14:23 UT



observations:

- i. There is a complete absence of discharge events
- ii. The electron flux variations are completely consistent with previous measurements from geosynchronous orbit (ATS-5, ATS-6, Geos-1, Geos-2), showing daily plasma-sheet encounters with entry occurring at 23-24 UT on 10 August, 19-20:30 UT on 7 September and 22-24 UT on 28 September.
- iii. There are no special or unusual features in the electron flux near the anomaly times
- iv. There are flux enhancements at low energy before 01 UT on 28 September when the satellite was in eclipse. Spacecraft charging to

negative potentials is common during eclipses because the current of photoelectrons leaving the spacecraft is cut off

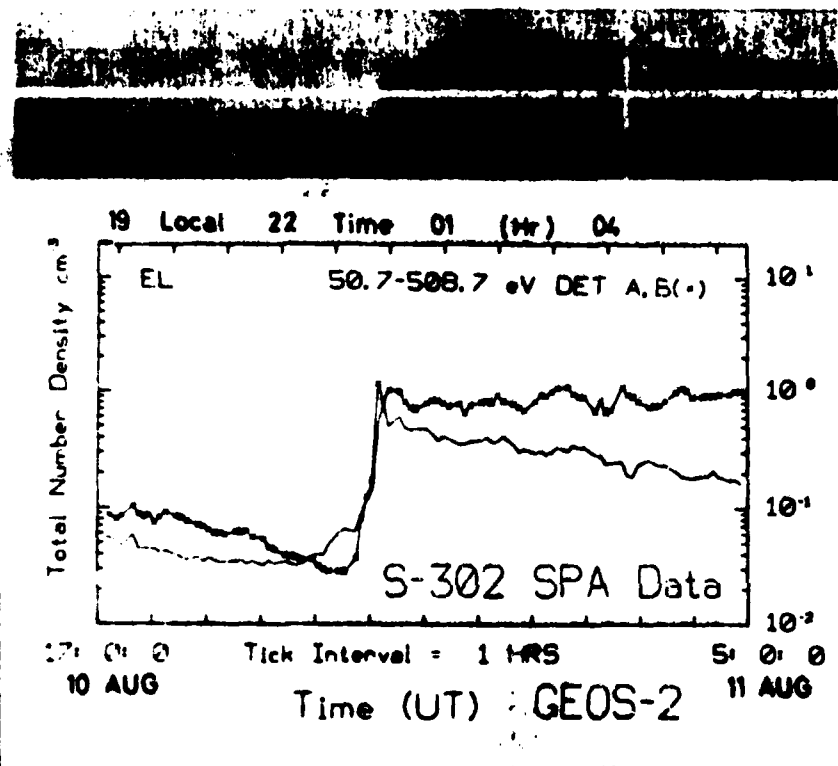
A review of four months of data establishes that no discharge events have been detected although the EEM experiment is functioning correctly. A small change in threshold voltage appears to be associated with battery charging following each eclipse. The electron spectrum frequently changes during eclipse and might indicate charging of the spacecraft to a few hundred volts. No such charging events are seen at other times. The electron data clearly show how the plasma-sheet boundary moves in response to changes in the solar wind, which are also

monitored by the geomagnetic activity index Kp. The inner edge of the plasma sheet is typically characterised by lower temperatures, and this gives rise to the energy dispersion observed at the boundary. Increased dispersion often results from particle-injection events near local midnight.

Geos-2 data

Geos-2, also in a geostationary orbit, but displaced in longitude from Meteosat-2 by between 25° and 37°, has a payload ideally suited to measuring the particle environment. Numerous attempts to use the data to understand the Meteosat-1 anomalies have met with little success, but the difference in local time (1.7-2.5 h) could be sufficient to prevent detection of the charging fluxes. Geos-2 now operates

METEOSAT F2 SPACECRAFT CHARGING MONITORS
DAILY SUMMARY FOR DAY 222 (10 AUG) - 223 (11 AUG) 1981



for only 12 h per day (17-05 UT), and not during eclipses.

Figure 7 presents densities of electrons with energies in the 50-500 eV range as measured by the MSSL experiment (S302) on Geos-2. These plots for 10/11 August can be compared with the SSJ/3 low-energy data for that day. The plasma-sheet entry at 22 UT is at a local time of 2330 which is virtually the same as the Meteosat-2 crossing. In quiet times the boundary remains stationary, but comparison of the two data sets for disturbed days gives a better measurement of the boundary motion than was previously available.

Higher densities are recorded at disturbed times, on 25 July 1981 for example a

strong compression drove Kp to 8 for 15 h and 50-500 eV electron densities exceeded 20 cm^{-3} at 6.6 Earth radii as the plasma sheet and the magnetopause approached the Earth.

Geos-2 data for 8 September confirm the lack of charging fluxes near the anomaly time. The only significant particle injection occurred just before 04 00 UT, well after the anomaly, at very high energies (30-37 keV electrons, recorded by Geos-2 experiment S321).

Conclusions

After four months of Meteosat-2 data compilation, it appears that anomalies are few and far between. The improved electromagnetic cleanliness of this second spacecraft could account for this,

although the decreasing activity on the Sun will also be a factor. The two radiometer position jumps observed cannot be explained simply by the data from the new experiments. There is no evidence for discharge events, but in both cases there was an unexplained telemetry break and it is possible that vital measurements were lost. Further investigation is needed to find out why these synchronisation failures occurred.

It is also possible that the EEM instrument has been set up with insufficient sensitivity, but this will only be proved if forthcoming status changes have full telemetry coverage.

The SSJ/3 instrument is providing reliable monitoring of the electron fluxes believed to produce surface charging, but for the two anomalies it is clear that significant enhancements did not occur at the critical times. This suggests either that the charging takes place very much earlier and the consequent discharge is triggered by some internal spacecraft event, or that the offending particles are of a different type. It has been proposed that very energetic penetrating radiation might be responsible for many spacecraft problems. The delayed-discharge theory must be carefully investigated and a lot more anomalies would certainly help, though satellite operators and users would obviously not agree!

The comparison of the Meteosat-2 and Geos-2 data has demonstrated once again the advantage of having two spacecraft available in orbit to discriminate between temporal and spatial changes. The SSJ/3 data promises to be most valuable for pursuing a number of studies in magnetospheric physics and copies of the daily summaries are to be made available for that purpose.

V. DATA ANALYSIS AND INTERPRETATION

1.0 AURORAL X-RAY CONTAMINATION OF THE LOW ENERGY PROTON SPECTROMETER ON THE S3-2 SATELLITE IN THE POLAR REGIONS

A low energy proton spectrometer (LEPS) was flown on the Air Force S3-2 polar orbiting satellite to observe primarily the trapped protons in the 0.1 to 6 MeV energy range (Pantazis et al., 1975). In the polar regions, which usually showed low proton fluxes, the LEPS recorded high counts in a single direction below the satellite horizon over the course of the five-month operational period. The same pattern of observations can be seen in the work of Imhof et al. (1974), where a Ge(Li) spectrometer was used to observe bremsstrahlung X-rays from the auroral zones. Although the LEPS is theoretically inefficient in detecting X-rays, in this report we contend that it is the X-ray aurora that best explains qualitatively the dominant feature of the LEPS polar observations.

During the last decade several researchers have correlated observed electron spectra with observed X-ray spectra in the auroral zones. In such research, bremsstrahlung X-ray measurements provide a broader picture of the auroral zones than the more spatially limited electron observations. This report offers qualitative observational information on the subject of the correlation between precipitating electrons and the emerging bremsstrahlung X-rays as observed by detectors on the S3-2 satellite.

The Air Force S3-2 satellite was launched December 5, 1975 into a polar orbit in the noon-midnight meridian with an apogee of 1540 km, perigee of 230 km, inclination of 96.3 degrees, and a period of 1.71 hours. The ascending node was on the nighttime equator. The satellite spin period was approximately 18.5 seconds, with the spin axis perpendicular to the orbital plane.

The LEPS provided useful proton observations in the trapping and precipitating latitudes during the operational period from launch, December 1975 to May 1976. However, in the polar regions, here defined as poleward of the precipitating regions, although evidence of any solar proton fluxes is sparse and restricted to solar active periods, the observation of varying high counts from a single preferred direction below the satellite horizon persists throughout the five

month period. Our study of the data provided by the LEPS over this time period has shown that these anomalous polar observations were the results of electromagnetic radiations, i.e. bremsstrahlung originating in the auroral zones.

The results of our investigation are contained in the Scientific Report #2, AFGL-TR-80-0265, included in the Appendices section of this final report (Appendix 1).

Reference

Imhof, W.L., G.H. Nakano, R.G. Johnson, and J.B. Reagan, Satellite observations of bremsstrahlung from widespread energetic electron precipitation events, J. Geophys. Res., 79, 565, 1976.

2.0 INVESTIGATION OF THE LOST COUNT PROBLEM OF THE LEPS INSTRUMENTS

In the course of the analysis of the data obtained with the proton telescope (LEPS) flown on Air Force Satellites S3-2 and S3-3, we were confronted with artifacts in that data which needed precise investigation. These artifacts were traced not to a simple pile-up effect as one would have expected, but to energy spectrum shifts which were count rate dependent. These spectrum shifts occurred in regions of high radiation environment, and only with large G-factor LEPS flown on S3-2 and S3-3. The small G-factor LEPS flown on S3-3 did have such spectrum shift problems by virtue of its narrow solid angle. The data from this instrument together with laboratory calibration, gave us a method for interpreting the data from the wide angle LEPS.

The results of the investigation of the energy spectrum shifts in the LEPS are presented in the special report in the Appendices section (Appendix 2).

3.0 PROTON FLUXES (0.08 - 100 MeV) AS MENTIONED BY THE AIR FORCE SATELLITES S3-2 AND S3-3 IN 1976

The entirety of the proton data obtained with several particle telescopes flown onboard Air Force Satellite S3-2 and S3-3 was prepared for publication as an AFGL report titled "Proton Fluxes (0.08 - 100 MeV) Measured by the Air Force Satellites S3-2 and S3-3". The data are presented in the form of graphs and tables.

S3-2

The low energy proton data 0.082 - 0.680 MeV, were presented in table form (AFGL report, to be published): Figure V-1 shows a typical page. Each block of data on this page summarizes all of the sample data for a small interval in L space. For a given L interval there are n blocks of 5 lines each. On the first line of a given 5-line block, the L- H_{min} coordinates are given, with H_{min} in kms. H_{min} is defined as follows: for a given set of B,L values B-L iso-contours are drawn in the northern and southern hemispheres. The minimum altitude for each set of these iso-contours is called H_{min} . The H_{min} value is the average value of this parameter for the set of observations as is B, the magnetic field, and the corresponding equatorial pitch angle, EQPA. The ratio of value of the average magnetic field, B, to the equatorial value, BEQ , corresponding to a particular L- H_{min} interval is also given as B/BEQ . In this analysis, we used the magnetic field model IGRF 1965, with time derivatives extrapolated to 1976.0, and McIlwain's Invar to calculate the L parameter.

The next line lists the 6 energy intervals from 0.082 to 0.680 MeV. The line labeled BKG represents the background fluxes (counts/sec-cm²-MeV) (together with the corresponding percentage statistical error, $2/\sqrt{N}$) in each of the 6 energy channels. These background fluxes were mostly due to high energy protons penetrating the shielding of the instrument and to the bremsstrahlung produced in the same shielding, and in the spacecraft by high energy electrons. These background counting rates (N_{BKG}) were recorded when the instrument's

aperture was parallel (pitch angle intervals 0-15 and 165-180 degrees) to the local magnetic field line. The observed background count rates were then properly normalized to the instrument aperture to yield background fluxes, J_{BGD} .

The OMNI line lists the 6 omnidirectional fluxes, J_{OMNI} (proton/sec-cm²-MeV) recorded in the 6 energy channels. The J_{OMNI} for a given energy channel was calculated according to the equation $J_{OMNI} = 2\pi^2 \langle J_1 \rangle_1$ where $\langle J_1 \rangle$ is the average value of the proton fluxes observed at different pitch angle values.

Finally the line DIR gives the mirroring fluxes (pitch angle 75 - 105 degrees) in proton/cm²-sec-MeV-ster. The OMNI and DIR fluxes are the NET fluxes with background subtracted, and should be reliable as long as the corresponding background flux is small relative to them.

For all the data tabulated, the dead time corrections were $\lesssim 4\%$. Data for which dead time corrections were greater than this value were not used.

The three numbers under the column marked TM give the length of the observation time, in seconds, for the particular L-H_{min}.

Note that the notation of a three digit number followed by a + sign and a single digit number stands for that number times 10 to the single digit number power, i.e. 193 + 3 is equivalent to 193,000.

The intermediate energy proton data (0.680 - 6.0 MeV) are prepared in tabular form. The data are organized in a similar fashion except for the 2nd column labeled -6.00, corresponding to the BKG, OMNI, and DIR fluxes for events with $E > 6$ MeV, and which are recorded by the back detector of the LEPS telescope (Pantazis et al., 1975).

The results of a preliminary analysis of data obtained with the P-Alpha instruments flown on S3-2 and S3-3 were published previously (Holeman et al., 1978). However, it was found that in certain B-L regions, the observed count rates were substantially contaminated by chance coincidences between the two detectors. These corrections have been applied to the data which have been retabulated. Data from the P-Alpha instrument, covering the energy range 5.5 - 100 MeV

in 6 energy channels, were considered for presentation here. However, because of the low statistical weight of the data, omni-directional fluxes could not be calculated accurately and therefore are not presented.

S3-3

The low and medium energy range data recorded by the narrow angle LEPS, and the high energy data from the P-Alpha from S3-3 will also be presented in an AFGL report to be published. It will be noted that a set of two LEPS was flown on this satellite. These instruments were similar in design, but differed from one another by their geometrical factor and threshold energy. Because of spectral distortions which occurred with the wide angle LEPS in regions of high fluxes, we are presenting only the data recorded with the narrow angle LEPS.

Several words of caution are in order to the potential users of these tables. Firstly, no correction to the effective geometrical factor of the instrument has been made to account for pitch angle distributions which are very steep ($\sin^n \alpha$, with $n \gtrsim 20$). Steep proton pitch angle distributions have been observed at low L values (1.15 - 1.20), and H_{min} (290 - 330 km) by Fisher et al. (1977).

Secondly, in several regions of space, intense electron fluxes are present. Sweeping magnets incorporated in front of the solid state detectors of the LEPS instruments do sweep away these electrons up to 400 keV and 600 keV for S3-2 and S3-3 respectively. Electrons above these energies will contribute to the total count rates in each instrument with a small but finite probability. These high electron fluxes exist in a region of space $L \lesssim 1.8$ and at higher L values during large magnetic disturbances.

Typical energy spectra obtained with the LEPS and P- α instruments on S2-2 are shown in Figures V-2 and V-3, and with the LEPS S3-3 in Figure V-4.

REFERENCES

Holeman, E.G., A.F. Davis and M.P. Hagan, Analysis of data from research satellites, Final Report, Emmanuel College, AFGL-TR-78-0181, July 1978.

Pantazis, J., A. Huber and M.P. Hagan, Design of a low energy proton spectrometer, Final Report, Emmanuel College, AFCRL-TR-75-0637, December 1975.

Fisher, H.M., V. Auschrat and F. Wibberentz, J. Geophys. Res., 82, 537-547, 1977.

[illegible]

S3-2 SATELLITE ENERGY SPECTRUM LISTING FOR LEPS WIDE ANGLE INSTRUMENT									
LINE	WAVELENGTH (nm)	WAVELENGTH (microns)	WAVELENGTH (cm ⁻¹)	WAVELENGTH (cm ⁻¹)	WAVELENGTH (cm ⁻¹)	WAVELENGTH (cm ⁻¹)	WAVELENGTH (cm ⁻¹)	WAVELENGTH (cm ⁻¹)	WAVELENGTH (cm ⁻¹)
1	1.07	0.935	10700	9350	10700	9350	10700	9350	10700
2	1.08	0.917	9170	9170	9170	9170	9170	9170	9170
3	1.09	0.910	9100	9100	9100	9100	9100	9100	9100
4	1.10	0.909	9090	9090	9090	9090	9090	9090	9090
5	1.11	0.901	9010	9010	9010	9010	9010	9010	9010
6	1.12	0.893	8930	8930	8930	8930	8930	8930	8930
7	1.13	0.886	8860	8860	8860	8860	8860	8860	8860
8	1.14	0.879	8790	8790	8790	8790	8790	8790	8790
9	1.15	0.872	8720	8720	8720	8720	8720	8720	8720
10	1.16	0.865	8650	8650	8650	8650	8650	8650	8650
11	1.17	0.858	8580	8580	8580	8580	8580	8580	8580
12	1.18	0.851	8510	8510	8510	8510	8510	8510	8510
13	1.19	0.844	8440	8440	8440	8440	8440	8440	8440
14	1.20	0.837	8370	8370	8370	8370	8370	8370	8370
15	1.21	0.830	8300	8300	8300	8300	8300	8300	8300
16	1.22	0.823	8230	8230	8230	8230	8230	8230	8230
17	1.23	0.816	8160	8160	8160	8160	8160	8160	8160
18	1.24	0.809	8090	8090	8090	8090	8090	8090	8090
19	1.25	0.802	8020	8020	8020	8020	8020	8020	8020
20	1.26	0.795	7950	7950	7950	7950	7950	7950	7950
21	1.27	0.788	7880	7880	7880	7880	7880	7880	7880
22	1.28	0.781	7810	7810	7810	7810	7810	7810	7810
23	1.29	0.774	7740	7740	7740	7740	7740	7740	7740
24	1.30	0.767	7670	7670	7670	7670	7670	7670	7670
25	1.31	0.760	7600	7600	7600	7600	7600	7600	7600
26	1.32	0.753	7530	7530	7530	7530	7530	7530	7530
27	1.33	0.746	7460	7460	7460	7460	7460	7460	7460
28	1.34	0.739	7390	7390	7390	7390	7390	7390	7390
29	1.35	0.732	7320	7320	7320	7320	7320	7320	7320
30	1.36	0.725	7250	7250	7250	7250	7250	7250	7250
31	1.37	0.718	7180	7180	7180	7180	7180	7180	7180
32	1.38	0.711	7110	7110	7110	7110	7110	7110	7110
33	1.39	0.704	7040	7040	7040	7040	7040	7040	7040
34	1.40	0.697	6970	6970	6970	6970	6970	6970	6970
35	1.41	0.690	6900	6900	6900	6900	6900	6900	6900
36	1.42	0.683	6830	6830	6830	6830	6830	6830	6830
37	1.43	0.676	6760	6760	6760	6760	6760	6760	6760
38	1.44	0.669	6690	6690	6690	6690	6690	6690	6690
39	1.45	0.662	6620	6620	6620	6620	6620	6620	6620
40	1.46	0.655	6550	6550	6550	6550	6550	6550	6550
41	1.47	0.648	6480	6480	6480	6480	6480	6480	6480
42	1.48	0.641	6410	6410	6410	6410	6410	6410	6410
43	1.49	0.634	6340	6340	6340	6340	6340	6340	6340
44	1.50	0.627	6270	6270	6270	6270	6270	6270	6270
45	1.51	0.620	6200	6200	6200	6200	6200	6200	6200
46	1.52	0.613	6130	6130	6130	6130	6130	6130	6130
47	1.53	0.606	6060	6060	6060	6060	6060	6060	6060
48	1.54	0.599	5990	5990	5990	5990	5990	5990	5990
49	1.55	0.592	5920	5920	5920	5920	5920	5920	5920
50	1.56	0.585	5850	5850	5850	5850	5850	5850	5850
51	1.57	0.578	5780	5780	5780	5780	5780	5780	5780
52	1.58	0.571	5710	5710	5710	5710	5710	5710	5710
53	1.59	0.564	5640	5640	5640	5640	5640	5640	5640
54	1.60	0.557	5570	5570	5570	5570	5570	5570	5570
55	1.61	0.550	5500	5500	5500	5500	5500	5500	5500
56	1.62	0.543	5430	5430	5430	5430	5430	5430	5430
57	1.63	0.536	5360	5360	5360	5360	5360	5360	5360
58	1.64	0.529	5290	5290	5290	5290	5290	5290	5290
59	1.65	0.522	5220	5220	5220	5220	5220	5220	5220
60	1.66	0.515	5150	5150	5150	5150	5150	5150	5150
61	1.67	0.508	5080	5080	5080	5080	5080	5080	5080
62	1.68	0.501	5010	5010	5010	5010	5010	5010	5010
63	1.69	0.494	4940	4940	4940	4940	4940	4940	4940
64	1.70	0.487	4870	4870	4870	4870	4870	4870	4870
65	1.71	0.480	4800	4800	4800	4800	4800	4800	4800
66	1.72	0.473	4730	4730	4730	4730	4730	4730	4730
67	1.73	0.466	4660	4660	4660	4660	4660	4660	4660
68	1.74	0.459	4590	4590	4590	4590	4590	4590	4590
69	1.75	0.452	4520	4520	4520	4520	4520	4520	4520
70	1.76	0.445	4450	4450	4450	4450	4450	4450	4450
71	1.77	0.438	4380	4380	4380	4380	4380	4380	4380
72	1.78	0.431	4310	4310	4310	4310	4310	4310	4310
73	1.79	0.424	4240	4240	4240	4240	4240	4240	4240
74	1.80	0.417	4170	4170	4170	4170	4170	4170	4170
75	1.81	0.410	4100	4100	4100	4100	4100	4100	4100
76	1.82	0.403	4030	4030	4030	4030	4030	4030	4030
77	1.83	0.396	3960	3960	3960	3960	3960	3960	3960
78	1.84	0.389	3890	3890	3890	3890	3890	3890	3890
79	1.85	0.382	3820	3820	3820	3820	3820	3820	3820
80	1.86	0.375	3750	3750	3750	3750	3750	3750	3750
81	1.87	0.368	3680	3680	3680	3680	3680	3680	3680
82	1.88	0.361	3610	3610	3610	3610	3610	3610	3610
83	1.89	0.354	3540	3540	3540	3540	3540	3540	3540
84	1.90	0.347	3470	3470	3470	3470	3470	3470	3470
85	1.91	0.340	3400	3400	3400	3400	3400	3400	3400
86	1.92	0.333	3330	3330	3330	3330	3330	3330	3330
87	1.93	0.326	3260	3260	3260	3260	3260	3260	3260
88	1.94	0.319	3190	3190	3190	3190	3190	3190	3190
89	1.95	0.312	3120	3120	3120	3120	3120	3120	3120
90	1.96	0.305	3050	3050	3050	3050	3050	3050	3050
91	1.97	0.298	2980	2980	2980	2980	2980	2980	2980
92	1.98	0.291	2910	2910	2910	2910	2910	2910	2910
93	1.99	0.284	2840	2840	2840	2840	2840	2840	2840
94	2.00	0.277	2770	2770	2770	2770	2770	2770	2770
95	2.01	0.270	2700	2700	2700	2700	2700	2700	2700
96	2.02	0.263	2630	2630	2630	2630	2630	2630	2630
97	2.03	0.256	2560	2560	2560	2560	2560	2560	2560
98	2.04	0.249	2490	2490	2490	2490	2490	2490	2490
99	2.05	0.242	2420	2420	2420	2420	2420	2420	2420
100	2.06	0.235	2350	2350	2350	2350	2350	2350	2350

Figure V-1.

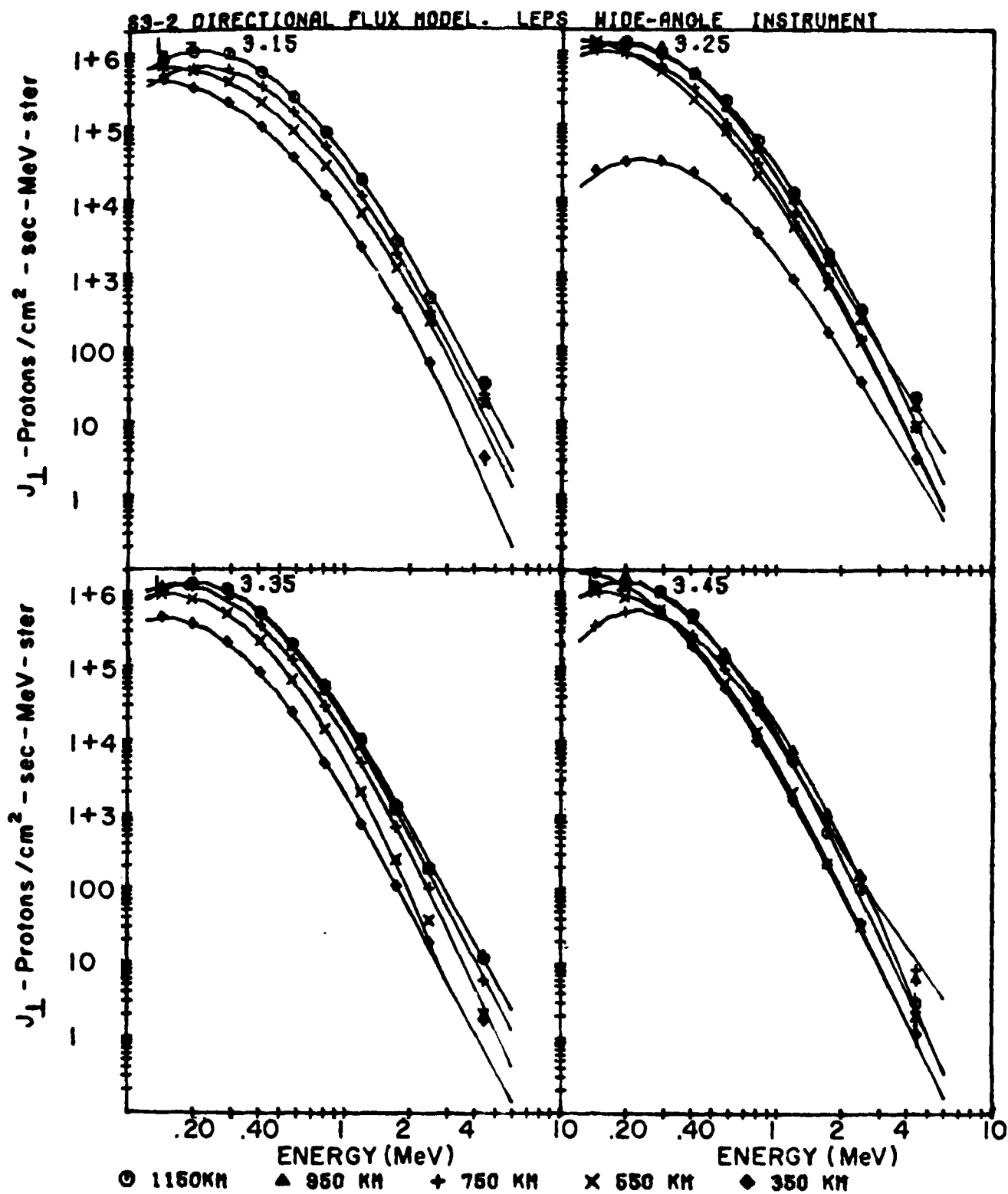


Figure V-2.

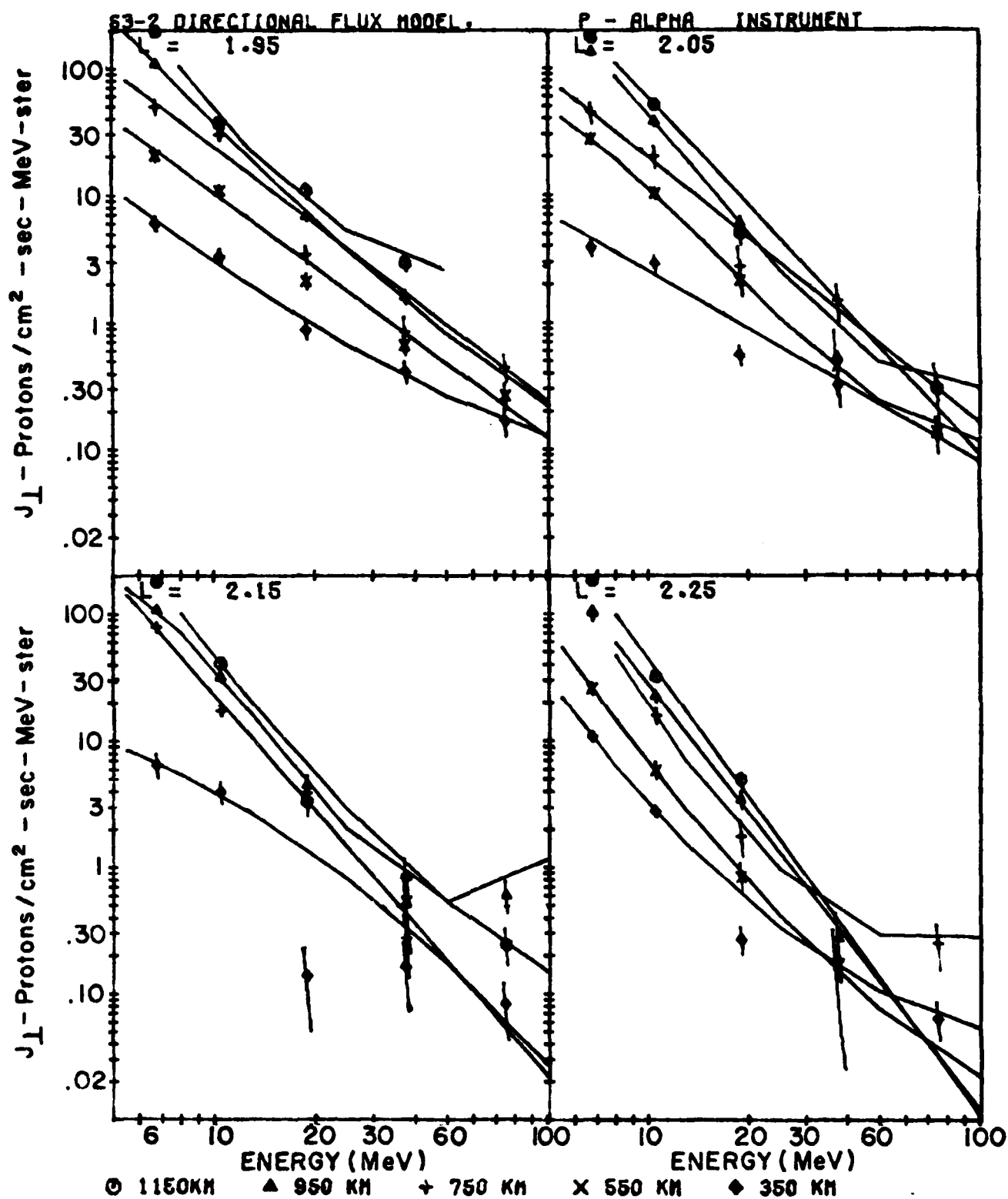


Figure V-3.

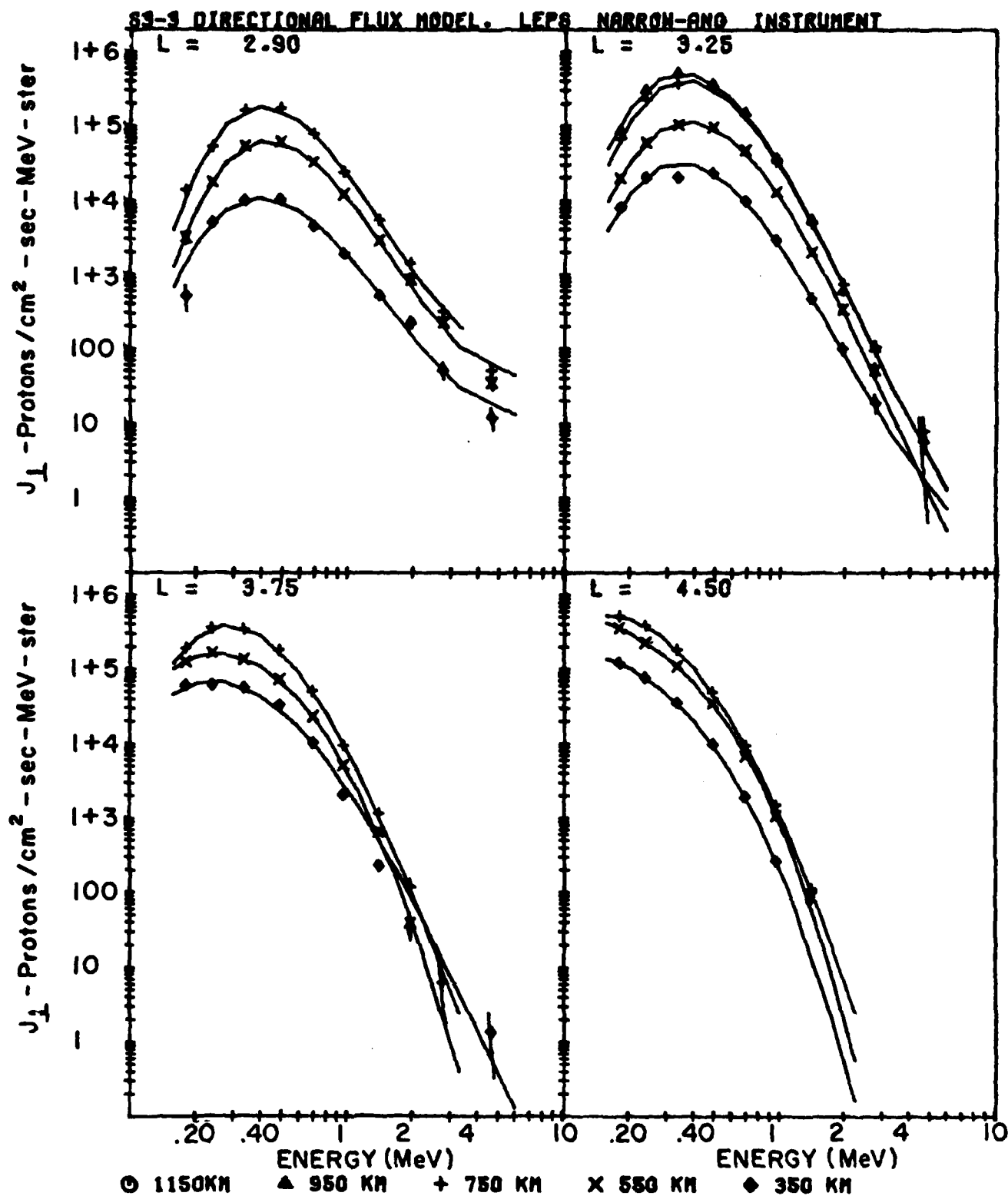


Figure V-4.

Further analysis of some selected data resulted in two publications.

In the first investigation, we studied the 55-MeV proton fluxes at low altitudes, between 275 km and 600 km, from 1961 until 1976. The data utilized were obtained from Air Force Satellite experiments flown from 1961 to 1972 together with data from the present S3-2, S3-3 experiments.

The analysis of these data showed that in spite of all the uncertainties involved, the agreement obtained between the theoretical calculations and the data was quite good. We concluded that the major determining factors of the 55-MeV proton fluxes in the inner zone were nearly constant since coupled with a solar cycle varying atmospheric ionization loss process.

The second investigation focused on the long term behavior of the $8.5 \leq E \leq 25$ MeV proton fluxes at low altitudes (600 - 900 km).

A five year continuous observation, 1963-1968, of the 8- to 25-MeV proton population, at $L < 2.0$, had shown a monotonic decrease in this population. We observed the same proton population from 1970 to 1976, using experiments flown on several USAF satellites (72-1, S3-2, S3-3). These data, together with published data from the DIAL satellite, showed that the decreases in the proton fluxes first observed from 1963 to 1968 continued unabated, at least until August 1976, and with the same original mean lives. The proton flux at $L = 1.35$ decayed over the 13-year period (1963-1976) with a mean life τ of 5.7 ± 0.5 years. At $L = 1.90$, τ was $4.55 \pm .16$ years. However, the proton flux at $L = 1.20$, which had first been reported as constant, started decreasing ~ 1970-1976 with $\tau = 3.07 \pm 0.25$ years (Figure V-5). Possible explanations for this phenomenon can be divided into the two categories of natural and artificial effects. We reviewed these different effects and conclude that most likely we are seeing the decay of the high energy protons redistributed by the 'Starfish' high-altitude nuclear explosion.

Copies of these 2 papers are included in the appendices (Appendix 1, Appendix 2).

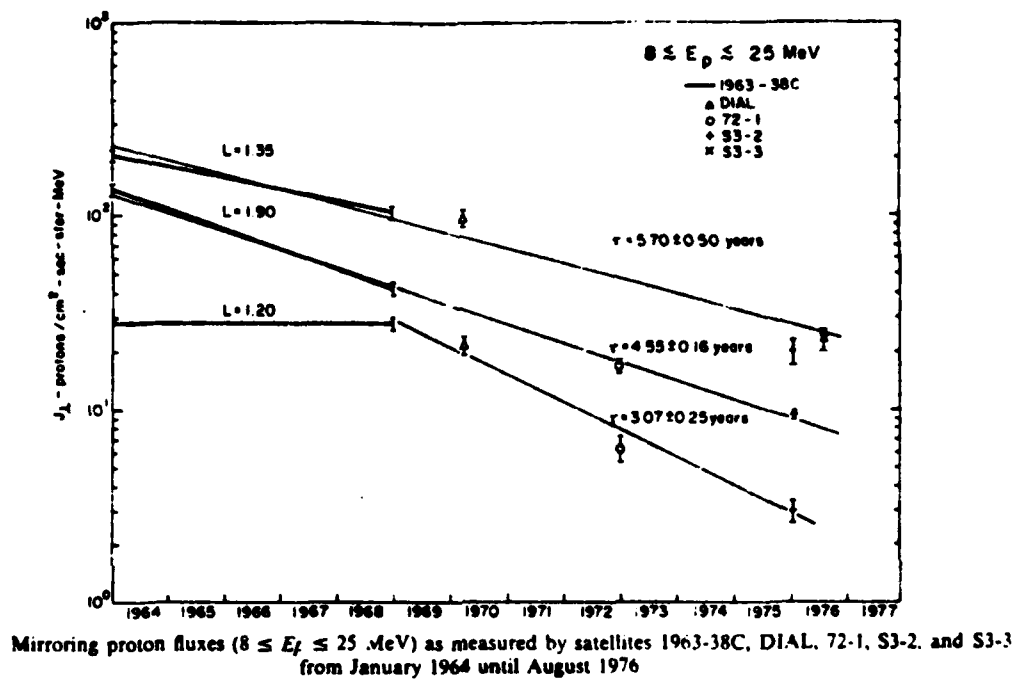


Figure V-5

4.0 ELECTRON PRECIPITATION OVER THE POLAR CAPS

The magnetic field lines over the polar cap regions extend in an antisunward direction and form the lobes of the magnetotail. They are furthermore interconnected through the magnetopause and the bow shock to the interplanetary magnetic field (IMF). Not much is known about the field structure within the polar magnetosphere, and a study of the low energy electron fluxes (50 eV - 20 keV) over these regions should provide an opportunity to study in detail this part of the magnetosphere which happens to be the most directly related to the Earth's interaction with the interplanetary medium. Other questions may be addressed using the electron data, such as the access of low energy solar flare electrons, or the intermittent acceleration processes undergone by these particles over the polar cap regions.

We have started a morphological study of the polar cap regions using the electron data obtained with the SSJ3 instrument onboard the Air Force Satellite DMSP-F2. The data covers a period extending from September 9, 1977 until the end of 1978. Although at the present time there exists gaps in the coverage, it is expected that these will be filled in the near future thus yielding a complete continuous coverage over a period of 15 months.

For the purpose of this investigation, we defined the polar cap region as the region starting and ending at the polarward boundaries of the diffused aurora.

At this time, we have completed the survey from Sept. 13, 1977 until March 31, 1978. We distinguish several patterns of electron precipitation, examples of which are given in the accompanying figures. Figure V-6 shows the first pattern which is a uniform electron precipitation across the polar cap region. These precipitations may also show an intensity gradient which decrease (Figure V-7) or increase the fluxes from the morning side to the evening side. Another type of precipitation was found to have a convex distribution with a broad maximum around the magnetic pole (Figure V-8). We also find a recurrent precipitation pattern where large and numerous "spikes" are observed superimposed over a relatively flat continuum (Figure V-9) or a concave

continuum (Figure V-10).

We undertook a detailed study of the events of a period centered on Feb. 13-18, 1978. During this period, significant enhancements of the precipitating electron fluxes over the polar caps were observed, accompanied by hardening of the electron energy spectra.

The Feb. 13-18, 1978 time period corresponded to the onset of a very large PCA event, actually the largest since mid-1974. The observations showed a large increase in the 50 eV - 20 keV fluxes over the polar caps especially over the south pole. At the onset of the PCA event (9:30 UT, Feb. 13) no flux increase was observed (see Figure V-11) indicating that the low energy particle did not have direct access to the cap region, although high energy particle fluxes over the same regions coincided with the event as evident from the large increase in the background of the instrument. As time progressed, the electron spectra became harder, and the flux intensity increased to a maximum. This increase was followed by a decrease as the PCA event subsided. Figures V-12, V-13, and V-14 showed typical spectra. On Day 44, the energy spectra could be fitted to a power law for $E \gtrsim 200$ eV: The spectral index α was 2.74 ± 0.11 . At 11:38 UT on day 45, $\alpha = 1.42 \pm 0.03$, and the flux intensity above ~ 1 keV increased from ~ 70 to a $700/\text{sec-cm}^2\text{-eV-ster}$ (Figure V-12). On day 46 (Figure V-13), the electron flux at $E \gtrsim 1$ keV further increased to $\sim 3000/\text{cm}^2\text{-sec-eV-ster}$, while for $E < 1$ keV it seems to reach a saturation at $\sim 6 \times 10^4/\text{cm}^2\text{-sec-eV-ster}$. The spectrum started to soften at $\sim 9:40$ UT with $\alpha = 1.66 \pm 0.03$. Figure V-11 shows typical spectra on the following day, day 47: $\alpha = 2.15 \pm 0.3$ at 11 UT. The intensity decreases eventually to the pre-PCA event level, with very little flux above 1 keV, and $\alpha \rightarrow 2.8$. During this decrease activity phase, evidence of electrostatic acceleration of the electron precipitation through 5-10 kilovolt potential drops along the geomagnetic field lines were observed. An example of such an acceleration is shown in Figures V-15 and V-16.

This investigation resulted in a paper presented at the 1980 AGU Spring Meeting in Toronto, Canada.

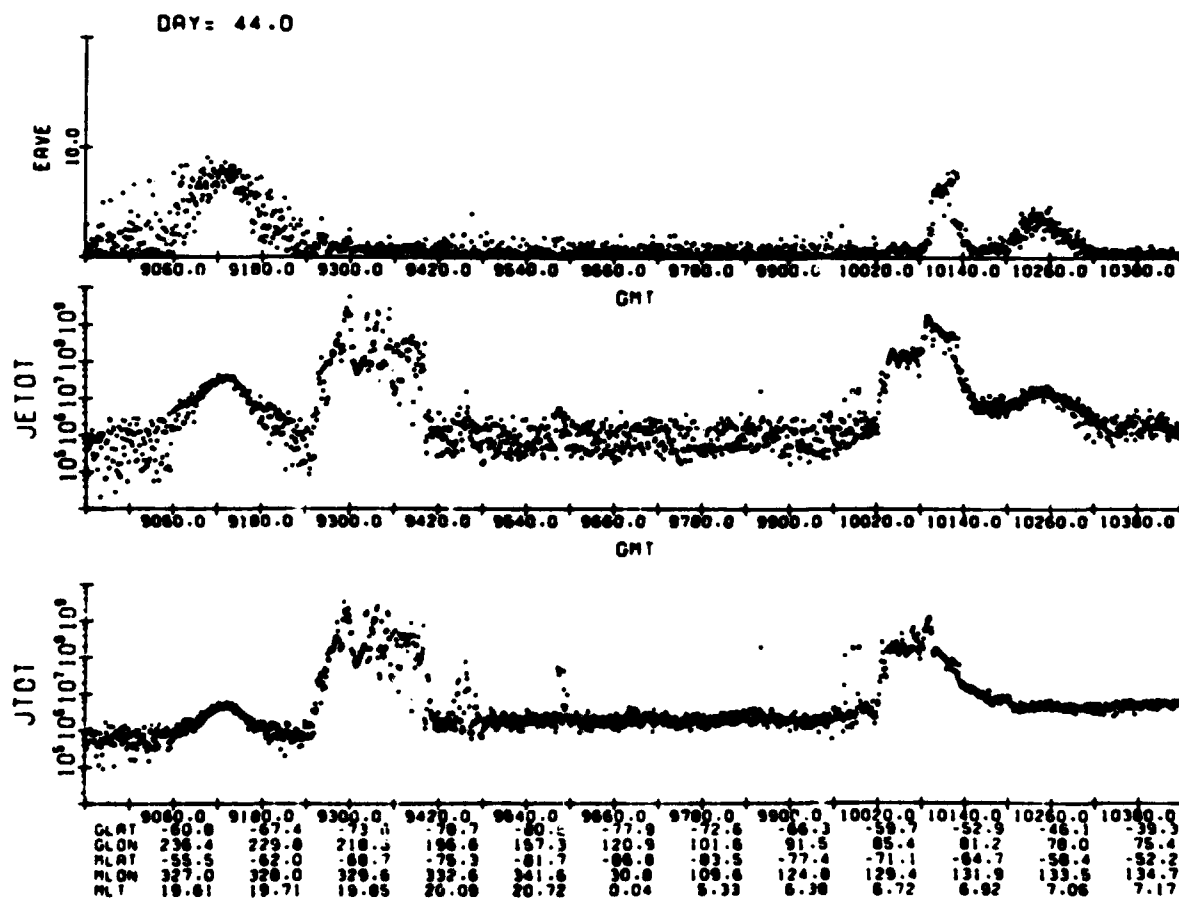


Figure V-6

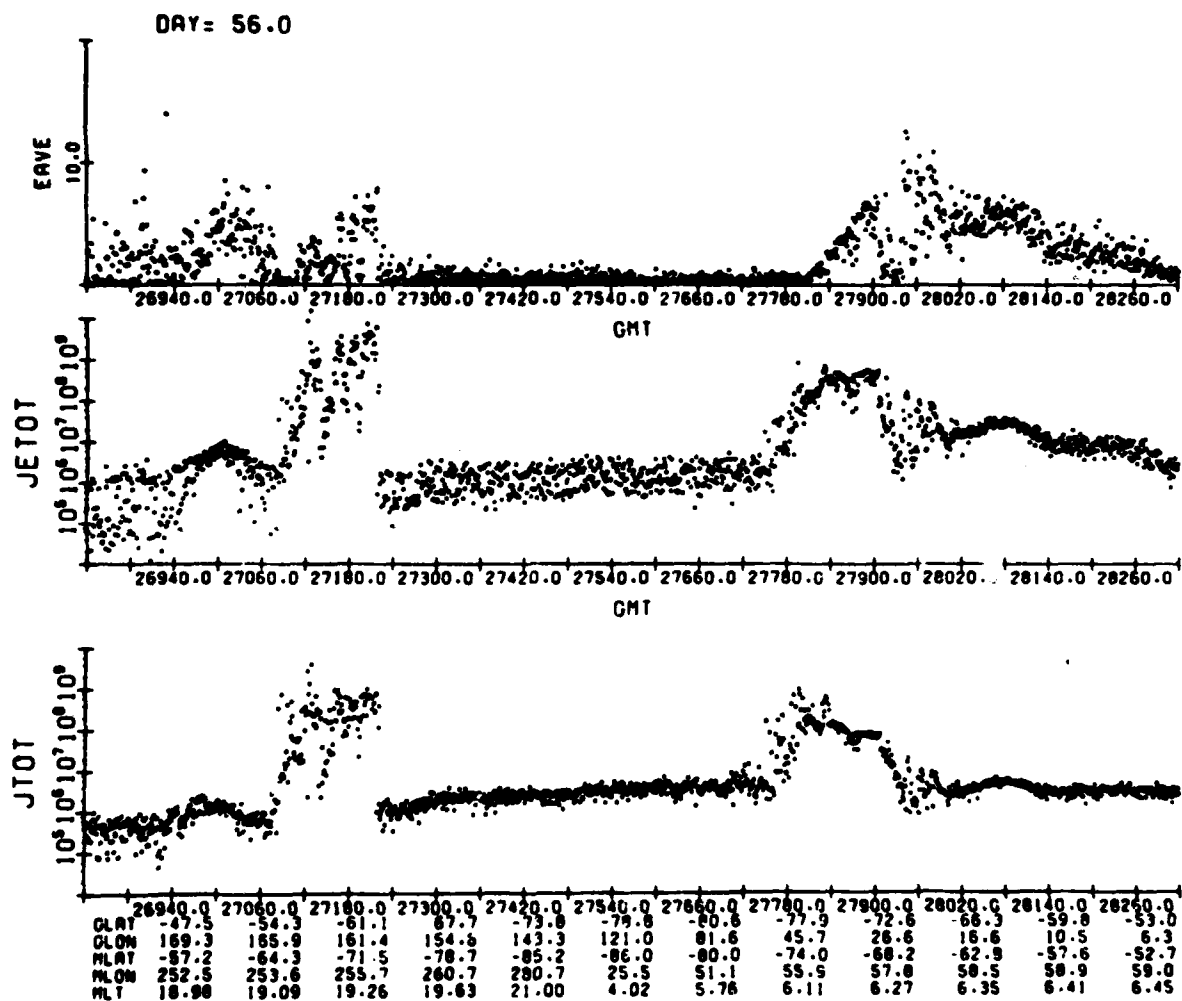


Figure V-7

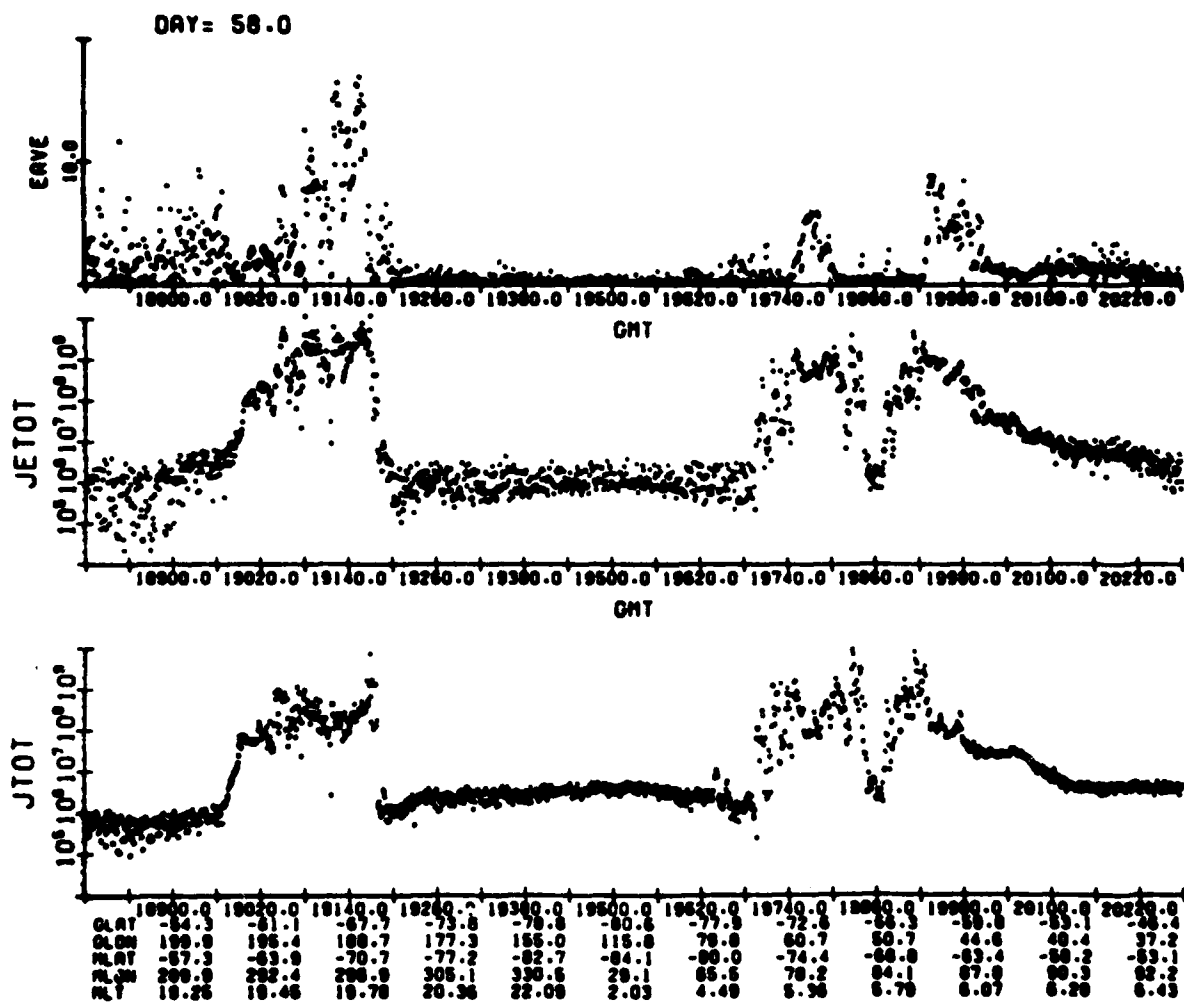


Figure V-8

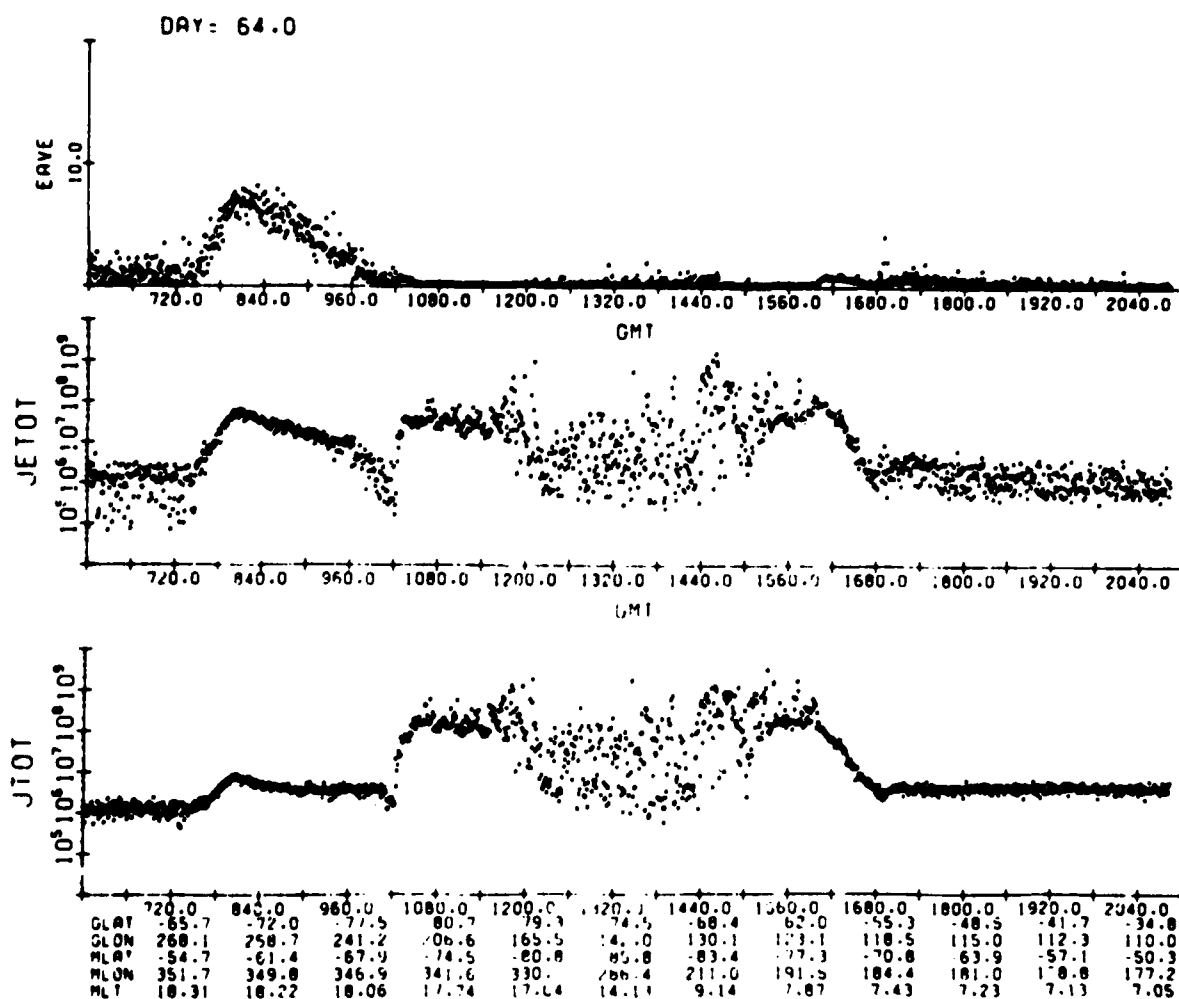


Figure V-9

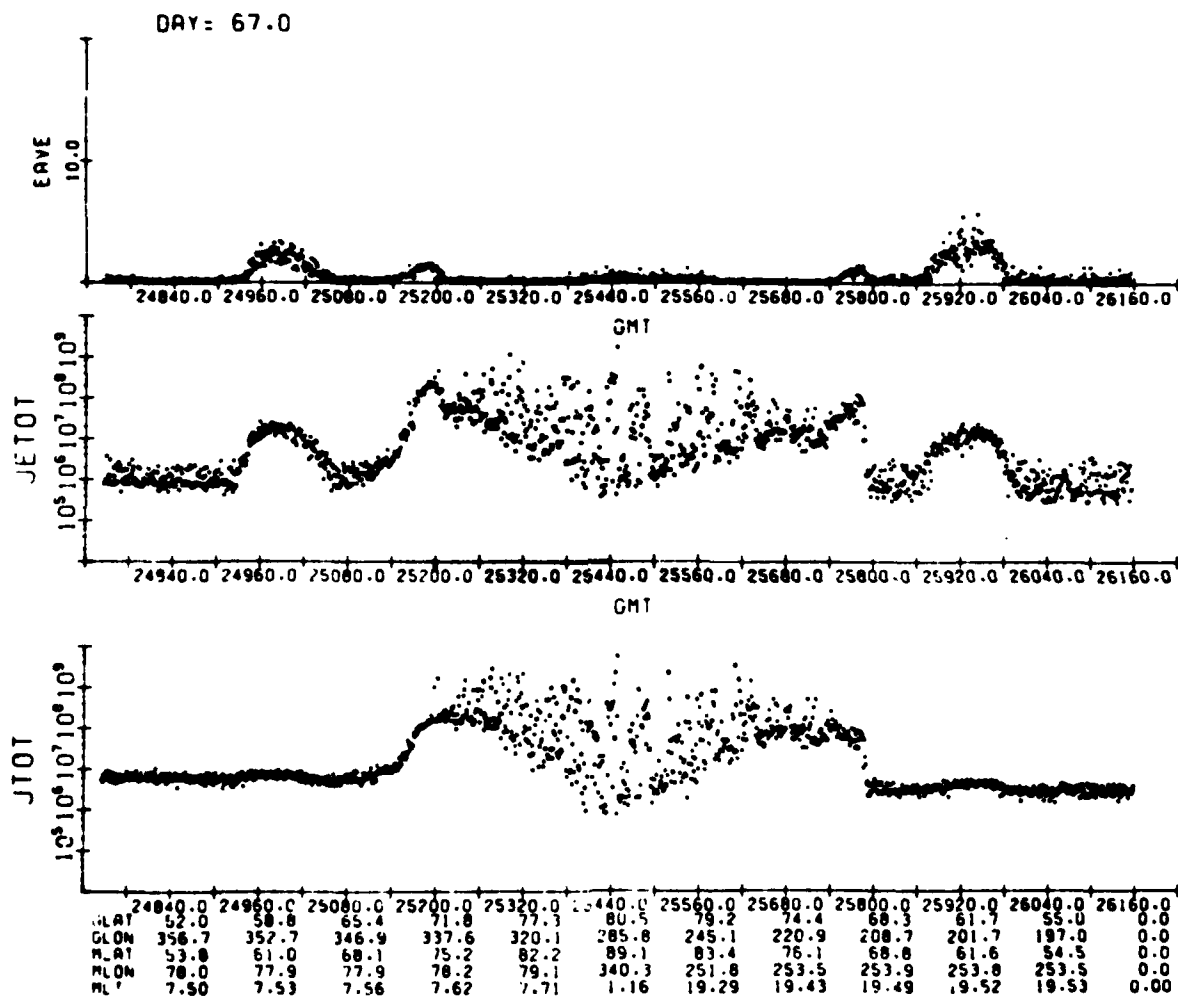


Figure V-10

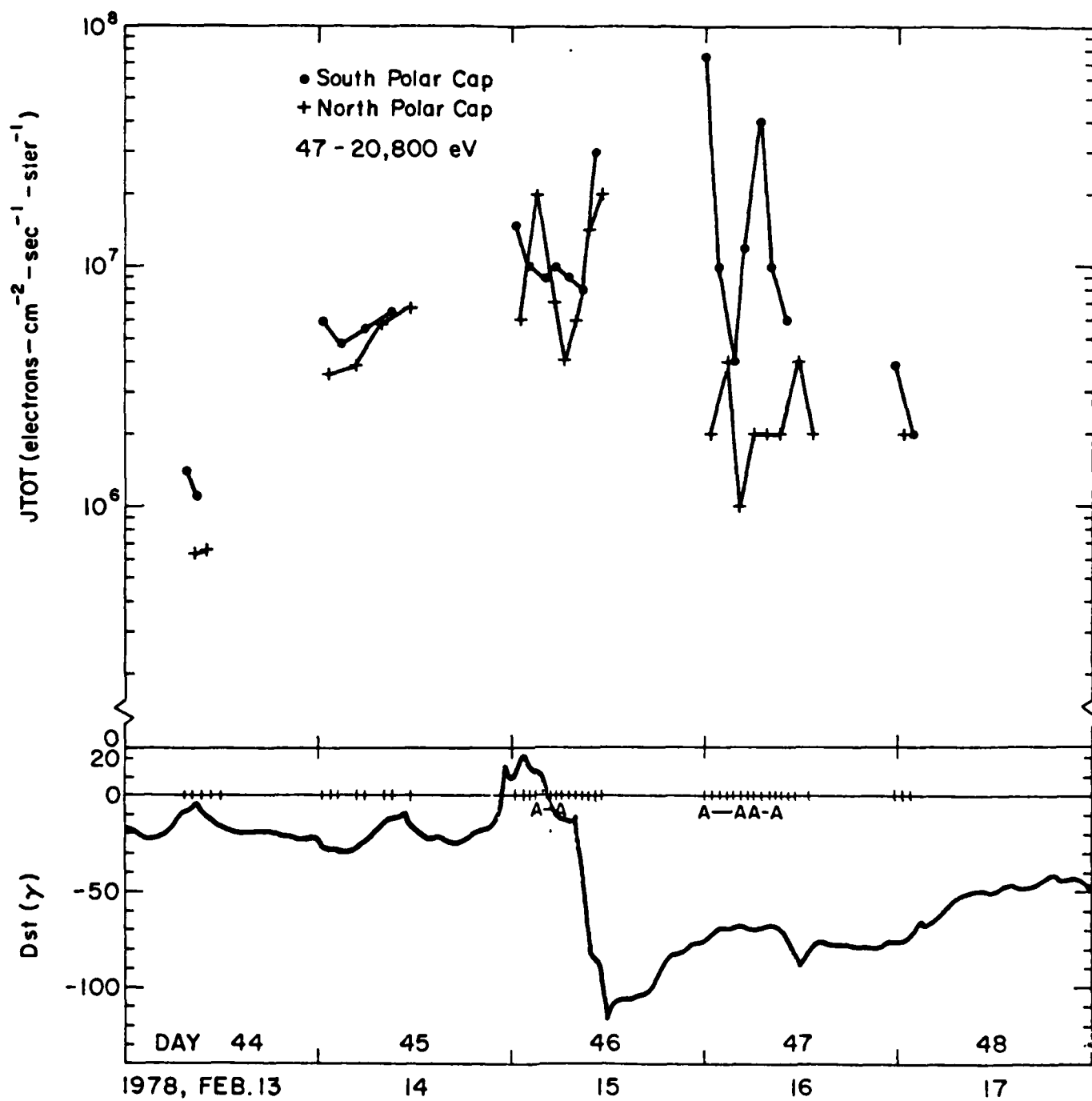


Figure V-11

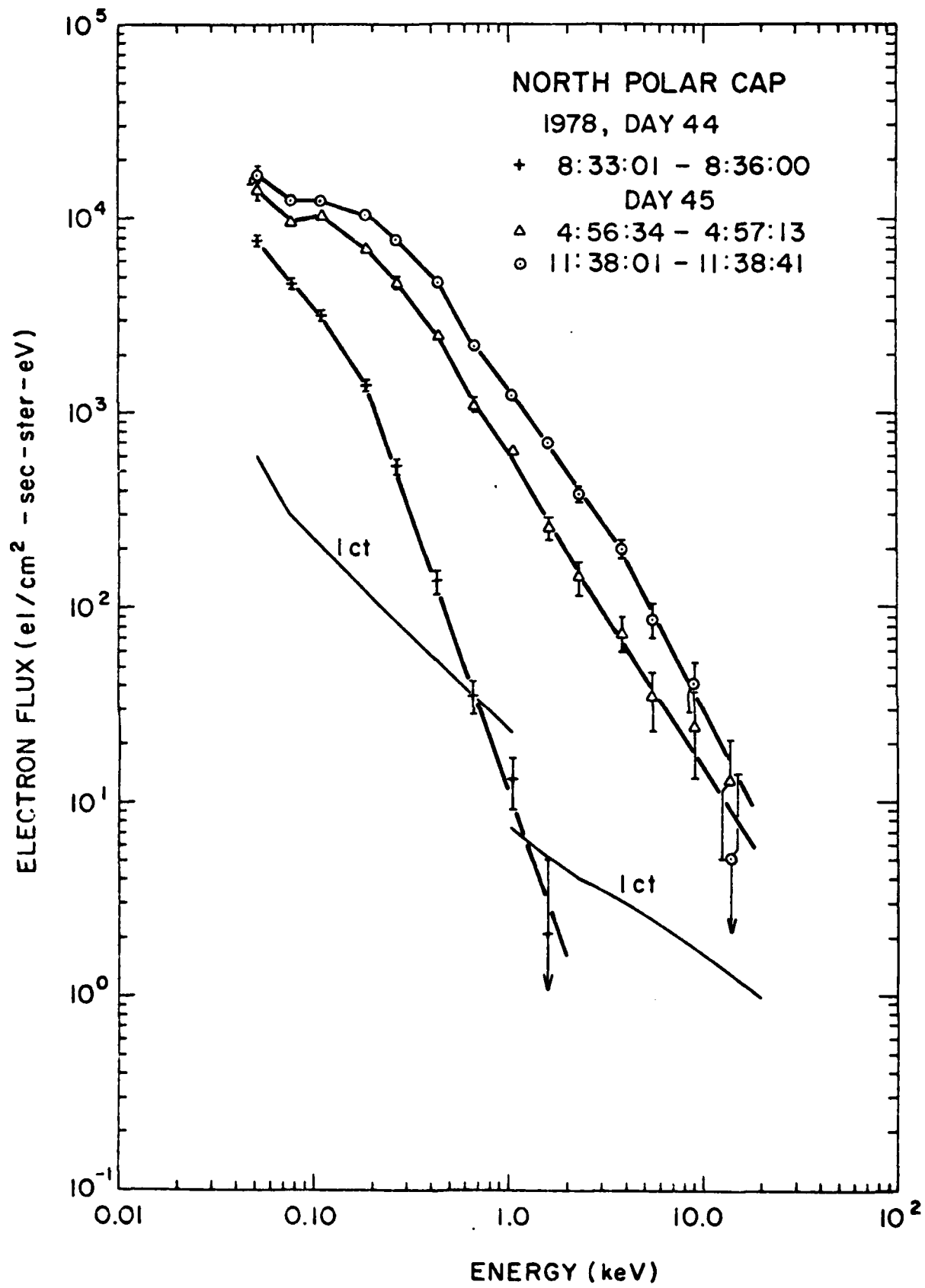


Figure V-12

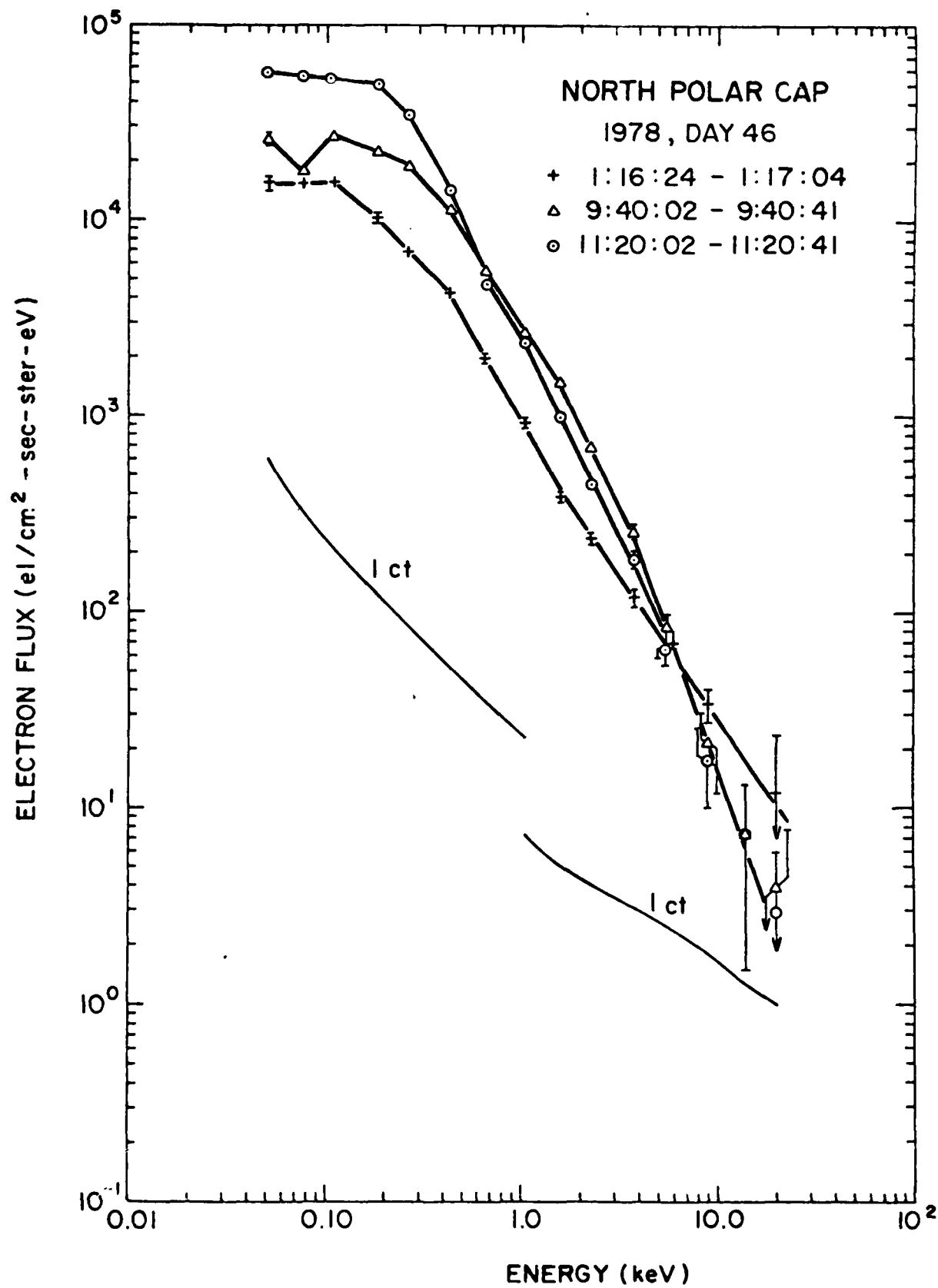


Figure V-13

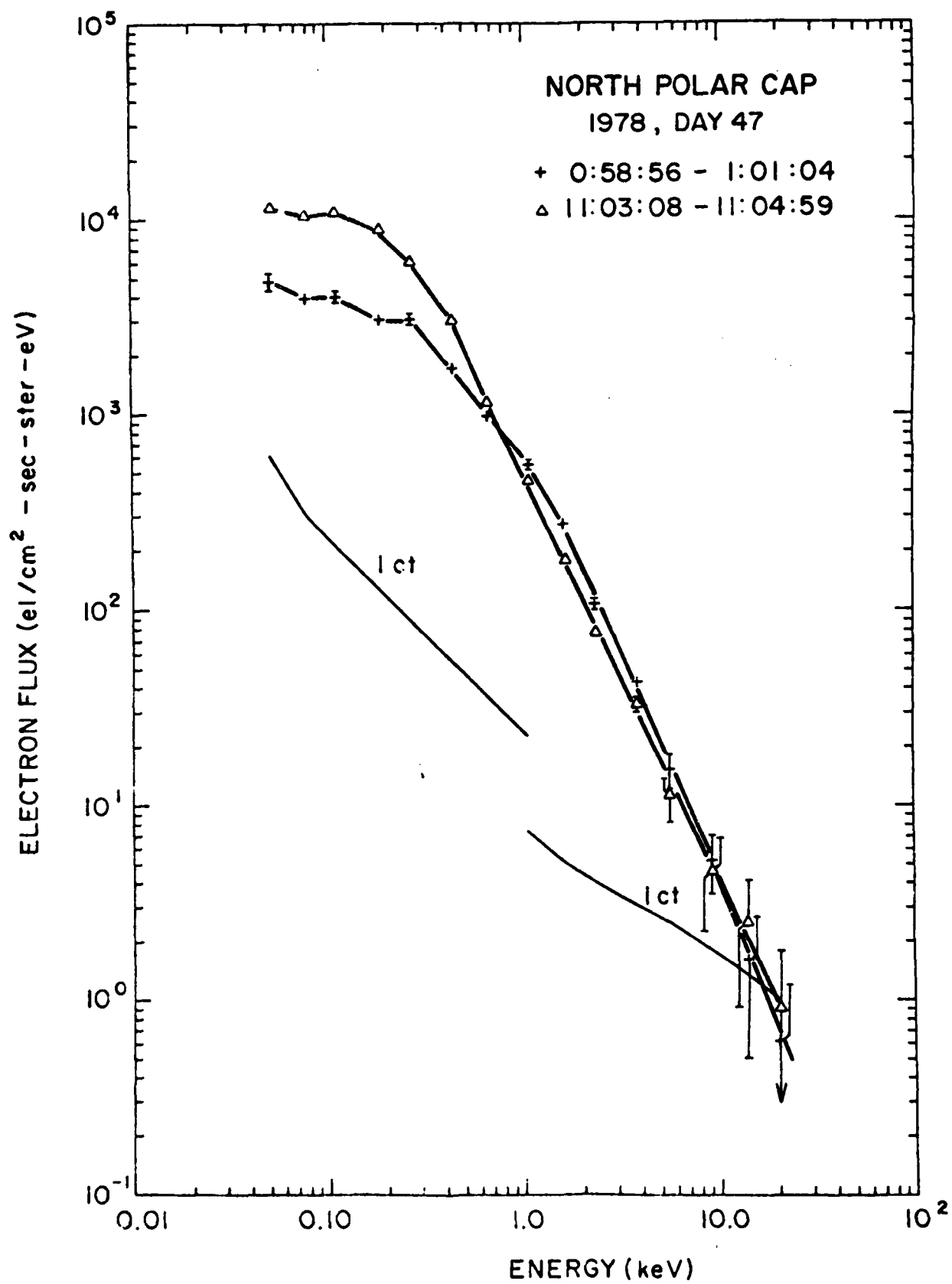


Figure V-14

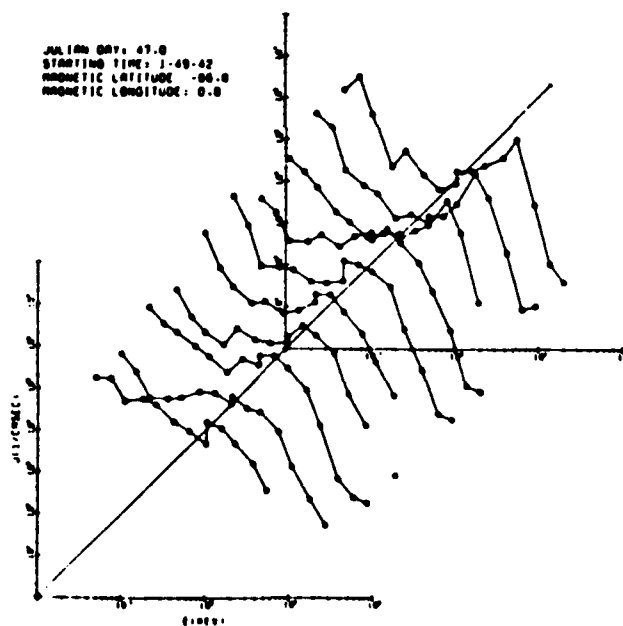
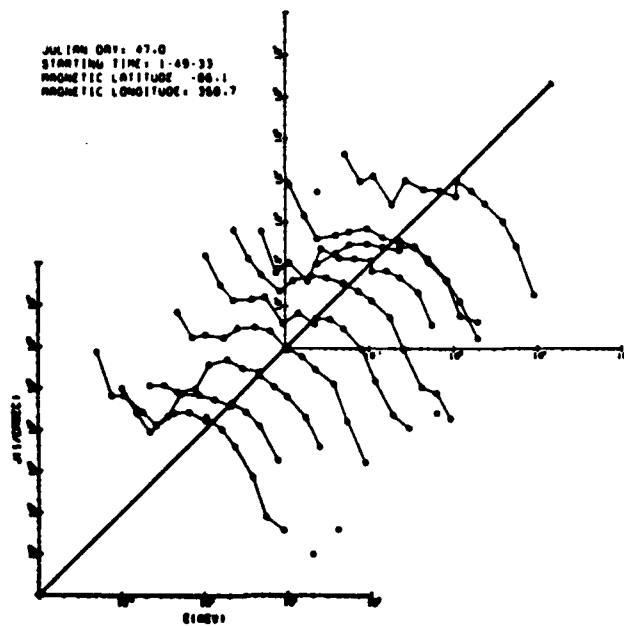


Figure V-15

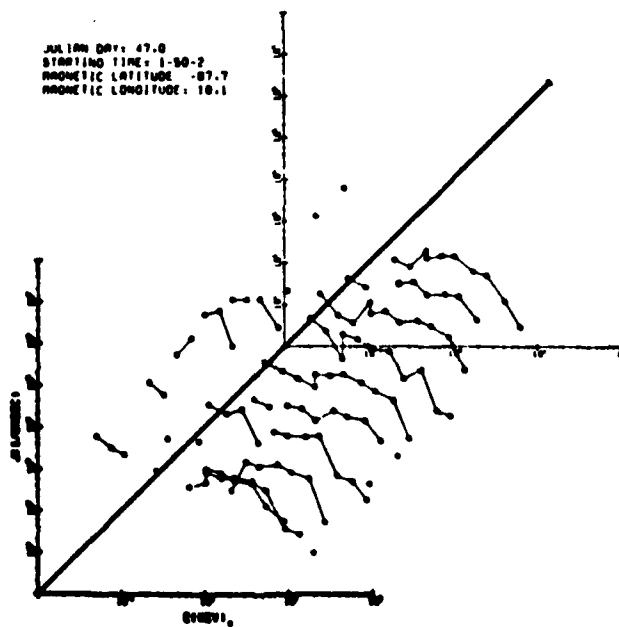
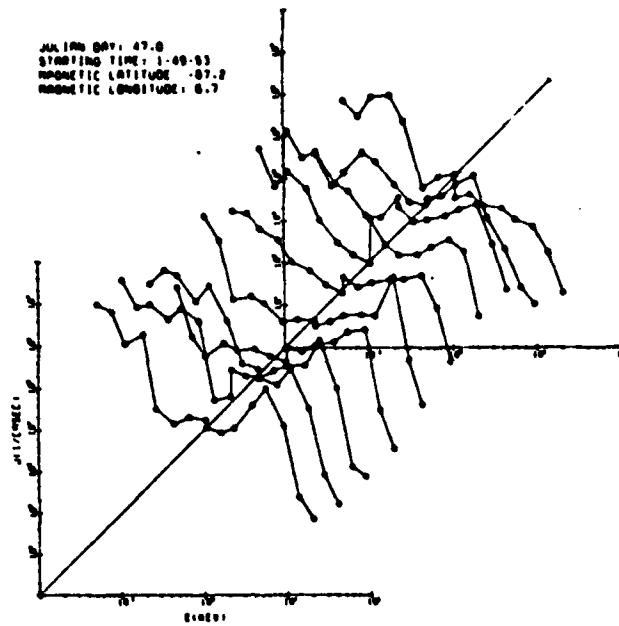


Figure V-16

VI. COSMIC RAY TRAJECTORY STUDIES

The differential equation describing the path of a particle of charge q and momentum p in the earth's magnetic field, B , is given by

$$\frac{d^2\vec{x}}{ds^2} = \frac{q}{p} \left[\frac{d\vec{x}}{ds} \times \vec{B}(\vec{x}) \right] \quad (1)$$

(e.g. Rossi and Olbert, 1970), where \vec{x} represents the position vector, s the arc length along the trajectory and $p = |\vec{p}|$. Unfortunately, this differential equation does not have a general analytic solution even if \vec{B} is expressed as a simple dipole field. It is, therefore, common practice nowadays to study the propagation of energetic charged particles in the earth's magnetosphere by numerical calculations using a mathematical model of the earth's magnetic field.

The numerical methods for the integration of equation (1) are well established and corresponding computer programs have been published by several authors (e.g. McCracken et al., 1962; Shea et al., 1976). As is done usually in cosmic ray physics, the particles are characterized in these programs by their rigidity

$$P = \frac{p c}{q} \quad (2)$$

where c is the velocity of light. The procedures then utilize the fact that equation (1) remains unchanged if the signs of q and ds are reversed.

The trajectory of a particle with rigidity P arriving at a specific location from a specific direction is, therefore, determined backwards by tracing the path of an identical particle, but with opposite charge, leaving that particular location in the specified direction.

The computer simulation of particle trajectories in space, i.e. the trajectory-tracing technique, has been used as a basis for the procedure followed in the analysis of the effects of the geomagnetic field on the cosmic radiation. The main field near the earth is normally represented by a sum of spherical harmonics with coefficients determined so as to produce the best fit to experimental data. The quiescent magnetic field was described by the International Geomagnetic Reference Field (IGRF) adjusted to predict the 1980.0 field from the IGRF 1975 field coefficients (IAGA Division 1, Study Group 1, 1975) projected forward to 1980 by use of the projected secular drift coefficients.

Cosmic ray cutoffs have been calculated for a satellite orbiting the earth at an altitude of 400 km. At each point, cosmic ray cutoffs were calculated for a total of 67 directions, starting in the vertical direction and extending to zenith angles of 120° from the vertical direction at 20° zenith angle increments.

Based on the requirements of many cosmic ray studies, two quantities were of special interest with respect to the effects of disturbances in the geomagnetic field: the cutoff rigidities of cosmic ray stations and the asymptotic directions of cosmic ray particles.

The cutoff rigidity of a specific location on the earth and of a specific direction of incidence is generally defined as the rigidity below which cosmic ray particles are inaccessible to that location from the specified direction. Following the procedure described by Shea et al. (1965) cosmic ray cutoff rigidities have been obtained by determining for the entire rigidity spectrum whether an individual rigidity had a trajectory accessible from infinity (i.e. had an allowed trajectory) or not. For a given location with geomagnetic coordinates Λ , ϕ and for a given direction, characterized by the zenith angle θ and the azimuthal angle ϕ , (see Figure VI-1 for the corresponding frames of reference) calculations were initiated at a rigidity well above the expected cutoff, and cosmic ray trajectories have been calculated at discrete rigidity intervals of $\Delta P = 0.01$ GV. As the calculations were progressing down through the rigidity spectrum, the results always changed from the easily allowed orbits to a complex structure of allowed, forbidden, and quasi trapped orbits and finally to trajectories which all intersected the solid earth. As illustrated in Figure VI-2, three distinct cutoff rigidities as defined by Shea et al. (1965) have been used to describe the resulting structure of allowed and forbidden trajectories:

$P_M(\Lambda, \phi, \theta, \phi)$ the lowest rigidity above which the trajectory calculations yielded allowed orbits for all rigidities. This trajectory-derived cutoff value is called main cutoff.

$P_S(\Lambda, \phi, \theta, \phi)$ the lowest rigidity for which the trajectory calculations yielded an allowed orbit. For the past 15 years this trajectory-derived value has been referred to as the Stormer cutoff.

$P_C(\Lambda, \phi, \theta, \phi)$ the effective cutoff, given by

$$P_C(\Lambda, \phi, \theta, \phi) = P_M(\Lambda, \phi, \theta, \phi) - \int_{P_S(\Lambda, \phi, \theta, \phi)}^{P_M(\Lambda, \phi, \theta, \phi)} C(P; \Lambda, \phi, \theta, \phi) dP$$

where

$$C(P; \Lambda, \phi, \theta, \phi) = \begin{cases} 1 & \text{if the orbit corresponding to } P \text{ is allowed} \\ 0 & \text{if the orbit corresponding to } P \text{ is forbidden.} \end{cases}$$

As illustrated in Figure VI-3, the asymptotic direction of a cosmic ray particle having a specific rigidity and arriving at a specific location on the earth from a specific direction of incidence is the direction of motion which this particle had in interplanetary space prior to its interaction with the earth's magnetic field. It is obvious that asymptotic directions are a primary means of relating cosmic ray intensity variations at the earth with the direction of the particles in interplanetary space (McCracken et al., 1962, 1968). The trajectory-tracing method enables an accurate determination of asymptotic directions for a specific model of the earth's magnetic field (e.g. Shea and Smart, 1975). In the relatively simple field models used in this analysis the asymptotic direction of a particle has been determined by its direction of motion, expressed in terms of the geocentric coordinate system, at 25 earth radii, where the effects of the geomagnetic field on the orbit become insignificant.

In order to understand specific aspects of the effects of the geomagnetic field on cosmic ray cutoff rigidities and asymptotic directions it was also necessary to study the detailed elements of particular, representative particle trajectories. For this purpose several computer programs were developed to give graphical representations of the particle orbits as well as of a number of characteristic parameters evaluated along the trajectories, such as a program to plot a side and top view of a particle trajectory in space as shown in Figure VI-4.

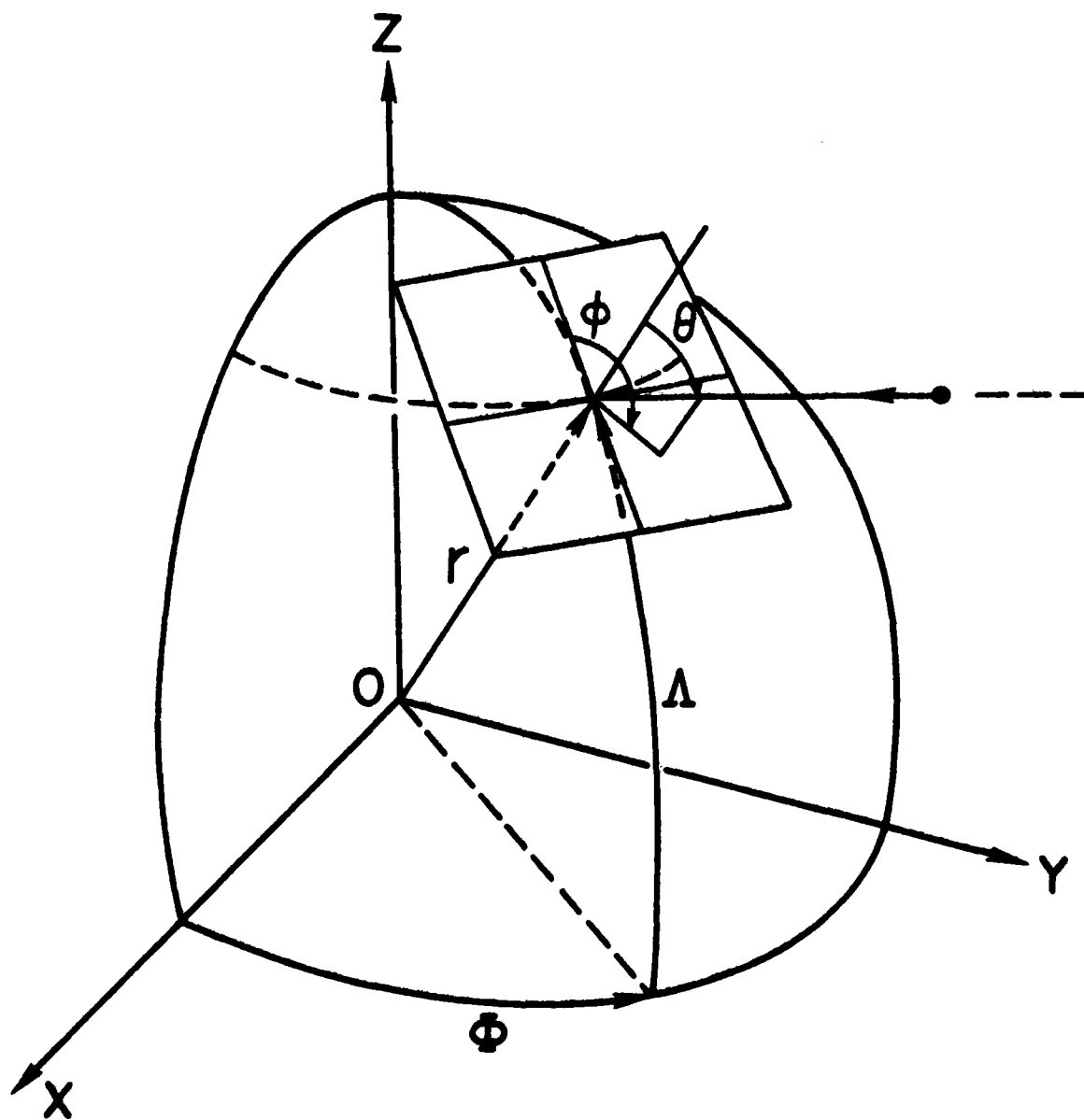


Figure VI-1

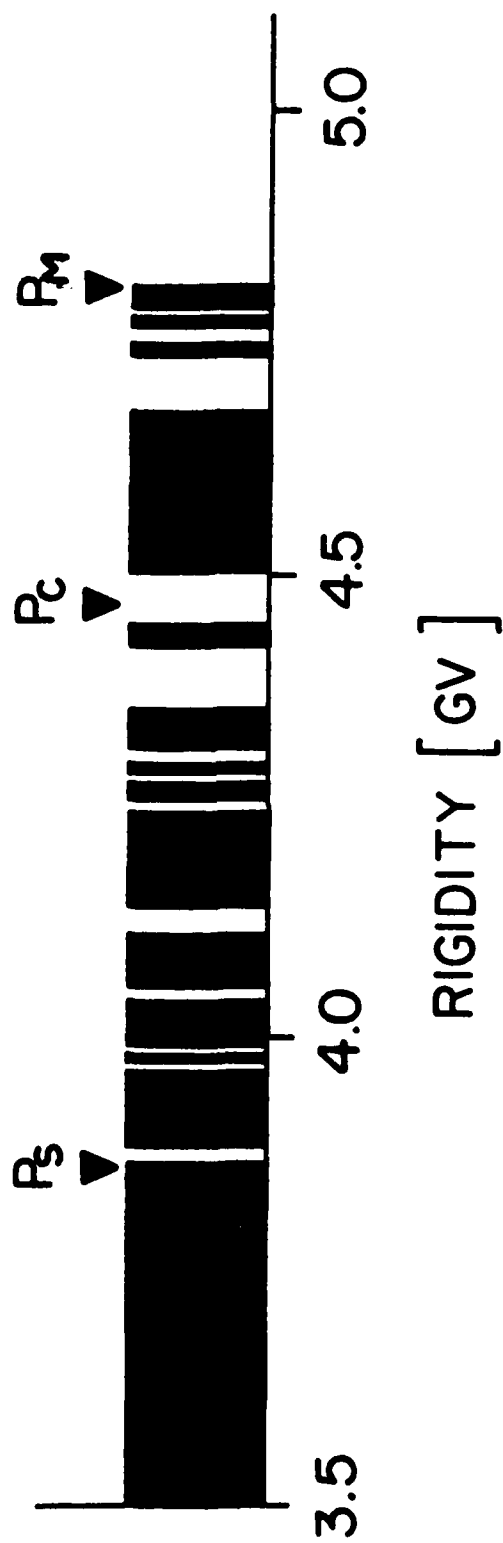


Figure VI-2

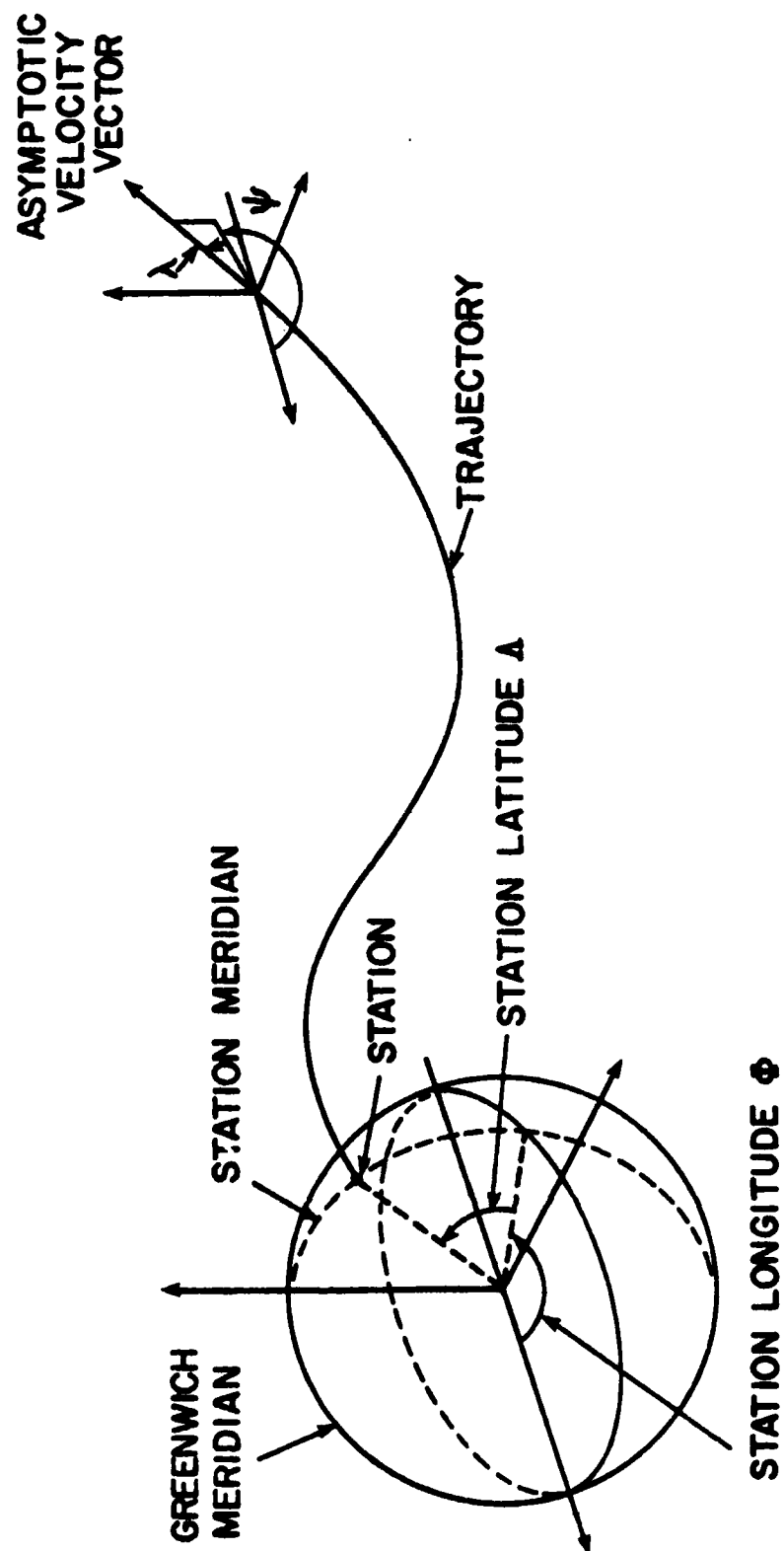


Figure VI-3

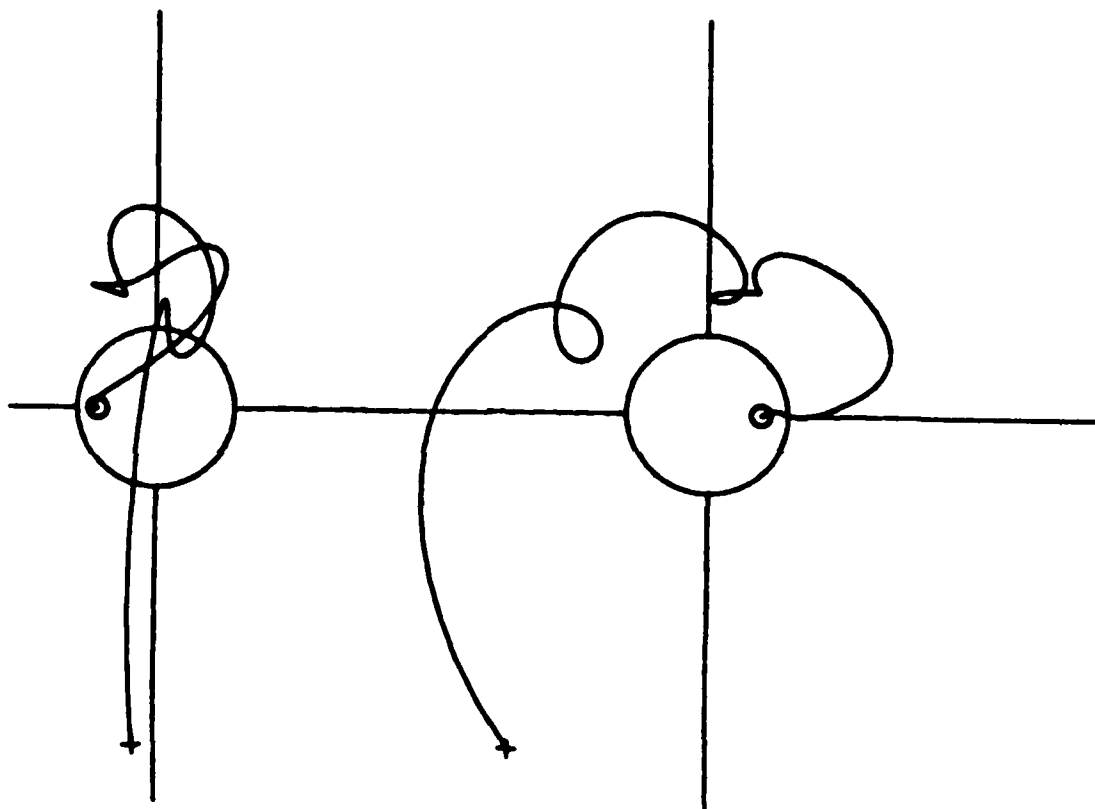


Figure VI-4

Appendix 1

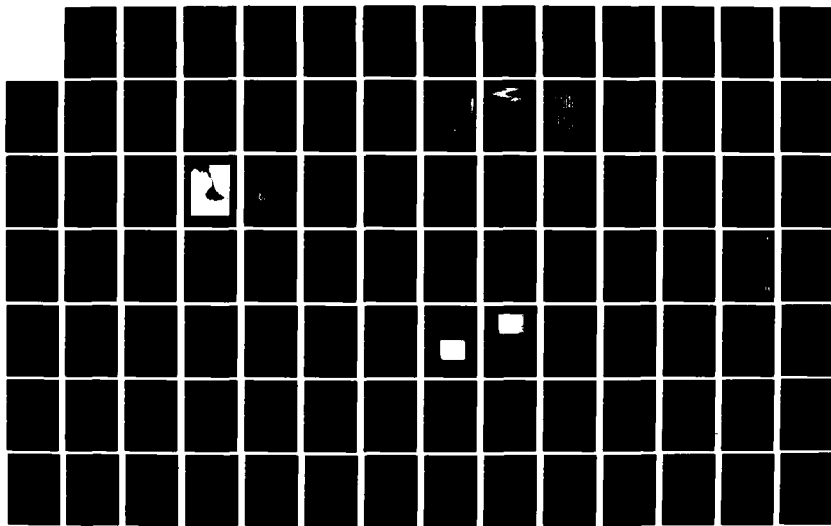
AD-A121 994

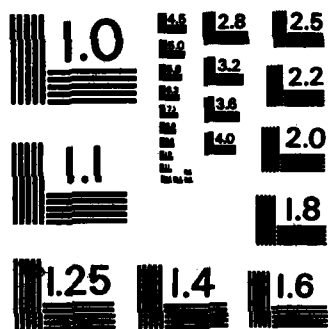
STUDY AND ANALYZE ENERGETIC PARTICLE AND MAGNETIC
ACTIVITY DATA(U) EMMANUEL COLL BOSTON MASS PHYSICS
RESEARCH DIV L GENTILE ET AL JUN 82 AFGL-TR-82-0217
F19628-79-C-0102 F/G 3/2

3/4

UNCLASSIFIED

NL





MICROCOPY RESOLUTION TEST CHART
NATIONAL BUREAU OF STANDARDS-1963-A

AFGL-TR-80-0265

**Auroral X-Ray Contamination of the Low Energy Proton Spectrometer
on the S3-2 Satellite in the Polar Regions**

Richard P. Boyle

Daniel R. Parsignault

**The Trustees of Emmanuel College
400 The Fenway
Boston MA 02115**

January 1981

Scientific Report No. 2

Approved for public release; distribution unlimited.

**Air Force Geophysics Laboratory
Air Force Systems Command
United States Air Force
Hanscom AFB Massachusetts 01731**

UNCLASSIFIED

MIL-STD-847A
31 January 1973

SECURITY CLASSIFICATION OF THIS PAGE (When Data Entered)

REPORT DOCUMENTATION PAGE		READ INSTRUCTIONS BEFORE COMPLETING FORM
1. REPORT NUMBER AFGL-TR-80-0265	2. GOVT ACCESSION NO.	3. RECIPIENT'S CATALOG NUMBER
4. TITLE (and Subtitle) Auroral X-Ray Contamination of the Low Energy Proton Spectrometer on the S3-2 Satellite in the Polar Regions		5. TYPE OF REPORT & PERIOD COVERED Scientific Report No.2 01JAN80 - 31AUG80
7. AUTHOR(s) Richard P. Boyle Daniel R. Parsignault		8. CONTRACT OR GRANT NUMBER(s) F19628-79-C-0102
9. PERFORMING ORGANIZATION NAME AND ADDRESS Emmanuel College 400 The Fenway Boston MA 02115		10. PROGRAM ELEMENT, PROJECT, TASK AREA & WORK UNIT NUMBERS 61102F 2311G1AK
11. CONTROLLING OFFICE NAME AND ADDRESS Air Force Geophysics Laboratory Hanscom AFB MA 01731 Contract Monitor: Robert O. Hutchinson/PHG		12. REPORT DATE 31 January 1981
14. MONITORING AGENCY NAME & ADDRESS (if different from Controlling Office)		13. NUMBER OF PAGES 30
		15. SECURITY CLASS. (of this report) Unclassified
		15a. DECLASSIFICATION DOWNGRADING SCHEDULE
16. DISTRIBUTION STATEMENT (of this Report) A - Approved for public release; distribution unlimited.		
17. DISTRIBUTION STATEMENT (of the abstract entered in Block 20, if different from Report) TECH, OTHER		
18. SUPPLEMENTARY NOTES		
19. KEY WORDS (Continue on reverse side if necessary and identify by block number) Auroral X-Rays LEPS (Low Energy Proton Spectrometer) Bremsstrahlung Electron Precipitation S3-2 Satellite		
20. ABSTRACT (Continue on reverse side if necessary and identify by block number) The Low Energy Proton Spectrometer (LEPS) on board the Air Force S3-2 polar orbiting satellite recorded, at polar latitudes (invariant latitude $\approx 70^\circ$), high anomalous counts coming from the auroral zone direction, over the December 1975 through April 1976 operational period. Despite the low sensitivity of the Si(Li) LEPS detector to X-rays, bremsstrahlung from		

DD FORM 1473 EDITION OF 1 NOV 65 IS OBSOLETE

UNCLASSIFIED

SECURITY CLASSIFICATION OF THIS PAGE (When Data Entered)

MIL-STD-847A
31 January 1973

UNCLASSIFIED

SECURITY CLASSIFICATION OF THIS PAGE (When Data Entered)

precipitating electrons in the hundred keV energy range is given as the source of these observations.

UNCLASSIFIED

SECURITY CLASSIFICATION OF THIS PAGE (When Data Entered)

TABLE OF CONTENTS

	Page
ABSTRACT	3
1. INTRODUCTION	4
2. OBSERVATIONS	5
3. DETECTOR SENSITIVITY	7
4. ANALYSIS	8
5. CONCLUSION	12
6. ACKNOWLEDGEMENTS	13
REFERENCES	14
LIST OF FIGURES	15
FIGURES AND TABLE	17

AURORAL X-RAY CONTAMINATION OF THE LOW ENERGY
PROTON SPECTROMETER ON THE S3-2 SATELLITE IN THE POLAR REGIONS

Richard P. Boyle and Daniel R. Parsignault

Emmanuel College
Boston MA 02115

ABSTRACT

The low energy proton spectrometer (LEPS) on board the Air Force S3-2 polar orbiting satellite recorded, at polar latitudes (invariant latitude $\lambda|70^\circ|$), high anomalous counts coming from the auroral zone direction, over the December 1975 through April 1976 operational period. Despite the low sensitivity of the Si(Li) LEPS detector to X-rays, bremsstrahlung from precipitating electrons in the hundred keV energy range is given as the source of these observations.

1. INTRODUCTION

A low energy proton spectrometer (LEPS) was flown on the Air Force S3-2 polar orbiting satellite to observe primarily the trapped protons in the 0.1 to 6 MeV energy range (Pantazis et al., 1975). In the polar regions, which usually showed low proton fluxes, the LEPS recorded high counts in a single direction below the satellite horizon over the course of the five-month operational period. The same pattern of observations can be seen in the work of Imhof et al. (1974), where a Ge(Li) spectrometer was used to observe bremsstrahlung X-rays from the auroral zones. Although the LEPS is theoretically inefficient in detecting X-rays, in this report we contend that it is the X-ray aurora that best explains qualitatively the dominant feature of the LEPS polar observations.

During the last decade several researchers have correlated observed electron spectra with observed X-ray spectra in the auroral zones. In such research, bremsstrahlung X-ray measurements provide a broader picture of the auroral zones than the more spatially limited electron observations. This report offers qualitative observational information on the subject of the correlation between precipitating electrons and the emerging bremsstrahlung X-rays as observed by detectors on the S3-2 satellite.

The Air Force S3-2 satellite was launched December 5, 1975 into a polar orbit in the noon-midnight meridian with an apogee of 1540 km, perigee of 230 km, inclination of 96.3 degrees, and a period of 1.71 hours. The ascending node was on the nighttime equator. The satellite spin period was approximately 18.5 seconds, with the spin axis perpendicular to the orbital plane.

The LEPS provided useful proton observations in the trapping and precipitating latitudes during the operational period from launch, December 1975 to May 1976. However, in the polar regions, here defined as poleward of the precipitating regions, although evidence of any solar proton fluxes is sparse and restricted to solar active periods, the observation of varying high counts from a single preferred direction below the satellite horizon persists throughout the five month period. This report explains that these anomalous polar observations

are the result of electromagnetic radiation, namely, bremsstrahlung X-rays originating in the auroral zones.

The following section gives a description of the LEPS polar observations. Since the most statistically significant counts are contained in the first energy channel (100 ± 20 keV), we will concentrate on that energy channel. Usually, only the first six channels have statistically significant counts ($82 \text{ keV} < E < 680 \text{ keV}$). Evidence that the observations must be due to the electromagnetic radiation necessitates the evaluation of the finite sensitivity of the LEPS to X-rays in the hundred keV energy range. Analysis of the observations will then give confirmation that X-ray aurorae and not solar particles, per se, are what were observed. Because of the low efficiency of this detector to X-rays, however, only qualitative, order of magnitude conclusions on these polar observations of the X-ray aurorae can be made.

2. OBSERVATIONS

From roughly 1100 S3-2 data tapes processed by the Air Force Geophysics Lab., 245 tapes, each containing a partial or full orbit during the 10 December 1975 to 26 April 1976 operational period for the LEPS, have been further processed. Figure 1 shows a typical data record of the spin-modulated counting rates plotted as a function of time for a northern hemisphere pass in the 100 keV energy channel of the LEPS. Night and day trapping, precipitating and polar regions are indicated in the figure. This pass shows a symmetry in the polar observations between night and day. In the northern hemisphere, orbital passes during the time interval of 18 to 24 hours UT fell close to the midnight-noon magnetic meridian. Orbital passes outside of this universal time interval fell toward the evening sector away from the midnight-noon magnetic meridian. Symmetry of the polar observations in passing from the night to dayside of the magnetic pole correlates well with the closeness of the orbit to the midnight-noon magnetic meridian. In contrast to the data shown in Figure 1, the dynamic range of the polar counts is demonstrated by the April 17, 1976 polar pass (cf Fig. 2) which shows minimal (near zero) counts during the time of very low

magnetic activity ($K_p = 2-$). In general, a correlation existed between the magnitude of the polar counts and the magnitude of the planetary magnetic three-hour-range indices, K_p , reproduced in Figure 3 for the five month period under consideration. In their recent work, Imhof et al. (1980) present evidence that the local dusk sector experiences the more intense electron precipitation, and hence X-ray bremsstrahlung, compared to any other local geomagnetic time region. The S3-2 LEPS north polar observations during the five months observing period tend to add evidence to this case. The S3-2 orbit did not traverse the northern dawn sector. But the comparison of the polar observations from orbits over late night to late morning vs. early evening to noon show that the dusk sector gives the relatively higher counts (proportional to the K_p of the time).

In Figure 4, a plot of the range in invariant latitude, local geomagnetic time covered by the satellite's north polar orbits is demonstrated. The $9^h \pm 3^h$ UT pass represents one extreme where the orbit passes along the dusk side over the auroral oval. The $21^h \pm 3^h$ UT pass gives the other extreme where a late evening to late morning crossing over the auroral oval is made. Orbits at other universal times lie in between these extremes. Approximate invariant latitude and local geomagnetic time for any of the counts vs. time plots, given its universal time, can be read off the auroral oval nomograph of Figure 4.

Figure 5 gives a representative selection of the data from the north polar region for the five month period. For active to quiet magnetic K_p indices, column A demonstrates the data for the dusk side passes and column B for the late evening to late morning passes.

The counts/second over a single 18-second spin period in the polar region show an asymmetric distribution with a persistent single enhanced peak (cf. print plot, Figure 10). In contrast, a monoenergetic beam of charged-particle radiation in the presence of a magnetic field and hence spiraling particles, must show a double peak of equal intensity to a detector viewing around a plane (cf. Figure 6). The spiraling charged radiation would give equal intensity peaks at $\pm \theta$ pitch angle. Although the LEPS polar observations usually contain two peaks within

a single spin, they are neither of equal intensity nor separated by $\pm \theta$ pitch angle. The peaks occur at pitch angles of -120° and $+110^\circ$ in the north night and day, respectively, and at pitch angles of -80° and $+70^\circ$ in the south night and day, respectively. Although this is a difference of only 10° , nevertheless the argument for a single peak is corroborated from the strong connection of the look direction angle of the peak to the geometrical location of the auroral zone. This will be explained more fully in a later section. Thus, the evidence is that the peak observation is not of charged particles, i.e., protons or electrons, but rather, is from viewing two discrete sources of electromagnetic radiation at two different directions.

3. DETECTOR SENSITIVITY

The LEPS was designed to detect and analyze protons in the 0.1 to 6 MeV energy range. Two totally depleted Si(Li) surface barrier detectors were used in an anticoincidence mode. Full description of the instrument can be found in Pantazis et al. (1975). Table 1 gives the energies of the eleven channels of the LEPS. The wide angle (46°) LEPS instrument on the S3-2 satellite gave useful proton observations in the high flux, trapping and precipitating regions during the five month operational period. The anomalous single peak observations in the polar regions raise the question of the sensitivity of the LEPS to X-rays.

An incident X-ray can generate an electronic charge in the detector's sensitive volume in three energy-dependent ways: by the photoelectric effect, by the Compton effect, and by pair-production. The fact that pair-production occurs above 1.1 MeV, where the LEPS in the polar regions sees no counts, makes it unnecessary to consider it here. Figure 7 shows the percent efficiency to charge generation from the photoelectric and Compton effects in the 300 μ silicon front detector. These curves are computed from the transmission equation

$$N = N_0 e^{-\mu x}$$

where N_0 = number of incident photons at a particular energy,

N = number of transmitted photons,

μ = absorption coefficient in silicon for particular energy,
 x = thickness of silicon.

It can be seen that the LEPS is about an order of magnitude more sensitive to electron charge generation by Compton scattered electrons than by photoelectrons at 100 keV. At higher energies the photoelectric effect is a much less efficient source of electron generation. Consequently, charge in the front detector, primarily due to Compton scattered electrons from an incident X-ray source, would give pulses or counts in the 100 keV to 6 MeV energy channels. Clearly, the LEPS is not immune to X-rays. In fact, in a space region devoid of protons, an X-ray flux could account for a significant counting rate by Compton scattering alone.

4. ANALYSIS

The source of the single peak polar observation will be explored and discussed in this section. For a detailed analysis we have selected the data acquired during a north polar pass in a magnetically active time. The same considerations and results to be expressed here apply, in form, to all the polar regions both north and south during the five month period.

The single peak observation by the LEPS when in the polar region is not due to a source local to the satellite. Protons cannot be a local source for two reasons. First, another experiment onboard the same S3-2 satellite showed that the proton flux, specifically at 100 keV, in the polar region was at background level with no preferential pitch angle peak (A.L. Vampola, private communication). Second, as stated earlier, a proton flux at any one energy and a preferred direction would show at least a double peak of equal intensity at pitch angles $\pm \theta$. The fact that the LEPS efficiently and accurately observed the proton flux outside the polar region is reason enough that any proton flux within the polar region would also be seen.

Likewise, electrons can be ruled out as a local source of the LEPS single-peak polar observations - either directly or as a source of local bremsstrahlung. Directly, the LEPS is immune to seeing electrons by

being equipped with a 1400 gauss sweeping magnet. This magnetic shielding efficiently swept away electrons up to 600 keV in the high flux trapping region, i.e., the trapped proton observations by the LEPS were uncontaminated by electron counts. Local bremsstrahlung cannot be a source of the single peak for two reasons. First the energetic electron flux seen by another experiment onboard the same S3-2 satellite (A.L. Vampola, private communication), while in the polar region, was at a low level. Second, if the LEPS were sensitive to local bremsstrahlung generated by the low-level electron flux despite the reasonably adequate shielding of the LEPS, then presumably the observation would be more or less omnidirectional and not at the single significant direction. Furthermore, the same sensitivity would be apparent in the trapped radiation regions where there are large fluxes of trapped electrons. The single preferred (consistently recurrent) direction of the polar observation is in fact explained in the following text by a source remote to the satellite, namely, the X-ray aurora.

It is known that the auroral zone emits X-rays isotropically by the bremsstrahlung process due to precipitating electrons incident on the atmosphere at approximately 100 km altitude. The single peak observed by the LEPS in the polar region is evidence of its sensitivity to electromagnetic radiation in the X-ray (100 keV) energies; the preferred direction of this single peak observed from various orbital vantage points is precisely the direction of the aurora.

Because of the extreme magnetic activity, we analyze in detail the data of orbit 1569 on March 26, 1976, 9^h UT in the following discussion (cf. Figure 8). Figure 9 shows to scale, in the orbiting plane, the north polar pass of the orbit 1569. The look angle from the local nadir at which the single peak is seen is portrayed from four orbital vantage points (a,b,c,d). Figure 10 shows the 100 keV observations during a single spin corresponding to the four vantage points. Here pitch angles are given.

As the satellite passes in the night side, from south of the aurora where the peak occurs at look angle +84° off the nadir to the north of the aurora where the peak is seen at -65° off the nadir, the angle of the peak might be expected to move through zero degrees. However, with the LEPS aperture of 46° at an altitude of approximately 1200 km, less

area of the aurora is in view when overhead than when oblique. Furthermore, when the aurora is viewed perpendicularly compared to nearly horizontally to its area, a decrease in X-ray intensity greater than an order of magnitude occurs. This effect is presented in detail by the recent work of Walt et al. (1979) who show that bremsstrahlung X-rays escape the auroral zone preferentially at angles near the horizontal. Also, this effect is more pronounced for the higher photon energies. At vantage point c (cf. Figure 9), the dayside peak has increased to a brightness equal to the decreasing nightside peak. As the satellite moves on to vantage point d, the look angle tends to move slightly closer to the nadir (from $+65^\circ$ now to $+60^\circ$) before the single peak is covered by the precipitating and trapping proton fluxes.

The auroral zone is located within the field of view of the 46° aperture of the LEPS when pointing at these look angles both for the night and dayside aurorae. Corroboration of this fact is obtained from the location of the precipitating electron regions given by two electron experiments on board the same S3-2 satellite for the same March 26, 1976 orbital pass as well as from a DMSP photograph of the visible aurora. Electron observations in the 36 to 317 keV energy range (A.L. Vampola, private communication) locate the precipitating, and consequently auroral, region between 49 to 61° magnetic latitude. Observations from an electron sensor in the 80 eV to 17 keV energy range (R. Vancour, private communication) locate the precipitating region between 52° and 60° magnetic latitude. The DMSP photograph (cf. Figure 11) of the visible aurora from an orbital pass crossing the same nighttime auroral area as the S3-2 satellite and just 25 minutes after the S3-2 pass puts the equatorward edge of the bright continuous aurora at a corrected geomagnetic latitude of 58° . Bright discrete arcs and bands are observed poleward to 68° . The sudden commencement of the major geomagnetic storm began at 0233 UT. The Ap value reached 138, making it the fifth highest value of the 20th solar cycle. The planetary magnetic three-hour-range index, Kp, for this date remained high for 24 hours. The earth's polar cap underwent a very large expansion during this storm. In Figure 12, both the S3-2 and DMSP orbits are plotted on the auroral

oval nomograph (Whalen, 1970) for the largest polar cap expansion given for a complete oval ($Q=7$). The discrete arcs and bright continuous aurora have been sketched in from the photograph to show that for this storm the auroral oval has expanded even more than indicated in the nomograph.

We have attempted to compute a predicted bremsstrahlung X-ray flux at the LEPS aperture given the observed precipitating electron flux. The observed count rate for the point under study is 10^4 cts/sec. This occurs at altitude ~ 900 km, magnetic latitude $\sim 70^\circ$, and UT $\sim 9^h$. An arrow on Figure 8 points out the time under study for the forthcoming comparison of observed vs. predicted count rate at the LEPS. A "best case" approach in estimating the configuration of the LEPS with respect to the auroral zone is taken in order to maximize the predicted count rate result. Referring to Figure 13, the opening angle of the LEPS is 46° and the subtended arc is

$$l = 2r \sin \frac{1}{2} \theta = 2(2886 \text{ km}) \sin 23^\circ$$

$$l = 2255 \text{ km},$$

assuming the satellite is 26° poleward from the average latitude of the aurora. From the S3-2 electron data of Vampola (private communication) the extent of the precipitating zone is approximately 15° in latitude or 1665 km. Thus, the emitting volume is $2255 \text{ km} \times 1665 \text{ km} = 3.75 \times 10^{16} \text{ cm}^2$. Based on the electron observations for the date, the flux of precipitating electrons over this auroral zone is, on the average, 3.5×10^6 electrons/ cm^2 -sec. From the area in view of the LEPS, the total electron flux is $\Phi = 1.3 \times 10^{23}$ electrons/sec. The total area A, of a sphere centered on the auroral area and having a radius equal to the satellite distance away is $1.05 \times 10^{18} \text{ cm}^2$. Thus, $\Phi/A = 1.25 \times 10^5$ electrons/ cm^2 -sec. We assume an isotropic distribution of the bremsstrahlung flux and further neglect the atmospheric absorption (justified because of the high (100 keV) energy considered along with the very small residual atmosphere between 100 km and the satellite altitude). In order to obtain the bremsstrahlung flux at the detector we use the numbers calculated by Berger and Seltzer (1972), $\Phi(K)/J_0 \text{ keV}^{-1}$, the differential bremsstrahlung flux per unit incident electron current and multiply by the above computed factor 1.25×10^5 . The e-folding

energy obtained from the electron data is approximately 40 keV.

Thus $\Phi(K)/J_0$ keV⁻¹ differential is 7×10^{-7} . The total bremsstrahlung flux computed for the 100 keV ($\Delta E = 41$ keV) channel of the LEPS is

$$7 \times 10^{-7} \frac{\text{photons}}{\text{electrons} \cdot \text{keV}} \times 1.25 \times 10^5 \frac{\text{electrons}}{\text{cm}^2 \cdot \text{sec}} \times 41 \text{ keV} \times 2 \text{ cm}^2 \times \epsilon =$$

$$7.2 \frac{\text{photons}}{\text{sec}} \times \epsilon, \text{ where } \epsilon = \text{efficiency of detector}$$

Referring to Figure 7 shows that the expected percent efficiency of the LEPS to 100 keV photoelectrons is only 0.2%. (A laboratory calibration of the LEPS for its sensitivity to X rays was not performed.) The final predicted photon counts/sec for this date of interest is

$$7.2 \times 0.2\% = 0.0144.$$

Thus there exists a great discrepancy between the predicted value of approximately 10^{-2} cts/sec and the observed value of approximately 10^4 cts/sec.

5. CONCLUSION

This study has shown that the LEPS is considerably more sensitive to X-rays than initially predicted.

A possible reason for this discrepancy could be that the Berger and Seltzer calculation assumes a simple exponential spectrum for the precipitating electrons. Some actual measurements, however, show a two (or more) component electron spectrum which probably results in a higher X-ray production rate. Also, this instrument was not carefully calibrated for X-rays prior to launch. There may be inherent design characteristics that result in a higher than expected counting rate by X-radiation. Compton scattering in the detector might well be a source of some of the counts adding up in the various energy channels, but this in itself does not resolve the discrepancy. The fact that the LEPS recorded a signal at times as large as 2×10^4 cts/sec in the auroral direction warrants attention in designing and operating any detectors similar in design and construction to the LEPS and operating them in any orbital configuration similar to that of the S3-2 satellite.

Finally, the relatively certain results in this study of the five

months observations are: the single high peak is always seen in the auroral zone direction; the peak is more intense the greater the Kp index, and the dynamic range of auroral X-rays of four or five orders of magnitude found in other auroral X-ray studies seems to be found in these observations.

6. ACKNOWLEDGEMENTS

Special thanks are given to D.F. Smart and M.A. Shea of AFGL for their direction and advice during the course of this research; to W.J. Burke of AFGL for valuable improvements and comments; to E.G. Holeman of Emmanuel College Physics Research for his essential contribution to the data reduction, and to Professor M.P. Hagan for her continuous support throughout the research.

REFERENCES

- Berger, M.J. and S.M. Seltzer, Bremsstrahlung in the atmosphere, J. Atmos. Terr. Phys., 34, 85, 1972.
- Imhof, W.L., J.R. Kilner, G.H. Nakano, and J.B. Reagan, Satellite X-ray mappings of sporadic auroral zone electron precipitation events in the local dusk sector, J. Geophys. Res., 85, 3347, 1980.
- Imhof, W.L., G.H. Nakano, R.G. Johnson, and J.B. Reagan, Satellite observations of bremsstrahlung from widespread energetic electron precipitation events, J. Geophys. Res., 79, 565, 1974.
- Pantazis, J., A. Huber, and M.P. Hagan, Design of a low energy proton spectrometer, AFCRL-TR-75-0637, Final Report, Contract No. F19628-71-C-0060, December 1975.
- Walt, M., L.L. Newkirk, and W.E. Francis, Bremsstrahlung produced by precipitating electrons, J. Geophys. Res., 84, 967, 1979.
- Whalen, J.A., Auroral oval plotter and nomograph for determining corrected geomagnetic local time, latitude, and longitude for high latitudes in the northern hemisphere, AFCRL-70-0422, Environmental Research Papers, No. 327, July 1970.

LIST OF FIGURES

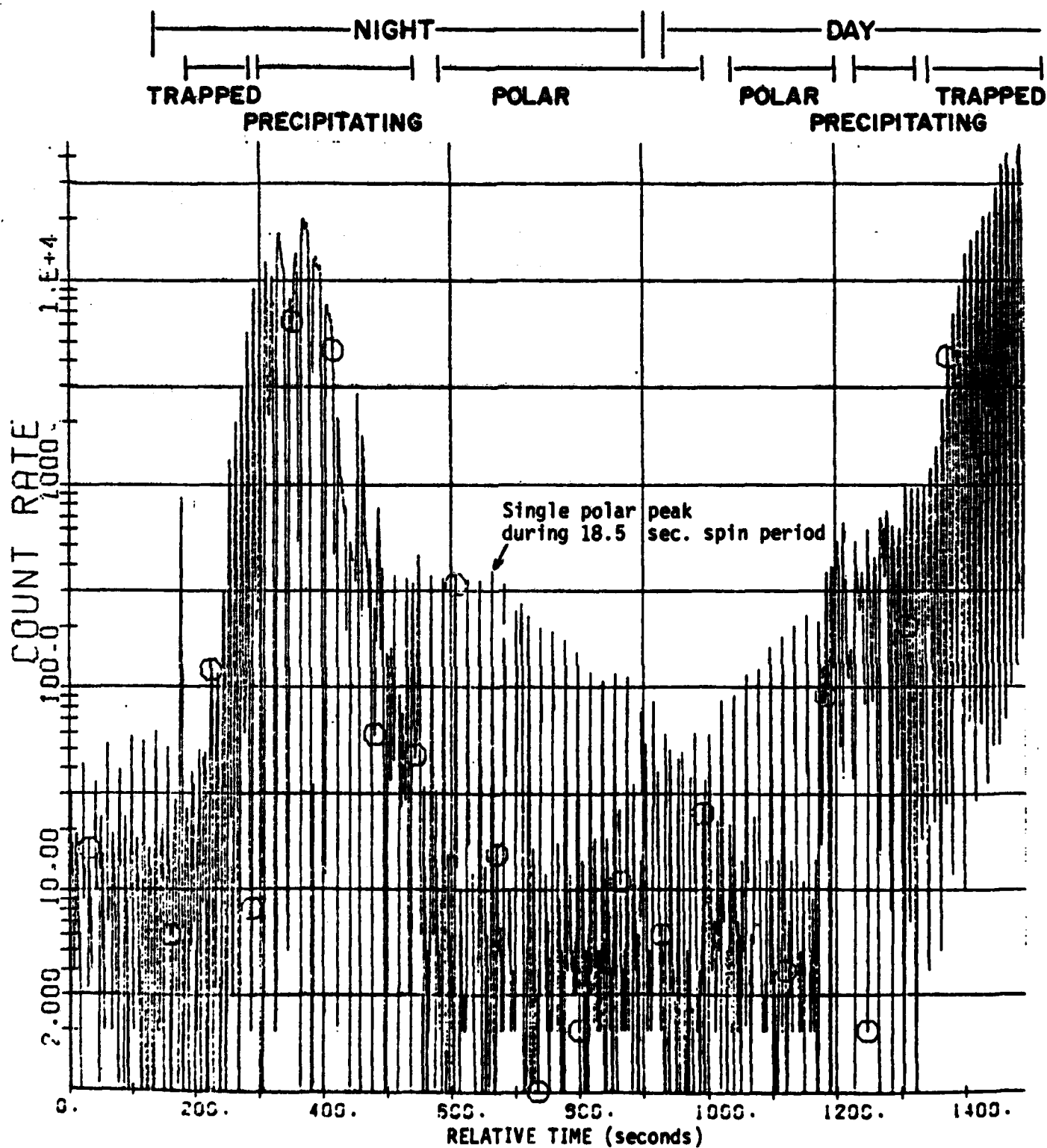
- Figure 1. Typical data record of northern hemisphere showing the anomalous single peak in the polar region. The peak is seen once per 18 second spin from a direction below the satellite's local horizon. The night peak at a particular pitch angle decreases as the pole is approached, and the day peak at a different pitch angle increases as the satellite recedes from the pole.
- Figure 2. Polar peak virtually disappears during this time of low magnetic activity ($K_p = 2-$).
- Figure 3. Planetary magnetic three-hour-range indices, December 10, 1975 to April 29, 1976.
- Figure 4. Projection of north polar pass of satellite orbits on an invariant latitude, magnetic local time diagram.
- Figure 5. Comparison of polar peak observations from dusk side (col. A) with midnight-noon passes (col. B) for high to low K_p index.
- Figure 6. A monoenergetic beam of spiraling charged particle radiation having particle velocity v would be observed at $\pm\theta$ pitch angle with respect to magnetic field line B by a detector spinning in a plane.
- Figure 7. Theoretical percent of X-rays absorbed in 300 μ silicon (LEPS front detector) due to photoelectric and Compton effects.
- Figure 8. The anomalous polar peak reaches an intensity of 2×10^4 counts/sec on this north polar pass, March 26, 1976. $K_p = 8-$; UT = 9^h.

- Figure 9. Surface of earth in the orbit plane under S3-2 north polar orbit track. Pictured are four orbital vantage points of the single peak observation of the obliquely viewed night and day auroral zone. Look angles with respect to the local nadir are labeled.
- Figure 10. Variation of polar peak corresponding to four orbital vantage points of Figure 9 (a,b,c,d) and selected from data of Figure 8. Peak always appears in the direction of the night or day aurora.
- Figure 11. DMSP satellite image of the visible nighttime continuous aurora plus discrete arcs and bands observed on March 26, 1976. A reference geographic coordinate grid at 100 km altitude overlays the image. The satellite subtrack is shown by a dashed vertical line. The crossing of the equatorward edge of the aurora occurred at 925 UT. The sunset terminator lies at the left of the image.
- Figure 12. S3-2 and DMSP satellite tracks plotted on invariant latitude, local geomagnetic time auroral oval nomograph for March 26, 1976, UT \sim 9^h. The image of the aurora from Figure 11 has been sketched in.
- Figure 13. The LEPS, at 2886 km away, with an aperture of 46° views an auroral area $15^\circ \times l = 1665 \text{ km} \times 2255 \text{ km}$.

Table 1. Energies (MeV) of LEPS Channels

Channel	1	2	3	4	5	6	7	8	9	10	11
Low energy cut off	.082	.123	.165	.232	.345	.477	.680	.948	1.445	2.038	2.927
High energy cut off	.123	.165	.232	.345	.477	.680	.948	1.445	2.038	2.927	6.0

UT ~ 2140

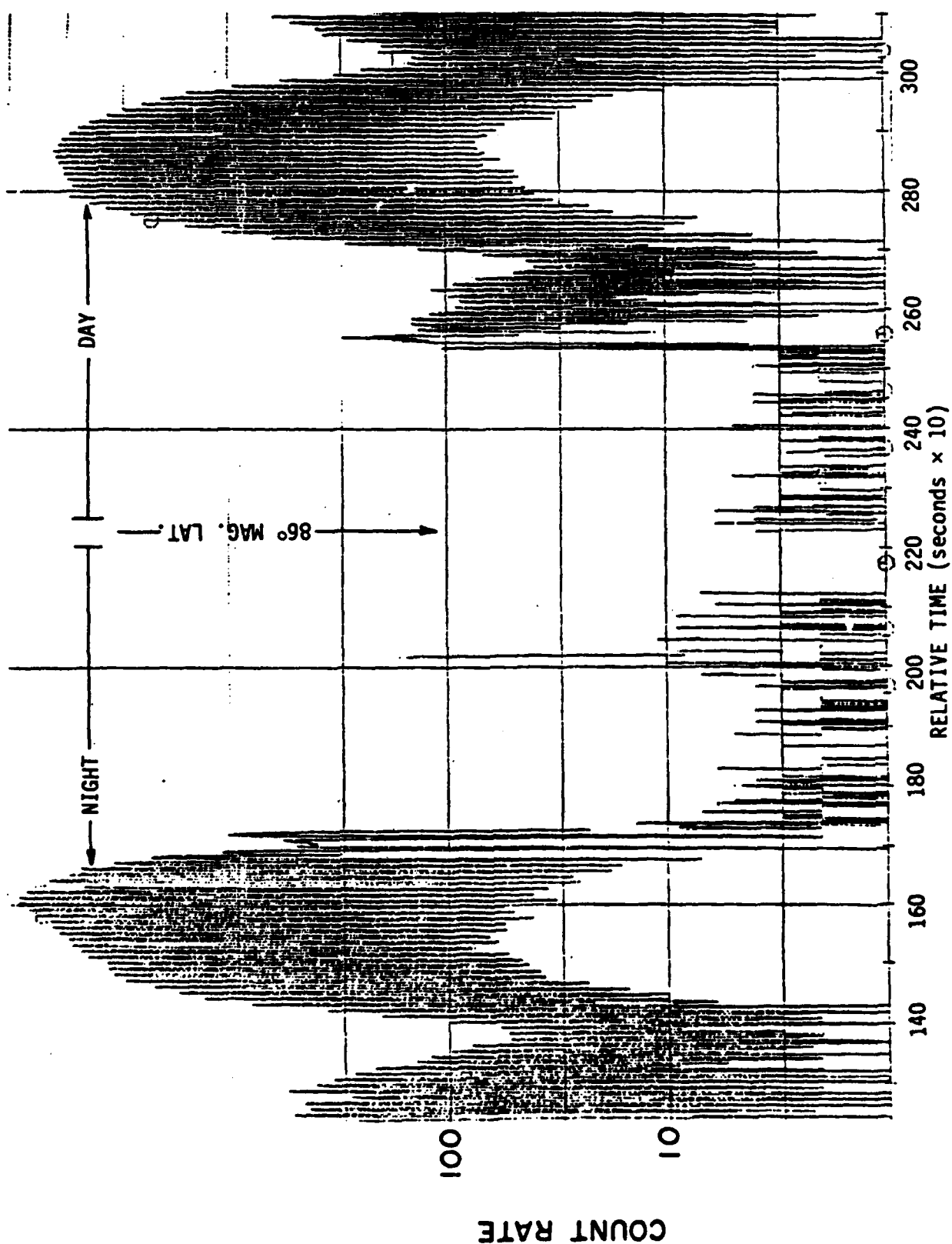


S3-2 LAPE GUAM1662 04/01/76

LOW ENERGY CHANNEL 100 keV

Figure 1.

UT ~ 1830



BOSS 1888 NORTH 4/17/76 Kp = 2-

Figure 2.

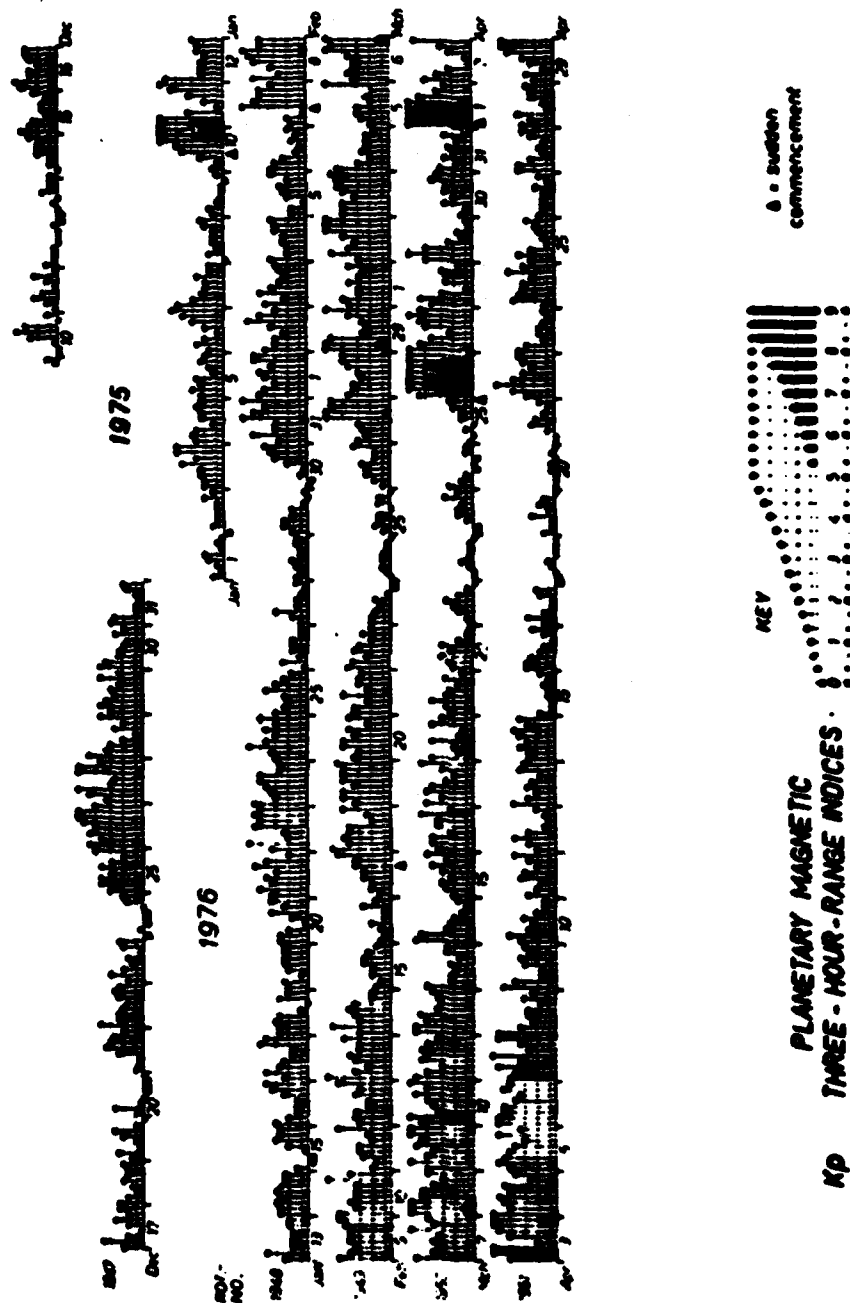


Figure 3.

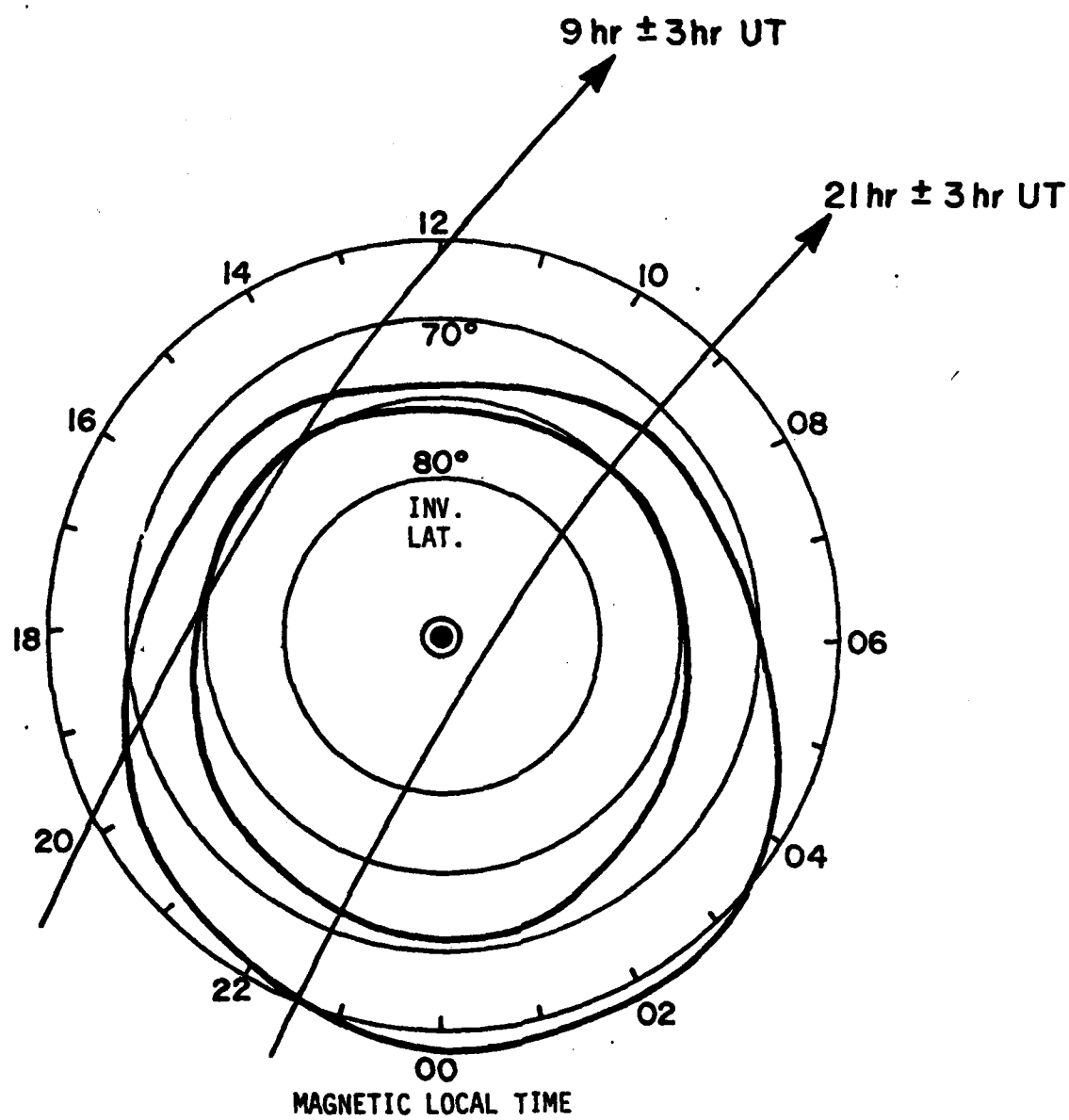
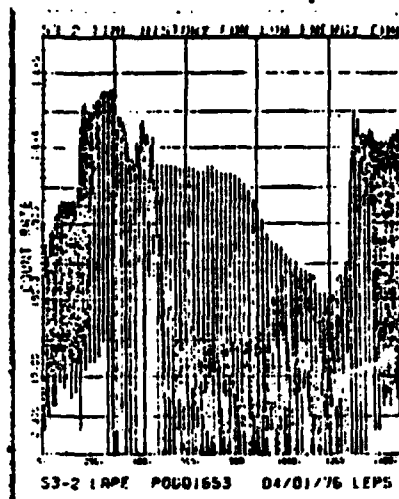
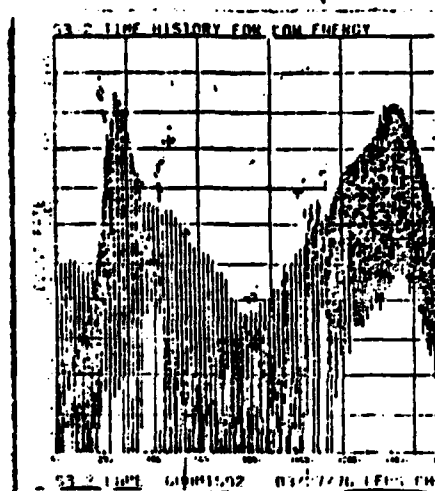


Figure 4.

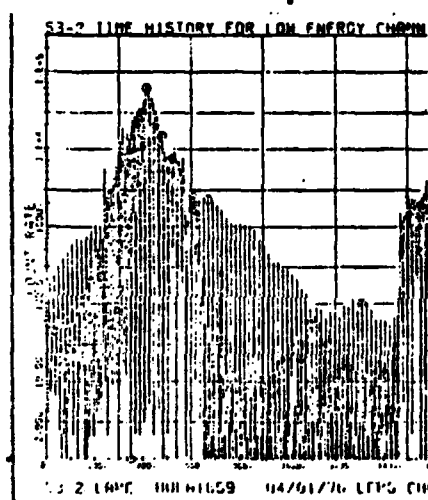
UT~0800 Kp=8+



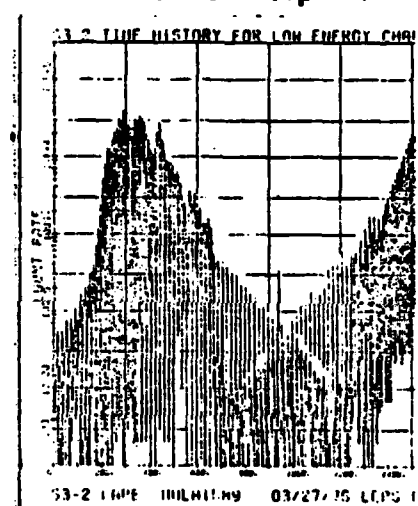
UT~2400 Kp=4+



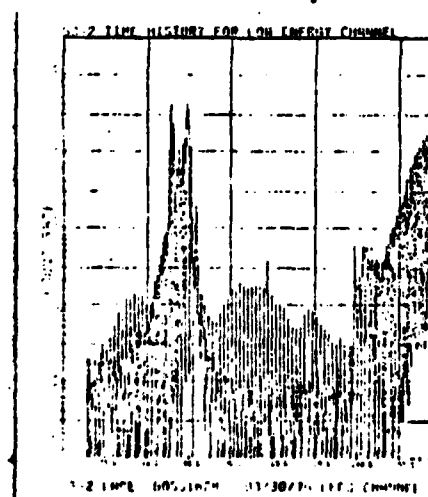
UT~1600 Kp=5+



UT~1900 Kp=4+

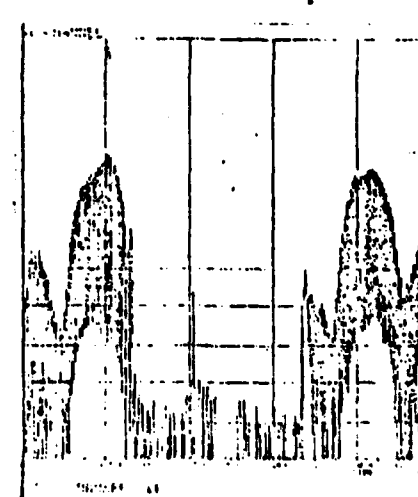


UT~1320 Kp=3-



Col. A

UT~1830 Kp=2-



Col. B

Figure 5.

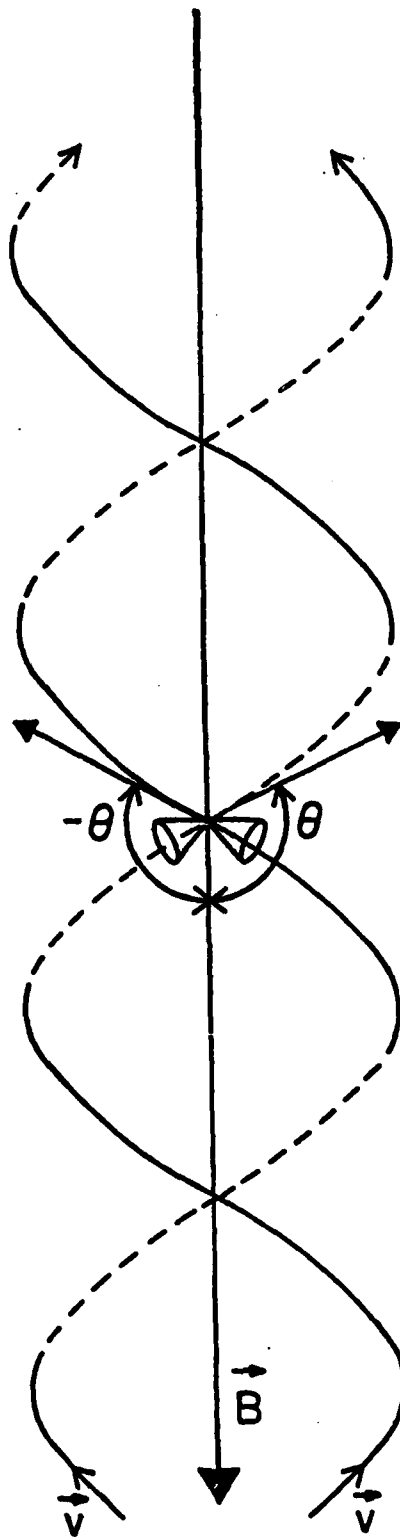


Figure 6.

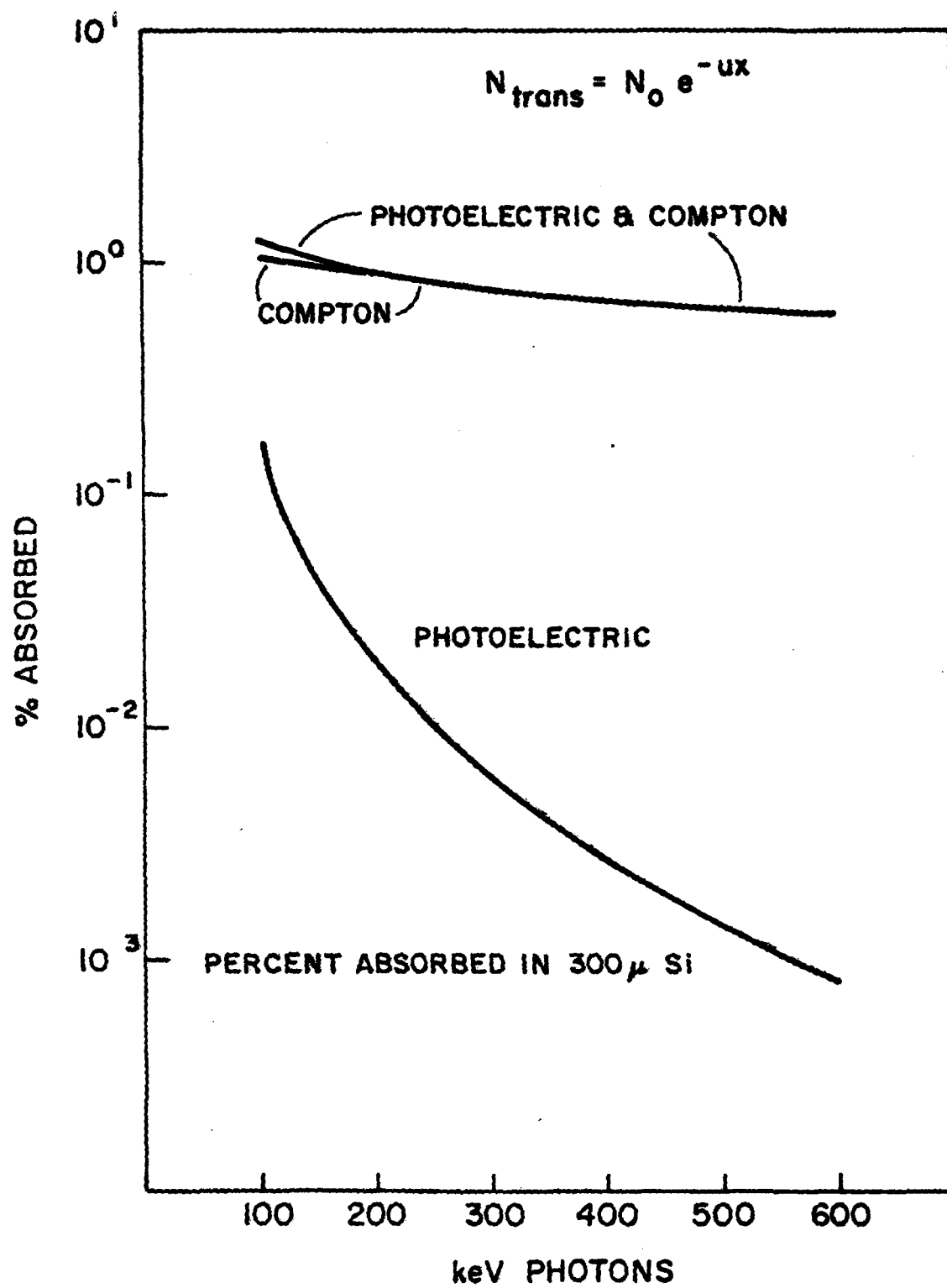
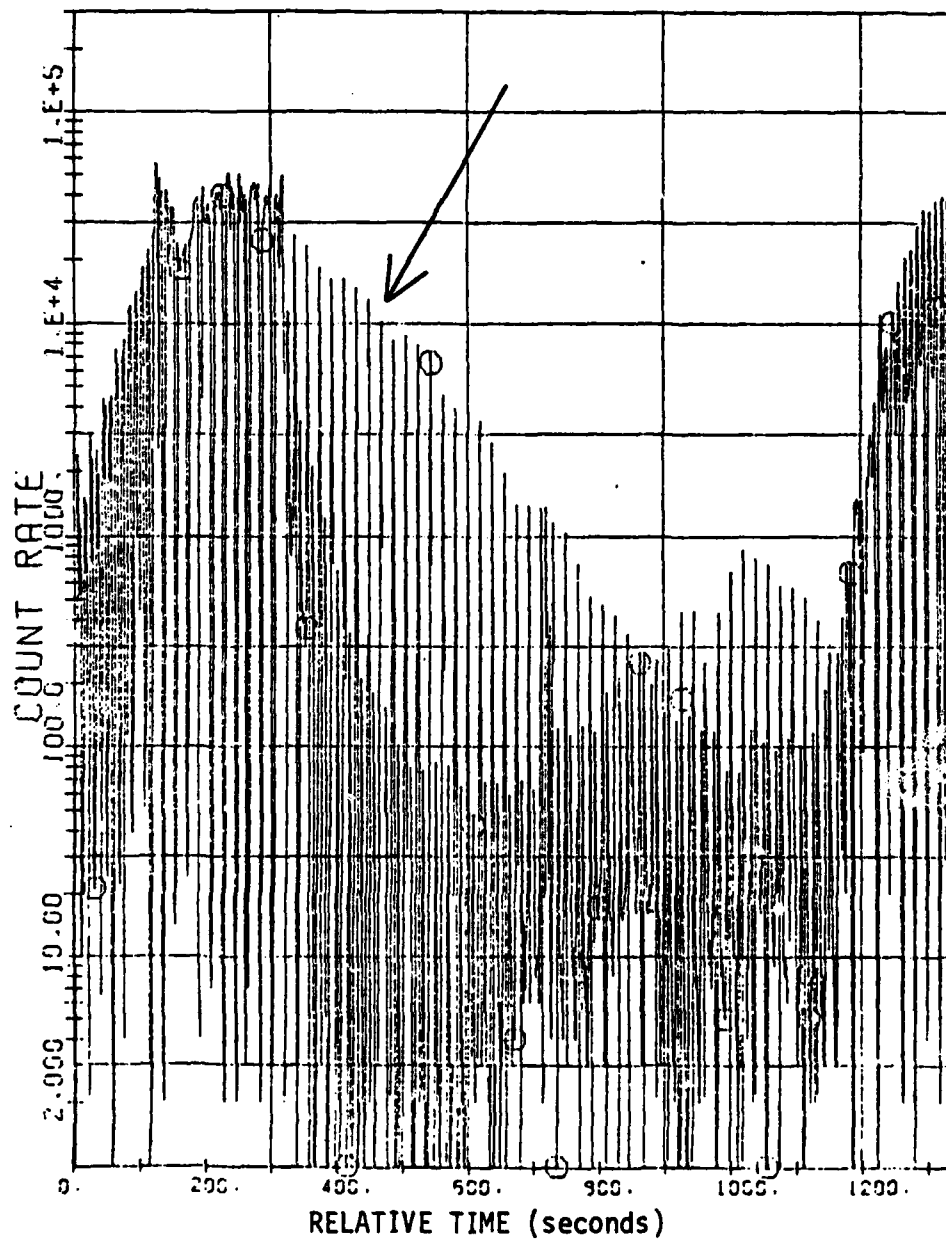


Figure 7.

UT = 0900

Kp = 8-



S3-2 LAPE P0001569 03/26/76

LOW ENERGY CHANNEL 100 keV

Figure 8.

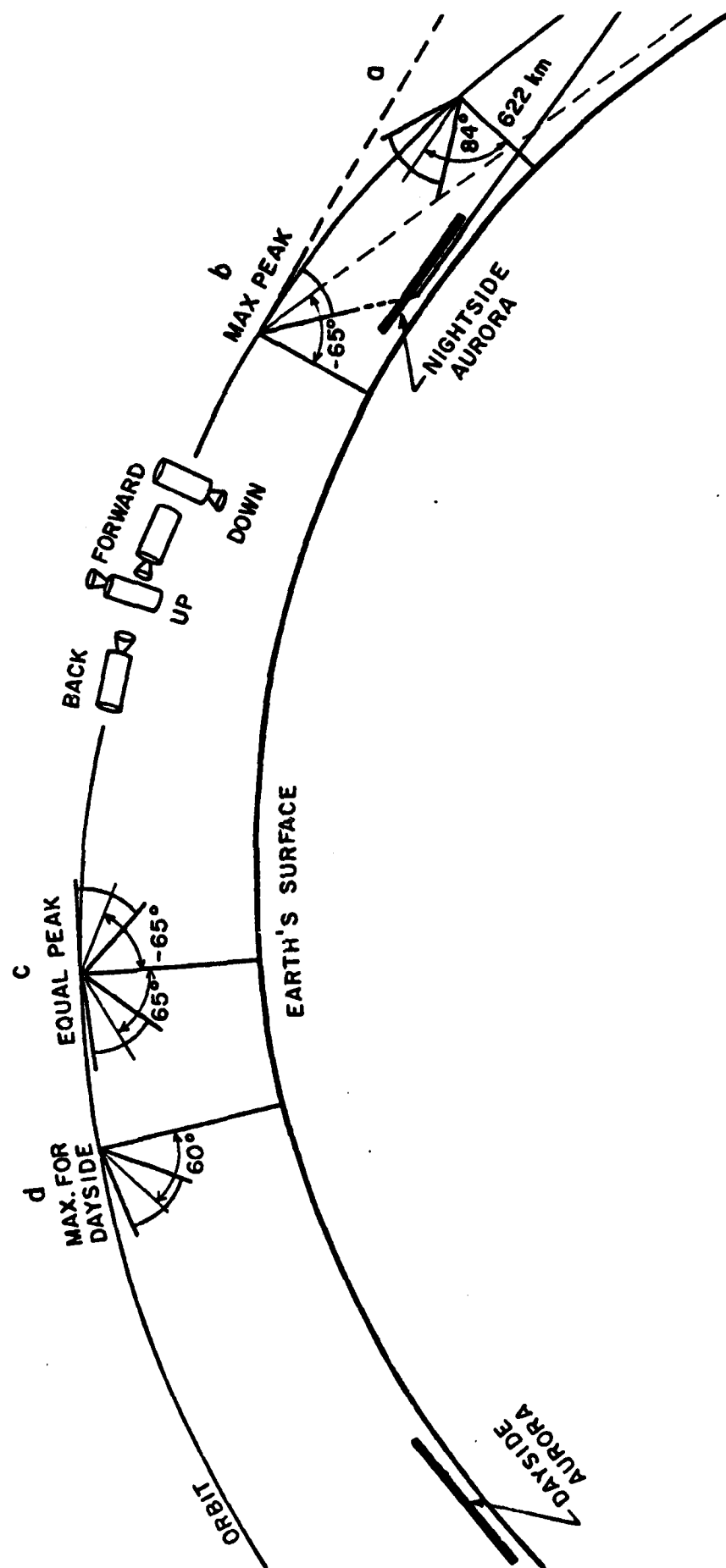


Figure 9.

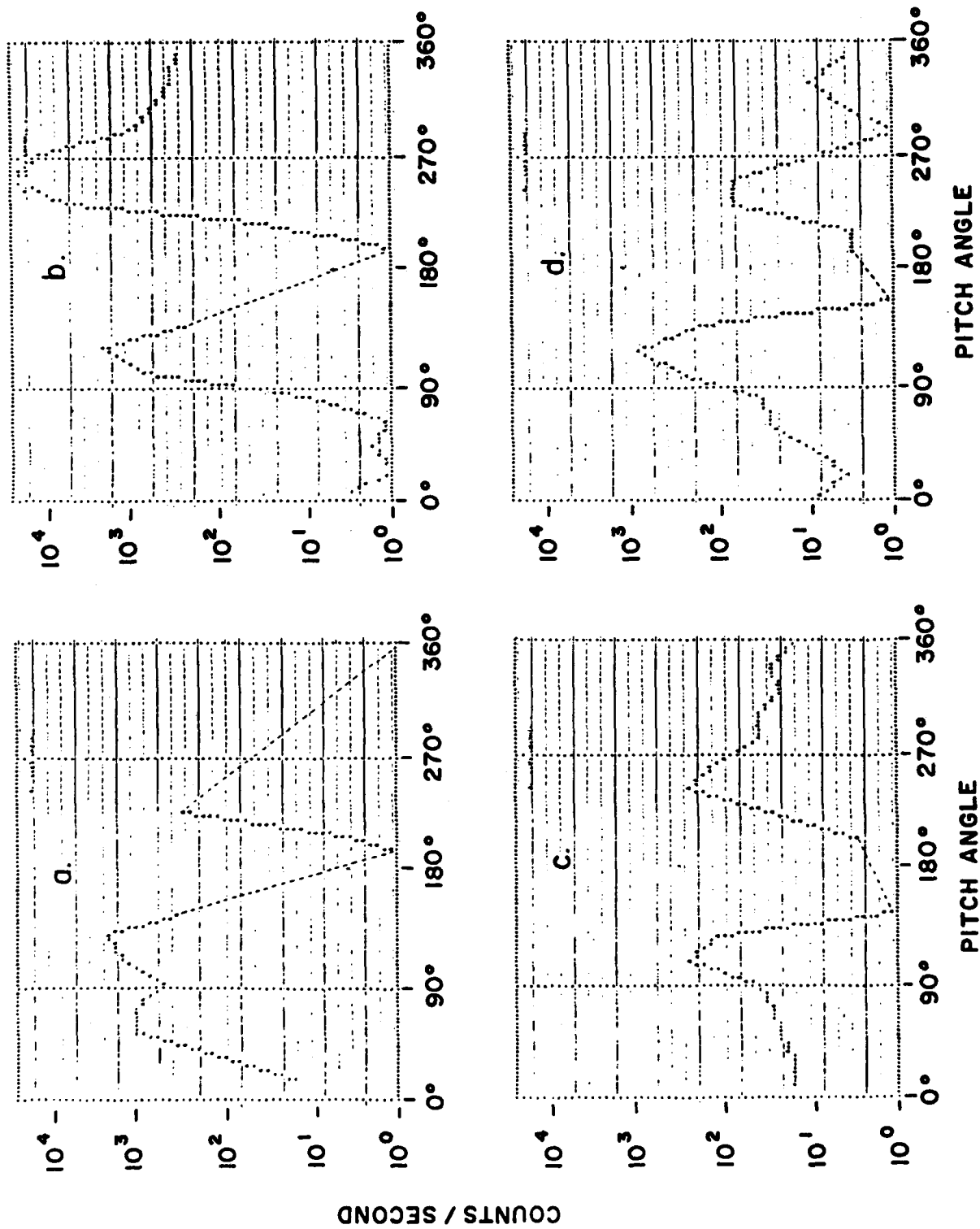


Figure 10.



Figure 11.

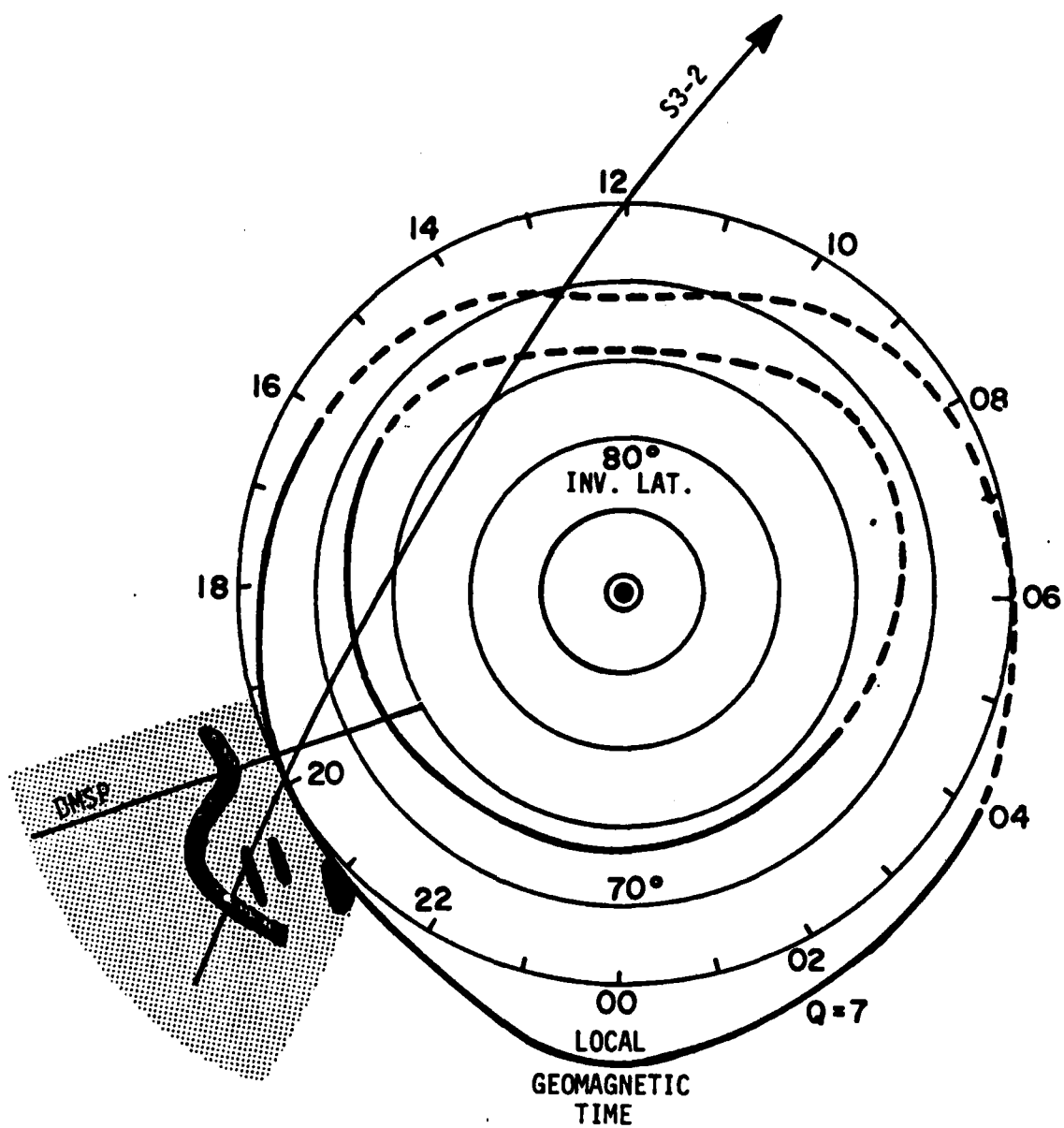


Figure 12.

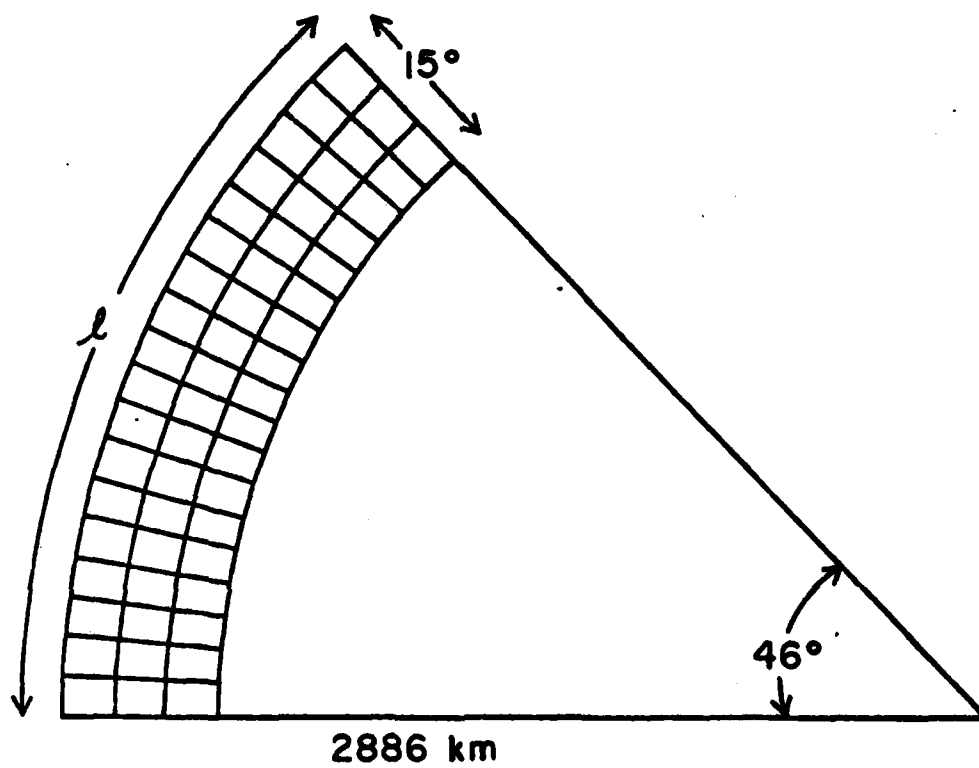


Figure 13.

Appendix 2

**SPECIAL REPORT ON THE
LOW ENERGY PROTON SPECTROMETER
EXPERIMENT**

**ERNEST HOLEMAN
EMMANUEL COLLEGE
PHYSICS RESEARCH DIVISION**

I. Introduction: Since the last meeting at AFGL relative to the LEPS simulation project, there have been several significant developments. Detailed measurements were made of the energy spectrum of the Am241 calibration source from the back-up LEPS with both the LEPS electronics and logic and using a pulse height analyzer (PHA) under laboratory conditions. The results show clearly that there is no loss of events due to an energy dependent dead time and show that significant numbers of events are being shifted downward in energy by the LEPS logic. We will present the hypothesis that the observed effects can be approximated by an energy dependent base-line shift of magnitude up to 1600 kev. We conclude that the narrow angle LEPS on S3-3 never encounters radiation conditions where the base-line shift is significant and present a method for interpreting the data from the wide angle LEPS.

II. The Am241 calibration Experiment: Using a laboratory PHA, a series of measurements were made of the energy spectrum of the Am241 source with the distance separating the source from the detector as a variable; thus effectively varying the counting rate as seen by the detector. The LEPS head assembly was used as a collimator and its front detector as the first element in the electronics. The measurements were made under vacuum at nominal separations of 2.5", 1.25", 0.64", 0.32" and 0.07". The latter separation corresponded to the standard position of the source in the LEPS calibration mode. With the PHA, sums were accumulated over a 100 second "live time" interval using the internal dead time correction mode. A lower threshold setting of 240.6 kev and a scale factor of 5.19 kev per channel gave 1024 channel coverage of the source spectrum. Thus:

$$(1) \quad E(k) = 5.19 \cdot k + 240.6 \text{ kev}$$

gave the energy correspondence for each PHA channel. The experiment was repeated using the back-up LEPS electronics package and reproducing the experimental conditions as closely as possible.

A comparison of the two sets of data are shown in table 1. The columns labeled LEPS are 100 second LEPS observations corrected for a dead time of 1.75 micro-seconds per event and converted to counts per second. To get the comparable PHA results, the PHA channel k_i corresponding to each of the LEPS nominal channel boundaries was determined from (1) and a count rate was calculated using the equation:

$$(2) \quad (PHA)_i = \sum_{j=k_i}^{1024} n_j - \sum_{j=k_i+1}^{1024} n_j$$

where n_j is the counting rate in the j 'th PHA channel in counts per second. The ratio of total counts was calculated and shows a maximum difference of 9.6%. We assigned a probable uncertainty of $\pm 0.05''$ for the 2.5" and 1.25" cases, $\pm 0.02''$ for the 0.64" and 0.32" cases and of $\pm .01''$ for the .07" case. These then imply the uncertainties given in the table for the LEPS/PHA ratios.

Table 1. illustrates two important points. First, the total count rates agree within the known uncertainties in all cases. Earlier simulations of the LEPS problem using data from the S3-3 satellite showed that the count rate losses in the wide angle S3-3 LEPS could be accounted for by an energy dependent dead time. All formulations of this theory however, required a- least 40 micro-second per event dead time for a 4.0 Mev pulse (the approximate mean of the channel 11 source counts). For the standard position, the 13500 cps in channel eleven alone would account for a 54% dead time and hence at least a factor of two difference between the LEPS and PHA total counts should be seen. Even an assumption of 10 micro-seconds should result in approximately 14% differences and this clearly is not the case. The calibration results thus prove an energy dependent dead time is not a factor to be considered. Secondly, the table shows a definite shift of events down in energy. For example, the differences in the channel 11 count rates can be interpreted as showing that 2.55, 4.9%, 9.0%, 29.0%, and 75.0% of the channel 11 PHA events are shifted to lower channels respectively for the five samples. For a closer

samples. For a closer look at what is probably happening at the other channels we wrote a computer model of the LEPS calibration source.

III. Simulation of the Calibration Source.

The data from the PHA for the standard .07" case was encoded to create a computer model of the calibration source. We have three sources we would like to compare using this model, that of the back-up LEPS and those from the narrow angle and wide angle LEPS on the S3-3 satellite. For the S3-3 source data we chose a sample representing an average of all the source data for one orbit of the satellite. This in fact was an average of 10 separate 2-second observations under various intensities of trapped radiation flux. The total count rate for this sample was 20600 for the narrow angle LEPS and 29900 for the wide angle LEPS. This would indicate the source on the narrow angle LEPS was essentially identical to that of the back-up LEPS while the wide angle LEPS was ~43% stronger.

The purpose of this simulation was to determine the magnitude of the energy shifts at several channel boundaries. In order to do this, one key assumption had to be made. We assumed that the net effect of the shifting of individual events down in energy could be approximated by shifting the nominal channel boundaries up in energy. The entire formulation and discussion that follows in this report is heavily dependent on that assumption.

The three calibration sources were simulated and the results are shown in Table 2A. To produce this table the relationship:

$$(3) \quad Sx \sum_{j=k_i}^{1024} n_j = \sum_{j=1}^{11} n_j$$

was solved numerically for k_i for channels $i=11, 10, 9$, and 8 for each of the three sources. In equation (3) N_j is the observed count rate for LEPS channel j ; n_j is the count rate for PHA channel j ; S is the relative strength of the source being simulated, and k_i is the PHA channel number

that gives equality at boundary i . Values of $S = 1.0$ were used for the back-up and narrow angle LEPS and a value of 1.43 for the wide angle LEPS. In table 2, the "E" column gives the nominal channel boundaries for each source. The "E'" column is the shifted channel boundaries using equations (1) to determine $E'(k_i)$. The " ΔE " column gives the differences. The same calculation could be made for the remaining boundaries, however, interpretation becomes difficult at the lower energies. For example, using the channel 1 boundary of the back-up LEPS as an illustration, a value of $S = 1.00$ forces a ΔE of 0.00. According to table 1, we know S only to $\pm 6.5\%$. If the maximum value of $S = 1.065$ is assumed, the calculation gives $\Delta E = 1281$ kev. The two S values can possibly be interpreted as giving a lower and upper limit respectively to the boundary solutions. The $S = 1.065$ results are given in Table 2B. Obviously, the higher energy channels are not completely free of this effect.

This simulation shows primarily the magnitude of the problem for the LEPS calibration mode. We will later show that the distorting effects are approximately proportional to the square of the energy and hence the count rates in the highest energy channels are a dominant factor in causing the distortions. The highest observed count rates for trapped radiation for the highest energy channel are 300 cps. and 4500 cps, while for the calibration mode they are 13500 and 19000 respectively. Hence the calibration mode is the most severe environment LEPS ever sees.

IV. Base-Line Shift Hypothesis.

As shown above, the 6.5% uncertainty in S prevents us from drawing strong conclusions about the nature of the distortion below channel 8 based on the calibration source simulation alone. We have other information that is relevant however. We know from the S3-3 experimental data that the calibration source completely dominates the LEPS instrument in the sense that even a large trapped radiation flux has no significant effect of the calibration mode observations. The calibration source and its mounting hardware block a maximum of 25% of the detector area and although this will be a large effect, it cannot account for the observations. The only remaining conclusion is that the channel boundaries below channel 8 must be shifted far enough to place a major portion

of the trapped radiation spectrum below the LEPS lower energy threshold.

In modeling the distortion, the simplest formulation consistent with the above arguments is a base-line shift of the form $E'_i = E_0 + E_i$ where E_i are the nominal LEPS channel boundaries, E_0 is some unknown function of count rate and energy, and E'_i is the effective channel boundaries. E_0 would then have a value of 1400 ± 300 for the back-up LEPS and the narrow angle LEPS and a value of 1600 ± 300 kev for the wide angle LEPS calibration mode. This model would be adequate to explain all of the calibration data. To formulate E_0 for less severe conditions and to test the general validity of this base-line shift hypothesis we must look in detail at samples from the S3-3 experimental data.

V. Testing the Base-Line Shift Hypothesis With the S3-3 Data.

If the LEPS distortion is due to a pure base-line shift given by some function E_0 (of count rate or energy or some other parameter) then what LEPS is actually measuring is the integral energy spectrum $J(E > E_0 + E_i)$ for each of the eleven nominal channel boundaries E_i . If some mechanism could be found for determining E_0 , the LEPS problem would be completely resolved. Conversely, if the energy spectrum were known, each data sample would represent an experimental determination of E_0 (in fact eleven estimates E_{0i} could be determined, one for each boundary E_i). The two LEPS instruments on S3-3 satellite allow us to do just that. We assume the energy spectrum is determined by the narrow angle LEPS and use the wide angle LEPS observations to determine E_{0i} from the integral equation:

$$(4) \quad \Omega_w \int_{E_{0i} + E_i}^{\infty} J dE = \sum_{j=1}^{11} N_j$$

where Ω_w is the solid angle of the wide angle LEPS and N_j is the observed count rate for channel j . This procedure is valid to whatever degree

the narrow angle LEPS data is free from distortion. To at least first order it should be a legitimate assumption since the geometric factor of the narrow angle instrument is smaller by a factor of 15.06 than that of the wide angle instrument. It should be less susceptible to distortion by approximately that factor and we will give further evidence later in this report to support that assumption.

For this determination, eleven samples were selected from the S3-3 data set. They were selected to give representative coverage of the observed count rate range of the narrow angle LEPS (500 cps. to ~50000 cps.). Samples 1 and 2 were included only for completeness. Each represented only 1 observation and at 520 and 1400 cps respectively were not statistically adequate for a meaningful energy spectrum determination. Samples three through six were in the range 3200 cps. to 18000 cps. Each of these represented an average of at least 10 consecutive observations at the peak of the local trapped radiation pitch angle distribution. The agreement between the two energy spectra were good, indicating no severe distortion in the wide angle LEPS data. The remaining five samples (covering the count range of 10000 cps. to 46000 cps.) all showed evidence of distortion in varying degrees and were numbered for reference in the order of its apparent severity.

A Monte-Carlo simulation was then done to give simultaneous solution at the eleven nominal energy boundaries E_i of the function E_{oi} for each of the eleven samples. As a first test of the legitimacy of this procedure, an experimental determination of the effective stopping power of the mylar shield in front of the wide angle LEPS was attempted. Using samples three through six, a curve $E'_i = \bar{E}_{oi} + E_i$ was constructed where \bar{E}_{oi} is the average of the E_{oi} 's at channel i for the four samples. The result is presented in figure 1. For comparison, the nominal boundaries E_i and the theoretical curves determined for 4.0 micron, 4.6 micron, and 5.2 micron mylar are plotted. The figure shows almost exact agreement between the E'_i curve and the theoretical 4.6 micron mylar shield for channels one through seven. The difference in channels 8 through 11

are possibly statistical and possibly due to the crudeness of the fit to the integral spectrum at higher energies. A power law fit:

$$(5) \quad E_i = E_i' - 24400 E_i'^{(-.763)}$$

was made to the 4.6 micron mylar curve and the simulation was repeated using that function to take into account the effect of the mylar shield.

The results of this second simulation are given in figure 2. Figure two shows that samples six and seven require no significant correction and that a base-line shift of ~ 50 kev would be an adequate description of sample eight. The curves for the remaining three samples show that the base-line shift is only a first order approximation to the apparent distortion.

The regularity of the curves suggest however a modified base-line shift of the form $E_i' = E_i - A E_i + E_0$ might give a significant improvement. A first approximation to A and E_0 were made from fits to the parameters given in table 3. giving:

$$(6) \quad E_0 = .003017 (E^2)_T + .07$$

$$A = .0056 + 1.0757 \times 10^{-3} E_T$$

Table three gives a set of parameters characterizing the eleven samples (sample 12 in the table is the wide angle LEPS calibration data). Columns one through four give the mean energy per event "E" in kev, the total energy " E_T " in kev per micro-second, the total "square energy" $(E^2)_T$ in kev^2 per micro-second, and the observed total count rate for each sample. Column 5 gives the observed E_0 and column 6 the E_0 value from equations (6).

A final simulation of the 11 samples was made using equations (6) as a representation of the distortion. The results are given as table 4. The table shows there is good agreement in total count rates with the exception of sample 10 (within $\sim 10\%$). The data also shows an average

RMS agreement within $\pm 15\%$ in the count rate spectrum, again excluding sample 10.

VI. Conclusions:

The above experimental evidence allows us to make the following statements on the quality of the LEPS data from the S3-3 and S3-2 satellites.

(a) The narrow angle LEPS data is not affected by the problems we have been studying in any important degree. In the most extreme trapped radiation environment it encounters the total squared energy it sees is $(E^2)_T = 2.4 \times 10^4 \text{ kev}^2$ per micro-second and a maximum count rate of 50000 cps. At this $(E^2)_T$ value equation (6) implies a base-line shift of $\sim 72 \text{ kev}$. This is in the region of figure 2 where the simple base-line shift looks good. For the simple base-line shift, the delta-E's used in the flux calculations are preserved and hence the real effect is ignorable. Also, the calibration experiment shows dead time losses at a count rate of 20000 cps are not detectible and hence they cannot be an important factor at a 50000 cps level, although the nominal dead time for the LEPS logic of 1.75 micro-seconds per event should be taken into account in the analysis (this is a nine percent correction at 50000 cps). The narrow angle LEPS is still susceptible to contamination by electrons and penetrating protons and no attempt has been made in this study to evaluate those effects. What has been shown is that the low energy wide angle LEPS data cannot be used to provide the electron contamination information. Even a small base-line shift makes it useless for that purpose.

b) The wide angle LEPS data on S3-3 can be interpreted and some useful information can be recovered from it. The simulation based on the procedures outlined in section V. were successful in giving the observed count rates within an average of $\pm 10\%$ for ten of the eleven samples considered and showed an average RMS precision of $\pm 15\%$ in reproducing the count rate spectrum for those ten samples. However, those procedures were crude and fits were based on only four points.

They were derived to show that a method exists with some potential for solving the problem rather than as an actual solution. If the correction is to be attempted, those procedures must be refined and fits to E_0 and to the mylar shield must be made based on many more samples. It is somewhat questionable whether this effort would be worthwhile. We have shown that the wide angle LEPS cannot provide the electron contamination information it was intended to give and the narrow angle LEPS will always give an energy spectrum with a higher confidence level since it requires no large corrections. The only improvement the wide angle instrument can make is better statistics in the higher energy channels.

c) The S3-2 wide angle LEPS data is not as severely distorted as its S3-3 counterpart since the S3-2 satellite was at a lower altitude and saw a correspondingly lower trapped radiation flux. We did not look at the S3-2 data in this study but equations (6) would be applicable and a conservative $(E^2)_T$ threshold of approximately $2.5 \times 10^4 \text{ kev}^2$ per microsecond could be set to separate out that portion requiring no large corrections.

Table 1.

Comparison of LEPS and PHA measurements
of the Am241 calibration source
from the back-up LEPS

		2.5 \pm .05"		1.25 \pm .05"		.64 \pm .02"	
		<u>LEPS</u>	<u>PHA</u>	<u>LEPS</u>	<u>PHA</u>	<u>LEPS</u>	<u>PHA</u>
channel*	11	168	179	662	717	1918	2050
	10	25.6	22.6	125	102	481	303
	9	6.55	6.45	30.1	26.1	97.9	78.7
	8	3.58	3.35	15.2	13.2	44.2	40.2
	7	2.07	1.97	8.10	7.90	23.4	23.3
	6	1.33	1.68	6.16	5.94	17.2	17.0
	5	1.25	1.16	4.84	4.58	13.0	13.5
	4	.94	1.04	3.51	3.77	12.4	11.6
totals		209.3	217.3	854.9	880.5	2607	2537
EPS/PHA		0.963		0.971		1.028	
		\pm .058		\pm .118		\pm .067	

		.32 \pm .02"		.07 \pm .01"	
		<u>LEPS</u>	<u>PHA</u>	<u>LEPS</u>	<u>PHA</u>
	11	3810	4910	3470	13500
	10	2201	822	9340	4800
	9	450	204	5260	1120
	8	144	101	1430	515
	7	68.6	57.5	582	265
	6	45.7	42.1	349	187
	5	32.6	33.5	220	145
	4	40.9	26.0	249	117
totals		6793	6196	20900	20649
EPS/PHA		1.096		1.012	
		\pm .104		\pm .065	

Table 2.

Calibration Mode Boundary Solutions

Table 2A: S = 1.00

						S = 1.43			
back-up LEPS			narrow angle LEPS			wide angle LEPS			
	E	E'	ΔE	E	E'	ΔE	E	E'	ΔE
11	3570	4573	1003	2936	4286	1350	3306	4922	1616
10	2275	3815	1540	2251	3750	1499	2233	3896	1663
9	1537	2689	1152	1747	3135	1388	1680	3328	1648
8	<u>1022</u>	<u>1911</u>	<u>899</u>	<u>1176</u>	<u>2386</u>	<u>1210</u>	<u>1116</u>	<u>2583</u>	<u>1467</u>
ug ΔE	=		1146			1362			1799

Table 2B:

S = 1.065				S = 1.523					
back-up LEPS				narrow angle LEPS			wide angle LEPS		
11	3570	4593	1023	2936	4301	1365	3306	4943	1637
10	2275	3903	1628	2251	3849	1598	2233	3968	1735
9	1537	3063	1526	1747	3389	1642	1680	3494	1814
8	<u>1022</u>	<u>2586</u>	<u>1564</u>	<u>1176</u>	<u>2889</u>	<u>1713</u>	<u>1116</u>	<u>2972</u>	<u>1856</u>
ug ΔE	=		1435	1580			1761		

Table 3.

Characteristic Parameters for the eleven selected
data samples from S3-3 + calibration source

sample #		kev/ct	kev/m-sec	kev ² /m-sec	observed	observed	fit
		\bar{E}	E_T	$(E^2)_T$	total cts	E_O	E'_O
1		385	2.297	1.582×10^3	$.5139 \times 10^4$	-	4.84
2		319	4.557	2.622"	1.1359"	-	7.98
3		303	9.100	5.008"	2.1442"	-	15.2
4		311	14.89	8.350"	3.2583"	-	25.3
5		239	14.82	6.934"	3.723"	-	21.0
6		236	1941	9.083"	4.882	-	27.5
7		252	27.62	1.371×10^4	5.945	14.0	41.4
8		255	38.51	1.923"	7.044"	50.9	58.1
9		710	91.34	1.362×10^5	5.415	425	411
10		372	176.1	1.165"	9.462	392	352
11		758	201.5	3.066"	6.025	905	925
12		3693	115.6	4.652"	2.759"	~1600	1404

$$E'_O = .003017 (E^2)_T + .07$$

Table 4.

SEISMOTRIC FACTOR TABLE.																
ANALYSIS FOR CH-3 THROUGH CH-9.				SIMULATION OF MODIFIED BASE-LINE SHIFT				EQUATIONS 6.)								
SARS	CH11	CH10	CH9	CH8	CH7	CH6	CH5	CH4	CH3	CH2	CH1	OBSD	SIMU	RMS %	O/S	SATU
1	4.22	9.55	3.36	9.93	16.51	16.53	15.16	15.76	21.08	14.75	12.56	4192	3876	20.55	1.08	.87
2	6.11	18.74	16.93	12.44	16.70	16.03	15.71	19.31	19.92	13.69	12.60	8992	7705	15.05	1.17	1.84
3	0.00	8.61	17.93	11.87	15.77	16.12	15.72	17.96	17.95	13.24	12.50	16781	14917	14.42	1.12	3.68
4	0.00	9.79	18.92	11.35	14.95	15.69	14.83	15.58	17.73	13.96	15.27	24631	23522	19.31	1.05	5.62
5	0.00	0.00	12.36	11.65	16.92	16.05	17.39	17.11	17.33	14.11	15.08	22807	20137	9.84	1.15	6.16
6	0.00	0.00	0.00	14.95	14.77	18.48	17.40	18.20	18.62	14.62	17.99	33955	28137	4.31	1.21	10.56
7	0.00	0.00	22.50	14.21	17.38	17.47	16.19	16.64	16.67	13.95	18.55	41874	37852	7.85	1.11	10.56
8	0.00	0.00	17.97	10.67	15.01	14.64	14.40	15.47	16.93	12.54	17.23	49750	48379	15.95	1.03	12.96
9	14.41	18.25	17.34	18.09	14.38	16.27	14.29	12.65	13.23	9.22	22.33	44254	45161	10.55	.94	9.41
10	0.00	21.14	26.96	12.54	15.49	15.10	13.37	11.47	10.27	6.57	17.01	75492	47454	30.33	.60	28.54
11	14.15	24.22	13.74	15.14	15.69	15.32	13.43	11.53	11.01	9.47	32.19	44177	49975	15.13	.90	18.54
12	14.40	21.22	14.03	15.23	15.88	15.32	14.92	14.63	15.27	11.50	17.69					

SIMULATION SUMMARY.										ANALYSIS FOR ALL CHANNELS.										SIMULATION OF MODIFIED BASE-LINE SHIFT (EQUATIONS 6.1)																																																																																																																																																																																																																																																																																																																																																																																																																																																																																																																																																																																																																																																																																																																																																																																																																																																																																																																																																																																																																																																																																																																																																																																																																																																																																																																																																																											
SAF	CH1	CH2	CH3	CH4	CH5	CH6	CH7	CH8	CH9	CH10	CH11	CH12	CH13	CH14	CH15	CH16	CH17	CH18	CH19	CH20	CH21	CH22	CH23	CH24	CH25	CH26	CH27	CH28	CH29	CH30	CH31	CH32	CH33	CH34	CH35	CH36	CH37	CH38	CH39	CH40	CH41	CH42	CH43	CH44	CH45	CH46	CH47	CH48	CH49	CH50	CH51	CH52	CH53	CH54	CH55	CH56	CH57	CH58	CH59	CH60	CH61	CH62	CH63	CH64	CH65	CH66	CH67	CH68	CH69	CH70	CH71	CH72	CH73	CH74	CH75	CH76	CH77	CH78	CH79	CH80	CH81	CH82	CH83	CH84	CH85	CH86	CH87	CH88	CH89	CH90	CH91	CH92	CH93	CH94	CH95	CH96	CH97	CH98	CH99	CH100	CH101	CH102	CH103	CH104	CH105	CH106	CH107	CH108	CH109	CH110	CH111	CH112	CH113	CH114	CH115	CH116	CH117	CH118	CH119	CH120	CH121	CH122	CH123	CH124	CH125	CH126	CH127	CH128	CH129	CH130	CH131	CH132	CH133	CH134	CH135	CH136	CH137	CH138	CH139	CH140	CH141	CH142	CH143	CH144	CH145	CH146	CH147	CH148	CH149	CH150	CH151	CH152	CH153	CH154	CH155	CH156	CH157	CH158	CH159	CH160	CH161	CH162	CH163	CH164	CH165	CH166	CH167	CH168	CH169	CH170	CH171	CH172	CH173	CH174	CH175	CH176	CH177	CH178	CH179	CH180	CH181	CH182	CH183	CH184	CH185	CH186	CH187	CH188	CH189	CH190	CH191	CH192	CH193	CH194	CH195	CH196	CH197	CH198	CH199	CH200	CH201	CH202	CH203	CH204	CH205	CH206	CH207	CH208	CH209	CH210	CH211	CH212	CH213	CH214	CH215	CH216	CH217	CH218	CH219	CH220	CH221	CH222	CH223	CH224	CH225	CH226	CH227	CH228	CH229	CH230	CH231	CH232	CH233	CH234	CH235	CH236	CH237	CH238	CH239	CH240	CH241	CH242	CH243	CH244	CH245	CH246	CH247	CH248	CH249	CH250	CH251	CH252	CH253	CH254	CH255	CH256	CH257	CH258	CH259	CH260	CH261	CH262	CH263	CH264	CH265	CH266	CH267	CH268	CH269	CH270	CH271	CH272	CH273	CH274	CH275	CH276	CH277	CH278	CH279	CH280	CH281	CH282	CH283	CH284	CH285	CH286	CH287	CH288	CH289	CH290	CH291	CH292	CH293	CH294	CH295	CH296	CH297	CH298	CH299	CH300	CH301	CH302	CH303	CH304	CH305	CH306	CH307	CH308	CH309	CH310	CH311	CH312	CH313	CH314	CH315	CH316	CH317	CH318	CH319	CH320	CH321	CH322	CH323	CH324	CH325	CH326	CH327	CH328	CH329	CH330	CH331	CH332	CH333	CH334	CH335	CH336	CH337	CH338	CH339	CH340	CH341	CH342	CH343	CH344	CH345	CH346	CH347	CH348	CH349	CH350	CH351	CH352	CH353	CH354	CH355	CH356	CH357	CH358	CH359	CH360	CH361	CH362	CH363	CH364	CH365	CH366	CH367	CH368	CH369	CH370	CH371	CH372	CH373	CH374	CH375	CH376	CH377	CH378	CH379	CH380	CH381	CH382	CH383	CH384	CH385	CH386	CH387	CH388	CH389	CH390	CH391	CH392	CH393	CH394	CH395	CH396	CH397	CH398	CH399	CH400	CH401	CH402	CH403	CH404	CH405	CH406	CH407	CH408	CH409	CH410	CH411	CH412	CH413	CH414	CH415	CH416	CH417	CH418	CH419	CH420	CH421	CH422	CH423	CH424	CH425	CH426	CH427	CH428	CH429	CH430	CH431	CH432	CH433	CH434	CH435	CH436	CH437	CH438	CH439	CH440	CH441	CH442	CH443	CH444	CH445	CH446	CH447	CH448	CH449	CH450	CH451	CH452	CH453	CH454	CH455	CH456	CH457	CH458	CH459	CH460	CH461	CH462	CH463	CH464	CH465	CH466	CH467	CH468	CH469	CH470	CH471	CH472	CH473	CH474	CH475	CH476	CH477	CH478	CH479	CH480	CH481	CH482	CH483	CH484	CH485	CH486	CH487	CH488	CH489	CH490	CH491	CH492	CH493	CH494	CH495	CH496	CH497	CH498	CH499	CH500	CH501	CH502	CH503	CH504	CH505	CH506	CH507	CH508	CH509	CH510	CH511	CH512	CH513	CH514	CH515	CH516	CH517	CH518	CH519	CH520	CH521	CH522	CH523	CH524	CH525	CH526	CH527	CH528	CH529	CH530	CH531	CH532	CH533	CH534	CH535	CH536	CH537	CH538	CH539	CH540	CH541	CH542	CH543	CH544	CH545	CH546	CH547	CH548	CH549	CH550	CH551	CH552	CH553	CH554	CH555	CH556	CH557	CH558	CH559	CH560	CH561	CH562	CH563	CH564	CH565	CH566	CH567	CH568	CH569	CH570	CH571	CH572	CH573	CH574	CH575	CH576	CH577	CH578	CH579	CH580	CH581	CH582	CH583	CH584	CH585	CH586	CH587	CH588	CH589	CH590	CH591	CH592	CH593	CH594	CH595	CH596	CH597	CH598	CH599	CH600	CH601	CH602	CH603	CH604	CH605	CH606	CH607	CH608	CH609	CH610	CH611	CH612	CH613	CH614	CH615	CH616	CH617	CH618	CH619	CH620	CH621	CH622	CH623	CH624	CH625	CH626	CH627	CH628	CH629	CH630	CH631	CH632	CH633	CH634	CH635	CH636	CH637	CH638	CH639	CH640	CH641	CH642	CH643	CH644	CH645	CH646	CH647	CH648	CH649	CH650	CH651	CH652	CH653	CH654	CH655	CH656	CH657	CH658	CH659	CH660	CH661	CH662	CH663	CH664	CH665	CH666	CH667	CH668	CH669	CH670	CH671	CH672	CH673	CH674	CH675	CH676	CH677	CH678	CH679	CH680	CH681	CH682	CH683	CH684	CH685	CH686	CH687	CH688	CH689	CH690	CH691	CH692	CH693	CH694	CH695	CH696	CH697	CH698	CH699	CH700	CH701	CH702	CH703	CH704	CH705	CH706	CH707	CH708	CH709	CH710	CH711	CH712	CH713	CH714	CH715	CH716	CH717	CH718	CH719	CH720	CH721	CH722	CH723	CH724	CH725	CH726	CH727	CH728	CH729	CH730	CH731	CH732	CH733	CH734	CH735	CH736	CH737	CH738	CH739	CH740	CH741	CH742	CH743	CH744	CH745	CH746	CH747	CH748	CH749	CH750	CH751	CH752	CH753	CH754	CH755	CH756	CH757	CH758	CH759	CH760	CH761	CH762	CH763	CH764	CH765	CH766	CH767	CH768	CH769	CH770	CH771	CH772	CH773	CH774	CH775	CH776	CH777	CH778	CH779	CH780	CH781	CH782	CH783	CH784	CH785	CH786	CH787	CH788	CH789	CH790	CH791	CH792	CH793	CH794	CH795	CH796	CH797	CH798	CH799	CH800	CH801	CH802	CH803	CH804	CH805	CH806	CH807	CH808	CH809	CH810	CH811	CH812	CH813	CH814	CH815	CH816	CH817	CH818	CH819	CH820	CH821	CH822	CH823	CH824	CH825	CH826	CH827	CH828	CH829	CH830	CH831	CH832	CH833	CH834	CH835	CH836	CH837	CH838	CH839	CH840	CH841	CH842	CH843	CH844	CH845	CH846	CH847	CH848	CH849	CH850	CH851	CH852	CH853	CH854	CH855	CH856	CH857	CH858	CH859	CH860	CH861	CH862	CH863	CH864	CH865	CH866	CH867	CH868	CH869	CH870	CH871	CH872	CH873	CH874	CH875	CH876	CH877	CH878	CH879	CH880	CH881	CH882	CH883	CH884	CH885	CH886	CH887	CH888	CH889	CH890	CH891	CH892	CH893	CH894	CH895	CH896	CH897	CH898	CH899	CH900	CH901	CH902	CH903	CH904	CH905	CH906	CH907	CH908	CH909	CH910	CH911	CH912	CH913	CH914	CH915	CH916	CH917	CH918	CH919	CH920	CH921	CH922	CH923	CH924	CH925	CH926	CH927	CH928	CH929	CH930	CH931	CH932	CH933	CH934	CH935	CH936	CH937	CH938	CH939	CH940	CH941	CH942	CH943	CH944	CH945	CH946	CH947	CH948	CH949	CH950	CH951	CH952	CH953	CH954	CH955	CH956	CH957	CH958	CH959	CH960	CH961	CH962	CH963	CH964	CH965	CH966	CH967	CH968	CH969	CH970	CH971	CH972	CH973	CH974	CH975	CH976	CH977	CH978	CH979	CH980	CH981	CH982	CH983	CH984	CH985	CH986	CH987	CH988	CH989	CH990	CH991	CH992	CH993	CH994	CH995	CH996	CH997	CH998	CH999	CH1000	CH1001	CH1002	CH1003	CH1004	CH1005	CH1006	CH1007	CH1008	CH1009	CH1010	CH1011	CH1012	CH1013	CH1014	CH1015	CH1016	CH1017	CH1018	CH1019	CH1020	CH1021	CH1022	CH1023	CH1024	CH1025	CH1026	CH1027	CH1028	CH1029	CH1030	CH1031	CH1032	CH1033	CH1034	CH1035	CH1036	CH1037	CH1038	CH1039	CH1040	CH1041	CH1042	CH1043	CH1044	CH1045	CH1046	CH1047	CH1048	CH1049	CH1050	CH1051	CH1052	CH1053	CH1054	CH1055	CH1056	CH1057	CH1058	CH1059	CH1060	CH1061	CH1062	CH1063	CH1064	CH1065	CH1066	CH1067	CH1068	CH1069	CH1070	CH1071	CH1072	CH1073	CH1074	CH1075	CH1076	CH1077	CH1078	CH1079	CH1080	CH1081	CH1082	CH1083	CH1084	CH1085	CH1086	CH1087	CH1088	CH1089	CH1090	CH1091	CH1092	CH1093	CH1094	CH1095	CH1096	CH1097	CH1098	CH1099	CH1100	CH1101	CH1102	CH1103	CH1104	CH1105	CH1106	CH1107	CH1108	CH1109	CH1110	CH1111	CH1112	CH1113	CH1114	CH1115	CH1116	CH1117	CH1118	CH1119	CH1120	CH1121	CH1122	CH1123	CH1124	CH1125	CH1126	CH1127	CH1128	CH1129	CH1130	CH1131	CH1132	CH1133	CH1134	CH1135	CH1136	CH1137	CH1138	CH1139	CH1140	CH1141	CH1142	CH1143	CH1144	CH1145	CH1146	CH1147	CH1148	CH1149	CH1150	CH1151	CH1152	CH1153	CH1154	CH1155	CH1156	CH1157	CH1158	CH1159	CH1160	CH1161	CH1162	CH1163	CH1164	CH1165	CH1166	CH1167	CH1168	CH1169	CH1170	CH1171	CH1172	CH1173	CH1174	CH1175	CH1176	CH1177	CH1178	CH1179	CH1180	CH1181	CH1182	CH1183	CH1184	CH1185	CH1186	CH1187	CH1188	CH1189	CH1190	CH1191	CH1192	CH1193	CH1194	CH1195	CH1196	CH1197	CH1198	CH1199	CH1200	CH1201	CH1202	CH1203	CH1204	CH1205	CH1206	CH1207	CH1208	CH1209	CH1210	CH1211	CH1212	CH1213	CH1214	CH1215	CH1216	CH1217	CH1218	CH1219	CH1220	CH1221	CH1222	CH1223	CH1224	CH1225	CH1226	CH1227	CH1228	CH1229	CH1230	CH1231	CH1232	CH1233	CH1234	CH1235	CH1236	CH1237	CH1238	CH1239	CH1240	CH1241	CH1242	CH1243	CH1244	CH1245	CH1246	CH1247	CH1248	CH1249	CH1250	CH1251	CH1252	CH1253	CH1254	CH1255	CH1256	CH1257	CH1258	CH1259	CH1260	CH1261	CH1262	CH1263	CH1264	CH1265	CH1266	CH1267	CH1268	CH1269	CH1270	CH1271	CH1272	CH1273	CH1274	CH1275	CH1276	CH1277	CH1278	CH1279	CH1280	CH1281	CH1282	CH1283	CH1284	CH1285	CH1286	CH1287	CH1288	CH1289	CH1290	CH1291	CH1292	CH1293	CH1294	CH1295	CH1296	CH1297	CH1298	CH1299	CH1300	CH1301	CH1302	CH1303	CH1304	CH1305	CH1306	CH1307	CH1308	CH1309	CH1310	CH1311	CH1312	CH1313	CH1314	CH1315	CH1316	CH1317	CH1318	CH1319	CH1320	CH1321	CH1322	CH1323	CH1324	CH1325	CH1326	CH1327	CH1328	CH1329	CH1330	CH1331	CH1332	CH1333	CH1334	CH1335	CH1336	CH1337	CH1338	CH1339	CH1340	CH1341	CH1342	

BOUNDARY SOLUTION FOR SAMPLES 3-6 COMPARED
WITH THEORETICAL EFFECT OF MYLAR SHIELD IN
WIDE ANGLE LEPS

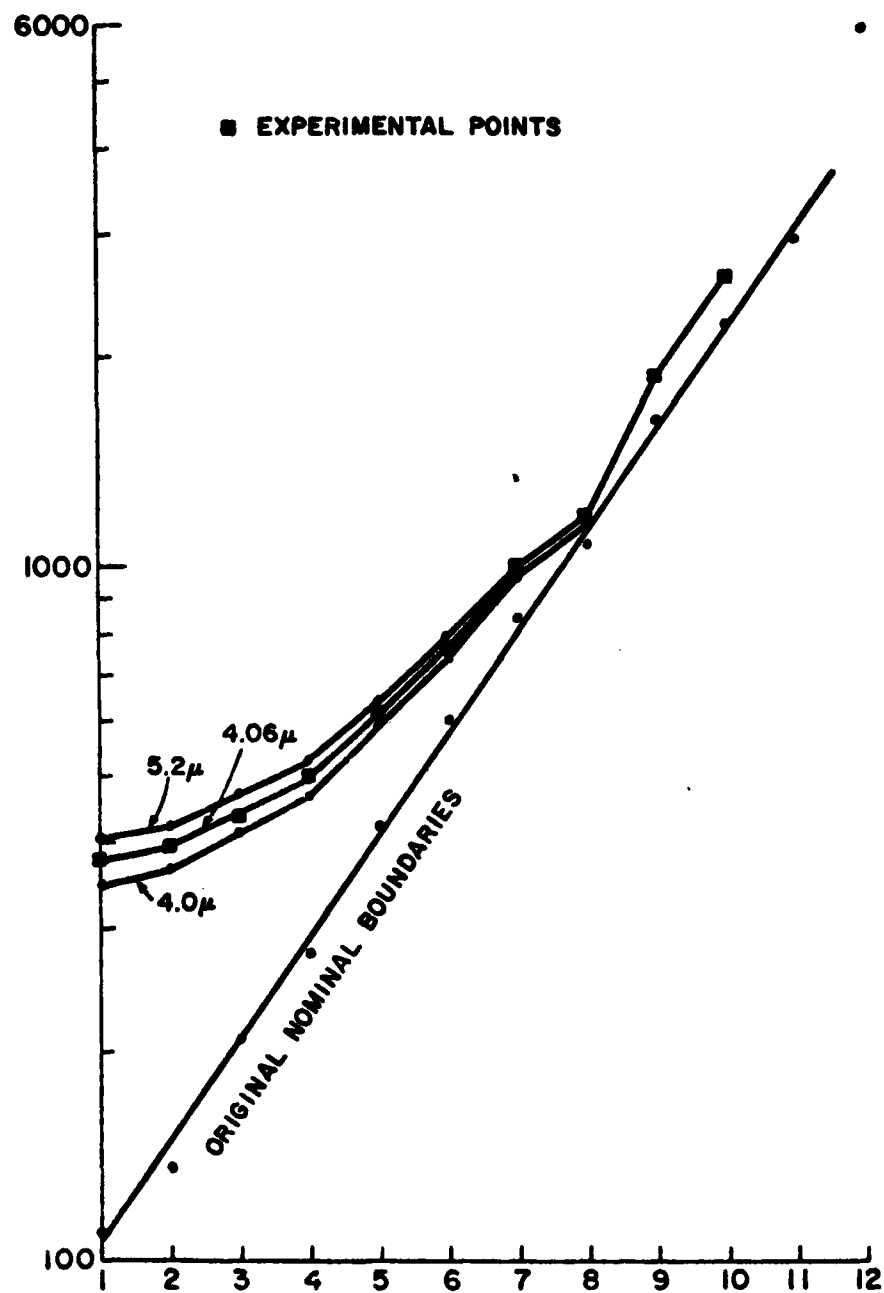


Fig. 1

BOUNDARY SOLUTIONS FOR HIGH COUNT RATE SAMPLES
WIDE ANGLE PLASTIC ABSORBER IS 4.6 MICRON MYLAR

ΔE VS. ENERGY $E_i = E_i + \Delta E_i$

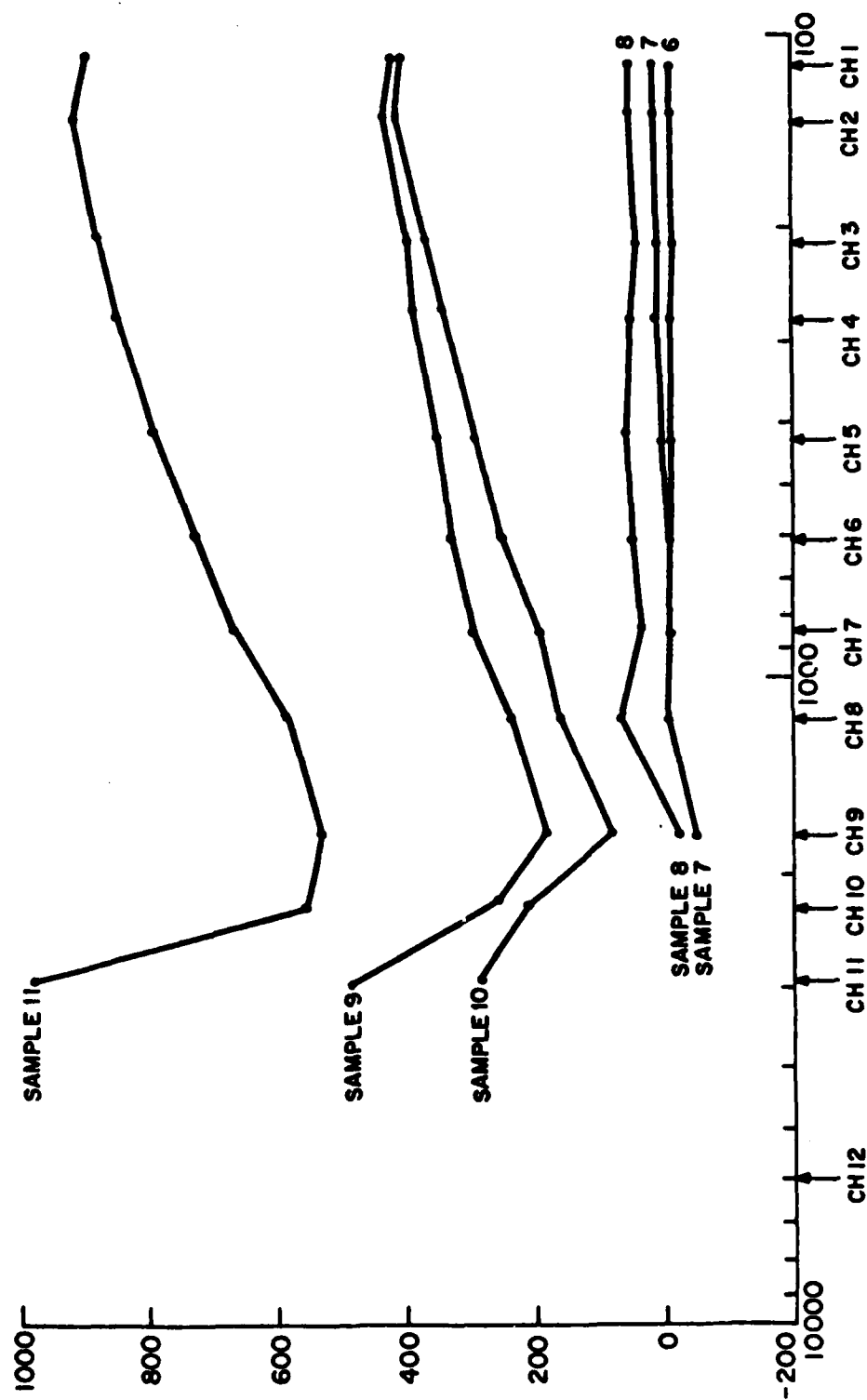


Fig. 2

PUBLICATIONS

Detection of low energy protons in CR-39 plastic track detector.
Y. V. Rao, A. Davis, R. C. Filz, P. McNulty and D. Shirkey
Bull. American Physical Soc., 24, 650, 1979.

Detection of protons in CR-39 plastic track detector.
Y. V. Rao, A. Davis, R. C. Filz, P. McNulty and D. Shirkey
Air Force Geophysics Laboratory Report No. AFGL-TR-79-0297, 1979.

Comment on confinement time of cosmic rays.
Y. V. Rao and R. C. Filz
Proc. 16th International Cosmic Ray Conference, Kyoto, 2, 212, 1979.

Calibration of CR-39 plastic track detector for heavy ions.
Y. V. Rao, A. Davis and R. C. Filz
Proc. 16th International Cosmic Ray Conference, Kyoto, 11, 96, 1979.

An experiment for measuring heavy cosmic ray spectra.
R. C. Filz, Y. V. Rao and A. Davis
Proc. 10th International Conference on Solid State Nuclear Track
Detectors, Lyon, Edited by H. Francois et al, page 1021, 1980.

A table of parameters for heavy ion tracks in CR-39 nuclear
track detector.
E. Holeman, T. Spencer, Y. V. Rao and M. P. Hagan
Air Force Geophysics Laboratory Report No. AFGL-TR-80-0035, 1980.

Detection of low energy protons and ^3He in CR-39 track detector.
Y. V. Rao, A. Davis, M. P. Hagan, R. C. Filz and J. Blue
Bull. American Physical Soc., 25, 484, 1980.

CR-39 plastic track detector experiment for measurement of charge
composition of primary cosmic rays.
Y. V. Rao, A. Davis, M. P. Hagan and R. C. Filz
Proc. IAU Symposium No. 94, Origin of Cosmic Rays, Bologna, Edited by
G. Setti, G. Spada and A. W. Wolfendale, D. Reidel Publishing Company,
Dordrecht, Holland, page 37, 1981.

Diameter evolution of proton tracks in CR-39 detector.
Y. V. Rao, A. Davis and R. C. Filz
Nucl. Instr. and Methods, 180, 153, 1981.

Application of CR-39 track detector for detection of protons; ^3He and ^4He ions.

Y. V. Rao, M. P. Hagan and J. Blue

Proc. 11th International Conference on Solid State Nuclear Track Detectors, Bristol, U.K., Edited by P. H. Fowler and V. M. Clapham, page 921, 1982.

Detection of 10-MeV protons, 70-MeV ^3He and 52-MeV ^4He ions in CR-39 track detector.

Y. V. Rao, M. P. Hagan and J. Blue

Nuclear Tracks, 6, No. 2, 1982.

0.1 - 100 MeV proton fluxes at the outer edge of the inner trapped region.

R. Filz and D.R. Parsignault

AGU, 1980.

Electron fluxes over the polar caps.

D.R. Parsignault

AGU, 1980.

A 13-year continuous decrease in the 8-25 MeV proton population at low L values.

D.R. Parsignault and E. Holeman

AGU, 1980.

The generalized geometrical factor of particle telescopes for trapped radiations.

P.S. Young, E.G. Holeman, D.R. Parsignault, M.P. Hagan, and R.C. Filz

1980

Solar cycle induced modulation of the 55-MeV proton fluxes at low altitudes.

D.R. Parsignault, E.G. Holeman, and R.C. Filz.

J. Geophys. Res., 86, 11439, 1981.

Long-term intensity decrease in the 8- to 25-MeV proton fluxes at low L values.

D.R. Parsignault, E.G. Holeman, and R.C. Filz

J. Geophys. Res., 86, 11447, 1981.

P. D. CLARK, D. C. WEISSER, The Australian National University.—Elastic and inelastic scattering angular distributions to the first excited states of ^{24}Mg and ^{28}Si were measured at $E_{\text{cm}} = 139$ MeV for $^{24}\text{Mg} + ^{208}\text{Pb}$ and at $E_{\text{cm}} = 145$ MeV for $^{28}\text{Si} + ^{208}\text{Pb}$ in the angular range from $0_{\text{cm}} = 10$ – 120° . The cross sections were analyzed using optical model and coupled channels calculations. These calculations utilized up to 250 partial waves. The exact calculations are compared to polarization potential calculations.¹ The extracted deformation lengths are compared with deformation lengths extracted from similar experiments using lighter projectiles and the scaling theory of Hendrie.²

*Supported in part by U. S. Department of Energy, Division of Chemical Sciences.

*Permanent Address: Kansas State University, Manhattan, Kansas 66506 USA. Supported in part by the U. S. National Science Foundation under the US-Australia Cooperative Science Program.

¹U. G. Love, T. Terrasawa and G. R. Satchler, *Nucl. Phys. A* **291**, 183 (1977).

²D. L. Hendrie, *Phys. Rev. Lett.* **31**, 478 (1973).

AF 15 An Investigation of γ -Ray and Out-of-Plane α -Particle Emission in the Heavy-Ion Reaction 670 MeV- $^{86}\text{Kr} + \text{natAg}$. G. J. WOZNIAK, L.G. SOBOTKA, G.U. NATTAZZI, C.C. HSU, S.K. BLAU, H. BOLOTIN, R.J. McDONALD A.J. PACHECO, and L.G. MORETTO, Lawrence Berkeley Laboratory.—To detect the projectile-like fragment and to define the reaction plane, a solid state ΔE -E telescope was used. To measure the out-of-plane correlation of the α -particles emitted from the target-like fragment, four ΔE -E telescopes were mounted on an arc on the opposite side of the beam axis along the recoil direction. The γ -ray multiplicity, M_γ , was measured with an array of 8 NaI detectors and moderate statistics triple coincidence (α - α - γ) data were obtained. The ratio of the in-plane to out-of-plane α -particle yields is approximately a factor of two. The dependence of the out-of-plane correlation on the reaction Q-value and on M_γ will be discussed. A comparison of the data with simple model calculations will be presented.

*Work supported by the Division of Nuclear Physics of the Office of High Energy and Nuclear Physics and by Nuclear Sciences of the Basic Energy Sciences Program of the U.S. Dept. of Energy under Contract No. W-7405-ENG-48.

SESSION AF: INSTRUMENTATION AND APPLICATIONS I

Monday morning, 28 April 1980

Annapolis Room, Sheraton Washington Hotel at 9:00 A.M.

H. Engle, presiding

AF 1 Emanation of Radon and Thoron from Fly Ash and Ceramics. GARY W. CARRIVEAU*, Metropolitan Museum of Art and Brookhaven National Laboratory and GABRIEL HARBOTTLE, Brookhaven National Laboratory. In the decay chains of uranium and thorium, the daughter product sequence goes through a gaseous phase (radon or thoron) approximately one-half way between the parent and the stable isotope of lead. The occurrence of gaseous escape (emanation) in some systems can seriously disrupt secular equilibrium. A simple technique for measuring radon and thoron emanation, through the determination of naturally emitted gamma rays, will be presented. Results will be given for two types of material: a) fly ash from coal fired power plants and b) ceramic shards. For the latter material, the effect of ground water on emanation suppression has been determined. Effects on environmental radiation and thermoluminescence. Dating calculations will be discussed.

* Guest Scientist, Chemistry Department, Brookhaven National Laboratory. Work at Brookhaven under contract with the U.S. Department of Energy and supported by its Division of Basic Energy Sciences.

AF 2 Processing of LMFB Test Fuel Pin Images.* M.L. BARNES, G.J. BERZINS, A.H. LUPKIN, J.M. POVELITES, Los Alamos Scientific Laboratory.**—The LASL Pinex system produces images of LMFB test fuel pins during transient power conditions at the TREAT reactor. Nuclear radiation emitted by the test section is imaged by single pinholes onto a scintillator. The resulting optical image on the scintillator is photographed with intensified TV cameras and stored on video recorder and film. The data are digitized into sets of 512×512 arrays. These images include a large background from the containment capsule as well as from ambient neutrons and gamma rays of the reactor core. During processing on a CDC 7600, the data are least squares smoothed, background subtracted, efficiency corrected and displayed in several representations. Results of such analysis demonstrate successful quantifying of fuel mass movement.

*Submitted by A. H. Lumpkin

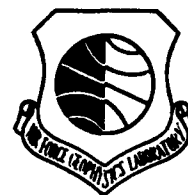
**Supported by DOE/RRT

AF 3 Tomography of an Irradiated Fast Reactor Fuel Pin. B. K. BARNES and R. L. PETTY, Los Alamos Scientific Laboratory.—A series of tomographic reconstructions have been made from betatron radiographs of an irradiated fast reactor fuel pin. Two hundred betatrons were made on a 20 MeV betatron at 1.8° intervals around the fuel pin. These were scanned for density at three axial locations using an automated scanning densitometer. The resulting six hundred density scans were used together with a filtered back projection tomographic algorithm to reconstruct an interior density image at three axial locations. The resulting reconstructions clearly show the cladding, the cladding-fuel gap, the enriched fuel inside the cladding, and melted fuel flow into the fuel cladding gap. This fuel flow was the artifact of interest which prompted the study. The interior details of the fuel (voids of varying sizes), however, evince a disappointing lack of agreement with metallographic sections taken at approximately the same locations. This lack of agreement will be discussed.

AF 4 Buffon Needle Method of Track Scanning at High Track Density.* R. GOLD, F. H. RUDDY, and J. H. ROBERTS, Westinghouse Hanford Company.—The observable invariably used for high accuracy Solid State Track Recorder (SSTR) applications is the track density, i.e. the number of tracks per unit area. Of the currently recognized limitations that exist in quantitative SSTR work, perhaps the most intrinsic is the high track density limitation produced by track pile-up. Hence, techniques which are capable of extending track scanning into the high density pile-up region would be quite useful. In particular, methods that can be applied independent of track size are highly desirable. To this end, the Buffon needle method of track scanning is advanced. This new method extends quantitative track scanning to track densities well up into the track pile-up regime. It is based on random sampling of the SSTR surface. This method has been applied to high fission track density mica SSTR observed with scanning electron microscopy. It is demonstrated that the Buffon needle method possesses a reduced dependence upon both source deposit non-uniformity and track size distribution. Sources of experimental error arising in the Buffon needle method are assessed.

*Work performed under the auspices of the U.S. Department of Energy and the U.S. Nuclear Regulatory Commission.

AF 5 Detection of Low Energy Protons in CR-39 Track Detector. Y. V. RAO, A. DAVIS and M. P. MAGAN, Emmanuel College, R. C. FILZ, AFGL and J. BLUM, NASA - LEVIS Research Center.—Samples of CR-39 plastic track detectors were irradiated with protons at NASA/Levins Cyclotron. Several incident beam energies in the range 6 MeV to 70 MeV were utilized for these irradiations. In this paper we discuss the registration characteristics of protons in CR-39 detector.



Detection of Protons in CR-39 Plastic Track Detector

**Y. V. RAO
A. DAVIS
R. C. FILZ
P. J. McNULTY
D. SHIRKEY**

11 December 1979

Approved for public release; distribution unlimited.

**SPACE PHYSICS DIVISION PROJECT 2311
AIR FORCE GEOPHYSICS LABORATORY
HANSCOM AFB, MASSACHUSETTS 01731**

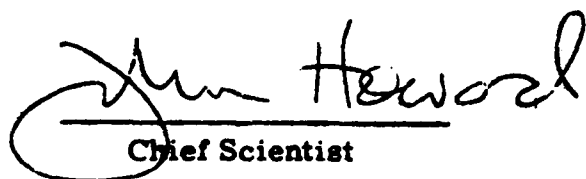
AIR FORCE SYSTEMS COMMAND, USAF



This report has been reviewed by the ESD Information Office (OI) and is releasable to the National Technical Information Service (NTIS).

This technical report has been reviewed and is approved for publication.

FOR THE COMMANDER


Chief Scientist

Qualified requestors may obtain additional copies from the Defense Documentation Center. All others should apply to the National Technical Information Service.

Unclassified

SECURITY CLASSIFICATION OF THIS PAGE (When Data Entered)

REPORT DOCUMENTATION PAGE		READ INSTRUCTIONS BEFORE COMPLETING FORM
1. REPORT NUMBER AFGL-TR-79-0297	2. GOVT ACCESSION NO.	3. RECIPIENT'S CATALOG NUMBER
4. TITLE (and Subtitle) DETECTION OF PROTONS IN CR-39* PLASTIC TRACK DETECTOR		5. TYPE OF REPORT & PERIOD COVERED Scientific. Interim.
		6. PERFORMING ORG. REPORT NUMBER ERP No. 688
7. AUTHOR(s) Y. V. Rao ** P. J. McNulty *** A. Davis ** D. Shirkey *** R. C. Filz		8. CONTRACT OR GRANT NUMBER(s)
9. PERFORMING ORGANIZATION NAME AND ADDRESS Air Force Geophysics Laboratory (PHG) Hanscom AFB Massachusetts 01731		10. PROGRAM ELEMENT, PROJECT, TASK AREA & WORK UNIT NUMBERS 61102F 2311G102
11. CONTROLLING OFFICE NAME AND ADDRESS Air Force Geophysics Laboratory (PHG) Hanscom AFB Massachusetts 01731		12. REPORT DATE 11 December 1979
		13. NUMBER OF PAGES 12
14. MONITORING AGENCY NAME & ADDRESS (if different from Controlling Office)		15. SECURITY CLASS. (of this report) Unclassified
		15a. DECLASSIFICATION/DOWNGRADING SCHEDULE
16. DISTRIBUTION STATEMENT (of this Report) Approved for public release, distribution unlimited.		
17. DISTRIBUTION STATEMENT (of the abstract entered in Block 20, if different from Report)		
18. SUPPLEMENTARY NOTES * Registered Trade Mark, Pittsburgh Plate Glass. ** Physics Research Division, Emmanuel College, Lexington, Mass. *** Physics Department, Clarkson College of Technology, Potsdam, N.Y.		
19. KEY WORDS (Continue on reverse side if necessary and identify by block number) Energetic proton detector Plastic track detector CR-39		
20. ABSTRACT (Continue on reverse side if necessary and identify by block number) CR-39 plastic is used as a detector to observe monoenergetic protons. Several samples of CR-39 were exposed to protons of energies 1.5 MeV, 2.2 MeV, 3.2 MeV and 4.3 MeV. After etching measurements were carried out on track diameters produced by protons in all samples. The diameter distributions clearly show an excellent energy resolution of protons of different energies. From our preliminary analysis of data, it appears that the response function for registering protons in CR-39 may be a lot less complicated than in cellulose nitrate.		

DD FORM 1 JAN 73 1473 EDITION OF 1 NOV 68 IS OBSOLETE

Unclassified

SECURITY CLASSIFICATION OF THIS PAGE (When Data Entered)

Preface

It is a pleasure to thank Drs. Norman Rohrig and Steve Marino of Brookhaven National Laboratory for help with proton irradiations.

Contents

1. INTRODUCTION	7
2. EXPERIMENTAL DETAILS	8
3. RESULTS	8

Illustrations

1. The Diameter Distribution of the Etch Pits of Protons (17 hour etch)	9
2. The Diameter Distribution of the Etch Pits of Protons (30 hour etch)	10
3. Etch Pit Diameter (D) as a Function of Proton Energy (E). The parameter on each curve represents etching time	10
4. Etch Pit Diameter (D) as a Function of Amount of Bulk Material Removed From One Surface (Vgt)	11
5. Tracks of 1.5 MeV Normal Incidence Protons in CR-39. The etching time was 30 hours	11
6. Tracks of 2.2 MeV Normal Incidence Protons in CR-39. The etching time was 30 hours	12

Detection of Protons in CR-39* Plastic Track Detector

1. INTRODUCTION

In recent years Solid State Nuclear Track Detectors have found widespread application.¹ The production of tracks by energetic ions in insulating materials is a widely used technique for detection and identification of these ions. The use of these detectors has been shown to be very successful in the study of very heavy primary cosmic rays and the recording of fission fragments. Also, there have been some investigations exploring the possibility of their application to detect protons. Cellulose Nitrate plastic has been employed as a detector to record protons, however, CN suffers from being inhomogeneous and anisotropic with regard to its physical characteristics. These defects manifest themselves in non-geometrical track profiles, differences in sensitivity in a given sheet, and variations in bulk etch rate. The use of plastic sheet cast from CR-39 monomer (allyl diglycol carbonate) with excellent etching properties, high sensitivity and high uniformity as a nuclear track detector was reported recently.² This material was found to

(Received for publication 3 December 1979)

*Registered Trade Mark, Pittsburgh Plate Glass.

1. Fleischer, R. L., Price, P. B., and Walker, R. M. (1975) Nuclear Tracks in Solids, University of California Press, Berkeley.
2. Cartwright, B. G., Shirk, E. K., and Price, P. B. (1978) Nucl. Instr. Methods 153:457.

have a lower detection threshold ($Z/\beta = 9$) than cellulose nitrate ($Z/\beta = 30$) and a smaller variation of response (~ 1 percent) to particles of a given ionization rate than Lexan polycarbonate (~ 3 to 8 percent). Commercially available CR-39 is capable of recording protons of 1 MeV and below as well as 6 MeV alpha particles. In this work, an attempt is made to investigate further the properties of CR-39 as a nuclear track detector with particular reference to the detection of protons.

2. EXPERIMENTAL DETAILS

For this study, Polytech CR-39 (1500 μ thick) was used. Samples of size (2.5 \times 2.5) cm were cut out and exposed to a beam of protons from the Van de Graaf generator at Brookhaven National Laboratory. The beam was tuned to four different energies (1.5 MeV, 2.2 MeV, 3.2 MeV and 4.3 MeV). The corresponding fluences were: 2.8×10^5 particles/cm², 0.44×10^6 particles/cm², 0.67×10^6 particles/cm² and 0.91×10^6 particles/cm². All irradiations were carried out in such a manner that particles are nearly normally incident to the surface of the plastic sheet. After irradiation the samples were etched in a solution of 6.25N NaOH at 50°C for different durations. The samples were suspended by means of nichrome wires in polyethylene vessels containing etchant. Temperature control was achieved by placing the polyethylene containers into a regulated water bath. Samples were selected from all four irradiations and etched in four different batches for 7 hours, 17 hours, 30 hours and 48 hours. In order to distinguish the background against tracks of protons, a virgin sample of CR-39 was always etched with each batch. All measurements were made on Koristka R4 microscope using 80 Zeiss objective and X10 wide field American Optical eyepiece. A total of 1000 tracks were measured to obtain data on track diameters.

3. RESULTS

In Figures 1 and 2 the distributions of track diameters for protons are shown. The sheets were etched for 17 hours and 30 hours. In the case of the 17 hour etch, there is some spread in track diameter distribution for 4.3 MeV protons. This may be of statistical nature and/or spread in the beam energy. The superior properties of CR-39 as a track detector is clearly demonstrated in Figure 2. Here, the energy resolution for protons is excellent. Once again the peak in track diameter distribution for 4.3 MeV protons is very broad. Figure 3 shows etch pit diameter as a function of proton energy. The samples etched for 48 hours show a maximum slope thereby indicating a better resolution. Figure 4 shows etch pit

diameter as a function of amount of bulk material removed from one surface. From our preliminary data, it appears that the dependence of etch pit diameter on the amount of bulk material removed from one surface seems to be less complicated than in CN. Particle identification by measurements of etch pit diameter was first suggested by Somogyi.³ Recently, Somogyi and Szalay⁴ discussed the kinetics of track diameter growth in considerable detail. In principle the method should work with particles incident at arbitrary angles on a solid surface, but in practice it is much simpler if the detector can be positioned such that particles are nearly normally incident. For tracks with large cone angles such as protons, the diameter is a more sensitive function of ionization rate than is track length. Finally, Figures 5 and 6 show tracks of 1.5 MeV and 2.2 MeV protons.

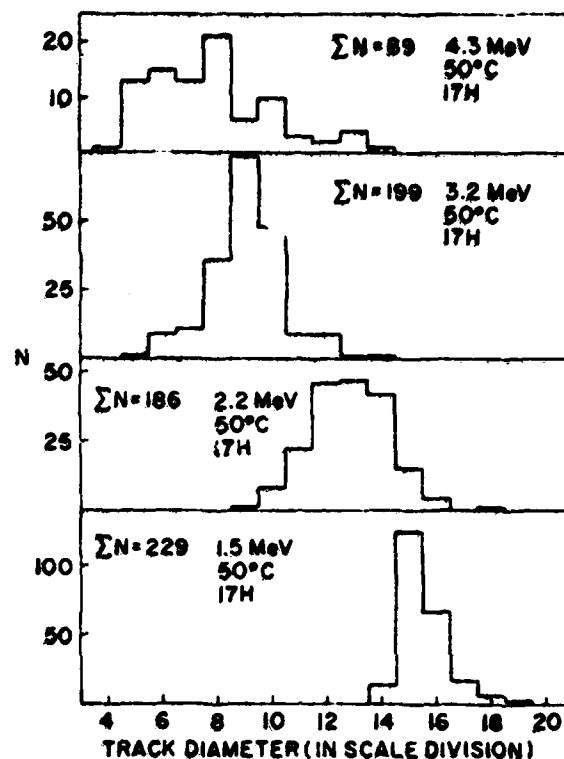


Figure 1. The Diameter Distribution of the Etch Pits of Protons (17 hour etch)

3. Somogyi, G. (1966) Nucl. Instr. Methods 42:312.

4. Somogyi, G., and Szalay, S. A. (1973) Nucl. Instr. Methods 109:211.

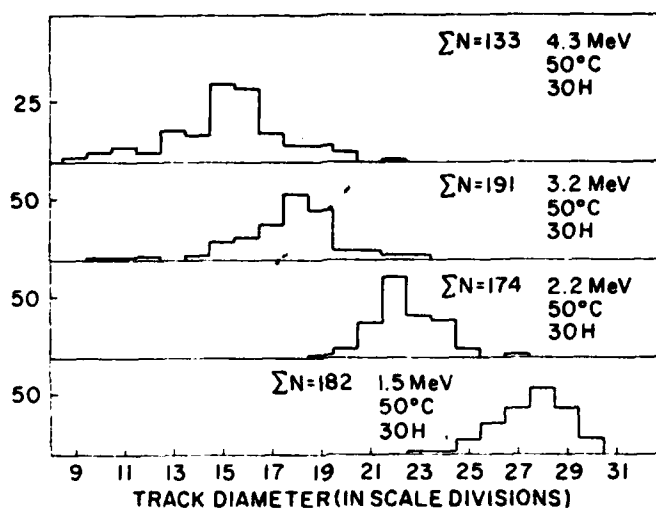


Figure 2. The Diameter Distribution of the Etch Pits of Protons (30 hour etch)

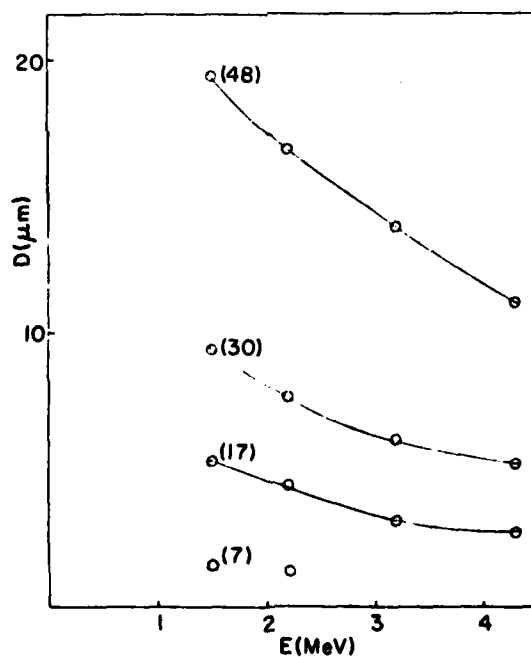


Figure 3. Etch Pit Diameter (D) as a Function of Proton Energy (E). The parameter on each curve represents etching time

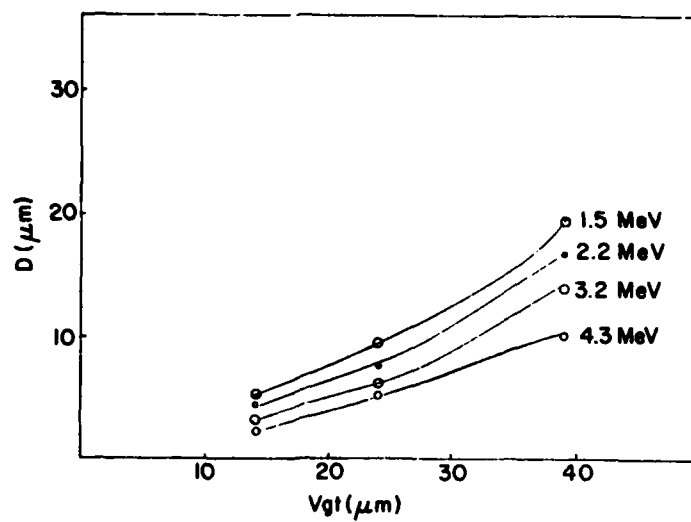


Figure 4. Etch Pit Diameter (D) as a Function of Amount of Bulk Material Removed From One Surface (Vgt)



Figure 5. Tracks of 1.5 MeV Normal Incidence Protons in CR-39. The etching time was 30 hours



Figure 6. Tracks of 2.2 MeV Normal Incidence Protons in CR-39. The etching time was 30 hours

COMMENT ON CONFINEMENT TIME OF COSMIC RAYS

Y. V. Rao

Physics Research Division, Emmanuel College, Lexington, Mass., USA.

R. Filz

AFGL, Hanscom Air Force Base, Bedford, Massachusetts, USA.

Theoretical ☒

Experimental ☐

Both ☐

The confinement time of cosmic rays is defined as the mean duration of time for which cosmic rays reside within the confinement volume of space. Recently several groups deduced the age of cosmic rays from Be^{10} abundance as well as from primary electron spectrum. The large abundance of nuclides with $Z > 90$ relative to the Pb group or the Pt group has been interpreted as implying the survival of some transuranic nuclides and thus a recent nucleosynthesis ($T \approx 10^7$ years). Thus the ratios of Pb-peak/Pt-peak and $Z > 90$ /Pb-peak can be used to deduce the lifetime of cosmic rays. In this paper we discuss the lifetime of cosmic rays obtained from these ratios and compare the values with Be and primary electron data.

Coordinates: OG 9.3

Mailing Address: Dr. Y. V. Rao
Physics Research Division
Emmanuel College
442 Marrett Road
Lexington, Massachusetts 02173, USA.

CALIBRATION OF CR-39 PLASTIC DETECTOR FOR HEAVY IONS

R. Filz

AFGL, Hanscom Air Force Base, Bedford, Massachusetts, USA.

A. Davis and Y. V. Rao

Physics Research Division, Emmanuel College, Lexington, Mass., USA.

Theoretical ☐

Experimental ☒

Both ☐

The use of plastic sheet cast from CR-39 monomer as a nuclear track detector was reported recently. This material was found to have a high sensitivity, lower detection threshold and a smaller variation of response to particles of a given ionization rate. Stacks consisting of CR-39 plastic were irradiated with high energy heavy ions at Berkeley Bevatron. We present results on calibration of this detector.

Coordinates: T.3

(Detectors for charge, mass, energy of primary cosmic ray particles)

Mailing Address: Dr. Y. V. Rao
Physics Research Division
Emmanuel College
442 Marrett Road
Lexington, Massachusetts 02173, USA.

Reprinted from
SOLID STATE NUCLEAR TRACK DETECTORS
Edited by
H. FRANCOIS *et al*
PERGAMON PRESS OXFORD and NEW YORK 1980

AN EXPERIMENT FOR MEASURING HEAVY COSMIC RAY SPECTRA

R. Filz*, Y. V. Rao** and A. Davis**

*AFGL, Hanscom Air Force Base, Bedford, Mass., U.S.A.

**Emmanuel College Physics Research Division, Lexington, Mass., U.S.A.

ABSTRACT

A balloon borne experiment consisting of 1 m² passive detector array has been designed in order to measure charge and energy spectra of primary cosmic rays and isotopic composition in the region of Fe peak. The stack profile consists of 65 sheets of CR-39 plastic track detector, three layers of 600 micron thick G5 emulsions at appropriate depth in the stack and twenty layers of Lexan polycarbonate plastic. The payload was flown successfully in June 1979 from Eielson Air Force Base, Alaska. The flight description and calibration of CR-39 track detector will be discussed.

KEYWORDS

Cosmic rays; nuclear composition; isotopes; tracks in plastics; detectors for charge; mass; energy of primary cosmic ray particles.

INTRODUCTION

A study of the relative abundances and energy spectra of heavy cosmic rays and isotopic composition in the region of Fe peak can yield significant information concerning the origin, acceleration and interstellar propagation. The relative abundances of the Fe isotopes measured near earth are of great astrophysical significance since isotopic composition of heavy cosmic ray nuclei is almost independent of the models of propagation and acceleration and such studies would lead to a better understanding of the nuclear processes in the source regions. In recent years solid state nuclear track detectors have been employed extensively to study heavy primary cosmic rays. Also it has been demonstrated that, at present, plastic track detectors present the best possibility of obtaining isotopic composition of heavy cosmic rays. In addition they have necessary large geometric factors for those heavy particles and a continuous sensitivity for the duration of an extended exposure. In the light of this, we designed a 1 m² passive detector array for exposure to cosmic radiation. Included in the array is a new type of nuclear track recording plastic, a polymer made from the monomer allyl diglycol carbonate (commercially known as CR-39). The track recording features of this plastic, viz., high sensitivity and high uniformity coupled with excellent etching properties

were recognized primarily by the workers at University of California, Berkeley (Cartwright, Shirk and Price, 1978). Recently (Rao and others, 1979) it has been shown that CR-39 plastic detector can be used as a detector to observe monoenergetic protons with energies up to 4.3 MeV. In this paper we report the details of our balloon borne experiment utilizing CR-39 as a detector.

PAYLOAD AND BALLOON FLIGHT

The stack was built as a set of nine modules where a module is essentially an aluminum box with dimensions (30x30x12) cm. We adopted three types of stack assembly for these modules; one consisting of 'pure' CR-39, the next one, a composite assembly of CR-39 with three layers of 600 micron thick G5 emulsions at appropriate depth in the stack and, the last one consisting of CR-39 and Lexan polycarbonate plastic. All three types are shown schematically in Fig. 1. The detector was exposed to the cosmic radiation aboard a balloon launched from Eielson Air Force Base, Alaska on June 19, 1979. A squib was fired to allow a spring loaded sliding plate to shift to a new position. This operation was successful and cosmic ray particles which penetrated at float altitude to the main stack below can be separated from particles which penetrated during the ascent phase. An attempt to stabilize and orient the payload utilizing a biaxial magnetometer combined with an electrical rotator was unsuccessful. The failure to orient the payload in a stable position would prevent us from determining the true direction of each cosmic ray particle and trace it backwards through the earth's magnetic field utilizing a computer tracing programme. The flight duration at float altitude and average ceiling were 3 hours 30 min and 3 g/cm² respectively.

NUCLEAR INTERACTIONS

In order to estimate nuclear interaction lengths (λ) of primary cosmic particles

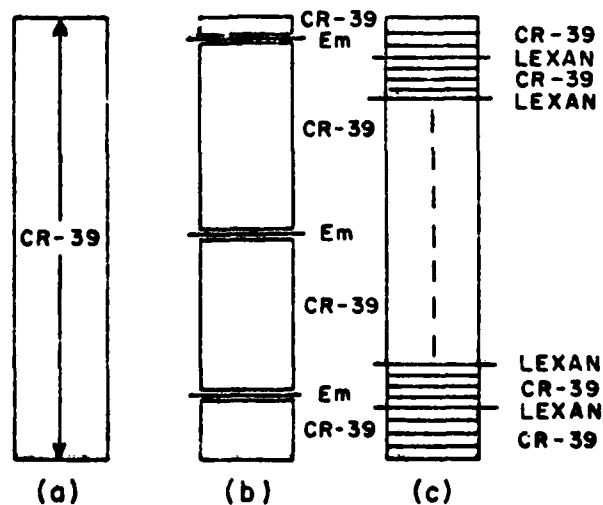


Fig. 1. Schematic diagram of the stack.

in CR-39, we used the overlap model of Bradt and Peters (1948) where λ is given by

$$\lambda = \frac{1}{\sum_i n_i \sigma_i} \quad (1)$$

where n_i is the number of atoms of the i th constituent of the medium per unit mass and σ_i is the nuclear interaction cross-section of the i th constituent and is given by

$$\sigma_i = \pi r_0^2 (A^{1/3} + A_i^{1/3} - 1)^2 \quad (2)$$

Here A_i is the atomic weight of the i th constituent,
 A is the atomic weight of the incident particle,
 $r_0 = 1.4$ fermis.

Figure 2 shows the interaction lengths for a range of incident particle atomic weights in CR-39 and lead.

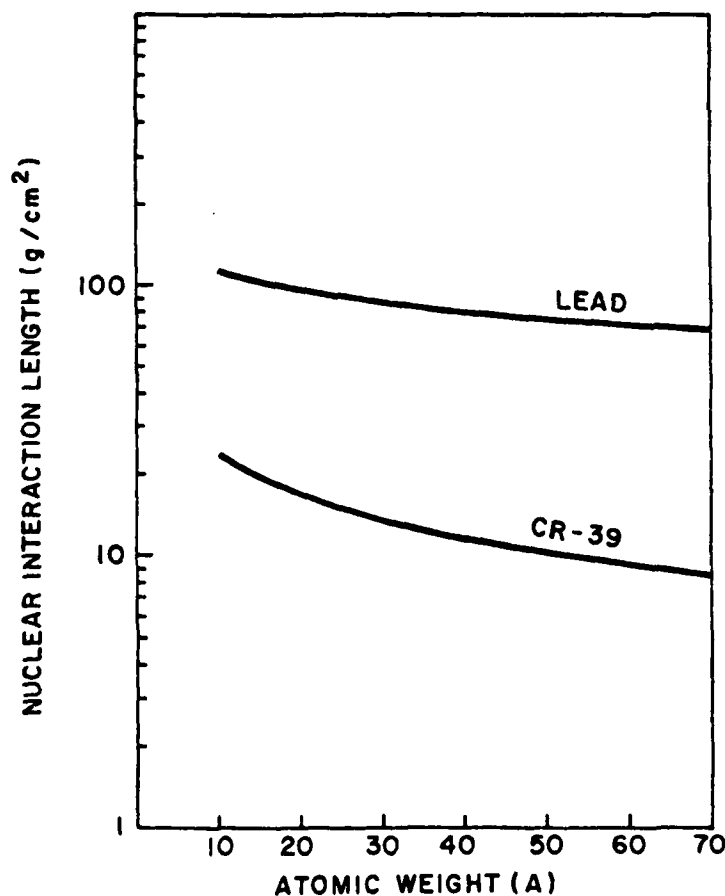


Fig. 2. Nuclear interaction lengths of nuclei in CR-39 and lead.

PROCESSING OF THE STACK AND PROCEDURE FOR CHARGE DETERMINATION

All nuclear emulsions, included in the stack for comparative purposes, have been developed. The plastic track detectors will be chemically processed to determine the track etching rate and residual range of each iron group nuclei. Our method of charge and mass identification depends on the mechanism whereby cosmic ray nuclei that penetrate the CR-39 plastic sheets produce radiation damage along the particle trajectory. Thus, the track etching rate is a unique function of the particle ionization. Identification will be based on the assumed relationship between etching rate (V_T) and ionization (J) of the form

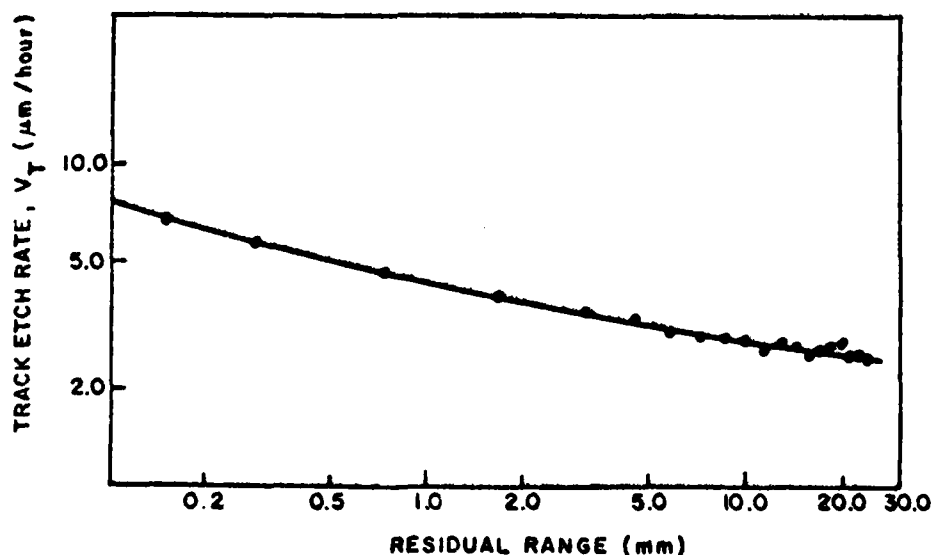
$$V_T = AJ^n \quad (3)$$

where

$$J = (Z_{eff}^2/\beta^2)[K + 2\ln(\beta\gamma) - \beta^2 - \delta(\beta)]$$

and the constants A and n are determined experimentally by calibration of the detector. The quantity $\delta(\beta)$ is the Sternheimer function.

To calibrate CR-39 plastic track detector, we exposed two stacks to a beam of 210 MeV/amu Ca^{48} ions at the Berkeley Bevatron. Our preliminary results suggest that the response of CR-39 to Ca ions can be represented as a function of $V_T = Z_{eff}^5/\beta^5$. Figure 3 shows the etch rate as a function of residual range for these ions.



ACKNOWLEDGEMENT

We wish to express our gratitude to Dr. John M. Kidd of Naval Research Laboratory, Washington, D.C. for exposing our stacks at the Berkeley Bevatron. We want to thank Tom Daneher of AFGL for arranging the balloon flight on short notice, Arthur Korn of AFGL for his design efforts and Mr. John Ground and members of the staff of New Mexico State University Physical Sciences Laboratory and AFGL personnel who participated in the actual flight operations.

REFERENCES

- Bradt, H.L., and B. Peters (1948). Phys. Rev., 74, 1828.
Cartwright, B.G., E.K. Shirk, and P.B. Price (1978). Nucl. Instr. and Methods, 153, 457-460.
Rao, Y.V., A. Davis, R.C. Filz, P.J. McNulty, and D. Shirkey (1979). Bull. American Physical Society, 24, 650.

AFGL-TR-80-0035

A Table of Parameters for Heavy Ion Tracks in CR-39 Nuclear Track Detector

E. Holeman
T. Spencer
Y.V. Rao
M.P. Hagan

The Trustees of Emmanuel College
400 The Fenway
Boston Massachusetts 02115

January 1980

Scientific Report No. 1

Approved for public release; distribution unlimited.

Air Force Geophysics Laboratory
Air Force Systems Command
United States Air Force
Hanscom AFB Massachusetts 01731

Qualified requestors may obtain additional copies from the Defense Documentation Center. All others should apply to the National Technical Information Service.

UNCLASSIFIED

MIL-STD-847A
31 January 1973

SECURITY CLASSIFICATION OF THIS PAGE (When Data Entered)

REPORT DOCUMENTATION PAGE		READ INSTRUCTIONS BEFORE COMPLETING FORM
1. REPORT NUMBER AFGL-TR-80-0035	2. GOVT ACCESSION NO.	3. RECIPIENT'S CATALOG NUMBER
4. TITLE (and Subtitle) A Table of Parameters for Heavy Ion Tracks in CR-39 Nuclear Track Detector		5. TYPE OF REPORT & PERIOD COVERED Scientific No. 1 01 APR 79 - 31 DEC 79
		6. PERFORMING ORG. REPORT NUMBER
7. AUTHOR(s) E. Holeman Y.V. Rao T. Spencer M.P. Hagan		8. CONTRACT OR GRANT NUMBER(s) F19628-79-C-0102
9. PERFORMING ORGANIZATION NAME AND ADDRESS Emmanuel College 400 The Fenway Boston MA 02115		10. PROGRAM ELEMENT PROJECT, TASK AREA & WORK UNIT NUMBERS 61102F 2311G1AK
11. CONTROLLING OFFICE NAME AND ADDRESS Air Force Geophysics Laboratory Hanscom AFB MA 01731 PHG Contract Monitor: Robert O. Hutchinson/		12. REPORT DATE
14. MONITORING AGENCY NAME & ADDRESS (if different from Controlling Office)		13. NUMBER OF PAGES 38
		15. SECURITY CLASS (of this report) UNCLASSIFIED
		16. DECLASSIFICATION DOWNGRADING SCHEDULE
16. DISTRIBUTION STATEMENT (of this Report) A - Approved for public release; distribution unlimited		
17. DISTRIBUTION STATEMENT (of the abstract entered in Block 20, if different from Report) TECH, OTHER		
18. SUPPLEMENTARY NOTES		
19. KEY WORDS (Continue on reverse side if necessary and identify by block number) Cosmic Rays Kinetic Energy per Nucleon Heavy Ion Tracks Effective Charge CR-39 Nuclear Track Detector Energy Loss Residual Ranges		
20. ABSTRACT (Continue on reverse side if necessary and identify by block number) A number of parameters that are generally used for the analysis of the heavy ion tracks in CR-39 Nuclear Track Detector have been computed. The parameters are: Residual Range(R), Velocity ($\beta=V/c$), Kinetic Energy per Nucleon ($e/\text{nucleon}$), Effective Charge (z_{eff}) and Energy Loss of		

DD FORM 1473 EDITION OF 1 NOV 65 IS OBSOLETE

UNCLASSIFIED

SECURITY CLASSIFICATION OF THIS PAGE (When Data Entered)

UNCLASSIFIED

SECURITY CLASSIFICATION OF THIS PAGE (When Data Entered)

20. heavy ions (dE/dx). The computation has been performed for isotopes of interest in cosmic ray work, with charges in the region $2 \leq z \leq 30$ and for residual range, $R \leq 30\text{cm}$.

UNCLASSIFIED

SECURITY CLASSIFICATION OF THIS PAGE (When Data Entered)

Introduction:

A knowledge of accurate range-energy relations for charged particles is an essential requirement in the use of a nuclear track detector. This report presents computed track parameters that are normally used for the analysis of the heavy ion tracks in CR-39 Nuclear Track Detector. Computation has been performed for tracks of isotopes in the charge region $2 \leq z \leq 30$.

In any Nuclear Track Detector, the residual range of a stopping particle is a very easily measured quantity. We have therefore used the residual range as the first entry in the track parameter table (Printout Table I). The corresponding velocity is given in the second column. The velocity provides a link with the rest of the parameters. All the entries in a row are interdependent and the table will give the value of these parameters if any one is known. The calculations are based on theoretical and empirical relations which can be found in earlier works¹⁻³.

Appendix I gives a brief description of CR-39 nuclear track detector and a number of constants relating to composition of the detector. In Appendix II (Printout Table I) are listed a few quantities that are generally used in calculations on relativistic ions.

Description of Formulae:

i) Residual Range:

The residual range R , of a heavy ion with charge z and mass M for a certain velocity, β , can be determined by the general expression given by Heckman et al¹⁾

$$R = \frac{M}{z^2} \left[\lambda(\beta) + B_z(\beta) \right] \quad \dots \quad (1)$$

Where $\lambda(\beta)$ is the range of the ideal proton as a function of its velocity. The function $B_z(\beta)$ corrects for the extension in range of an ion owing to charge-pickup at low velocities. In practice the quantity $B_z(\beta)$ is obtained by scaling the corresponding experimental expression for emulsion to other materials.

ii) Kinetic Energy:

The kinetic energy per nucleon, E , for an ion of mass M and mass number A with a velocity β is given by

$$E = M m_p c^2 (\gamma - 1) \quad \dots \quad (2)$$

where

$$\gamma = (1 - \beta^2)^{-1/2}$$

$$M = \frac{A}{1.008}$$

and m_p is rest mass of proton.

iii) Effective Charge:

The effective charge, z_{eff} , of an ion of atomic number z and with a velocity β can be expressed as

$$z_{\text{eff}} = z \left[1 - \exp(-130\beta z^{-2/3}) \right] \quad \dots \quad (3)$$

iv) Energy Loss:

The rate of loss of energy for an ion with effective charge, z_{eff} ,

and velocity β is given by

$$dE/dx = \frac{2\pi n z_{\text{eff}}^2 r_o^2 m_o c^2}{\beta^2} \left[\ln \frac{2m_o c^2 \beta^2 \gamma^2 W_{\text{max}}^2}{I_{\text{adj}}^2} - 2\beta^2 - 2c/Z - \delta^2 \right] \dots (4)$$

where

n = the electron density in the stopping medium

m = the mass of an electron

r_o = $e^2/m_o c^2$, the classical electron radius

I_{adj} = the mean ionization potential of the atoms of the stopping medium

W_{max} = the maximum energy transfer from the incident particle to the atomic electron

c/Z = tight binding shell correction, and

δ = a correction term which accounts for the density effect at high velocities.

Appendix I

CR-39 allyl diglycol carbonate is a colorless, liquid organic ester of low volatility and low viscosity⁴⁾. It is miscible or compatible with a wide variety of solvents, plasticizers and resinuous or plastic materials. If heated with a polymerization catalyst such as benzoyl peroxide, the liquid gradually thickens to form a soft gel. With further heating, the gel hardens into a insoluble, clear colorless solid. Because of its unique combination of properties, such as high abrasion resistance, clarity and low color, combined with solvent and temperature resistance, polymeric CR-39 is useful in the form of clear sheets. So far the main uses of CR-39 plastics have been as eye wear lenses and instrument gauge covers. Examples of other uses include glazing, safety shields and guards, navigation equipment, laboratory equipment and photographic filters.

In recent years solid state nuclear track detectors have found widespread application⁵⁾. The production of tracks by energetic ions in insulating materials is a widely used technique for detection and identification of ions. Their utilization showed to be very successful in the study of very heavy primary cosmic rays, recording of fission fragments and innumerable applications in the studies on radiation dosimetry. Also, there have been some investigations exploring the possibility of their application to detect protons.

The use of plastic sheet cast from CR-39 monomer with excellent etching properties, high sensitivity and high uniformity as a nuclear track detector was reported recently⁶⁾. This material was found to have

a lower detection threshold ($z/\beta = 9$) than cellulose nitrate ($z/\beta = 20$) and a smaller variation of response ($\sim 1\%$) to particles of a given ionization rate than lexan polycarbonate (~ 3 to 8%). Commercially available CR-39 is capable of recording protons of 1 MeV and below as well as 6 MeV alpha particles. Recently, it has been shown that CR-39 plastic can be used as a detector to observe monoenergetic protons with energies up to 4.3 MeV⁷⁾.

Constants for CR-39 Detector:

Density	1.32 gm/cm ³
Effective A/Z	1.877

PRINTOUT TABLE I

Velocity (β), Energy (E , MeV/amu), Effective Charge (z_{eff}), Rate of Loss
of Energy (dE/dx , MeV/cm) as a function of Heavy Ion Range (R , cm)

RANGE -ENERGY DATA FOR CR-39

ION IS 1 P 1				
RANGE (CM)	BETA (V/C)	ENERGY (MEV/AMU)	ZEFF	DE/DX MEV/CM
.0025	.0506	1.2	.999	300.008
.0050	.0625	1.8	1.000	224.375
.0075	.0707	2.3	1.000	187.875
.0100	.0770	2.8	1.000	165.066
.0200	.0942	4.2	1.000	119.956
.0300	.1057	5.2	1.000	99.066
.0400	.1145	6.2	1.000	86.768
.0500	.1218	7.0	1.000	78.592
.0600	.1280	7.7	1.000	72.485
.0700	.1335	8.4	1.000	67.695
.0800	.1384	9.0	1.000	63.806
.0900	.1428	9.6	1.000	60.565
.1000	.1471	10.2	1.000	57.675
.1500	.1644	12.8	1.000	47.842
.2000	.1778	15.1	1.000	41.907
.3000	.1984	18.9	1.000	34.789
.4000	.2142	22.1	1.000	30.502
.5000	.2273	25.0	1.000	27.555
.6000	.2385	27.7	1.000	25.368
.7000	.2484	30.1	1.000	23.661
.8000	.2572	32.4	1.000	22.280
.9000	.2652	34.6	1.000	21.133
1.0000	.2726	36.6	1.000	20.159
1.5000	.3026	45.8	1.000	16.837
2.0000	.3257	53.7	1.000	14.841
2.5000	.3446	60.8	1.000	13.470
3.0000	.3607	67.2	1.000	12.454
3.5000	.3749	73.2	1.000	11.661
4.0000	.3875	78.9	1.000	11.019
5.0000	.4093	89.4	1.000	10.035
6.0000	.4279	99.1	1.000	9.305
7.0000	.4440	108.1	1.000	8.735
8.0000	.4584	116.6	1.000	8.275
9.0000	.4714	124.6	1.000	7.892
10.0000	.4832	132.4	1.000	7.568
15.0000	.5303	167.2	1.000	6.462
20.0000	.5653	197.7	1.000	5.798
30.0000	.6164	251.3	1.000	5.007

ION IS 2 HE 3				
RANGE (CM)	BETA (V/C)	ENERGY (MEV/AMU)	ZEFF	DE/DX MEV/CM
.0025	.0545	1.4	1.977	1085.157
.0050	.0677	2.1	1.992	799.705
.0075	.0767	2.7	1.996	664.619
.0100	.0835	3.3	1.998	581.947
.0200	.1021	4.9	2.000	420.131
.0300	.1144	6.2	2.000	347.628
.0400	.1239	7.2	2.000	305.860
.0500	.1317	8.2	2.000	276.970
.0600	.1383	9.0	2.000	255.431
.0700	.1442	9.8	2.000	233.326
.0800	.1497	10.6	2.000	224.074
.0900	.1546	11.3	2.000	212.215
.1000	.1592	12.0	2.000	202.142
.1500	.1778	15.1	2.000	167.683
.2000	.1922	17.7	2.000	146.912
.3000	.2142	22.1	2.000	122.027
.4000	.2312	25.9	2.000	107.050
.5000	.2452	29.3	2.000	96.761
.6000	.2572	32.4	2.000	89.128
.7000	.2677	35.3	2.000	83.170
.8000	.2772	38.0	2.000	78.351
.9000	.2857	40.5	2.000	74.348
1.0000	.2936	42.9	2.000	70.952
1.5000	.3257	53.7	2.000	59.365
2.0000	.3502	63.0	2.000	52.403
2.5000	.3703	71.3	2.000	47.623
3.0000	.3875	78.9	2.000	44.079
3.5000	.4025	86.0	2.000	41.313
4.0000	.4158	92.7	2.000	39.077
5.0000	.4389	105.1	2.000	35.644
6.0000	.4584	116.6	2.000	33.099
7.0000	.4754	127.3	2.000	31.114
8.0000	.4905	137.4	2.000	29.509
9.0000	.5040	147.0	2.000	28.175
10.0000	.5163	156.2	2.000	27.045
15.0000	.5653	197.7	2.000	23.194
20.0000	.6014	234.3	2.000	20.885
30.0000	.6534	298.9	2.000	18.139

ION IS 2 HE 4				
RANGE (CM)	BETA (V/C)	ENERGY (MEV/AMU)	ZEFF	DE/DX MEV/CM
.0025	.0497	1.1	1.966	1229.573
.0050	.0620	1.8	1.988	908.803
.0075	.0702	2.3	1.994	758.046
.0100	.0767	2.7	1.996	664.619
.0200	.0940	4.1	1.999	481.449
.0300	.1056	5.2	2.000	397.173
.0400	.1144	6.2	2.000	347.628
.0500	.1217	7.0	2.000	314.771
.0600	.1279	7.7	2.000	290.250
.0700	.1334	8.4	2.000	271.030
.0800	.1383	9.0	2.000	255.431
.0900	.1427	9.6	2.000	242.436
.1000	.1470	10.2	2.000	230.853
.1500	.1644	12.8	2.000	191.452
.2000	.1778	15.1	2.000	167.683
.3000	.1984	18.9	2.000	139.187
.4000	.2142	22.1	2.000	122.027
.5000	.2273	25.0	2.000	110.235
.6000	.2385	27.7	2.000	101.484
.7000	.2483	30.1	2.000	94.653
.8000	.2572	32.4	2.000	89.128
.9000	.2652	34.6	2.000	84.537
1.0000	.2726	36.6	2.000	80.642
1.5000	.3026	45.8	2.000	67.352
2.0000	.3257	53.7	2.000	59.365
2.5000	.3446	60.8	2.000	53.882
3.0000	.3607	67.2	2.000	49.816
3.5000	.3749	73.2	2.000	46.644
4.0000	.3875	78.9	2.000	44.079
5.0000	.4093	89.4	2.000	40.140
6.0000	.4279	99.1	2.000	37.220
7.0000	.4440	108.1	2.000	34.941
8.0000	.4584	116.6	2.000	33.099
9.0000	.4714	124.6	2.000	31.569
10.0000	.4832	132.4	2.000	30.272
15.0000	.5303	167.2	2.000	25.848
20.0000	.5653	197.7	2.000	23.194
30.0000	.6164	251.3	2.000	20.030

ION IS 3 LI 6				
RANGE (CM)	BETA (V/C)	ENERGY (MEV/AMU)	ZEFF	DE/DX MEV/CM
.0025	.0550	1.4	2.903	2412.375
.0050	.0693	2.2	2.960	1741.232
.0075	.0787	2.9	2.978	1436.249
.0100	.0859	3.5	2.986	1252.628
.0200	.1052	5.2	2.996	898.425
.0300	.1180	6.5	2.998	744.688
.0400	.1277	7.7	2.999	654.683
.0500	.1358	8.7	2.999	592.589
.0600	.1426	9.6	3.000	546.378
.0700	.1489	10.5	3.000	508.593
.0800	.1545	11.3	3.000	478.097
.0900	.1596	12.1	3.000	452.737
.1000	.1643	12.8	3.000	431.208
.1500	.1835	16.1	3.000	357.630
.2000	.1983	18.9	3.000	313.329
.3000	.2210	23.6	3.000	260.295
.4000	.2384	27.7	3.000	228.396
.5000	.2528	31.3	3.000	206.489
.6000	.2652	34.6	3.000	190.239
.7000	.2760	37.6	3.000	177.559
.8000	.2857	40.5	3.000	167.303
.9000	.2945	43.2	3.000	158.784
1.0000	.3026	45.8	3.000	151.558
1.5000	.3355	57.3	3.000	126.905
2.0000	.3607	67.2	3.000	112.092
2.5000	.3813	76.1	3.000	101.924
3.0000	.3989	84.3	3.000	94.385
3.5000	.4142	91.9	3.000	88.503
4.0000	.4279	99.1	3.000	83.746
5.0000	.4514	112.4	3.000	76.445
6.0000	.4714	124.6	3.000	71.031
7.0000	.4887	136.1	3.000	66.809
8.0000	.5040	147.0	3.000	63.396
9.0000	.5178	157.3	3.000	60.561
10.0000	.5303	167.2	3.000	58.158
15.0000	.5800	211.9	3.000	49.971
20.0000	.6164	251.3	3.000	45.068
30.0000	.6686	321.1	3.000	39.239

ION IS 3 LI 7				
RANGE (CM)	BETA (V/C)	ENERGY (MEV/AMU)	ZEFF	DE/DX MEV/CM
.0025	.0520	1.3	2.884	2592.289
.0050	.0659	2.0	2.951	1873.850
.0075	.0750	2.6	2.972	1545.303
.0100	.0820	3.1	2.982	1347.959
.0200	.1007	4.8	2.994	967.777
.0300	.1130	6.0	2.997	797.995
.0400	.1224	7.1	2.999	701.439
.0500	.1302	8.0	2.999	634.801
.0600	.1368	8.8	2.999	585.193
.0700	.1426	9.6	3.000	546.378
.0800	.1480	10.4	3.000	513.474
.0900	.1529	11.1	3.000	486.215
.1000	.1575	11.8	3.000	463.673
.1500	.1760	14.8	3.000	383.962
.2000	.1902	17.3	3.000	336.318
.3000	.2121	21.7	3.000	279.267
.4000	.2289	25.4	3.000	244.946
.5000	.2428	28.7	3.000	221.372
.6000	.2547	31.8	3.000	203.885
.7000	.2652	34.6	3.000	190.239
.8000	.2745	37.2	3.000	179.201
.9000	.2830	39.7	3.000	170.032
1.0000	.2908	42.1	3.000	162.255
1.5000	.3227	52.6	3.000	135.720
2.0000	.3470	61.7	3.000	119.776
2.5000	.3670	69.8	3.000	108.832
3.0000	.3840	77.3	3.000	100.716
3.5000	.3989	84.3	3.000	94.385
4.0000	.4121	90.8	3.000	89.265
5.0000	.4350	103.0	3.000	81.405
6.0000	.4545	114.2	3.000	75.577
7.0000	.4714	124.6	3.000	71.031
8.0000	.4863	134.5	3.000	67.356
9.0000	.4998	143.9	3.000	64.304
10.0000	.5121	152.9	3.000	61.716
15.0000	.5608	193.5	3.000	52.896
20.0000	.5968	229.3	3.000	47.609
30.0000	.6487	292.4	3.000	41.317

ION IS 4 BE 7				
RANGE (CM)	BETA (V/C)	ENERGY (MEV/AMU)	ZEFF	DE/DX MEV/CM
.0025	.0613	1.8	3.831	3653.686
.0050	.0778	2.8	3.928	2597.128
.0075	.0885	3.7	3.958	2124.253
.0100	.0966	4.4	3.973	1843.408
.0200	.1181	6.6	3.991	1322.149
.0300	.1322	8.2	3.996	1100.649
.0400	.1430	9.7	3.997	967.303
.0500	.1522	11.0	3.998	871.426
.0600	.1601	12.2	3.999	800.597
.0700	.1671	13.3	3.999	745.320
.0800	.1733	14.3	3.999	700.605
.0900	.1789	15.3	4.000	663.451
.1000	.1842	16.2	4.000	631.934
.1500	.2054	20.3	4.000	524.367
.2000	.2218	23.8	4.000	459.704
.3000	.2469	29.8	4.000	382.383
.4000	.2662	34.9	4.000	335.918
.5000	.2821	39.4	4.000	304.025
.6000	.2957	43.6	4.000	280.374
.7000	.3076	47.5	4.000	261.923
.8000	.3183	51.1	4.000	247.002
.9000	.3280	54.5	4.000	234.608
1.0000	.3369	57.8	4.000	224.097
1.5000	.3729	72.4	4.000	188.241
2.0000	.4004	85.0	4.000	166.700
2.5000	.4228	96.4	4.000	151.916
3.0000	.4418	106.8	4.000	140.954
3.5000	.4584	116.6	4.000	132.403
4.0000	.4731	125.8	4.000	125.489
5.0000	.4984	142.9	4.000	114.878
6.0000	.5197	158.7	4.000	107.013
7.0000	.5381	173.5	4.000	100.882
8.0000	.5543	187.6	4.000	95.927
9.0000	.5688	201.0	4.000	91.814
10.0000	.5819	213.9	4.000	88.329
15.0000	.6335	272.3	4.000	76.475
20.0000	.6707	324.2	4.000	69.397
30.0000	.7230	416.8	4.000	61.028

ION IS 4 BE 9				
RANGE (CM)	BETA (V/C)	ENERGY (MEV/AMU)	ZEFF	DE/DX MEV/CM
.0025	.0558	1.5	3.775	4039.724
.0050	.0716	2.4	3.900	2943.804
.0075	.0818	3.1	3.941	2404.701
.0100	.0895	3.8	3.960	2086.457
.0200	.1099	5.7	3.986	1482.845
.0300	.1233	7.2	3.993	1232.901
.0400	.1335	8.4	3.996	1082.777
.0500	.1419	9.5	3.997	979.577
.0600	.1493	10.6	3.998	899.871
.0700	.1559	11.5	3.999	837.579
.0800	.1617	12.4	3.999	787.189
.0900	.1671	13.3	3.999	745.320
.1000	.1720	14.1	3.999	709.804
.1500	.1920	17.7	4.000	588.577
.2000	.2074	20.7	4.000	515.695
.3000	.2311	25.9	4.000	428.534
.4000	.2493	30.4	4.000	376.151
.5000	.2643	34.3	4.000	340.192
.6000	.2771	37.9	4.000	313.525
.7000	.2884	41.3	4.000	292.721
.8000	.2985	44.5	4.000	275.897
.9000	.3076	47.5	4.000	261.923
1.0000	.3160	50.3	4.000	250.071
1.5000	.3502	63.0	4.000	209.641
2.0000	.3763	73.9	4.000	185.352
2.5000	.3977	83.7	4.000	168.681
3.0000	.4158	92.7	4.000	156.320
3.5000	.4316	101.1	4.000	146.677
4.0000	.4457	109.0	4.000	138.879
5.0000	.4700	123.8	4.000	126.911
6.0000	.4905	137.3	4.000	118.038
7.0000	.5083	150.1	4.000	111.119
8.0000	.5240	162.1	4.000	105.526
9.0000	.5381	173.5	4.000	100.882
10.0000	.5509	184.5	4.000	96.946
15.0000	.6014	234.3	4.000	83.542
20.0000	.6382	278.3	4.000	75.523
30.0000	.6907	356.4	4.000	66.007

ION IS 4 BE 10				
RANGE (CM)	BETA (V/C)	ENERGY (MEV/AMU)	ZEFF	DE/DX MEV/CM
.0025	.0536	1.3	3.748	4203.918
.0050	.0690	2.2	3.886	3102.088
.0075	.0791	2.9	3.932	2534.629
.0100	.0866	3.5	3.954	2195.341
.0200	.1066	5.3	3.984	1561.921
.0300	.1197	6.7	3.992	1293.196
.0400	.1297	7.9	3.995	1135.409
.0500	.1379	9.0	3.997	1026.954
.0600	.1450	9.9	3.998	945.154
.0700	.1514	10.9	3.998	879.659
.0800	.1571	11.7	3.999	826.680
.0900	.1623	12.5	3.999	782.661
.1000	.1671	13.3	3.999	745.320
.1500	.1866	16.6	4.000	617.866
.2000	.2017	19.5	4.000	541.236
.3000	.2247	24.4	4.000	449.590
.4000	.2425	28.6	4.000	394.507
.5000	.2571	32.4	4.000	356.694
.6000	.2696	35.8	4.000	328.652
.7000	.2806	39.0	4.000	306.774
.8000	.2905	42.0	4.000	289.082
.9000	.2994	44.8	4.000	274.386
1.0000	.3076	47.5	4.000	261.923
1.5000	.3410	59.4	4.000	219.406
2.0000	.3666	69.7	4.000	193.863
2.5000	.3875	78.9	4.000	176.331
3.0000	.4052	87.4	4.000	163.331
3.5000	.4208	95.3	4.000	153.190
4.0000	.4346	102.7	4.000	144.990
5.0000	.4584	116.6	4.000	132.403
6.0000	.4786	129.3	4.000	123.071
7.0000	.4961	141.2	4.000	115.792
8.0000	.5115	152.5	4.000	109.909
9.0000	.5254	163.3	4.000	105.023
10.0000	.5331	173.5	4.000	100.882
15.0000	.5881	220.1	4.000	86.775
20.0000	.6246	261.2	4.000	78.329
30.0000	.6770	334.0	4.000	68.295

ION IS 5 B 11				
RANGE	BETA	ENERGY	ZEFF	DE/DX
(CM)	(V/C)	(MEV/AMU)		MEV/CM
.0025	.0586	1.6	4.630	5578.838
.0050	.0757	2.7	4.828	4188.030
.0075	.0869	3.5	4.895	3409.299
.0100	.0953	4.3	4.928	2944.232
.0200	.1172	6.5	4.973	2089.754
.0300	.1315	8.2	4.986	1734.342
.0400	.1424	9.6	4.991	1521.906
.0500	.1516	10.9	4.994	1370.187
.0600	.1596	12.1	4.996	1258.041
.0700	.1665	13.2	4.997	1170.663
.0800	.1728	14.2	4.998	1100.065
.0900	.1785	15.2	4.998	1041.459
.1000	.1837	16.1	4.999	991.780
.1500	.2050	20.2	4.999	822.446
.2000	.2214	23.7	5.000	720.797
.3000	.2465	29.6	5.000	599.366
.4000	.2657	34.7	5.000	526.445
.5000	.2816	39.3	5.000	476.411
.6000	.2952	43.4	5.000	439.317
.7000	.3071	47.3	5.000	410.383
.8000	.3178	50.9	5.000	386.987
.9000	.3275	54.3	5.000	367.556
1.0000	.3363	57.6	5.000	351.078
1.5000	.3724	72.2	5.000	294.874
2.0000	.3998	84.7	5.000	261.113
2.5000	.4222	96.0	5.000	237.943
3.0000	.4412	106.5	5.000	220.765
3.5000	.4578	116.2	5.000	207.365
4.0000	.4725	125.3	5.000	196.531
5.0000	.4977	142.4	5.000	179.904
6.0000	.5190	158.2	5.000	167.581
7.0000	.5374	173.0	5.000	157.973
8.0000	.5536	187.0	5.000	150.208
9.0000	.5681	200.3	5.000	143.764
10.0000	.5812	213.1	5.000	138.304
15.0000	.6328	271.4	5.000	119.728
20.0000	.6699	323.1	5.000	108.637
30.0000	.7223	415.3	5.000	95.522

ION IS 6 C 12				
RANGE	BETA	ENERGY	ZEFF	DE/DX
(CM)	(V/C)	(MEV/AMU)		MEV/CM
.0025	.0627	1.8	5.492	7052.545
.0050	.0813	3.1	5.755	5264.838
.0075	.0934	4.1	5.848	4353.495
.0100	.1024	4.9	5.894	3751.410
.0200	.1261	7.5	5.958	2671.870
.0300	.1414	9.5	5.977	2215.305
.0400	.1535	11.2	5.986	1932.633
.0500	.1635	12.7	5.990	1739.369
.0600	.1720	14.1	5.993	1596.619
.0700	.1795	15.4	5.995	1485.546
.0800	.1862	16.6	5.996	1395.891
.0900	.1922	17.7	5.997	1321.525
.1000	.1978	18.8	5.998	1258.525
.1500	.2206	23.5	5.999	1044.037
.2000	.2382	27.6	5.999	915.450
.3000	.2650	34.5	6.000	761.981
.4000	.2855	40.5	6.000	669.384
.5000	.3025	45.8	6.000	606.714
.6000	.3169	50.6	6.000	559.892
.7000	.3296	55.1	6.000	523.375
.8000	.3410	59.4	6.000	493.852
.9000	.3512	63.4	6.000	469.333
1.0000	.3606	67.2	6.000	448.541
1.5000	.3988	84.2	6.000	377.634
2.0000	.4278	99.0	6.000	335.046
2.5000	.4514	112.4	6.000	305.824
3.0000	.4713	124.6	6.000	284.159
3.5000	.4887	136.1	6.000	267.263
4.0000	.5040	146.9	6.000	253.604
5.0000	.5303	167.2	6.000	232.648
6.0000	.5524	185.9	6.000	217.122
7.0000	.5714	203.4	6.000	205.023
8.0000	.5881	220.1	6.000	195.250
9.0000	.6029	236.0	6.000	187.143
10.0000	.6164	251.3	6.000	180.277
15.0000	.6686	321.1	6.000	156.959
20.0000	.7059	383.4	6.000	143.084
30.0000	.7575	495.1	6.000	126.770

ION IS 6 C 13				
RANGE (CM)	BETA (V/C)	ENERGY (MEV/AMU)	ZEFF	DE/DX MEV/CM
.0025	.0607	1.7	5.451	7270.616
.0050	.0790	2.9	5.732	5456.570
.0075	.0909	3.9	5.833	4537.091
.0100	.0999	4.7	5.882	3910.179
.0200	.1233	7.2	5.953	2774.653
.0300	.1383	9.0	5.974	2298.306
.0400	.1501	10.7	5.984	2007.392
.0500	.1598	12.1	5.989	1806.233
.0600	.1682	13.5	5.992	1657.707
.0700	.1755	14.7	5.994	1542.169
.0800	.1821	15.8	5.995	1448.928
.0900	.1881	16.9	5.996	1371.596
.1000	.1936	17.9	5.997	1306.090
.1500	.2159	22.5	5.999	1083.109
.2000	.2332	26.4	5.999	949.454
.3000	.2595	33.0	6.000	789.952
.4000	.2797	38.7	6.000	694.243
.5000	.2963	43.8	6.000	628.599
.6000	.3105	48.4	6.000	579.944
.7000	.3230	52.7	6.000	541.999
.8000	.3341	56.8	6.000	511.322
.9000	.3442	60.6	6.000	485.844
1.0000	.3535	64.3	6.000	464.241
1.5000	.3910	80.6	6.000	390.563
2.0000	.4196	94.7	6.000	346.313
2.5000	.4428	107.4	6.000	315.949
3.0000	.4625	119.1	6.000	293.438
3.5000	.4796	130.0	6.000	275.881
4.0000	.4948	140.3	6.000	261.687
5.0000	.5208	159.6	6.000	239.908
6.0000	.5426	177.4	6.000	223.770
7.0000	.5615	194.1	6.000	211.193
8.0000	.5780	209.9	6.000	201.032
9.0000	.5928	225.1	6.000	192.601
10.0000	.6062	239.6	6.000	185.460
15.0000	.6583	305.8	6.000	161.195
20.0000	.6955	364.8	6.000	146.741
30.0000	.7474	470.5	6.000	129.713

ION IS 7 N 14				
RANGE (CM)	BETA (V/C)	ENERGY (MEV/AMU)	ZEFF	DE/DX MEV/CM
.0025	.0643	1.9	6.287	8866.284
.0050	.0838	3.3	6.643	6629.791
.0075	.0964	4.4	6.772	5499.953
.0100	.1060	5.3	6.838	4795.725
.0200	.1309	8.1	6.933	3421.967
.0300	.1471	10.2	6.962	2822.330
.0400	.1598	12.1	6.976	2459.238
.0500	.1702	13.8	6.983	2211.743
.0600	.1791	15.3	6.988	2029.357
.0700	.1869	16.7	6.991	1887.669
.0800	.1938	18.0	6.993	1773.437
.0900	.2002	19.2	6.994	1678.768
.1000	.2060	20.4	6.995	1598.626
.1500	.2297	25.6	6.998	1326.132
.2000	.2479	30.0	6.999	1163.002
.3000	.2757	37.5	7.000	968.493
.4000	.2971	44.0	7.000	851.852
.5000	.3146	49.8	7.000	771.877
.6000	.3295	55.1	7.000	712.613
.7000	.3427	60.0	7.000	666.400
.8000	.3544	64.6	7.000	629.042
.9000	.3650	69.0	7.000	598.018
1.0000	.3747	73.2	7.000	571.713
1.5000	.4141	91.8	7.000	482.013
2.0000	.4440	108.0	7.000	428.148
2.5000	.4682	122.6	7.000	391.191
3.0000	.4886	136.1	7.000	363.797
3.5000	.5064	148.7	7.000	342.436
4.0000	.5221	160.6	7.000	325.169
5.0000	.5489	182.8	7.000	298.683
6.0000	.5714	203.4	7.000	279.067
7.0000	.5906	222.8	7.000	263.785
8.0000	.6076	241.2	7.000	251.446
9.0000	.6226	258.8	7.000	241.215
10.0000	.6361	275.7	7.000	232.553
15.0000	.6886	352.9	7.000	203.175
20.0000	.7257	422.2	7.000	185.739
30.0000	.7766	546.8	7.000	165.326

ION IS 7 N 15				
RANGE	BETA	ENERGY	ZEFF	DE/DX
(CM)	(V/C)	(MEV/AMU)		MEV/CM
.0025	.0625	1.8	6.240	9098.567
.0050	.0817	3.1	6.616	6837.093
.0075	.0942	4.2	6.754	5681.213
.0100	.1036	5.0	6.824	4972.070
.0200	.1283	7.8	6.927	3535.799
.0300	.1442	9.8	6.958	2918.528
.0400	.1567	11.6	6.973	2541.686
.0500	.1669	13.3	6.981	2285.273
.0600	.1757	14.7	6.986	2096.408
.0700	.1833	16.1	6.990	1949.735
.0800	.1902	17.3	6.992	1831.511
.0900	.1964	18.5	6.993	1733.551
.1000	.2022	19.6	6.995	1650.634
.1500	.2255	24.6	6.998	1368.769
.2000	.2434	28.9	6.999	1200.071
.3000	.2708	36.1	7.000	998.957
.4000	.2918	42.4	7.000	878.369
.5000	.3091	47.9	7.000	795.694
.6000	.3238	53.0	7.000	734.431
.7000	.3367	57.8	7.000	686.661
.8000	.3483	62.2	7.000	648.045
.9000	.3588	66.4	7.000	615.978
1.0000	.3684	70.4	7.000	588.788
1.5000	.4072	88.4	7.000	496.073
2.0000	.4367	103.9	7.000	440.398
2.5000	.4606	117.9	7.000	402.199
3.0000	.4808	130.8	7.000	373.883
3.5000	.4984	142.9	7.000	351.801
4.0000	.5139	154.3	7.000	333.952
5.0000	.5105	175.6	7.000	306.569
6.0000	.5628	195.3	7.000	286.287
7.0000	.5820	213.9	7.000	270.483
8.0000	.5988	231.5	7.000	257.721
9.0000	.6138	248.3	7.000	247.136
10.0000	.6273	264.5	7.000	238.174
15.0000	.6797	338.3	7.000	207.758
20.0000	.7168	404.3	7.000	189.683
30.0000	.7681	522.9	7.000	168.480

ION IS 8 O 16				
RANGE	BETA	ENERGY	ZEFF	DE/DX
(CM)	(V/C)	(MEV/AMU)		MEV/CM
.0025	.0656	2.0	7.051	10806.409
.0050	.0859	3.5	7.510	8097.150
.0075	.0991	4.6	7.681	6717.998
.0100	.1090	5.6	7.769	5853.541
.0200	.1351	8.6	7.901	4239.938
.0300	.1522	11.0	7.943	3486.231
.0400	.1654	13.0	7.963	3032.051
.0500	.1762	14.8	7.974	2725.519
.0600	.1854	16.4	7.981	2499.575
.0700	.1934	17.9	7.985	2324.346
.0800	.2007	19.3	7.988	2183.248
.0900	.2072	20.7	7.990	2066.426
.1000	.2132	21.9	7.992	1967.603
.1500	.2378	27.5	7.996	1632.050
.2000	.2566	32.3	7.998	1431.467
.3000	.2853	40.4	7.999	1192.542
.4000	.3073	47.4	8.000	1049.371
.5000	.3254	53.6	8.000	951.244
.6000	.3408	59.3	8.000	878.546
.7000	.3543	64.6	8.000	821.867
.8000	.3664	69.6	8.000	776.053
.9000	.3773	74.3	8.000	738.011
1.0000	.3873	78.8	8.000	705.758
1.5000	.4277	99.0	8.000	595.789
2.0000	.4583	116.5	8.000	529.766
2.5000	.4831	132.3	8.000	484.474
3.0000	.5040	146.9	8.000	450.907
3.5000	.5221	160.6	8.000	424.734
4.0000	.5380	173.5	8.000	403.583
5.0000	.5653	197.7	8.000	371.146
6.0000	.5880	220.1	8.000	347.130
7.0000	.6076	241.2	8.000	328.428
8.0000	.6246	261.2	8.000	313.334
9.0000	.6398	280.4	8.000	300.823
10.0000	.6534	298.8	8.000	290.236
15.0000	.7059	383.4	8.000	254.377
20.0000	.7427	459.3	8.000	233.152
30.0000	.7928	596.5	8.000	208.419

ION IS 9 F 19				
RANGE	BETA	ENERGY	ZEFF	DE/DX
(CM)	(V/C)	(MEV/AMU)		MEV/CM
.0025	.0652	2.0	7.730	13109.025
.0050	.0861	3.5	8.323	9894.696
.0075	.0996	4.7	8.548	8223.118
.0100	.1098	5.7	8.667	7169.167
.0200	.1365	8.8	8.851	5255.795
.0300	.1541	11.3	8.912	4313.388
.0400	.1677	13.4	8.942	3748.433
.0500	.1787	15.2	8.958	3365.163
.0600	.1882	16.9	8.968	3083.359
.0700	.1964	18.5	8.975	2864.935
.0800	.2038	20.0	8.980	2691.504
.0900	.2105	21.3	8.984	2546.770
.1000	.2166	22.6	8.987	2424.455
.1500	.2416	28.4	8.994	2009.875
.2000	.2607	33.4	8.996	1762.527
.3000	.2899	41.8	8.999	1468.280
.4000	.3123	49.0	8.999	1292.125
.5000	.3306	55.5	9.000	1171.452
.6000	.3463	61.4	9.000	1082.079
.7000	.3600	66.9	9.000	1012.415
.8000	.3722	72.1	9.000	956.113
.9000	.3833	77.0	9.000	909.369
1.0000	.3934	81.7	9.000	869.741
1.5000	.4343	102.6	9.000	734.653
2.0000	.4653	120.8	9.000	653.565
2.5000	.4903	137.2	9.000	597.947
3.0000	.5114	152.4	9.000	556.732
3.5000	.5296	166.6	9.000	524.600
4.0000	.5457	180.1	9.000	498.635
5.0000	.5732	205.2	9.000	458.822
6.0000	.5961	228.5	9.000	429.352
7.0000	.6157	250.5	9.000	406.407
8.0000	.6328	271.4	9.000	387.893
9.0000	.6480	291.4	9.000	372.551
10.0000	.6616	310.6	9.000	359.572
15.0000	.7141	398.9	9.000	315.641
20.0000	.7507	478.3	9.000	289.679
30.0000	.8003	622.0	9.000	259.503

ION IS 10 NE 20				
RANGE	BETA	ENERGY	ZEFF	DE/DX
(CM)	(V/C)	(MEV/AMU)		MEV/CM
.0025	.0676	2.1	8.496	15004.318
.0050	.0895	3.8	9.185	11312.617
.0075	.1036	5.0	9.450	9390.801
.0100	.1142	6.1	9.591	8216.637
.0200	.1419	9.5	9.812	6026.241
.0300	.1606	12.2	9.889	4962.933
.0400	.1748	14.6	9.925	4312.279
.0500	.1863	16.6	9.946	3871.090
.0600	.1961	18.4	9.959	3546.846
.0700	.2047	20.2	9.968	3295.624
.0800	.2124	21.7	9.974	3093.571
.0900	.2194	23.3	9.979	2928.027
.1000	.2258	24.7	9.982	2787.343
.1500	.2518	31.0	9.991	2311.065
.2000	.2717	36.4	9.995	2027.271
.3000	.3020	45.6	9.998	1689.958
.4000	.3252	53.5	9.999	1488.148
.5000	.3442	60.6	9.999	1349.945
.6000	.3604	67.1	10.000	1247.610
.7000	.3745	73.1	10.000	1167.852
.8000	.3872	78.8	10.000	1103.401
.9000	.3986	84.2	10.000	1049.894
1.0000	.4091	89.3	10.000	1004.536
1.5000	.4512	112.3	10.000	849.939
2.0000	.4830	132.3	10.000	757.159
2.5000	.5087	150.4	10.000	693.536
3.0000	.5302	167.1	10.000	646.398
3.5000	.5489	182.8	10.000	609.658
4.0000	.5653	197.6	10.000	579.975
5.0000	.5932	225.4	10.000	534.480
6.0000	.6163	251.3	10.000	500.823
7.0000	.6361	275.6	10.000	474.634
8.0000	.6534	298.8	10.000	453.516
9.0000	.6686	321.0	10.000	436.027
10.0000	.6823	342.5	10.000	421.243
15.0000	.7345	440.9	10.000	371.310
20.0000	.7706	529.8	10.000	341.933
30.0000	.8189	691.4	10.000	308.046

ION IS 10 NE 21				
RANGE	BETA	ENERGY	ZEFF	DE/DX
(CM)	(V/C)	(MEV/AMU)		MEV/CM
.0025	.0662	2.0	8.434	15268.434
.0050	.0879	3.6	9.147	11559.312
.0075	.1018	4.9	9.423	9609.070
.0100	.1123	5.9	9.570	8396.193
.0200	.1399	9.2	9.801	6159.583
.0300	.1583	11.9	9.881	5083.397
.0400	.1723	14.1	9.920	4415.812
.0500	.1837	16.1	9.942	3963.208
.0600	.1935	17.9	9.956	3630.628
.0700	.2020	19.6	9.965	3372.985
.0800	.2096	21.2	9.972	3165.795
.0900	.2165	22.6	9.977	2994.477
.1000	.2228	24.0	9.981	2851.547
.1500	.2485	30.2	9.991	2363.362
.2000	.2682	35.4	9.995	2072.593
.3000	.2982	44.4	9.998	1727.085
.4000	.3211	52.1	9.999	1520.414
.5000	.3399	59.0	9.999	1378.898
.6000	.3560	65.3	10.000	1274.117
.7000	.3700	71.1	10.000	1192.457
.8000	.3825	76.6	10.000	1126.471
.9000	.3938	81.9	10.000	1071.691
1.0000	.4042	86.9	10.000	1025.255
1.5000	.4460	109.2	10.000	866.986
2.0000	.4775	128.6	10.000	772.004
2.5000	.5030	146.2	10.000	706.869
3.0000	.5244	162.4	10.000	658.609
3.5000	.5429	177.6	10.000	620.991
4.0000	.5592	192.1	10.000	590.598
5.0000	.5870	219.0	10.000	544.009
6.0000	.6101	244.1	10.000	509.536
7.0000	.6298	267.7	10.000	482.708
8.0000	.6471	290.1	10.000	461.069
9.0000	.6623	311.6	10.000	443.146
10.0000	.6759	332.4	10.000	427.991
15.0000	.7282	427.5	10.000	376.769
20.0000	.7645	513.4	10.000	346.588
30.0000	.8133	669.2	10.000	311.687

ION IS 10 NE 22				
RANGE	BETA	ENERGY	ZEFF	DE/DX
(CM)	(V/C)	(MEV/AMU)		MEV/CM
.0025	.0649	2.0	8.374	15514.993
.0050	.0863	3.5	9.109	11797.238
.0075	.1002	4.7	9.395	9820.614
.0100	.1106	5.7	9.549	8566.643
.0200	.1379	9.0	9.790	6289.187
.0300	.1561	11.6	9.874	5201.179
.0400	.1700	13.8	9.914	4517.030
.0500	.1813	15.7	9.938	4053.252
.0600	.1910	17.5	9.952	3712.512
.0700	.1994	19.1	9.962	3446.583
.0800	.2069	20.6	9.970	3236.365
.0900	.2137	22.0	9.975	3060.908
.1000	.2200	23.4	9.979	2914.277
.1500	.2454	29.4	9.990	2414.431
.2000	.2649	34.5	9.994	2116.838
.3000	.2946	43.2	9.997	1763.320
.4000	.3173	50.7	9.999	1551.900
.5000	.3359	57.5	9.999	1407.149
.6000	.3518	63.6	9.999	1299.980
.7000	.3657	69.3	10.000	1216.463
.8000	.3781	74.7	10.000	1148.978
.9000	.3893	79.8	10.000	1092.956
1.0000	.3996	84.6	10.000	1045.468
1.5000	.4411	106.4	10.000	883.617
2.0000	.4723	125.3	10.000	786.487
2.5000	.4976	142.3	10.000	719.877
3.0000	.5189	158.1	10.000	670.522
3.5000	.5373	172.9	10.000	632.050
4.0000	.5535	186.9	10.000	600.964
5.0000	.5812	213.1	10.000	553.308
6.0000	.6042	237.4	10.000	518.041
7.0000	.6239	260.3	10.000	490.590
8.0000	.6410	282.1	10.000	468.445
9.0000	.6563	302.9	10.000	450.098
10.0000	.6699	323.0	10.000	434.583
15.0000	.7223	415.2	10.000	382.108
20.0000	.7587	498.3	10.000	351.149
30.0000	.8079	648.9	10.000	315.267

ION IS 11 NA 23				
RANGE (CM)	BETA (V/C)	ENERGY (MEV/AMU)	ZEFF	DE/DX MEV/CM
.0025	.0671	2.1	9.112	17514.147
.0050	.0895	3.7	9.952	13307.453
.0075	.1038	5.1	10.282	11066.512
.0100	.1147	6.2	10.460	9693.305
.0200	.1430	9.7	10.743	7114.703
.0300	.1620	12.5	10.844	5898.769
.0400	.1765	14.9	10.894	5122.542
.0500	.1883	17.0	10.922	4596.479
.0600	.1983	18.9	10.940	4210.095
.0700	.2071	20.6	10.952	3910.898
.0800	.2149	22.3	10.961	3670.381
.0900	.2220	23.8	10.968	3471.572
.1000	.2285	25.3	10.973	3303.655
.1500	.2549	31.8	10.986	2737.798
.2000	.2751	37.4	10.992	2400.960
.3000	.3058	46.8	10.996	2001.188
.4000	.3293	55.0	10.998	1762.264
.5000	.3485	62.3	10.999	1598.740
.6000	.3649	69.0	10.999	1477.698
.7000	.3792	75.2	10.999	1383.384
.8000	.3920	81.0	11.000	1307.183
.9000	.4036	86.6	11.000	1243.930
1.0000	.4141	91.8	11.000	1190.317
1.5000	.4567	115.5	11.000	1007.619
2.0000	.4887	136.2	11.000	898.004
2.5000	.5146	154.8	11.000	822.848
3.0000	.5363	172.1	11.000	767.174
3.5000	.5551	188.3	11.000	723.785
4.0000	.5715	203.6	11.000	688.735
5.0000	.5996	232.3	11.000	635.023
6.0000	.6228	259.0	11.000	595.296
7.0000	.6427	284.2	11.000	564.392
8.0000	.6599	308.2	11.000	539.478
9.0000	.6752	331.2	11.000	518.851
10.0000	.6888	353.4	11.000	501.419
15.0000	.7409	455.3	11.000	442.590
20.0000	.7768	547.5	11.000	408.036
30.0000	.8247	715.3	11.000	368.294

ION IS 12 MG 24				
RANGE (CM)	BETA (V/C)	ENERGY (MEV/AMU)	ZEFF	DE/DX MEV/CM
.0025	.0691	2.2	9.835	19567.597
.0050	.0923	4.0	10.784	14866.538
.0075	.1072	5.4	11.160	12352.606
.0100	.1184	6.6	11.364	10856.891
.0200	.1478	10.3	11.693	7952.470
.0300	.1675	13.3	11.812	6579.700
.0400	.1825	15.9	11.870	5751.252
.0500	.1947	18.2	11.904	5160.675
.0600	.2051	20.2	11.926	4726.995
.0700	.2142	22.1	11.941	4391.245
.0800	.2223	23.9	11.952	4121.399
.0900	.2296	25.6	11.960	3898.387
.1000	.2363	27.1	11.966	3710.058
.1500	.2636	34.1	11.983	3074.400
.2000	.2845	40.1	11.990	2696.767
.3000	.3162	50.3	11.995	2248.990
.4000	.3403	59.1	11.977	1981.554
.5000	.3601	67.0	11.998	1798.580
.6000	.3770	74.2	11.999	1663.169
.7000	.3917	80.9	11.999	1557.676
.8000	.4048	87.2	11.999	1472.453
.9000	.4167	93.2	12.000	1401.718
1.0000	.4275	98.9	12.000	1341.766
1.5000	.4711	124.5	12.000	1137.505
2.0000	.5038	146.8	12.000	1014.984
2.5000	.5302	167.0	12.000	930.999
3.0000	.5522	185.8	12.000	868.800
3.5000	.5713	203.3	12.000	820.338
4.0000	.5880	220.0	12.000	781.202
5.0000	.6163	251.2	12.000	721.251
6.0000	.6397	280.3	12.000	676.938
7.0000	.6597	307.8	12.000	642.489
8.0000	.6770	334.0	12.000	614.736
9.0000	.6922	359.1	12.000	591.776
10.0000	.7058	383.3	12.000	572.388
15.0000	.7575	495.1	12.000	507.108
20.0000	.7927	596.4	12.000	468.956
30.0000	.8393	781.8	12.000	425.452

ION 1s 12 Mg 25				
RANGE	BETA	ENERGY	ZEFF	DE/DX
(CM)	(V/C)	(MEV/AMU)		MEV/CM
.0025	.0678	2.1	9.766	19839.467
.0050	.0909	3.9	10.740	15134.529
.0075	.1057	5.2	11.127	12592.158
.0100	.1168	6.4	11.337	11054.286
.0200	.1460	10.1	11.679	8105.257
.0300	.1655	13.0	11.802	6706.568
.0400	.1803	15.5	11.863	5867.013
.0500	.1925	17.7	11.899	5263.595
.0600	.2028	19.8	11.921	4820.528
.0700	.2118	21.6	11.937	4477.547
.0800	.2198	23.3	11.949	4201.918
.0900	.2271	25.0	11.957	3974.148
.1000	.2337	26.5	11.964	3781.817
.1500	.2608	33.4	11.981	3131.425
.2000	.2814	39.2	11.989	2747.075
.3000	.3128	49.2	11.995	2290.103
.4000	.3368	57.8	11.997	2017.242
.5000	.3564	65.5	11.998	1830.581
.6000	.3731	72.5	11.999	1692.453
.7000	.3878	79.0	11.999	1584.850
.8000	.4008	85.2	11.999	1497.924
.9000	.4125	91.0	12.000	1425.779
1.0000	.4233	96.6	12.000	1364.633
1.5000	.4666	121.6	12.000	1156.309
2.0000	.4991	143.4	12.000	1031.352
2.5000	.5253	163.1	12.000	945.695
3.0000	.5473	181.4	12.000	882.253
3.5000	.5662	198.5	12.000	832.820
4.0000	.5828	214.8	12.000	792.897
5.0000	.6111	245.2	12.000	731.733
6.0000	.6345	273.5	12.000	686.514
7.0000	.6544	300.2	12.000	651.354
8.0000	.6717	325.7	12.000	623.022
9.0000	.6869	350.1	12.000	599.577
10.0000	.7006	373.7	12.000	579.774
15.0000	.7523	482.3	12.000	513.048
20.0000	.7878	580.7	12.000	473.986
30.0000	.8349	760.4	12.000	429.317

ION 1S 12 MG 26				
RANGE	BETA	ENERGY	ZEFF	DE/DX
(CM)	(V/C)	(MEV/AMU)		MEV/CM
.0025	.0666	2.1	9.697	20097.899
.0050	.0895	3.7	10.696	15394.107
.0075	.1042	5.1	11.095	12825.347
.0100	.1152	6.2	11.312	11246.907
.0200	.1441	9.8	11.663	8261.441
.0300	.1635	12.7	11.792	6830.754
.0400	.1782	15.2	11.856	5990.606
.0500	.1903	17.3	11.893	5364.582
.0600	.2005	19.3	11.917	4912.295
.0700	.2094	21.1	11.933	4562.212
.0800	.2174	22.8	11.945	4280.902
.0900	.2246	24.4	11.954	4049.457
.1000	.2312	25.9	11.961	3852.195
.1500	.2581	32.6	11.980	3188.628
.2000	.2785	38.4	11.988	2796.391
.3000	.3097	48.1	11.994	2330.392
.4000	.3335	56.5	11.997	2052.210
.5000	.3529	64.0	11.998	1861.933
.6000	.3695	70.9	11.999	1721.141
.7000	.3840	77.3	11.999	1611.468
.8000	.3969	83.3	11.999	1522.875
.9000	.4086	89.0	12.000	1449.348
1.0000	.4193	94.5	12.000	1387.032
1.5000	.4623	118.9	12.000	1174.728
2.0000	.4946	140.2	12.000	1047.381
2.5000	.5206	159.5	12.000	960.089
3.0000	.5425	177.3	12.000	895.431
3.5000	.5613	194.0	12.000	845.049
4.0000	.5779	209.8	12.000	804.355
5.0000	.6061	239.5	12.000	742.004
6.0000	.6294	267.1	12.000	695.900
7.0000	.6493	293.2	12.000	660.044
8.0000	.6666	318.0	12.000	631.146
9.0000	.6818	341.8	12.000	607.228
10.0000	.6955	364.7	12.000	587.020
15.0000	.7474	470.4	12.000	518.883
20.0000	.7831	566.1	12.000	478.936
30.0000	.8305	740.5	12.000	433.136

ION IS 13 AL 26				
RANGE (CM)	BETA (V/C)	ENERGY (MEV/AMU)	ZEFF	DE/DX MEV/CM
.0025	.0696	2.3	10.469	21962.638
.0050	.0935	4.1	11.557	16758.990
.0075	.1088	5.6	11.993	13933.706
.0100	.1203	6.8	12.231	12270.910
.0200	.1505	10.7	12.622	8983.908
.0300	.1706	13.9	12.765	7434.193
.0400	.1859	16.5	12.836	6499.121
.0500	.1984	18.9	12.878	5855.297
.0600	.2091	21.0	12.905	5362.683
.0700	.2184	23.0	12.923	4981.401
.0800	.2267	24.9	12.937	4675.036
.0900	.2342	26.6	12.947	4421.902
.1000	.2411	28.3	12.955	4208.181
.1500	.2690	35.6	12.977	3485.665
.2000	.2902	41.9	12.986	3057.772
.3000	.3225	52.6	12.993	2550.404
.4000	.3472	61.8	12.996	2247.660
.5000	.3673	70.0	12.998	2040.632
.6000	.3845	77.5	12.998	1887.468
.7000	.3994	84.5	12.999	1768.169
.8000	.4128	91.2	12.999	1671.808
.9000	.4248	97.4	12.999	1591.839
1.0000	.4358	103.4	13.000	1524.069
1.5000	.4800	130.3	13.000	1293.213
2.0000	.5131	153.7	13.000	1154.779
2.5000	.5398	175.0	13.000	1059.908
3.0000	.5620	194.6	13.000	989.661
3.5000	.5812	213.1	13.000	934.940
4.0000	.5981	230.7	13.000	890.758
5.0000	.6265	263.6	13.000	823.100
6.0000	.6500	294.2	13.000	773.112
7.0000	.6700	323.2	13.000	734.270
8.0000	.6873	350.3	13.000	702.994
9.0000	.7026	377.3	13.000	677.133
10.0000	.7161	402.9	13.000	655.306
15.0000	.7674	521.2	13.000	581.943
20.0000	.8023	628.6	13.000	539.217
30.0000	.8480	825.7	13.000	490.805

ION IS 13 AL 27				
RANGE (CM)	BETA (V/C)	ENERGY (MEV/AMU)	ZEFF	DE/DX MEV/CM
.0025	.0684	2.2	10.395	22235.444
.0050	.0921	4.0	11.509	17036.333
.0075	.1073	5.4	11.958	14183.066
.0100	.1187	6.6	12.203	12476.574
.0200	.1487	10.5	12.606	9143.244
.0300	.1687	13.5	12.754	7566.510
.0400	.1839	16.1	12.828	6614.670
.0500	.1963	18.5	12.871	5963.303
.0600	.2069	20.6	12.900	5460.818
.0700	.2161	22.5	12.919	5071.927
.0800	.2243	24.4	12.933	4759.477
.0900	.2318	26.1	12.944	4501.335
.1000	.2386	27.7	12.952	4283.403
.1500	.2663	34.9	12.975	3546.777
.2000	.2874	41.0	12.985	3110.469
.3000	.3194	51.5	12.993	2593.414
.4000	.3439	60.5	12.996	2284.972
.5000	.3638	68.5	12.997	2074.076
.6000	.3809	75.9	12.998	1918.065
.7000	.3957	82.8	12.999	1796.555
.8000	.4090	89.2	12.999	1698.413
.9000	.4209	95.4	12.999	1616.968
1.0000	.4318	101.2	12.999	1547.948
1.5000	.4758	127.5	13.000	1312.844
2.0000	.5087	150.4	13.000	1171.862
2.5000	.5352	171.2	13.000	1075.242
3.0000	.5574	190.4	13.000	1003.696
3.5000	.5765	208.4	13.000	947.959
4.0000	.5933	225.6	13.000	902.954
5.0000	.6217	257.7	13.000	834.025
6.0000	.6452	287.6	13.000	783.089
7.0000	.6651	315.8	13.000	743.502
8.0000	.6824	342.7	13.000	711.618
9.0000	.6977	368.6	13.000	685.248
10.0000	.7113	393.5	13.000	662.986
15.0000	.7627	508.7	13.000	588.099
20.0000	.7978	613.2	13.000	544.411
30.0000	.8439	804.6	13.000	494.756

ION IS 14 SI 28				
RANGE	BETA	ENERGY	ZEFF	DE/DX
(CM)	(V/C)	(MEV/AMU)		MEV/CM
.0025	.0700	2.3	11.079	24421.671
.0050	.0945	4.2	12.313	18723.077
.0075	.1102	5.7	12.812	15577.907
.0100	.1220	7.0	13.087	13744.305
.0200	.1530	11.1	13.543	10058.955
.0300	.1735	14.3	13.712	8324.988
.0400	.1891	17.1	13.797	7278.716
.0500	.2019	19.6	13.847	6560.044
.0600	.2128	21.8	13.880	6027.382
.0700	.2223	23.9	13.903	5598.521
.0800	.2308	25.8	13.920	5253.988
.0900	.2384	27.7	13.933	4969.369
.1000	.2455	29.4	13.942	4729.107
.1500	.2739	37.0	13.970	3917.193
.2000	.2956	43.6	13.981	3435.023
.3000	.3285	54.7	13.991	2865.904
.4000	.3536	64.3	13.995	2526.238
.5000	.3741	72.9	13.997	2291.082
.6000	.3915	80.8	13.998	2122.383
.7000	.4067	88.1	13.998	1988.679
.8000	.4202	95.0	13.999	1880.700
.9000	.4324	101.5	13.999	1791.101
1.0000	.4436	107.8	13.999	1715.178
1.5000	.4884	135.9	14.000	1456.608
2.0000	.5219	160.4	14.000	1301.601
2.5000	.5487	182.7	14.000	1195.397
3.0000	.5712	203.3	14.000	1116.775
3.5000	.5905	222.7	14.000	1055.544
4.0000	.6074	241.0	14.000	1006.116
5.0000	.6360	275.5	14.000	930.449
6.0000	.6596	307.7	14.000	874.571
7.0000	.6796	338.2	14.000	831.173
8.0000	.6969	367.2	14.000	796.247
9.0000	.7121	395.1	14.000	767.384
10.0000	.7256	422.1	14.000	743.038
15.0000	.7765	546.7	14.000	661.347
20.0000	.8110	660.2	14.000	613.947
30.0000	.8558	868.9	14.000	560.597

ION IS 15 P 31				
RANGE	BETA	ENERGY	ZEFF	DE/DX
(CM)	(V/C)	(MEV/AMU)		MEV/CM
.0025	.0693	2.2	11.538	27205.675
.0050	.0942	4.2	12.999	21048.730
.0075	.1102	5.7	13.578	17550.231
.0100	.1222	7.0	13.898	15496.013
.0200	.1536	11.2	14.438	11347.990
.0300	.1745	14.5	14.640	9393.638
.0400	.1903	17.3	14.743	8213.786
.0500	.2032	19.8	14.805	7403.235
.0600	.2142	22.1	14.846	6802.339
.0700	.2239	24.2	14.875	6340.300
.0800	.2325	26.2	14.896	5949.367
.0900	.2402	28.1	14.912	5626.479
.1000	.2473	29.9	14.924	5353.966
.1500	.2762	37.7	14.959	4433.508
.2000	.2981	44.4	14.974	3887.254
.3000	.3313	55.7	14.987	3241.827
.4000	.3566	65.5	14.993	2857.415
.5000	.3773	74.3	14.995	2594.860
.6000	.3949	82.4	14.997	2400.765
.7000	.4102	89.8	14.998	2249.666
.8000	.4238	96.9	14.998	2127.667
.9000	.4361	103.6	14.999	2026.451
1.0000	.4474	110.0	14.999	1940.696
1.5000	.4924	138.7	15.000	1648.718
2.0000	.5261	163.8	15.000	1473.739
2.5000	.5531	186.5	15.000	1353.876
3.0000	.5757	207.6	15.000	1265.157
3.5000	.5951	227.4	15.000	1196.073
4.0000	.6120	246.3	15.000	1140.314
5.0000	.6407	281.6	15.000	1054.972
6.0000	.6643	314.6	15.000	991.966
7.0000	.6843	345.8	15.000	943.047
8.0000	.7016	375.5	15.000	903.688
9.0000	.7167	404.1	15.000	871.171
10.0000	.7302	431.8	15.000	843.751
15.0000	.7810	559.7	15.000	751.935
20.0000	.8151	676.3	15.000	698.609
30.0000	.8596	890.9	15.000	638.915

ION IS 16 S 32				
RANGE (CM)	BETA (V/C)	ENERGY (MEV/AMU)	ZEFF	DE/DX MEV/CM
.0025	.0707	2.3	12.235	29499.179
.0050	.0964	4.4	13.775	22851.555
.0075	.1128	6.0	14.410	19094.944
.0100	.1250	7.4	14.763	16860.812
.0200	.1574	11.8	15.363	12334.516
.0300	.1788	15.2	15.588	10211.133
.0400	.1950	18.2	15.705	8929.726
.0500	.2082	20.9	15.775	8049.623
.0600	.2195	23.3	15.821	7397.273
.0700	.2294	25.5	15.854	6888.752
.0800	.2382	27.6	15.878	6484.780
.0900	.2462	29.6	15.896	6133.319
.1000	.2535	31.4	15.911	5836.703
.1500	.2830	39.7	15.951	4834.962
.2000	.3055	46.8	15.969	4240.598
.3000	.3395	58.8	15.985	3537.283
.4000	.3653	69.1	15.991	3119.667
.5000	.3864	78.4	15.994	2834.120
.6000	.4043	86.9	15.996	2623.082
.7000	.4200	94.9	15.997	2458.824
.8000	.4339	102.3	15.998	2326.219
.9000	.4464	109.4	15.998	2216.216
1.0000	.4578	116.2	15.999	2123.025
1.5000	.5036	146.7	15.999	1805.798
2.0000	.5377	173.3	16.000	1615.748
2.5000	.5651	197.5	16.000	1485.600
3.0000	.5878	219.9	16.000	1389.297
3.5000	.6074	241.0	16.000	1314.330
4.0000	.6245	261.0	16.000	1253.842
5.0000	.6533	298.7	16.000	1161.307
6.0000	.6769	333.9	16.000	1093.039
7.0000	.6969	367.2	16.000	1040.074
8.0000	.7141	399.0	16.000	997.494
9.0000	.7292	429.6	16.000	962.346
10.0000	.7426	459.2	16.000	932.735
15.0000	.7927	596.4	16.000	833.742
20.0000	.8262	721.8	16.000	776.756
30.0000	.8694	953.5	16.000	713.543

ION IS 17 CL 35				
RANGE (CM)	BETA (V/C)	ENERGY (MEV/AMU)	ZEFF	DE/DX MEV/CM
.0025	.0699	2.3	12.697	32361.057
.0050	.0960	4.3	14.425	25315.949
.0075	.1127	6.0	15.145	21200.317
.0100	.1251	7.4	15.548	18735.269
.0200	.1580	11.8	16.239	13716.043
.0300	.1796	15.4	16.503	11356.970
.0400	.1960	18.4	16.640	9932.552
.0500	.2094	21.1	16.723	8954.065
.0600	.2208	23.6	16.779	8228.757
.0700	.2308	25.8	16.818	7663.360
.0800	.2396	27.9	16.847	7206.547
.0900	.2477	30.0	16.870	6827.444
.1000	.2551	31.9	16.887	6510.184
.1500	.2850	40.3	16.937	5391.612
.2000	.3077	47.5	16.960	4728.280
.3000	.3420	59.7	16.980	3943.767
.4000	.3681	70.3	16.988	3476.649
.5000	.3893	79.8	16.992	3159.073
.6000	.4074	88.4	16.994	2923.915
.7000	.4231	96.5	16.996	2740.944
.8000	.4371	104.1	16.997	2593.267
.9000	.4497	111.4	16.998	2470.786
1.0000	.4612	118.3	16.998	2367.038
1.5000	.5072	149.3	16.999	2013.977
2.0000	.5415	176.5	17.000	1802.532
2.5000	.5689	201.1	17.000	1657.765
3.0000	.5918	224.0	17.000	1550.664
3.5000	.6114	245.5	17.000	1467.305
4.0000	.6285	266.0	17.000	1400.056
5.0000	.6573	304.4	17.000	1297.200
6.0000	.6810	340.4	17.000	1221.339
7.0000	.7009	374.4	17.000	1162.501
8.0000	.7181	406.9	17.000	1115.214
9.0000	.7332	438.2	17.000	1076.193
10.0000	.7466	468.5	17.000	1043.329
15.0000	.7965	608.8	17.000	933.574
20.0000	.8298	737.4	17.000	870.530
30.0000	.8726	974.9	17.000	800.676

ION IS 18 AR 36				
RANGE (CM)	BETA (V/C)	ENERGY (MEV/AMU)	ZEFF	DE/DX MEV/CM
.0025	.0711	2.4	13.311	34738.415
.0050	.0978	4.5	15.175	27224.506
.0075	.1149	6.2	15.956	22844.275
.0100	.1277	7.7	16.394	20191.112
.0200	.1614	12.4	17.152	14769.619
.0300	.1835	16.1	17.442	12230.434
.0400	.2003	19.3	17.594	10697.739
.0500	.2140	22.1	17.686	9645.095
.0600	.2256	24.6	17.748	8864.931
.0700	.2358	27.0	17.792	8256.835
.0800	.2449	29.2	17.825	7765.564
.0900	.2531	31.3	17.850	7357.888
.1000	.2606	33.3	17.870	7012.467
.1500	.2912	42.2	17.927	5822.592
.2000	.3144	49.7	17.953	5107.827
.3000	.3494	62.6	17.976	4262.610
.4000	.3759	73.7	17.985	3759.428
.5000	.3976	83.7	17.990	3416.862
.6000	.4159	92.8	17.993	3163.554
.7000	.4319	101.3	17.995	2966.500
.8000	.4462	109.3	17.996	2807.481
.9000	.4590	116.9	17.997	2675.609
1.0000	.4706	124.2	17.998	2563.919
1.5000	.5173	156.9	17.999	2183.918
2.0000	.5520	185.5	17.999	1956.419
2.5000	.5796	211.6	18.000	1800.709
3.0000	.6027	235.7	18.000	1685.550
3.5000	.6224	258.5	18.000	1595.948
4.0000	.6396	280.1	18.000	1523.687
5.0000	.6685	320.6	18.000	1413.221
6.0000	.6921	358.9	18.000	1331.809
7.0000	.7120	395.0	18.000	1268.715
8.0000	.7292	429.5	18.000	1218.052
9.0000	.7441	462.8	18.000	1176.282
10.0000	.7574	494.9	18.000	1141.136
15.0000	.8067	644.4	18.000	1024.105
20.0000	.8393	781.6	18.000	957.313
30.0000	.8909	1036.2	18.000	884.421

ION IS 18 AR 38				
RANGE (CM)	BETA (V/C)	ENERGY (MEV/AMU)	ZEFF	DE/DX MEV/CM
.0025	.0691	2.2	13.135	35228.318
.0050	.0956	4.3	15.055	27841.277
.0075	.1126	6.0	15.864	23369.675
.0100	.1252	7.4	16.318	20670.419
.0200	.1586	11.9	17.105	15144.687
.0300	.1805	15.5	17.409	12542.328
.0400	.1971	18.6	17.568	10970.115
.0500	.2106	21.4	17.666	9889.920
.0600	.2221	23.9	17.731	9089.179
.0700	.2322	26.2	17.778	8464.975
.0800	.2412	28.3	17.813	7960.656
.0900	.2493	30.4	17.839	7542.134
.1000	.2567	32.3	17.860	7187.514
.1500	.2869	40.9	17.921	5969.110
.2000	.3099	48.2	17.949	5234.258
.3000	.3445	60.7	17.974	4365.561
.4000	.3708	71.5	17.984	3848.552
.5000	.3923	81.1	17.989	3495.734
.6000	.4104	90.0	17.992	3236.300
.7000	.4263	98.2	17.994	3033.916
.8000	.4404	106.0	17.996	2870.614
.9000	.4530	113.3	17.997	2735.200
1.0000	.4646	120.4	17.997	2620.516
1.5000	.5109	152.0	17.999	2230.354
2.0000	.5454	179.7	17.999	1996.774
2.5000	.5729	204.9	18.000	1836.890
3.0000	.5958	228.3	18.000	1718.629
3.5000	.6154	250.2	18.000	1626.600
4.0000	.6326	271.1	18.000	1552.367
5.0000	.6615	310.4	18.000	1438.856
6.0000	.6851	347.1	18.000	1355.162
7.0000	.7051	381.9	18.000	1290.269
8.0000	.7222	415.2	18.000	1238.133
9.0000	.7373	447.2	18.000	1195.124
10.0000	.7506	478.1	18.000	1158.915
15.0000	.8003	621.8	18.000	1038.117
20.0000	.8334	753.5	18.000	968.889
30.0000	.8757	997.2	18.000	892.737

AD-A121 994

STUDY AND ANALYZE ENERGETIC PARTICLE AND MAGNETIC
ACTIVITY DATA(U) EMMANUEL COLL BOSTON MASS PHYSICS
RESEARCH DIV L GENTILE ET AL. JUN 82 AFGL-TR-82-0217
F19628-79-C-0102 F/G 3/2

4/4

UNCLASSIFIED

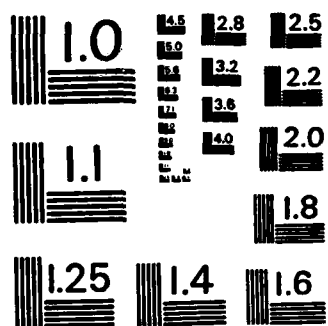
NL

END

FILMED

+

DTIC



MICROCOPY RESOLUTION TEST CHART
NATIONAL BUREAU OF STANDARDS-1963-A

ION IS 18 AR 40				
RANGE	BETA	ENERGY	ZEFF	DE/DX
(CM)	(V/C)	(MEV/AMU)		MEV/CM
.0025	.0673	2.1	12.964	35669.396
.0050	.0936	4.1	14.937	28427.286
.0075	.1104	5.7	15.773	23870.229
.0100	.1229	7.1	16.244	21133.625
.0200	.1559	11.5	17.059	15508.841
.0300	.1776	15.0	17.376	12845.550
.0400	.1940	18.0	17.543	11235.059
.0500	.2074	20.7	17.645	10128.127
.0600	.2188	23.1	17.714	9307.397
.0700	.2288	25.4	17.763	8667.536
.0800	.2377	27.5	17.800	8150.528
.0900	.2457	29.5	17.828	7721.458
.1000	.2531	31.3	17.850	7357.888
.1500	.2830	39.7	17.915	6111.936
.2000	.3057	46.8	17.945	5357.473
.3000	.3400	59.0	17.971	4465.858
.4000	.3660	69.4	17.982	3935.358
.5000	.3872	78.8	17.988	3573.400
.6000	.4053	87.4	17.992	3307.137
.7000	.4210	95.4	17.994	3099.556
.8000	.4349	102.9	17.995	2932.078
.9000	.4475	110.1	17.996	2793.211
1.0000	.4590	116.9	17.997	2675.609
1.5000	.5049	147.6	17.999	2275.553
2.0000	.5391	174.4	17.999	2036.056
2.5000	.5665	198.8	18.000	1872.113
3.0000	.5893	221.4	18.000	1750.836
3.5000	.6089	242.7	18.000	1656.448
4.0000	.6260	262.9	18.000	1580.301
5.0000	.6543	300.9	18.000	1463.833
6.0000	.6785	336.3	18.000	1377.926
7.0000	.6984	369.9	18.000	1311.288
8.0000	.7157	402.0	18.000	1257.726
9.0000	.7308	432.9	18.000	1213.519
10.0000	.7441	462.8	18.000	1176.282
15.0000	.7942	601.2	18.000	1051.850
20.0000	.8276	727.8	18.000	980.284
30.0000	.8707	961.8	18.000	901.024

ION IS 19 K 39				
RANGE	BETA	ENERGY	ZEFF	DE/DX
(CM)	(V/C)	(MEV/AMU)		MEV/CM
.0025	.0702	2.3	13.729	37643.177
.0050	.0974	4.4	15.790	29811.808
.0075	.1148	6.2	16.662	25072.333
.0100	.1277	7.7	17.153	22180.219
.0200	.1619	12.4	18.011	16238.803
.0300	.1842	16.2	18.342	13449.593
.0400	.2012	19.4	18.517	11764.982
.0500	.2150	22.3	18.625	10607.795
.0600	.2267	24.9	18.697	9750.102
.0700	.2370	27.3	18.749	9081.572
.0800	.2462	29.6	18.788	8541.482
.0900	.2545	31.7	18.818	8093.302
.1000	.2621	33.7	18.841	7713.568
.1500	.2929	42.7	18.910	6417.641
.2000	.3163	50.4	18.941	5629.311
.3000	.3516	63.5	18.969	4697.502
.4000	.3784	74.8	18.981	4143.005
.5000	.4002	84.9	18.987	3764.643
.6000	.4186	94.2	18.991	3486.604
.7000	.4348	102.8	18.993	3268.964
.8000	.4490	111.0	18.995	3093.863
.9000	.4619	118.7	18.996	2948.683
1.0000	.4737	126.1	18.997	2825.742
1.5000	.5205	159.4	18.999	2407.592
2.0000	.5554	188.5	18.999	2157.346
2.5000	.5831	215.0	19.000	1986.111
3.0000	.6062	239.7	19.000	1859.493
3.5000	.6260	262.8	19.000	1760.992
4.0000	.6432	284.9	19.000	1681.567
5.0000	.6721	326.4	19.000	1560.177
6.0000	.6957	365.2	19.000	1470.741
7.0000	.7156	402.0	19.000	1401.451
8.0000	.7327	437.2	19.000	1345.829
9.0000	.7477	471.1	19.000	1299.987
10.0000	.7609	503.9	19.000	1261.429
15.0000	.8100	656.5	19.000	1133.170
20.0000	.8424	796.7	19.000	1060.141
30.0000	.8836	1057.1	19.000	980.801

ION IS 20 CA 40

RANGE (CM)	BETA (V/C)	ENERGY (MEV/AMU)	ZEFF	DE/DX MEV/CM
.0025	.0713	2.4	14.311	40082.831
.0050	.0991	4.6	16.516	31816.576
.0075	.1168	6.4	17.452	26809.513
.0100	.1300	8.0	17.982	23721.824
.0200	.1650	12.9	18.911	17356.243
.0300	.1878	16.9	19.272	14376.466
.0400	.2051	20.2	19.463	12577.201
.0500	.2192	23.2	19.581	11341.478
.0600	.2311	25.9	19.661	10425.693
.0700	.2416	28.4	19.718	9711.950
.0800	.2510	30.8	19.761	9135.374
.0900	.2594	33.0	19.794	8656.944
.1000	.2671	35.1	19.821	8251.598
.1500	.2985	44.5	19.897	6876.852
.2000	.3224	52.5	19.932	6033.958
.3000	.3583	66.2	19.964	5037.746
.4000	.3856	78.0	19.978	4444.993
.5000	.4077	88.6	19.985	4040.565
.6000	.4265	98.3	19.989	3741.901
.7000	.4428	107.4	19.992	3510.395
.8000	.4573	115.9	19.994	3323.243
.9000	.4704	124.0	19.995	3168.094
1.0000	.4823	131.8	19.996	3036.725
1.5000	.5297	166.7	19.998	2590.021
2.0000	.5648	197.2	19.999	2322.788
2.5000	.5923	225.1	19.999	2139.990
3.0000	.6160	250.9	20.000	2004.866
3.5000	.6359	275.3	20.000	1899.788
4.0000	.6531	298.5	20.000	1815.088
5.0000	.6821	342.2	20.000	1685.705
6.0000	.7057	383.1	20.000	1590.455
7.0000	.7255	421.9	20.000	1516.722
8.0000	.7425	459.0	20.000	1457.588
9.0000	.7574	494.9	20.000	1408.897
10.0000	.7705	529.6	20.000	1367.983
15.0000	.8189	691.2	20.000	1232.316
20.0000	.8507	840.0	20.000	1155.607
30.0000	.8907	1117.3	20.000	1073.414

ION IS 20 CA 44

RANGE (CM)	BETA (V/C)	ENERGY (MEV/AMU)	ZEFF	DE/DX MEV/CM
.0025	.0677	2.1	13.945	40938.605
.0050	.0950	4.2	16.260	33054.919
.0075	.1125	6.0	17.254	27888.438
.0100	.1256	7.4	17.818	24714.200
.0200	.1599	12.1	18.808	18138.776
.0300	.1823	15.9	19.198	15028.088
.0400	.1992	19.1	19.405	13146.447
.0500	.2131	21.9	19.534	11853.177
.0600	.2248	24.5	19.621	10894.376
.0700	.2351	26.9	19.684	10146.946
.0800	.2443	29.1	19.731	9543.079
.0900	.2526	31.2	19.768	9041.963
.1000	.2601	33.2	19.797	8617.375
.1500	.2909	42.1	19.882	7172.282
.2000	.3143	49.7	19.922	6299.547
.3000	.3496	62.7	19.958	5253.844
.4000	.3764	73.9	19.974	4631.967
.5000	.3982	83.9	19.982	4207.813
.6000	.4166	93.1	19.987	3894.655
.7000	.4327	101.7	19.990	3651.139
.8000	.4469	109.8	19.992	3455.558
.9000	.4598	117.4	19.994	3292.942
1.0000	.4715	124.7	19.995	3155.267
1.5000	.5183	157.7	19.998	2687.191
2.0000	.5531	186.5	19.999	2407.184
2.5000	.5808	212.7	19.999	2215.619
3.0000	.6039	237.0	20.000	2073.983
3.5000	.6236	260.0	20.000	1963.804
4.0000	.6408	281.8	20.000	1874.962
5.0000	.6697	322.7	20.000	1739.175
6.0000	.6934	361.1	20.000	1639.124
7.0000	.7133	397.4	20.000	1561.599
8.0000	.7304	432.2	20.000	1499.358
9.0000	.7454	465.6	20.000	1448.051
10.0000	.7586	498.1	20.000	1404.888
15.0000	.8078	648.7	20.000	1261.220
20.0000	.8404	787.0	20.000	1179.299
30.0000	.8818	1043.6	20.000	1090.042

ION IS 20 CA 49

RANGE (CM)	BETA (V/C)	ENERGY (MEV/AMU)	ZEFF	DE/DX MEV/CM
.0025	.0646	1.9	13.600	41614.224
.0050	.0914	3.9	16.014	34177.052
.0075	.1087	5.5	17.061	28931.610
.0100	.1216	7.0	17.658	25647.291
.0200	.1553	11.4	18.708	18881.831
.0300	.1773	15.0	19.124	15648.532
.0400	.1940	18.0	19.348	13689.038
.0500	.2076	20.7	19.487	12341.172
.0600	.2192	23.2	19.581	11341.478
.0700	.2293	25.5	19.650	10561.983
.0800	.2383	27.6	19.701	9932.118
.0900	.2464	29.6	19.741	9409.379
.1000	.2539	31.5	19.773	8966.445
.1500	.2841	40.0	19.867	7458.805
.2000	.3071	47.3	19.911	6553.606
.3000	.3418	59.7	19.952	5460.437
.4000	.3681	70.3	19.970	4810.648
.5000	.3896	79.9	19.979	4367.600
.6000	.4077	88.6	19.985	4040.565
.7000	.4236	96.8	19.989	3786.301
.8000	.4376	104.4	19.991	3581.229
.9000	.4503	111.7	19.993	3412.156
1.0000	.4618	118.7	19.994	3268.448
1.5000	.5080	149.9	19.997	2779.950
2.0000	.5424	177.2	19.999	2487.752
2.5000	.5699	202.0	19.999	2287.830
3.0000	.5928	225.1	19.999	2139.990
3.5000	.6124	246.7	20.000	2024.958
4.0000	.6296	267.3	20.000	1932.178
5.0000	.6584	306.0	20.000	1790.310
6.0000	.6821	342.2	20.000	1685.705
7.0000	.7021	376.4	20.000	1604.589
8.0000	.7193	409.2	20.000	1539.411
9.0000	.7343	440.7	20.000	1485.635
10.0000	.7477	471.1	20.000	1440.352
15.0000	.7976	612.4	20.000	1289.178
20.0000	.8308	741.9	20.000	1202.409
30.0000	.8734	981.2	20.000	1106.667

ION IS 21 SC 45

RANGE (CM)	BETA (V/C)	ENERGY (MEV/AMU)	ZEFF	DE/DX MEV/CM
.0025	.0687	2.2	14.502	43403.700
.0050	.0966	4.4	16.966	35137.546
.0075	.1145	6.2	18.029	29700.702
.0100	.1278	7.7	18.632	26326.017
.0200	.1629	12.6	19.699	19310.500
.0300	.1857	16.5	20.120	16000.199
.0400	.2030	19.8	20.345	13998.296
.0500	.2171	22.3	20.485	12622.618
.0600	.2291	25.4	20.580	11602.855
.0700	.2396	27.9	20.649	10807.960
.0800	.2489	30.3	20.701	10165.829
.0900	.2573	32.5	20.741	9632.973
.1000	.2651	34.5	20.773	9181.514
.1500	.2964	43.8	20.867	7645.088
.2000	.3202	51.8	20.911	6724.438
.3000	.3561	65.3	20.952	5611.037
.4000	.3833	77.0	20.970	4948.955
.5000	.4055	87.5	20.979	4497.413
.6000	.4242	97.1	20.985	4164.057
.7000	.4405	106.0	20.989	3904.850
.8000	.4550	114.5	20.991	3695.777
.9000	.4680	122.5	20.993	3523.246
1.0000	.4798	130.2	20.994	3376.707
1.5000	.5272	164.6	20.997	2878.623
2.0000	.5623	194.8	20.999	2580.777
2.5000	.5902	222.3	20.999	2377.076
3.0000	.6134	247.9	20.999	2226.516
3.5000	.6332	271.9	21.000	2109.437
4.0000	.6505	294.8	21.000	2015.056
5.0000	.6794	337.9	21.000	1970.884
6.0000	.7031	378.3	21.000	1764.733
7.0000	.7229	415.5	21.000	1682.548
8.0000	.7400	453.2	21.000	1616.621
9.0000	.7548	489.5	21.000	1562.325
10.0000	.7680	522.7	21.000	1516.690
15.0000	.8165	681.9	21.000	1365.244
20.0000	.8485	828.4	21.000	1279.454
30.0000	.8889	1101.2	21.000	1187.179

ION IS 22 TI 46				
RANGE (CM)	BETA (V/C)	ENERGY (MEV/AMU)	ZEFF	DE/DX MEV/CM
.0025	.0696	2.3	15.048	45884.853
.0050	.0981	4.5	17.664	37250.481
.0075	.1163	6.4	18.794	31544.890
.0100	.1299	8.0	19.439	27967.514
.0200	.1657	13.1	20.585	20504.336
.0300	.1890	17.1	21.038	16990.954
.0400	.2066	20.5	21.281	14866.665
.0500	.2210	23.6	21.433	13407.120
.0600	.2332	26.4	21.537	12325.319
.0700	.2438	29.0	21.612	11482.161
.0800	.2533	31.4	21.668	10801.050
.0900	.2619	33.7	21.712	10235.897
.1000	.2698	35.9	21.747	9757.093
.1500	.3016	45.5	21.851	8127.732
.2000	.3259	53.8	21.900	7158.498
.3000	.3624	67.9	21.945	5976.192
.4000	.3900	80.1	21.965	5273.186
.5000	.4125	91.0	21.976	4793.766
.6000	.4315	101.0	21.983	4439.851
.7000	.4480	110.4	21.987	4164.675
.8000	.4626	119.2	21.990	3942.735
.9000	.4758	127.5	21.992	3758.781
1.0000	.4878	135.5	21.993	3603.739
1.5000	.5356	171.5	21.997	3075.108
2.0000	.5710	203.1	21.998	2759.120
2.5000	.5992	231.9	21.999	2543.088
3.0000	.6225	258.6	21.999	2383.467
3.5000	.6424	283.8	21.999	2259.380
4.0000	.6597	307.8	22.000	2159.393
5.0000	.6886	353.0	22.000	2006.734
6.0000	.7122	395.3	22.000	1894.422
7.0000	.7320	435.5	22.000	1807.539
8.0000	.7489	474.1	22.000	1737.907
9.0000	.7637	511.2	22.000	1680.613
10.0000	.7767	547.2	22.000	1632.507
15.0000	.8247	715.0	22.000	1473.363
20.0000	.8560	869.9	22.000	1383.849
30.0000	.8953	1159.1	22.000	1288.934

ION IS 22 TI 48				
RANGE (CM)	BETA (V/C)	ENERGY (MEV/AMU)	ZEFF	DE/DX MEV/CM
.0025	.0680	2.2	14.859	46242.307
.0050	.0962	4.3	17.529	37866.392
.0075	.1144	6.1	18.688	32095.520
.0100	.1279	7.7	19.351	28478.725
.0200	.1634	12.7	20.529	20911.028
.0300	.1865	16.6	20.997	17330.142
.0400	.2040	20.0	21.249	15163.093
.0500	.2182	23.0	21.407	13673.607
.0600	.2303	25.7	21.514	12569.402
.0700	.2409	28.2	21.592	11708.692
.0800	.2503	30.6	21.651	11013.358
.0900	.2588	32.8	21.697	10436.381
.1000	.2666	35.0	21.734	9947.549
.1500	.2982	44.4	21.842	8284.022
.2000	.3222	52.5	21.894	7297.405
.3000	.3584	66.3	21.942	6089.148
.4000	.3858	78.2	21.963	5370.875
.5000	.4081	88.8	21.974	4881.120
.6000	.4270	98.6	21.981	4519.614
.7000	.4434	107.7	21.986	4238.556
.8000	.4579	116.3	21.989	4011.886
.9000	.4710	124.4	21.991	3824.018
1.0000	.4829	132.2	21.993	3665.605
1.5000	.5305	167.3	21.997	3125.770
2.0000	.5657	198.1	21.998	2803.094
2.5000	.5938	226.1	21.999	2582.474
3.0000	.6170	252.1	21.999	2419.443
3.5000	.6369	276.6	21.999	2292.687
4.0000	.6541	299.9	22.000	2190.532
5.0000	.6831	343.8	22.000	2034.518
6.0000	.7067	385.0	22.000	1919.689
7.0000	.7266	424.0	22.000	1830.816
8.0000	.7436	461.4	22.000	1759.550
9.0000	.7584	497.4	22.000	1700.880
10.0000	.7715	532.3	22.000	1651.589
15.0000	.8193	694.9	22.000	1488.212
20.0000	.8515	844.7	22.000	1395.918
30.0000	.8915	1124.0	22.000	1297.190

ION IS 23 V 51				
RANGE	BETA	ENERGY	ZEFF	DE/DX
(CM)	(V/C)	(MEV/AMU)		MEV/CM
.0025	.0673	2.1	15.198	49043.061
.0050	.0959	4.3	18.074	40632.885
.0075	.1143	6.1	19.335	34540.194
.0100	.1279	7.7	20.058	30682.024
.0200	.1639	12.8	21.350	22553.404
.0300	.1873	16.8	21.867	18695.559
.0400	.2050	20.2	22.147	16359.180
.0500	.2193	23.2	22.323	14752.935
.0600	.2315	26.0	22.443	13562.080
.0700	.2422	28.6	22.531	12633.807
.0800	.2517	31.0	22.598	11883.894
.0900	.2603	33.2	22.649	11261.636
.1000	.2681	35.4	22.691	10734.451
.1500	.3000	45.0	22.815	8940.499
.2000	.3242	53.2	22.874	7866.535
.3000	.3607	67.2	22.930	6581.154
.4000	.3983	79.3	22.955	5805.141
.5000	.4107	90.1	22.969	5276.122
.6000	.4297	100.1	22.977	4885.695
.7000	.4462	109.3	22.982	4582.192
.8000	.4609	118.1	22.986	4337.445
.9000	.4741	126.4	22.989	4134.614
1.0000	.4860	134.3	22.991	3962.932
1.5000	.5338	170.0	22.996	3380.542
2.0000	.5692	201.3	22.998	3032.364
2.5000	.5973	229.8	22.998	2794.376
3.0000	.6206	256.3	22.999	2618.553
3.5000	.6405	281.3	22.999	2481.878
4.0000	.6578	305.1	22.999	2371.749
5.0000	.6867	349.8	23.000	2203.602
6.0000	.7103	391.8	23.000	2079.888
7.0000	.7301	431.6	23.000	1984.173
8.0000	.7471	469.7	23.000	1907.451
9.0000	.7619	506.5	23.000	1844.313
10.0000	.7749	542.1	23.000	1791.291
15.0000	.8230	708.2	23.000	1615.775
20.0000	.8545	861.3	23.000	1516.909
30.0000	.8940	1147.1	23.000	1411.760

ION IS 24 CK 50				
RANGE	BETA	ENERGY	ZEFF	DE/DX
(CM)	(V/C)	(MEV/AMU)		MEV/CM
.0025	.0696	2.3	15.907	51234.650
.0050	.0990	4.6	18.888	42216.798
.0075	.1178	6.5	20.191	35913.413
.0100	.1318	8.2	20.939	31884.523
.0200	.1688	13.6	22.283	23393.433
.0300	.1928	17.8	22.819	19391.211
.0400	.2109	21.4	23.110	16969.960
.0500	.2256	24.6	23.293	15306.224
.0600	.2381	27.6	23.418	14073.110
.0700	.2490	30.3	23.510	13112.075
.0800	.2587	32.8	23.579	12335.793
.0900	.2675	35.2	23.633	11691.711
.1000	.2756	37.5	23.676	11146.070
.1500	.3082	47.6	23.905	9289.490
.2000	.3329	56.3	23.868	8178.111
.3000	.3702	71.2	23.926	6851.303
.4000	.3985	84.1	23.953	6047.938
.5000	.4213	95.6	23.967	5500.223
.6000	.4407	106.2	23.975	5095.979
.7000	.4575	116.0	23.981	4781.729
.8000	.4724	125.3	23.985	4528.315
.9000	.4858	134.2	23.988	4318.305
1.0000	.4980	142.6	23.990	4140.550
1.5000	.5465	180.7	23.995	3537.433
2.0000	.5822	214.2	23.997	3177.072
2.5000	.6106	244.6	23.998	2930.862
3.0000	.6341	273.0	23.999	2749.049
3.5000	.6540	299.7	23.999	2607.790
4.0000	.6714	325.2	23.999	2494.028
5.0000	.7003	373.3	24.000	2320.480
6.0000	.7238	418.4	24.000	2192.949
7.0000	.7435	461.2	24.000	2094.416
8.0000	.7603	502.3	24.000	2015.548
9.0000	.7749	541.9	24.000	1950.746
10.0000	.7877	580.4	24.000	1896.417
15.0000	.8348	760.1	24.000	1717.509
20.0000	.8653	926.4	24.000	1617.934
30.0000	.9032	1238.3	24.000	1514.637

ION IS 24 CR 52				
RANGE (CM)	BETA (V/C)	ENERGY (MEV/AMU)	ZEFF	DE/DX MEV/CM
.0025	.0680	2.2	15.711	51537.743
.0050	.0972	4.4	18.745	42839.246
.0075	.1159	6.3	20.079	36481.904
.0100	.1299	8.0	20.845	32416.462
.0200	.1666	13.2	22.222	23819.752
.0300	.1904	17.3	22.774	19747.156
.0400	.2083	20.9	23.074	17281.097
.0500	.2229	24.0	23.263	15585.935
.0600	.2354	26.9	23.393	14329.293
.0700	.2462	29.6	23.488	13349.820
.0800	.2558	32.1	23.559	12558.596
.0900	.2646	34.4	23.615	11902.094
.1000	.2726	36.6	23.661	11345.918
.1500	.3049	46.6	23.795	9453.456
.2000	.3295	55.1	23.860	8320.606
.3000	.3665	69.6	23.922	6970.175
.4000	.3945	82.2	23.950	6150.716
.5000	.4173	93.5	23.965	5592.105
.6000	.4365	103.8	23.974	5179.859
.7000	.4532	113.4	23.980	4859.412
.8000	.4680	122.5	23.984	4601.013
.9000	.4813	131.2	23.987	4386.880
1.0000	.4935	139.4	23.989	4205.639
1.5000	.5417	176.6	23.995	3590.654
2.0000	.5773	209.2	23.997	3223.234
2.5000	.6056	239.0	23.998	2972.183
3.0000	.6290	266.6	23.999	2786.772
3.5000	.6489	292.7	23.999	2642.695
4.0000	.6663	317.5	23.999	2526.643
5.0000	.6952	364.3	24.000	2349.549
6.0000	.7188	408.2	24.000	2219.353
7.0000	.7385	449.8	24.000	2118.708
8.0000	.7554	489.8	24.000	2038.107
9.0000	.7700	528.3	24.000	1971.841
10.0000	.7830	565.7	24.000	1916.247
15.0000	.8304	740.2	24.000	1732.803
20.0000	.8613	901.4	24.000	1630.218
30.0000	.8998	1203.2	24.000	1522.727

ION IS 25 MN 53				
RANGE (CM)	BETA (V/C)	ENERGY (MEV/AMU)	ZEFF	DE/DX MEV/CM
.0025	.0688	2.2	16.215	54039.007
.0050	.0985	4.5	19.407	45071.325
.0075	.1176	6.5	20.816	38452.219
.0100	.1317	8.2	21.626	34178.194
.0200	.1691	13.6	23.090	25106.933
.0300	.1933	17.9	23.678	20816.391
.0400	.2116	21.6	23.998	18218.671
.0500	.2264	24.8	24.201	16433.226
.0600	.2390	27.8	24.340	15109.785
.0700	.2501	30.6	24.442	14078.326
.0800	.2599	33.1	24.519	13245.156
.0900	.2687	35.6	24.580	12553.883
.1000	.2768	37.9	24.629	11968.272
.1500	.3096	48.1	24.774	9975.794
.2000	.3345	56.9	24.846	8783.162
.3000	.3721	72.0	24.913	7366.797
.4000	.4005	85.1	24.943	6503.226
.5000	.4235	96.7	24.960	5914.569
.6000	.4430	107.5	24.970	5480.169
.7000	.4599	117.5	24.977	5142.518
.8000	.4749	126.9	24.982	4870.260
.9000	.4884	135.9	24.985	4644.653
1.0000	.5006	144.5	24.988	4453.711
1.5000	.5493	183.1	24.994	3805.683
2.0000	.5851	217.1	24.997	3418.738
2.5000	.6135	248.0	24.998	3154.444
3.0000	.6370	276.8	24.998	2959.323
3.5000	.6570	304.0	24.999	2807.755
4.0000	.6744	329.9	24.999	2685.715
5.0000	.7033	378.7	24.999	2499.586
6.0000	.7268	424.5	25.000	2362.861
7.0000	.7464	468.0	25.000	2257.262
8.0000	.7632	509.8	25.000	2172.773
9.0000	.7777	550.1	25.000	2103.379
10.0000	.7905	589.3	25.000	2045.225
15.0000	.8374	772.2	25.000	1853.976
20.0000	.8676	941.6	25.000	1747.855
30.0000	.9052	1259.7	25.000	1638.479

ION IS 25 MN 54				
RANGE (CM)	BETA (V/C)	ENERGY (MEV/AMU)	ZEFF	DE/DX MEV/CM
.0025	.0680	2.2	16.116	54170.510
.0050	.0976	4.5	19.334	45379.408
.0075	.1167	6.4	20.758	38738.022
.0100	.1308	8.1	21.578	34447.127
.0200	.1681	13.4	23.059	25323.630
.0300	.1922	17.7	23.654	20997.491
.0400	.2104	21.3	23.980	18377.016
.0500	.2252	24.5	24.185	16575.588
.0600	.2377	27.5	24.327	15240.175
.0700	.2487	30.2	24.430	14199.330
.0800	.2585	32.8	24.509	13358.554
.0900	.2673	35.2	24.571	12660.956
.1000	.2754	37.4	24.620	12069.982
.1500	.3081	47.6	24.769	10059.234
.2000	.3329	56.3	24.842	8855.671
.3000	.3703	71.3	24.910	7427.384
.4000	.3986	84.1	24.942	6555.603
.5000	.4216	95.7	24.959	5961.387
.6000	.4410	106.3	24.969	5522.906
.7000	.4578	116.2	24.976	5182.093
.8000	.4728	125.6	24.981	4907.292
.9000	.4862	134.4	24.985	4679.582
1.0000	.4984	142.9	24.987	4486.863
1.5000	.5470	181.1	24.994	3832.312
2.0000	.5828	214.7	24.996	3442.238
2.5000	.6111	245.2	24.998	3175.473
3.0000	.6346	273.7	24.998	2978.516
3.5000	.6546	300.5	24.999	2825.510
4.0000	.6719	326.1	24.999	2702.301
5.0000	.7009	374.3	24.999	2514.362
6.0000	.7244	419.5	25.000	2376.276
7.0000	.7440	462.5	25.000	2269.598
8.0000	.7608	503.7	25.000	2184.222
9.0000	.7754	543.5	25.000	2114.079
10.0000	.7883	582.1	25.000	2055.278
15.0000	.8353	762.4	25.000	1861.701
20.0000	.8653	929.4	25.000	1754.030
30.0000	.9036	1242.5	25.000	1642.478

ION IS 25 MN 55				
RANGE (CM)	BETA (V/C)	ENERGY (MEV/AMU)	ZEFF	DE/DX MEV/CM
.0025	.0673	2.1	16.018	54291.901
.0050	.0968	4.4	19.262	45680.131
.0075	.1158	6.3	20.700	39019.231
.0100	.1299	8.0	21.530	34712.473
.0200	.1670	13.3	23.027	25538.015
.0300	.1911	17.5	23.631	21176.784
.0400	.2092	21.1	23.961	18533.822
.0500	.2239	24.3	24.170	16716.585
.0600	.2364	27.2	24.314	15369.323
.0700	.2474	29.9	24.419	14319.187
.0800	.2571	32.4	24.499	13470.878
.0900	.2659	34.8	24.561	12767.018
.1000	.2740	37.0	24.612	12170.732
.1500	.3065	47.1	24.764	10141.888
.2000	.3313	55.7	24.838	8927.496
.3000	.3685	70.5	24.908	7487.422
.4000	.3968	83.3	24.940	6607.500
.5000	.4197	94.7	24.958	6007.774
.6000	.4390	105.2	24.968	5565.248
.7000	.4558	115.0	24.976	5221.301
.8000	.4707	124.2	24.981	4943.981
.9000	.4841	133.0	24.984	4714.187
1.0000	.4963	141.4	24.987	4519.706
1.5000	.5447	179.2	24.994	3859.182
2.0000	.5804	212.3	24.996	3465.519
2.5000	.6088	242.6	24.998	3196.308
3.0000	.6322	270.7	24.998	2997.534
3.5000	.6522	297.2	24.999	2843.104
4.0000	.6695	322.5	24.999	2718.739
5.0000	.6985	370.1	24.999	2529.009
6.0000	.7220	414.7	25.000	2389.576
7.0000	.7417	457.1	25.000	2281.832
8.0000	.7585	497.8	25.000	2195.579
9.0000	.7732	537.1	25.000	2124.696
10.0000	.7860	575.2	25.000	2065.256
15.0000	.8333	753.0	25.000	1869.384
20.0000	.8639	917.6	25.000	1760.187
30.0000	.9020	1225.9	25.000	1646.504

ION IS 26 FE 54				
RANGE (CM)	BETA (V/C)	ENERGY (MEV/AMU)	ZEFF	DE/DX MEV/CM
.0025	.0695	2.3	16.709	56545.066
.0050	.0997	4.7	20.062	47328.250
.0075	.1191	6.7	21.546	40450.511
.0100	.1335	8.4	22.402	35966.754
.0200	.1716	14.0	23.954	26414.710
.0300	.1962	18.5	24.578	21903.080
.0400	.2147	22.2	24.920	19171.747
.0500	.2298	25.6	25.136	17294.669
.0600	.2426	28.7	25.285	15903.430
.0700	.2538	31.5	25.394	14819.205
.0800	.2637	34.2	25.477	13943.463
.0900	.2727	36.7	25.542	13216.899
.1000	.2810	39.1	25.595	12601.414
.1500	.3142	49.7	25.753	10507.432
.2000	.3395	58.8	25.830	9254.130
.3000	.3775	74.4	25.903	7761.231
.4000	.4063	87.9	25.937	6862.613
.5000	.4296	100.0	25.955	6243.461
.6000	.4493	111.1	25.967	5786.578
.7000	.4664	121.5	25.974	5431.468
.8000	.4815	131.3	25.979	5145.147
.9000	.4951	140.6	25.983	4907.899
1.0000	.5075	149.5	25.986	4707.114
1.5000	.5565	189.6	25.993	4025.264
2.0000	.5926	224.8	25.996	3618.861
2.5000	.6211	257.0	25.997	3341.148
3.0000	.6447	286.9	25.998	3136.196
3.5000	.6647	315.2	25.999	2977.051
4.0000	.6821	342.2	25.999	2848.959
5.0000	.7110	393.0	25.999	2653.716
6.0000	.7344	440.8	26.000	2510.418
7.0000	.7539	486.2	26.000	2399.844
8.0000	.7706	529.8	26.000	2311.461
9.0000	.7850	571.9	26.000	2238.946
10.0000	.7977	612.8	26.000	2178.244
15.0000	.8439	804.2	26.000	1979.330
20.0000	.8736	982.0	26.000	1869.877
30.0000	.9102	1316.5	26.000	1759.110

ION IS 26 FE 56				
RANGE (CM)	BETA (V/C)	ENERGY (MEV/AMU)	ZEFF	DE/DX MEV/CM
.0025	.0680	2.2	16.507	56787.682
.0050	.0980	4.5	19.911	47951.877
.0075	.1173	6.5	21.426	41033.861
.0100	.1317	8.2	22.302	36517.377
.0200	.1695	13.7	23.888	26859.696
.0300	.1939	18.0	24.529	22275.084
.0400	.2123	21.7	24.881	19497.013
.0500	.2273	25.0	25.103	17587.094
.0600	.2400	28.0	25.257	16171.249
.0700	.2511	30.8	25.370	15067.736
.0800	.2610	33.4	25.456	14176.361
.0900	.2699	35.9	25.523	13436.802
.1000	.2781	38.2	25.577	12810.295
.1500	.3111	48.6	25.741	10678.776
.2000	.3362	57.6	25.821	9403.021
.3000	.3740	72.9	25.898	7883.425
.4000	.4026	86.1	25.933	6970.278
.5000	.4257	97.9	25.953	6339.694
.6000	.4453	108.8	25.964	5874.416
.7000	.4623	119.0	25.972	5512.803
.8000	.4774	128.5	25.978	5221.252
.9000	.4909	137.6	25.982	4979.678
1.0000	.5032	146.3	25.985	4775.237
1.5000	.5520	185.6	25.993	4080.982
2.0000	.5880	220.0	25.996	3667.124
2.5000	.6165	251.4	25.997	3384.323
3.0000	.6400	280.7	25.998	3175.589
3.5000	.6600	308.3	25.999	3013.481
4.0000	.6774	334.6	25.999	2882.979
5.0000	.7063	384.2	25.999	2684.002
6.0000	.7298	430.7	25.999	2537.893
7.0000	.7493	475.0	26.000	2425.089
8.0000	.7661	517.5	26.000	2334.871
9.0000	.7806	558.5	26.000	2260.804
10.0000	.7933	598.3	26.000	2198.761
15.0000	.8399	784.5	26.000	1995.003
20.0000	.8700	957.2	26.000	1882.302
30.0000	.9071	1281.5	26.000	1766.934

ION IS 26 FE 58				
RANGE	BETA	ENERGY	ZEFF	DE/DX
(CM)	(V/C)	(MEV/AMU)		MEV/CM
.0025	.0666	2.1	16.310	56990.822
.0050	.0964	4.4	19.764	48545.967
.0075	.1156	6.3	21.309	41598.844
.0100	.1299	8.0	22.203	37053.706
.0200	.1675	13.3	23.824	27295.525
.0300	.1917	17.6	24.481	22639.949
.0400	.2100	21.2	24.842	19816.207
.0500	.2249	24.5	25.071	17874.133
.0600	.2375	27.4	25.229	16434.173
.0700	.2486	30.2	25.345	15311.743
.0800	.2584	32.7	25.434	14405.030
.0900	.2672	35.1	25.504	13652.717
.1000	.2754	37.4	25.560	13015.392
.1500	.3082	47.6	25.729	10847.019
.2000	.3331	56.4	25.813	9549.213
.3000	.3706	71.4	25.893	8003.399
.4000	.3990	84.3	25.929	7076.056
.5000	.4220	96.0	25.950	6434.230
.6000	.4415	106.6	25.962	5960.699
.7000	.4584	116.6	25.971	5592.694
.8000	.4734	125.9	25.977	5296.003
.9000	.4868	134.9	25.981	5050.178
1.0000	.4991	143.4	25.984	4842.144
1.5000	.5477	181.8	25.992	4135.705
2.0000	.5836	215.5	25.995	3714.530
2.5000	.6120	246.2	25.997	3426.735
3.0000	.6354	274.8	25.998	3214.291
3.5000	.6554	301.7	25.998	3049.277
4.0000	.6728	327.4	25.999	2916.415
5.0000	.7018	375.9	25.999	2713.779
6.0000	.7253	421.3	25.999	2564.919
7.0000	.7449	464.5	26.000	2449.936
8.0000	.7617	505.9	26.000	2357.926
9.0000	.7763	545.9	26.000	2282.344
10.0000	.7891	584.7	26.000	2218.992
15.0000	.8361	766.0	26.000	2010.522
20.0000	.8665	933.9	26.000	1894.676
30.0000	.9042	1248.8	26.000	1774.886

ION IS 27 CO 59				
RANGE	BETA	ENERGY	ZEFF	DE/DX
(CM)	(V/C)	(MEV/AMU)		MEV/CM
.0025	.0673	2.1	16.784	59476.179
.0050	.0975	4.5	20.401	50854.020
.0075	.1171	6.4	22.024	43655.700
.0100	.1316	8.2	22.965	38900.277
.0200	.1698	13.7	24.678	28650.932
.0300	.1945	18.1	25.374	23766.722
.0400	.2131	21.9	25.757	20804.515
.0500	.2282	25.2	26.000	18767.415
.0600	.2410	28.3	26.169	17257.128
.0700	.2522	31.1	26.293	16079.962
.0800	.2622	33.7	26.388	15129.085
.0900	.2711	36.2	26.462	14340.164
.1000	.2794	38.6	26.523	13671.850
.1500	.3126	49.1	26.705	11398.198
.2000	.3379	58.2	26.795	10037.480
.3000	.3759	73.7	26.882	8416.803
.4000	.4046	87.1	26.922	7448.927
.5000	.4277	99.1	26.944	6775.451
.6000	.4476	110.1	26.958	6270.586
.7000	.4647	120.4	26.967	5892.462
.8000	.4798	130.2	26.974	5581.177
.9000	.4934	139.4	26.978	5323.272
1.0000	.5058	148.2	26.982	5105.025
1.5000	.5548	188.0	26.991	4364.008
2.0000	.5909	223.0	26.995	3921.765
2.5000	.6194	254.9	26.996	3620.441
3.0000	.6429	284.6	26.997	3397.794
3.5000	.6630	312.6	26.998	3224.918
4.0000	.6803	339.3	26.999	3085.778
5.0000	.7093	389.7	26.999	2873.687
6.0000	.7327	437.1	26.999	2719.010
7.0000	.7522	482.1	26.999	2597.867
8.0000	.7689	525.3	27.000	2501.818
9.0000	.7834	567.0	27.000	2422.998
10.0000	.7961	607.5	27.000	2357.003
15.0000	.8424	797.0	27.000	2140.580
20.0000	.8723	972.9	27.000	2021.271
30.0000	.9091	1303.8	27.000	1900.019

ION IS 28 NI 58				
RANGE (CM)	BETA (V/C)	ENERGY (MEV/AMU)	ZEFF	DE/DX MEV/CM
.0025	.0693	2.2	17.457	61782.747
.0050	.1003	4.7	21.188	52563.813
.0075	.1202	6.8	22.859	45142.948
.0100	.1350	8.6	23.827	40204.649
.0200	.1742	14.5	25.598	29563.315
.0300	.1994	19.1	26.316	24522.863
.0400	.2183	23.0	26.711	21468.890
.0500	.2338	26.5	26.963	19369.668
.0600	.2468	29.7	27.137	17813.738
.0700	.2583	32.7	27.266	16601.196
.0800	.2684	35.5	27.364	15621.854
.0900	.2776	38.1	27.441	14809.376
.1000	.2860	40.6	27.503	14121.145
.1500	.3197	51.6	27.692	11779.922
.2000	.3456	61.2	27.786	10378.847
.3000	.3843	77.5	27.876	8710.130
.4000	.4136	91.6	27.918	7716.102
.5000	.4373	104.2	27.941	7022.500
.6000	.4573	115.9	27.956	6510.762
.7000	.4746	126.8	27.965	6113.075
.8000	.4900	137.0	27.972	5792.468
.9000	.5038	146.8	27.977	5526.845
1.0000	.5163	156.1	27.981	5302.074
1.5000	.5658	198.2	27.990	4539.004
2.0000	.6022	235.2	27.994	4083.752
2.5000	.6307	269.0	27.996	3773.566
3.0000	.6545	300.5	27.997	3544.567
3.5000	.6746	330.3	27.998	3366.856
4.0000	.6920	358.6	27.998	3223.907
5.0000	.7208	412.2	27.999	3006.210
6.0000	.7441	462.6	27.999	2846.634
7.0000	.7635	510.6	27.999	2723.664
8.0000	.7800	556.7	28.000	2625.513
9.0000	.7942	601.3	28.000	2545.107
10.0000	.8067	644.5	28.000	2477.909
15.0000	.8520	847.6	28.000	2258.852
20.0000	.8810	1036.3	28.000	2139.799
30.0000	.9163	1394.1	28.000	2022.652

ION IS 28 NI 60				
RANGE (CM)	BETA (V/C)	ENERGY (MEV/AMU)	ZEFF	DE/DX MEV/CM
.0025	.0679	2.2	17.249	61960.413
.0050	.0986	4.6	21.031	53183.458
.0075	.1185	6.6	22.733	45738.226
.0100	.1333	8.4	23.722	40771.984
.0200	.1722	14.1	25.528	30026.080
.0300	.1972	18.7	26.263	24910.293
.0400	.2161	22.5	26.669	21807.764
.0500	.2314	26.0	26.927	19674.351
.0600	.2444	29.1	27.107	18092.782
.0700	.2557	32.0	27.239	16860.134
.0800	.2658	34.7	27.340	15864.492
.0900	.2749	37.3	27.420	15038.465
.1000	.2833	39.8	27.484	14338.741
.1500	.3170	50.6	27.679	11958.384
.2000	.3425	60.0	27.776	10533.905
.3000	.3810	76.0	27.870	8837.369
.4000	.4101	89.8	27.914	7828.475
.5000	.4336	102.2	27.938	7122.925
.6000	.4535	113.6	27.953	6602.412
.7000	.4708	124.3	27.963	6197.928
.8000	.4861	134.3	27.970	5871.855
.9000	.4998	143.9	27.976	5601.710
1.0000	.5122	153.0	27.980	5373.117
1.5000	.5616	194.2	27.990	4597.079
2.0000	.5979	230.5	27.994	4134.065
2.5000	.6265	263.5	27.996	3818.523
3.0000	.6501	294.3	27.997	3585.561
3.5000	.6702	323.4	27.998	3404.744
4.0000	.6876	351.2	27.998	3259.268
5.0000	.7164	403.6	27.999	3037.651
6.0000	.7398	452.8	27.999	2875.120
7.0000	.7592	499.6	27.999	2749.803
8.0000	.7758	544.6	28.000	2649.717
9.0000	.7901	588.0	28.000	2567.671
10.0000	.8027	630.2	28.000	2499.053
15.0000	.8484	828.1	28.000	2274.839
20.0000	.8777	1012.1	28.000	2152.291
30.0000	.9136	1359.1	28.000	2030.115

ION IS 30 ZN 64				
RANGE	BETA	ENERGY	ZEFF	DE/DX
(CM)	(V/C)	(MEV/AMU)		MEV/CM
.0025	.0677	2.1	17.944	67029.630
.0050	.0991	4.6	22.105	58513.911
.0075	.1195	6.7	24.001	50582.310
.0100	.1347	8.6	25.107	45171.237
.0200	.1746	14.5	27.142	33314.502
.0300	.2002	19.2	27.976	27649.486
.0400	.2195	23.3	28.439	24210.575
.0500	.2352	26.9	28.736	21845.250
.0600	.2484	30.1	28.942	20091.655
.0700	.2600	33.2	29.095	18724.944
.0800	.2703	36.0	29.212	17621.053
.0900	.2796	38.7	29.305	16705.253
.1000	.2881	41.2	29.380	15929.517
.1500	.3225	52.5	29.610	13290.845
.2000	.3485	62.3	29.725	11712.007
.3000	.3876	79.0	29.838	9831.864
.4000	.4171	93.4	29.891	8706.172
.5000	.4410	106.3	29.921	7940.929
.6000	.4612	118.3	29.940	7363.062
.7000	.4787	129.4	29.952	6914.063
.8000	.4942	139.9	29.961	6552.149
.9000	.5081	149.9	29.968	6252.345
1.0000	.5207	159.5	29.973	5998.683
1.5000	.5706	202.7	29.986	5137.793
2.0000	.6071	240.6	29.992	4624.419
2.5000	.6359	275.3	29.994	4274.243
3.0000	.6596	307.7	29.996	4016.399
3.5000	.6796	338.2	29.997	3816.225
4.0000	.6970	367.4	29.997	3655.273
5.0000	.7258	422.5	29.998	3410.302
6.0000	.7490	474.3	29.999	3230.875
7.0000	.7683	523.7	29.999	3092.720
8.0000	.7847	571.1	29.999	2982.541
9.0000	.7989	617.0	29.999	2892.363
10.0000	.8113	661.6	29.999	2817.070
15.0000	.8562	871.0	30.000	2572.360
20.0000	.8847	1066.3	30.000	2440.327
30.0000	.9194	1436.1	30.000	2312.590

Appendix II

In Table II are listed some quantities which are useful for calculations on relativistic ions. The first column in the table lists the kinetic energy per nucleon. The energy is linked to other parameters by common relativistic dynamics.

Momentum:

Starting from relativistic invariant

$$E^2 = p^2 c^2 + m_0^2 c^4 \quad \text{.....} \quad \Lambda 2-1$$

the momentum p (MeV/c) of a proton with mass m_p (MeV) is given by

$$p = \frac{1}{c} (E^2 - m_p^2 c^4)^{1/2} \quad \text{.....} \quad \Lambda 2-2$$

$$\text{or} \quad pc = (E^2 - m_p^2 c^4)^{1/2} \quad \text{.....} \quad \Lambda 2-3$$

Rigidity:

The rigidity $p(a,z)$ of a heavy ion with mass number Λ and charge z is given by

$$p(\Lambda, z) = \frac{\Lambda}{z} pc \quad \Lambda 2-4$$

The momentum times c can be found in column four.

Λ and z for a certain ion can be found in the track parameter table.

PRINTOUT TABLE II

Velocity (β), Momentum times Velocity (pc, MeV) as a
function of Heavy Ion Energy (E, MeV/amu)

ENERGY MEV/AMU	BETA (U/C)	GAMMA	PC (MEV)
5.	.1032	1.01	96.6
10.	.1454	1.01	136.8
20.	.2040	1.02	194.0
30.	.2479	1.03	238.3
40.	.2840	1.04	275.8
50.	.3152	1.05	309.2
60.	.3426	1.06	339.6
70.	.3674	1.08	367.8
80.	.3898	1.09	394.2
90.	.4105	1.10	419.2
100.	.4296	1.11	443.0
200.	.5678	1.21	642.2
300.	.6542	1.32	805.4
400.	.7146	1.43	951.3
500.	.7594	1.54	1086.8
600.	.7938	1.64	1215.5
700.	.8211	1.75	1339.3
800.	.8430	1.86	1459.4
900.	.8611	1.97	1576.7
1000.	.8761	2.07	1691.8
1100.	.8887	2.18	1805.1
1200.	.8995	2.29	1917.0
1300.	.9083	2.40	2027.6
1400.	.9168	2.50	2137.1
1500.	.9237	2.61	2245.8
1600.	.9299	2.72	2353.6
1700.	.9353	2.83	2460.9
1800.	.9401	2.93	2567.5
1900.	.9444	3.04	2673.6
2000.	.9482	3.15	2779.3
2500.	.9625	3.68	3302.4
3000.	.9715	4.22	3819.3
3500.	.9777	4.76	4332.2
4000.	.9820	5.30	4842.4
4500.	.9852	5.83	5350.7
5000.	.9876	6.37	5857.6
6000.	.9909	7.44	6868.3
7000.	.9931	8.52	7876.3
8000.	.9946	9.59	8882.5
9000.	.9956	10.67	9887.4
10000.	.9964	11.74	10891.4

References:

1. H.H. Heckman, B.L. Perkins, W.C. Simon, F.M. Smith and W.H. Barkas
Phys. Rev., 117, 544, 1960.
2. W.H. Barkas, Nuclear Research Emulsions, Vol. I, Academic Press, N.Y., 1963.
3. W.H. Barkas and M.J. Berger, National Academy of Sciences-NRC Publication,
1133, 103, 1964.
4. PPG Industries, Pittsburgh, Pa., CR-39 allyl diglycol carbonate,
Bulletin #45A, Bulletin #300 and Bulletin #304.
5. R.L. Fleischer, P.B. Price and R.M. Walker, Nuclear Tracks in Solids,
University of California Press, Berkeley, 1975.
6. B.G. Cartwright, E.K. Shirk and P.B. Price, Nuclear Instruments
and Methods, 153, 457, 1978.
7. Y.V. Rao, A. Davis, R.C. Filz, P.J. McNulty and D. Shirkey, Bulletin
American Phys. Soc., 24, 650, 1979.

DETECTION OF 10-MeV PROTONS, 70-MeV ^3He IONS, AND 52-MeV
 ^4He IONS IN CR-39 TRACK DETECTOR

Y. V. RAO AND M. P. HAGAN

PHYSICS RESEARCH DIVISION, EMMANUEL COLLEGE

LEXINGTON, MASSACHUSETTS 02173

AND

J. BLUE

NASA-LEWIS RESEARCH CENTER

CLEVELAND, OHIO 44135

INTRODUCTION

The thermoset plastic sheet cast from CR-39 monomer has been found by Cartwright, Shirk and Price (1978) to have a unique sensitivity and resolution in the recording of nuclear particle tracks by the track etching technique. Furthermore, it was found to have a lower detection threshold and a smaller variation of response to particles of a given rate of loss of energy due to ionization. Somogyi and Hunyadi (1979) and Benton *et al.* (1979) reported the registration characteristics of protons and alpha particles in a CR-39 detector. The energy ranges covered by these authors are 0.5 to 6.0 MeV for protons and 1 to 6.1 MeV for alpha particles. Recently, we have utilized CR-39 plastic to detect monoenergetic protons up to 4 MeV (Rao *et al.*, 1979 and 1981) and to determine charge composition of heavy primary cosmic rays (Rao *et al.*, 1981a). The sheets of CR-39 which we have used in the present investigation were obtained from Pershore Mouldings, Ltd., England. Thin sheets (100 μm and 500 μm thick) were cast from allyl diglycol carbonate monomer manufactured by Arinor Ltd., Paris. We have employed this detector for the detection of 10-MeV protons, 70-MeV ^3He ions, and 52-MeV ^4He ions and have obtained a smooth variation of normalized track etching rate as a function of residual range. Our results also indicate that CR-39 will register perpendicularly-incident particles with a value of Z/β as low as 7.

ETCHING PROCEDURE AND MEASUREMENTS

Three stacks of CR-39 sheets were exposed to 10-MeV protons, 70-MeV ^3He ions and 52-MeV ^4He ions. For proton and ^4He irradiations, sheets of thin CR-39 (each 100 μm thick) were used, while for ^3He exposure sheets of thick CR-39 (each 500 μm thick) were employed. In all these irradiations the beam was normally incident to the surface of the detector.

The etching procedure was described by Rao *et al.* (1981) in an earlier publication. The stacks exposed to protons, ^3He ions, and ^4He ions were etched for 74, 49.5 and 47 hours respectively in a solution of 6.25 N NaOH at 50°C. In order to distinguish background against tracks due to beam particles, a virgin sheet of CR-39 was etched simultaneously. To estimate the value of the bulk etching rate (V_g) for CR-39, small areas of detectors were irradiated in vacuum with fission fragments from a ^{252}Cf source and then etched for a definite period of time. The bulk etching rate is given by $V_g = D/2t$ where D is the diameter of fission fragment tracks and t is the etching time.

Precision measurements were made on the surface diameter of tracks due to protons, ^3He ions, and ^4He ions in all sheets. The measurements were made with a Koristka R4 microscope using a X80 Zeiss dry objective and X10 widefield American Optical eyepiece. It should be pointed out that no attempt was made to follow individual tracks into various sheets. Rather,

a large sample of tracks was measured on each surface of the detector, and the mean diameter was computed. The track etching rate was estimated using the relation:

$$V_T/V_g = \frac{h^2 + r^2}{h^2 - r^2} \quad \dots (1)$$

where V_T is the track etching rate, V_g is the bulk etching rate, r is the surface radius, and $h(= V_g t)$ is the amount of bulk material removed from one surface during an etching time t .

The particle's residual range is determined by adding the thickness of each sheet from the stopping point to the top of the stack, taking into account the surface layer removed during etching. The residual ranges of 10-MeV protons, 70-MeV ^3He ions, and 52-MeV ^4He ions were compared with range-energy tables of Holeman *et al.* (1980) and found to be in good agreement. For each value of track etching rate, an appropriate value of residual range was assigned to obtain an experimental point on an etching rate versus residual-range curve.

RESULTS AND DISCUSSION

Figure 2 shows the variation of normalized track etching rate as a function of residual range. Following the phenomenological approach of Price *et al.* (1967), the experimental data have been fitted with the function:

$$V_T/V_g = AJ^n \quad \dots \quad (2)$$

$$\text{where } J = (Z_{\text{eff}}^2 \beta^{-2}) \left[K + \ln \beta^2 \gamma^2 - \beta^2 \right] \quad \dots \quad (3)$$

The effective charge, Z_{eff} , of an ion of atomic number Z and with a velocity β can be expressed as

$$Z_{\text{eff}} = Z \left[1 - \exp(-130\beta Z^{-2/3}) \right] \quad \dots \quad (4)$$

A and n are constants.

Assuming $K=20$, the data have been fitted with the above function. Our results suggest that the response of CR-39 to protons can be represented as a function of $V = 0.801 J^{0.036}$ while $V = 0.516 J^{0.112}$ for the ^3He and ^4He .

A CR-39 detector is being developed for inclusion in the Long-Duration-Exposure Facility of NASA (DiBattista, 1977) to study the flux and energy spectra of trapped protons. It is an extremely suitable* detector for this experiment because very low-energy proton tracks are registered and good discrimination is possible between protons and heavier particles. The track etching rate is only slightly greater than bulk etching rate for protons, and hence normally incident protons are recorded. The latent damage trails produced in the detector are stable

*It should be pointed out that the detectors need proper thermal insulation since there is a sensitivity dependence on temperature during registration (O'Sullivan and Thompson, 1980).

thermally (Khan and Khan, 1980) and this in effect reduces the thermal problems encountered with other passive detectors.

Recently there have been several investigations of light-ion production associated with collimated fast-neutron beams (August *et al.*, 1979; Lambert *et al.*, 1980). A significant component of light-ion flux has been attributed as responsible in part for the greater-than-anticipated late-skin reactions observed in connection with fast-neutron cancer therapy. Also, by identifying the light ions, it is possible to estimate roughly their contribution to the epidermal and subcutaneous doses in tissue. By exposing stacks of thin CR-39 sheets to fast-neutron beams, and with subsequent etching and precision measurements, it is also possible to estimate the light-ion component in neutron therapy beams.

In Table I are presented the detection thresholds for various track detectors. A value of $Z/\beta=7$ for CR-39 plastic makes it an excellent detector to study the charge composition of heavy cosmic rays over a wide range of Z . Hayashi and Doke (1980) arrived at similar conclusions from a study of relativistic heavy primary cosmic rays. Finally, a comparison was made between track densities due to protons, ^3He ions, and ^4He ions in CR-39 sheets and the counts given by the silicon detector, and it was found that the registration efficiencies were close to 100%. In Fig. 3 are shown photomicrographs of mouths of etched tracks of protons, ^3He ions, and ^4He ions incident normally on CR-39 plastic sheet.

The work at Emmanuel College was supported by Air Force Geophysics Laboratory under Contract No. F19628-79-0102. The authors thank Mr. E. Holeman for the programming assistance and Mr. A. Davis for his part in the initial phase of this work.

REFERENCES

August, L.S., Shapiro, P. and Beach, L.A. (1979) Light-ion production associated with collimated fast-neutron beams in air. Bull. Am. Phys. Soc. 24, 855.

Benton, E.V., Preston, C.C., Ruddy, F.H., Gold, R. and Roberts, J.M. (1979) Proton and alpha particle response characteristics of CR-39 polymer for reactor and dosimetry applications. In: Proc. 10th Int. Conf. Solid State Nuclear Track Detectors, Lyon, pp. 459-467, Pergamon Press, Oxford.

Cartwright, B.G., Shirk, E.K. and Price, P.B. (1978) A nuclear-track-recording polymer of unique sensitivity and resolution. Nucl. Instrum. Meth. 153, 457-460.

DiBattista, J.D. (1977) Long duration exposure facility-a free-flying experiment carrier. Space Research, 17, 847-853.

Hayashi, T. and Doke, T. (1980) Characteristics of plastic CR-39 for detection of relativistic cosmic ray heavy nuclei. Nucl. Instrum. Meth. 174, 349-355.

Holeman, E., Spencer, T., Rao, Y.V. and Hagan, M.P. (1980) A table of parameters for heavy ion tracks in CR-39 nuclear track detector. Air Force Geophysics Laboratory Report No. AFGL-TR-80-0035, 1-38.

Khan, H.A. and Khan, N.A. (1980) A new plastic track detector for fast neutron dosimetry. Int. J. Appl. Radiat. Isotopes. 31, 775-779.

Lambert, J.M., Treado, P.A., Allas, R.G., Peterson, E.L. and Shapiro, P. (1980) Charged-particle detector-telescope measurements of the light-ion flux from collimated and uncollimated high energy neutron beams. Bull. Am. Phys. Soc. 25, 585-586.

O'Sullivan, D. and Thompson, A. (1980) Nuclear Tracks 4, 271-276.

Price, P.B., Fleischer, R.L., Peterson, D.D., O'Ceallaigh, C., O'Sullivan, D. and Thompson, A. (1967) Identification of isotopes of energetic particles with dielectric track detectors. Phys. Rev. 164, 1618-1620.

Rao, Y.V., Davis, A., Filz, R.C., McNulty, P.J. and Shirkey, D. (1979) Detection of protons in CR-39 plastic track detector. Bull. Am. Phys. Soc. 24, 650.

Rao, Y.V., Davis, A., Spencer, T. and Filz, R.C. (1981) Diameter evolution of proton tracks in CR-39 detector. Nucl. Instrum. Meth. 180, 153-156.

Rao, Y.V., Davis, A., Hagan, M.P. and Filz, R.C. (1981a) CR-39 plastic track detector experiment for measurement of charge composition of primary cosmic rays. Origin of Cosmic Rays (Eds. G. Setti, G. Spada and A.W. Wolfendale) D. Reidel Publishing Company, Dordrecht-Holland/Boston-U.S.A. 37-38.

Somogyi, G. and Hunyadi, I. (1979) Etching properties of the CR-39 polymer nuclear track detector. In: Proc. 10th Int. Conf. Solid State Nuclear Track Detectors, Lyon, pp. 443-452, Pergamon Press, Oxford.

TABLE I
DETECTION THRESHOLDS FOR VARIOUS TRACK DETECTORS

	Lexan Polycarbonate	Cellulose Nitrate	CR-39
Z/β	60	32	7

FIGURE CAPTIONS

Figure 1. Schematic representation of irradiation arrangement

Figure 2. Normalized track etching rate as a function of residual range for protons, ^3He and ^4He

Figure 3. Photomicrographs of the mouths of etched tracks of a) 10-MeV protons, b) 70-MeV ^3He and c) 52-MeV ^4He incident normally on CR-39 plastic sheet. In Fig. 3(a), the shallow low-contrast etched pits are due to 10-MeV protons.

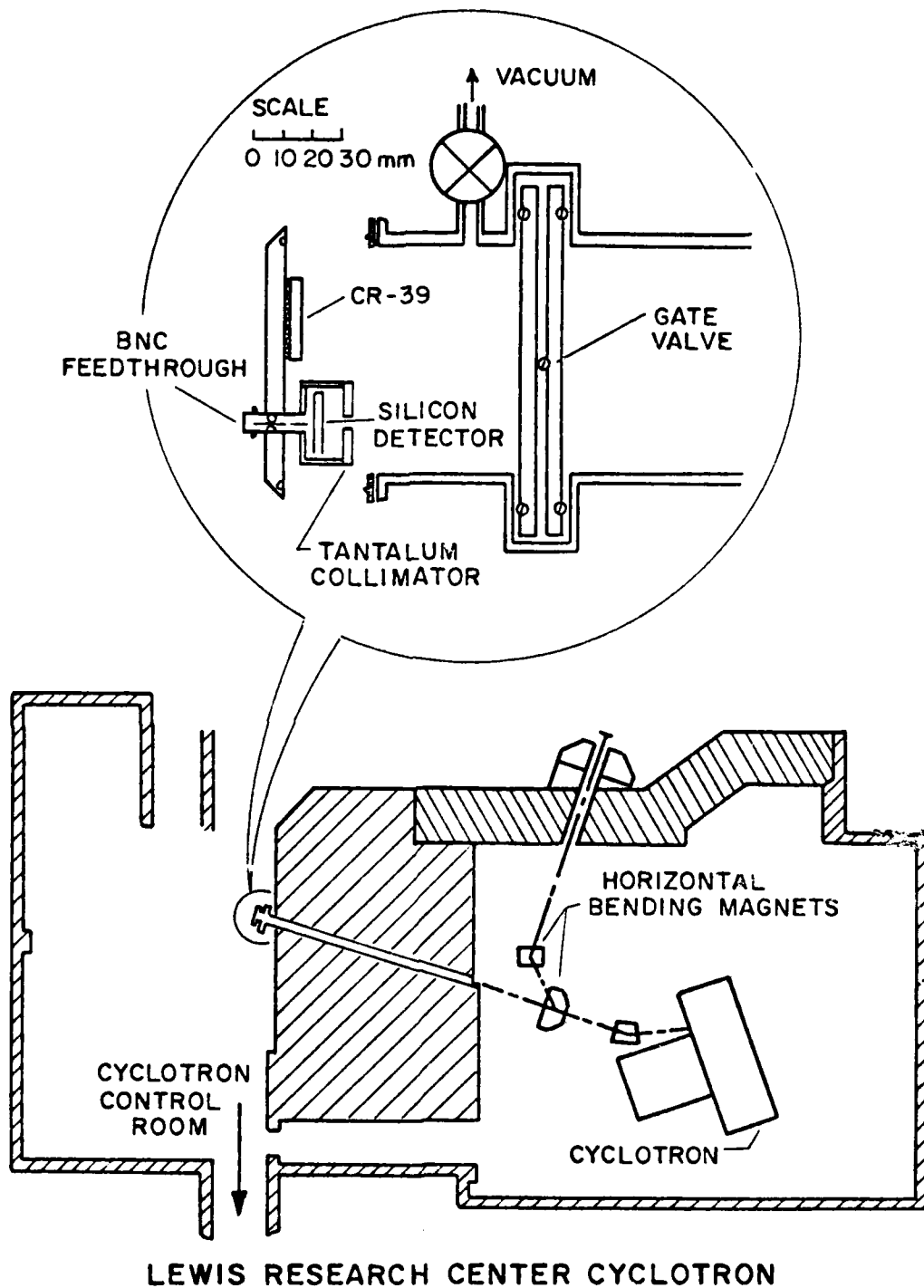


Figure 1

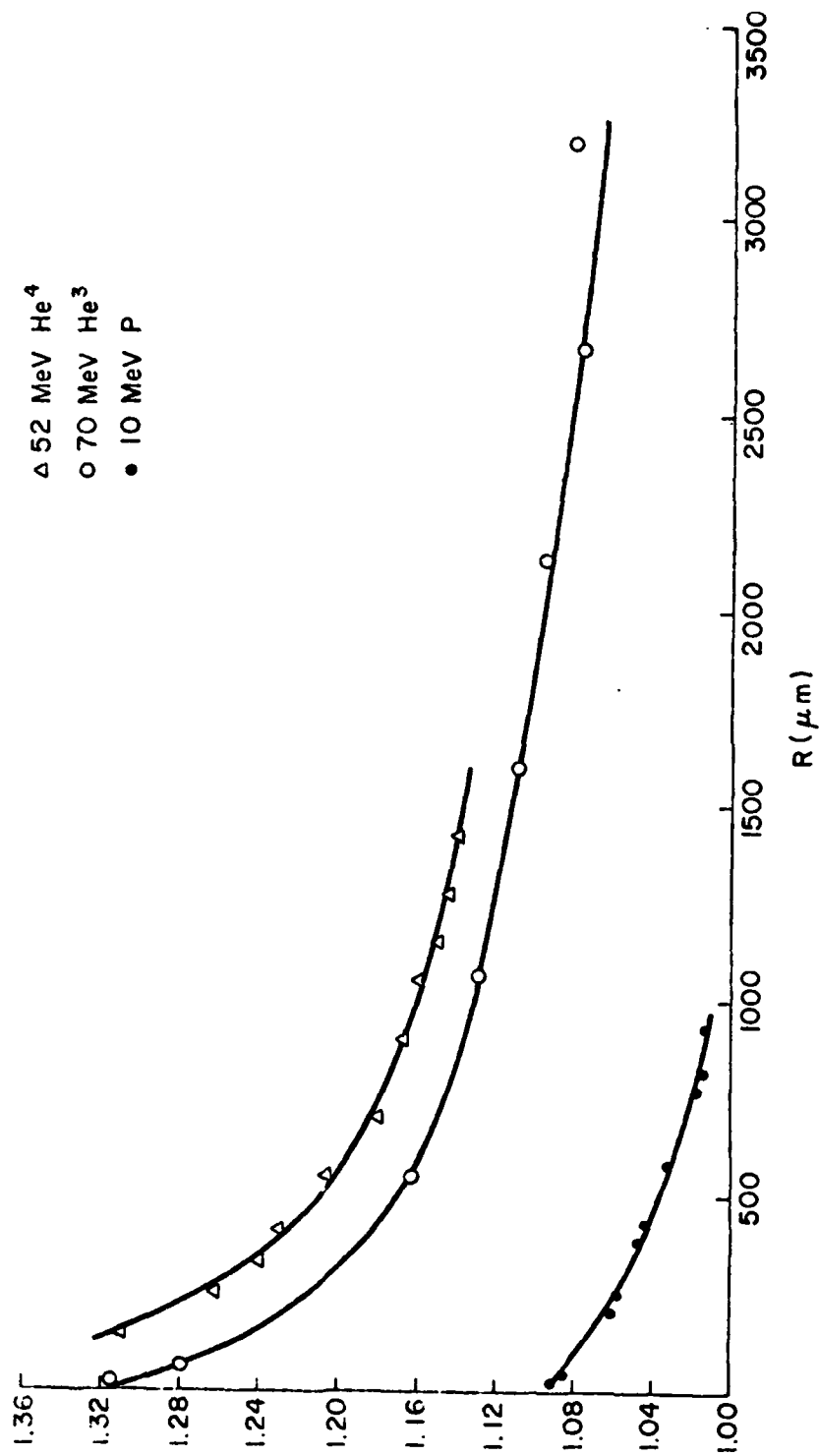


Figure 2.

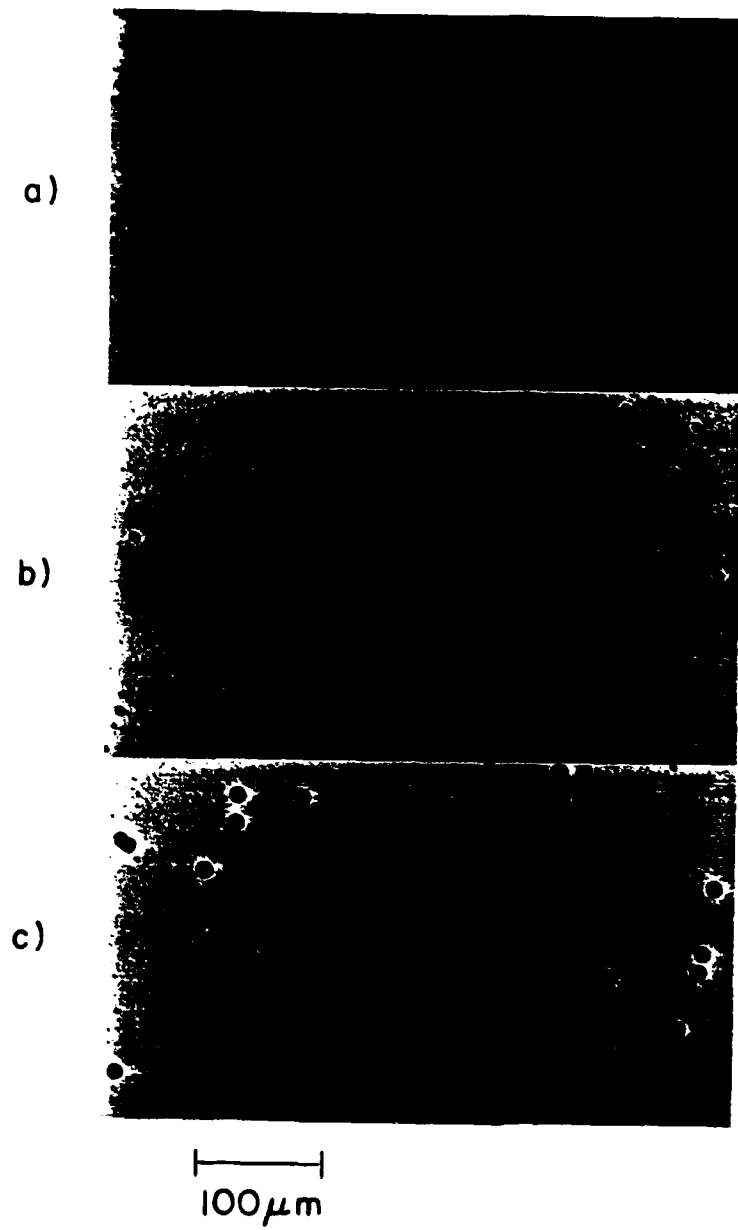


Figure 3.

CR-39 PLASTIC TRACK DETECTOR EXPERIMENT FOR MEASUREMENT OF
CHARGE COMPOSITION OF PRIMARY COSMIC RAYS

Y.V. Rao, A. Davis and M.P. Hagan
Physics Research Division, Emmanuel College,
Lexington MA 02173, USA and
R.C. Filz
Air Force Geophysics Laboratory, Hanscom AFB MA 01731, USA

A study of the relative abundances and energy spectra of heavy cosmic rays and isotopic composition in the region of Fe peak can yield significant information concerning their origin, acceleration and interstellar propagation. In recent years solid state nuclear track detectors have been employed extensively to study heavy primary cosmic rays. Plastic track detectors necessarily have large geometric factors for heavy primaries, and a continuous sensitivity for the duration of an extended exposure. A balloon-borne experiment consisting of 1 m² passive detector array has been designed in order to obtain charge and energy spectra of primary cosmic rays in the region of Fe peak. Included in the array is a new type of nuclear-track-recording plastic, a polymer made from the monomer allyl diglycol carbonate (commercially known as CR-39). The stack was built as a set of nine modules. Three types of stack assembly was adopted for these modules: one consisting of 'pure' CR-39 plastic track detector; the next one, a composite assembly of CR-39 with three layers of 600 micron thick nuclear emulsions; and the last one with CR-39 and Lexan Polycarbonate. The payload was flown successfully in June 1979 from Eielson Air Force Base, Alaska. The flight was aloft for 3 hours 30 min at an average ceiling of 3 gm/cm² of residual atmosphere. An attempt to stabilize and orient the payload utilizing a biaxial magnetometer combined with and electrical rotator was unsuccessful. The failure to orient the payload in a stable position would prevent us from determining the true direction of each cosmic ray particle and trace it backwards through the earth's magnetic field using a computer tracing program. Recovery of the payload was routine and all materials were in perfect condition.

CR-39 from one of the modules has been etched in a solution of 6.25N Sodium Hydroxide Solution at 50°C for 120 hours. The etching was carried out in a precisely controlled bath that is stable to $\pm 0.1^\circ\text{C}$. Optical scanning of CR-39 was performed using an Olympus SZ-3 stereo microscope. The top fifteen sheets have been scanned for stopping and relativistic cosmic ray nuclei. In this scanning 200 stopping particles and several relativistic primaries were detected. The relativistic nuclei passed completely through the entire stack of

thickness 14 gm/cm^2 with no diminution in ionization. Optical measurements on a sample of 50 stopping particles were carried out using Koristka R4 and Leitz/Ortholux Microscopes. We confined our measurements to only those events with high etch rates, and measurements were performed on only three pairs of cones and the ender. No attempt was made to follow the track to the top of the stack in these preliminary measurements. Fig. 1 shows the normalized track etch rate as a function of residual range. Two features stand out very clearly in this figure, i) a smooth variation of track etch rate with range is indicated for individual particles, ii) in the high etch rate region there is no evidence of saturation of etch rate, which is in excellent agreement with the results of Fowler et al ¹⁾. The charge estimates for these particles should become available in the near future after the completion of calibration of CR-39.

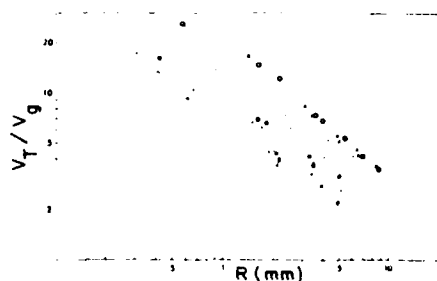


Fig. 1

Fig. 1 Normalized track etch rate as a function of residual range.

Fig. 2 Response of CR-39 to various particles.

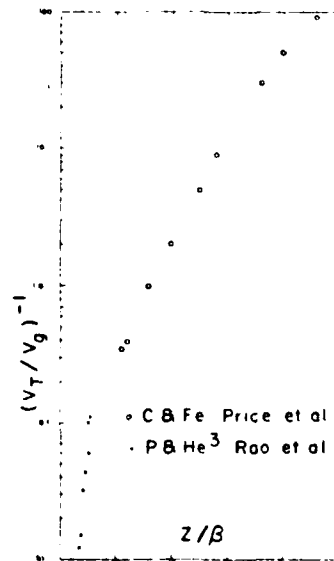


Fig. 2

Fig. 2 shows the response of CR-39 to various particles. Included in the figure are the data of Price et al ²⁾ and our own data ³⁾ from protons and He^3 . It is clear from Fig. 2 that the normalized track etch rate approaches unity very slowly as Z/B decreases. We conclude that CR-39 will detect vertically-incident particles with Z/B as low as 8-10.

Emmanuel College authorship is sponsored by Contract F19628-79-C-0102 with AFGL. The authors thank E. Holeman for the programming assistance.

References:

1. Fowler, P.H., V.M. Clapham, D.L. Henshaw, S. Amin, Proc. ICCR, Kyoto, 11 (1979) 97.
2. Price, P.B., E.K. Shirk, K. Kinoshita, G. Tarle, Proc. ICCR, Kyoto, 11 (1979) 80.
3. Rao, Y.V., A. Davis, M.P. Hagan, R.C. Filz, J. Blue, Bull. AM. Phys. Soc. 25 (1980) 484.

REPRINTED FROM:

NUCLEAR INSTRUMENTS & METHODS

A JOURNAL ON ACCELERATORS, INSTRUMENTATION
AND TECHNIQUES IN NUCLEAR PHYSICS AND RELATED FIELDS

Volume 180, No. 1, 15 February 1981

DIAMETER EVOLUTION OF PROTON TRACKS IN CR-39 DETECTOR

Y.V. RAO, A. DAVIS, T. SPENCER

Physics Research Division, Emmanuel College, Lexington, Massachusetts 02173, U.S.A.

and

R.C. FILZ

Air Force Geophysics Laboratory, Hanscom Air Force Base, Massachusetts 01731, U.S.A.

pp. 153-156



NORTH-HOLLAND PUBLISHING COMPANY — AMSTERDAM

DIAMETER EVOLUTION OF PROTON TRACKS IN CR-39 DETECTOR

Y.V. RAO, A. DAVIS, T. SPENCER

Physics Research Division, Emmanuel College, Lexington, Massachusetts 02173, U.S.A.

and

R.C. FILZ

Air Force Geophysics Laboratory, Hanscom Air Force Base, Massachusetts 01731, U.S.A.

Received 31 March 1979 and in revised form 29 September 1980

We report here first detailed measurements on detection of low energy protons in the new type of solid state track detector, CR-39 (Allyl Diglycol Carbonate). Several samples of CR-39 were exposed to protons of energies 1.5 MeV, 2.2 MeV, 3.2 MeV and 4.3 MeV at Brookhaven National Laboratory. After irradiation the detectors were chemically etched to produce optically visible tracks. The detection efficiency at these energies is close to 100%. The track diameter evolution of etch pits due to protons is described. The diameter distributions clearly show an excellent energy resolution for protons of different energies. The etch pit diameter as a function of amount of bulk material removed from one surface for various etch times and for all incident energies has been obtained.

1. Introduction

In recent years solid state nuclear track detectors have found widespread applications [1]. Track etching technique has been successfully employed in many insulating materials for detection and identification of charged particles, e.g. in the study of heavy primary cosmic rays, the search for superheavy elements and exotic particles, recording of fission fragments and innumerable applications in radiation dosimetry. Early in the past decade cellulose nitrate was recognized as the most sensitive of all track detectors, and so has been used as a detector to record protons [2-4]. However, cellulose nitrate suffers from being inhomogeneous and anisotropic with regard to its physical characteristics. These defects reveal themselves in non-geometrical track profiles, differences in sensitivity in a given sheet, and varying bulk etch rate.

CR-39 is a very useful addition to the range of plastic track detectors that are available for studies relating to primary cosmic rays, radiation dosimetry and other applications. The thermoset plastic sheet cast from CR-39 monomer has been found by Cartwright, Shirk, and Price [5] to have a unique sensitivity and resolution in recording of nuclear particles. This material was found to have a lower detection

threshold ($Z/\beta = 9$) than cellulose nitrate ($Z/\beta = 30$) and a smaller variation of response ($\approx 1\%$) to particles of a given ionization rate than lexan polycarbonate ($\approx 3-8\%$).

In this paper, the first detailed measurements on detection of low energy protons in CR-39 detector are presented. The detector is being developed for inclusion in the Long Duration Exposure Facility (AFGL-Emmanuel Package) to study the flux and energy spectra of trapped protons [6]. CR-39 is an ideal detector for this experiment because very low energy protons are registered [7]. The track etch rate is only slightly greater than bulk etch rate for protons, and hence normally incident protons are recorded. Also thermal problems are greatly reduced compared to those encountered with any other passive detector.

2. Experimental details

The samples of CR-39 which we have used were obtained from Polytech Incorporated, Owensville, Missouri. The sheets (1500 μm thick) were cast from Allyl Diglycol Carbonate monomer manufactured by Pittsburgh Plate Glass Company. Samples of size

(2.5×2.5) cm^2 were exposed to a beam of protons from the Van de Graaff generator at Brookhaven National Laboratory. The beam was tuned to four different energies, viz., 1.5 MeV, 2.2 MeV, 3.2 MeV and 4.3 MeV. The corresponding fluences were: 2.8×10^5 particles/ cm^2 , 0.44×10^6 particles/ cm^2 , 0.67×10^6 particles/ cm^2 and 0.91×10^6 particles/ cm^2 . All irradiations were carried out in such a manner that particles are nearly normally incident to the surface of the plastic sheet.

The etching was carried out in a precisely controlled bath that is stable to $\pm 0.1^\circ\text{C}$. The etchant is contained in a plastic tank which is surrounded by 1 cm of polyurethane foam and an outer tank made of plywood. A stainless steel stirrer, driven by a small motor is used to stir the etchant continuously. The etchant is heated from outside the plastic tank (instead of quartz immersion heater) by employing two 50 W heating mats of flexible silicone rubber. The resistance wire in the mat is made by spiralling fine nickel alloy wire around a glass string. The etchant is maintained at a set point temperature by means of a thermoregulator. For temperature control, the thermoregulator is combined with a Versa Therm electronic control relay. The solid state relay has a transistorised voltage amplifier; its response time is in milliseconds. Heating or cooling procedures and temperature maintenance can be controlled reliably and consistently to a remarkably fine tolerance by this system.

After irradiation the samples were etched in a solution of 6.25N sodium hydroxide at 50°C in four different batches for 7 h, 17 h, 30 h and 48 h. In order to distinguish the background against tracks due to protons, a virgin sample of CR-39 was always etched with each batch. After etching, the samples were washed in tap water at etch-bath temperature, and then left for drying.

3. Results and discussion

All measurements were made on a Koristka R4 microscope using a X80 Zeiss dry objective and X10 widefield American Optical eyepiece. A total of 1000 tracks were measured on all samples etched in the four different batches. In fig. 1 are shown the distributions of track diameters for protons from samples etched for 30 h for all incident energies. The distributions clearly show an excellent energy resolution for protons of different energies. Fig. 2 shows etch pit

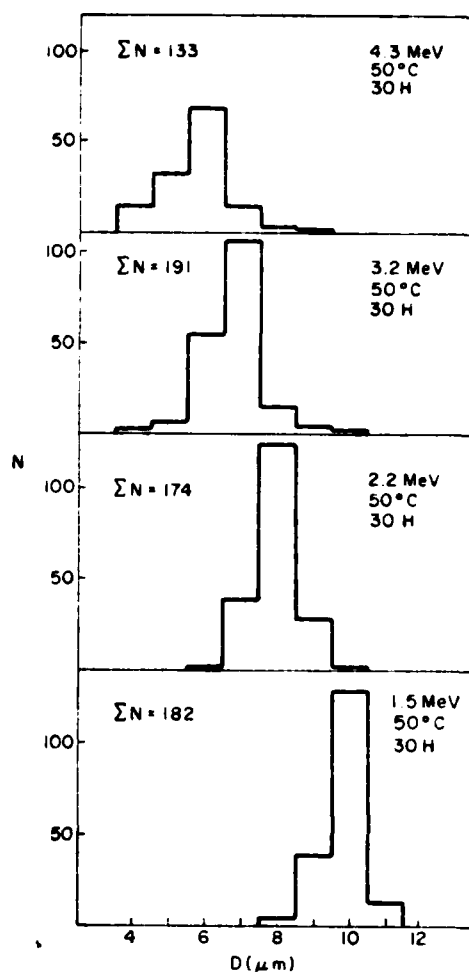


Fig. 1. The diameter distribution of etch pits of protons.

diameter as a function of proton energy. The samples etched for 48 h show a maximum slope, thereby indicating a better resolution.

Fleischer et al. [8] gave the main theoretical basis to describe the track geometry in a wide range of experimental situations. In other investigations [9–11] it has been recognized that measurements of track diameter (D) as a function of the amount of bulk material removed (h) can be used for identification of nuclear particles. This method is applicable for particle track which lie in the region of detection limit such as protons where the track diameter is a more sensitive function of ionization rate than track length. In principle the method should work for particles incident at arbitrary angles on a solid surface.

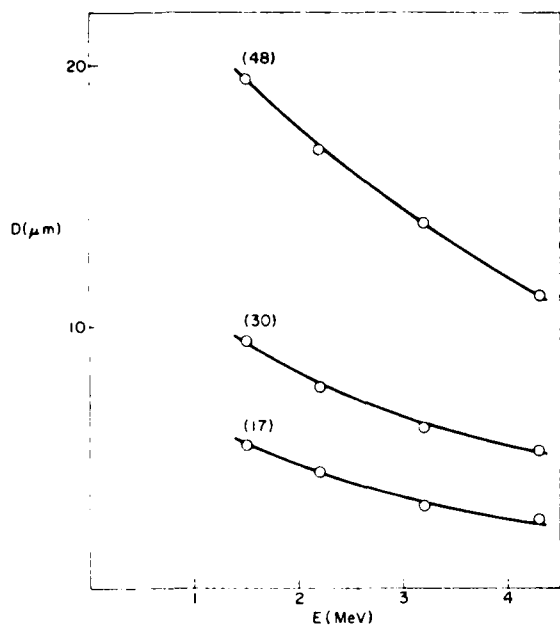


Fig. 2. Etch pit diameter (D) as a function of proton energy (E). The parameter on each curve represents etch time.

but in practice it is much simpler if the detector can be positioned such that particles are nearly normally incident. The amount of bulk material removed is defined as

$$h = \int_0^t V_g dt,$$

where V_g is the bulk etch rate. In order to determine the value of V_g for CR-39, small areas of detectors

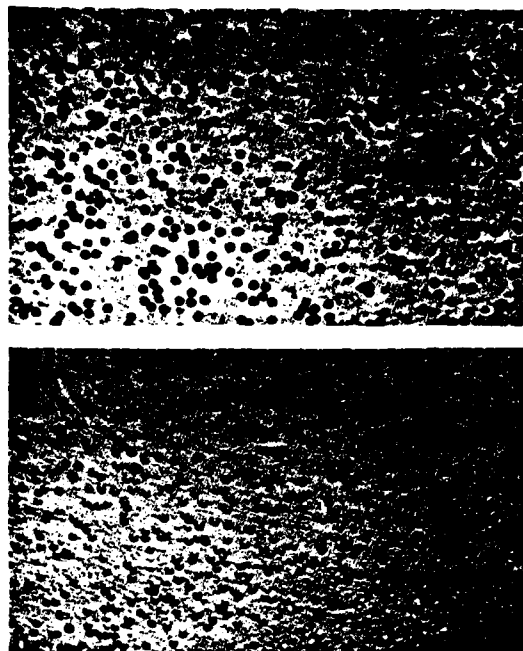


Fig. 4. Photomicrographs of mouths of etched tracks of normally incident protons. a) 1.5 MeV protons, b) 2.2 MeV protons.

were irradiated in vacuum with fission fragments from ^{252}Cf source and then etched for a definite period of time. The bulk etch rate is given by

$$V_g = D/2t,$$

where D is the diameter of fission fragment tracks and t is the etch time and finally h is given by $V_g t$. Fig. 3 shows etch pit diameter as a function of

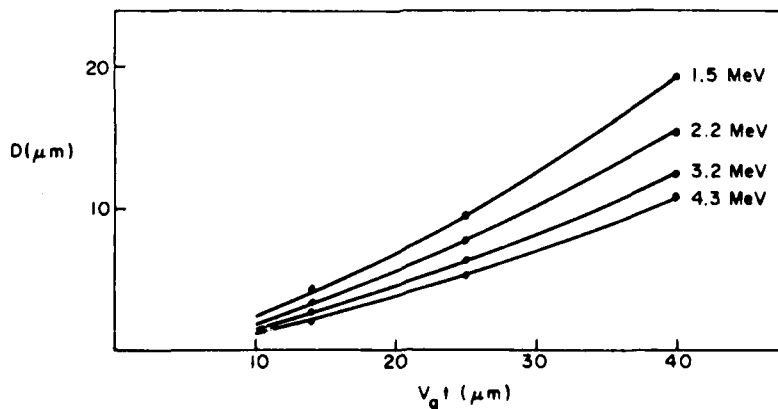


Fig. 3. Etch pit diameter (D) as a function of bulk material removed from one surface ($V_g t$).

amount of bulk material removed from one surface for various etch times and for all incident energies. The theoretical form of $D-h$ curves in fig. 3 were obtained using the procedure described by Somogyi et al. [11]. In fig. 4 are shown photomicrographs of the mouths of etched tracks of normally incident 1.5 MeV and 2.2 MeV protons. The etch pits were photographed with a X12 objective using Leitz Ortholux microscope.

It is a pleasure to thank John Pantazis and Alan Huber for invaluable advice on instrumentation. The research grant at Emmanuel College was supported by Air Force Geophysics Laboratory under contract No. F19628-79-C-0102.

References

- [1] R.L. Fleischer, P.B. Price and R.M. Walker, *Nuclear Tracks in Solids* (Univ. of California Press, Berkely, 1975).
- [2] B.S. Carpenter and P.D. Lafleur, *Intern. J. of Appl. Rad. and Isotopes* 23 (1972) 157.
- [3] H.B. Luck, *Nucl. Instr. and Meth.* 116 (1974) 613.
- [4] G.V. McKinley, *Radiation Effects* 37 (1978) 199.
- [5] B.G. Cartwright, E.K. Shirk and P.B. Price, *Nucl. Instr. and Meth.* 153 (1978) 457.
- [6] R.C. Filz, Air Force Geophysics Laboratory, *Instrumentation Papers*, No. 277, 1979.
- [7] We are currently investigating the possibility of detecting higher energy protons using CR-39. Irradiations are being carried out at Cyclotron Laboratory, NASA-Lewis Research Center, Cleveland.
- [8] R.L. Fleischer, P.B. Price and R.M. Walker, *Ann. Rev. Nucl. Sci.* 15 (1965) 1.
- [9] G. Somogyi, *Nucl. Instr. and Meth.* 42 (1966) 312.
- [10] G. Somogyi and S.A. Szalay, *Nucl. Instr. and Meth.* 109 (1973) 211.
- [11] G. Somogyi, K. Grabisch, R. Scherzer and W. Enge, *Nucl. Instr. and Meth.* 134 (1976) 129.

APPLICATION OF CR-39 TRACK DETECTOR FOR DETECTION OF PROTONS; ^3He AND ^4He IONS

Y. V. Rao*, M. P. Hagan* and J. Blue**

*Physics Research Division, Emmanuel College, Lexington,
Massachusetts 02173, USA

**NASA-Lewis Research Center, Cleveland, Ohio 44135 USA

ABSTRACT

We report here the successful detection of 10-MeV protons, 70-MeV ^3He ions, and 52-MeV ^4He ions in CR-39 plastic track detector. The normalized track etching rate as a function of residual range for these particles has been obtained. Our results suggest that the response of CR-39 track detector to protons, ^3He ions and ^4He ions in these energy bands can be represented as a function of $Z_{\text{eff}}^2(1+0.05\ln\beta^2-0.05\beta^2)$. We conclude that CR-39 will register tracks of perpendicularly-incident particles with Z/β as low as 8. The implications of these results with particular reference to detection of light-ion flux in the neutron beams used for cancer therapy are discussed. Our results also indicate that clear discrimination would be possible between ^3He ions and ^4He ions in these energy bands.

KEYWORDS

CR-39 plastic; nuclear track detection; protons; ^3He and ^4He ions.

INTRODUCTION

The thermoset plastic sheet cast from CR-39 monomer has been found by Cartwright, Shirk and Price (1978) to have a unique sensitivity and resolution in the recording of nuclear particle tracks by track etching technique. Recently we have utilized CR-39 plastic to detect monoenergetic protons up to 4 MeV (Rao et al., 1981) and to determine charge composition of heavy primary cosmic rays (Rao et al., 1981a). The sheets of CR-39 which we have used in the present investigation were obtained from Pershore Mouldings, Ltd., England. We have for the first time employed this detector for the detection of 10-MeV protons, 70 MeV ^3He ions, and 52-MeV ^4He ions and have obtained a smooth variation of normalized track etching rate as a function of residual range. Our results also indicate that CR-39 will register perpendicularly-incident particles with a value of Z/β as low as 8.

IRRADIATION PROCEDURE

The irradiation arrangement at the NASA-Lewis Research Center's cyclotron is shown schematically in Fig. 1. This drawing shows the pertinent part of the beam line where bending and focusing magnets are adjusted to produce a 10 mm beam spot upon a 2.5 μm tantalum foil. This foil is centered in a 0.1 m diameter beam duct at a position immediately in front of a 6 m shielding wall. Small angle scattering in the foil produces a uniform flux distribution over a 75 mm diameter circle located at the far side of the shield wall. A measurement of the induced radioactivity at this position showed that the particle flux varies less than $\pm 5\%$.

The inset in Fig. 1 shows the 75 mm diameter end plate onto which the CR-39

sheets were affixed with double-face adhesive tape. A gold surface barrier detector was mounted to a BNC feed-through connector. This detector was used to monitor the number of particles passing through the 3 mm diameter tantalum collimator located immediately in front of the detector. Because of the uniformity of the particle distribution, the total number of detector pulses in an irradiation was used to determine the particle fluence of the CR-39 sheet.

After mounting the CR-39 sheets, the end plate was held against the "O" ring at the end of the beam duct and the roughing valve V opened to remove most of the air. Then atmospheric pressure holds the end plate in position and the gate valve was opened to place the sheets in the high vacuum of the beam duct.

Following the above procedure, three stacks of CR-39 sheets were exposed to 10-MeV protons, 70-MeV ^3He ions and 52-MeV ^4He ions. For proton and ^4He irradiations, sheets of thin CR-39 (each 100 μm thick) were used, while for ^3He exposure sheets of thick CR-39 (each 500 μm thick) were employed. In all these irradiations the beam was normally incident to the surface of the detector.

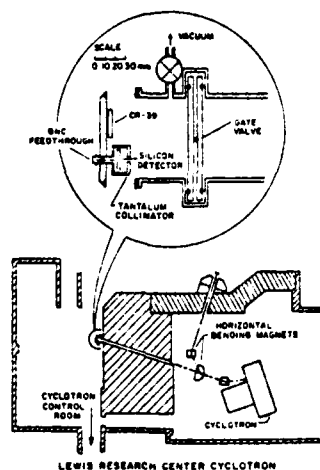


Fig. 1. Schematic representation of irradiation arrangement

ETCHING PROCEDURE AND MEASUREMENTS

The etching procedure was described by Rao et al. (1981) in an earlier publication. The stacks exposed to protons, ^3He ions, and ^4He ions were etched for 74, 49.5 and 47 hours respectively in a solution of 6.25 N NaOH at 50°C. In order to distinguish background against tracks due to beam particles, a virgin sheet of CR-39 was etched simultaneously. The bulk etch rate for CR-39 was determined from the track diameter measurements on tracks due to fission fragments from a ^{252}Cf source. Precision measurements were made on the surface diameter of tracks due to protons, ^3He and ^4He in all sheets. The measurements were made with a Koristka R4 microscope using a X80 Zeiss dry objective and X10 widefield American Optical eyepiece. It should be pointed out that no attempt was made to follow individual tracks into various sheets. Rather, a large sample of tracks was measured on each surface of the detector, and the mean diameter was computed. The track etching rate was estimated from mean diameter of the tracks. The particle's residual range is determined by adding the thickness of each sheet from the stopping point to the top of the stack, taking into account the surface layer removed during etching. For each value of track etching rate, an appropriate value of residual range was assigned to obtain an experimental point on an etching rate versus residual range curve.

RESULTS AND DISCUSSION

Figure 2 shows the variation of normalized track etching rate as a function of residual range. Following the phenomenological approach of Price et al. (1967), the experimental data have been fitted with the function:

$$V_T/V_g = AJ^n \quad (1)$$

where

$$J = (Z_{\text{eff}}^2 \beta^{-2}) \left[K + \ln \beta^2 \gamma^2 - \beta^2 \right] \quad (2)$$

The effective charge, Z_{eff} , of an ion of atomic number Z and with velocity β can be expressed as

$$Z_{\text{eff}} = Z \left[1 - \exp(-130\beta Z^{-2/3}) \right] \quad (3)$$

A and n are constants.

Our results suggest that the response of CR-39 to 10-MeV protons, 70-MeV ^3He ions, and 52-MeV ^4He ions can be represented as a function of

$$(Z_{\text{eff}}^2 \beta^{-2}) \left[1 + 0.05 \ln \beta^2 \gamma^2 - 0.05 \beta^2 \right]$$

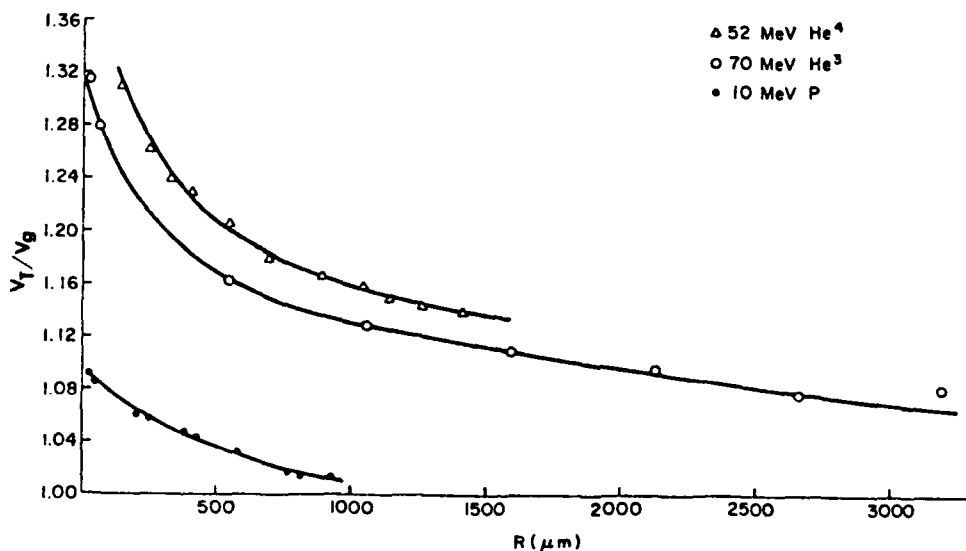


Fig. 2. Normalized track etching rate as a function of residual range for protons, ^3He and ^4He

Recently there have been several investigations of light-ion production associated with collimated fast-neutron beams (August et al., 1979; Lambert et al., 1980). A significant component of light-ion flux has been attributed as responsible in part for the greater-than-anticipated late-skin reactions observed in connection with fast-neutron cancer therapy. Also, by identifying the light ions, it is possible to estimate roughly their contribution to epidermal and subcutaneous doses in tissue. By exposing stacks of thin CR-39 sheets to fast-neutron beams, and with subsequent etching and precision measurements, it is also possible to estimate the light-ion component in neutron therapy beams. Finally, a comparison was made between track densities due to protons, ^3He ions, and ^4He ions in CR-39 sheets and the counts given by silicon detector, and it was found that the registration efficiencies were close to 100%.

The work at Emmanuel College was supported by Air Force Geophysics Laboratory under Contract No. F19628-79-0102.

REFERENCES

- August, L.S., Shapiro, P. and Beach, L.A. Bull. Am. Phys. Soc. 24, 855, 1979
- Cartwright, B.G., Shirk, E.K. and Price, P.B. Nucl. Instrum. Meth. 153, 457, 1978
- Lambert, J.M., Treado, P.A., Allas, R.G., Peterson, E.L. and Shapiro, P. Bull. Am. Phys. Soc. 25, 585, 1980
- Price, P.B., Fleischer, R.L., Peterson, D.D., O'Ceallaigh, C., O'Sullivan, D. and Thompson, A. Phys. Rev. 164, 1618, 1967
- Rao, Y.V., Davis, A., Spencer, T. and Filz, R.C. Nucl. Instrum. Meth. 180, 153, 1981
- Rao, Y.V., Davis, A., Hagan, M.P. and Filz, R.C. Origin of Cosmic Rays (Eds. G. Setti, G. Spada and A.W. Wolfendale) D. Reidel Publishing Company, Dordrecht-Holland/Boston-U.S.A., page 37, 1981a

DETECTION OF 10-MeV PROTONS, 70-MeV ^3He ions, AND 52-MeV ^4He IONS IN CR-39 TRACK DETECTOR

Y. V. RAO and M. P. HAGAN

Physics Research Division, Emmanuel College Lexington, MA 02173, U.S.A.

and

J. BLUE

NASA-Lewis Research Center Cleveland, OH 44135, U.S.A.

(Received 28 July 1981; in revised form 8 March 1982)

1. Introduction

THE THERMOSET plastic sheet cast from CR-39 monomer has been found by Cartwright, Shirk and Price (1978) to have a unique sensitivity and resolution in the recording of nuclear particle tracks by the track etching technique. Furthermore, it was found to have a lower detection threshold and a smaller variation of response to particles of a given rate-of-loss of energy due to ionization. Somogyi and Hunyadi (1980) and Benton *et al.* (1980) reported the registration characteristics of protons and alpha particles in a CR-39 detector. The energy ranges covered by these authors are 0.5 to 7.0 MeV for protons and 1 to 6.1 MeV for alpha particles. Recently, we have utilized CR-39 plastic to detect monoenergetic protons up to 4 MeV (Rao *et al.*, 1979 and 1981) and to determine charge composition of heavy primary cosmic rays (Rao *et al.*, 1981a). The sheets of CR-39 which we have used in the present investigation were obtained from Pershore Mouldings, Ltd., England. Thin sheets (100 μm and 500 μm thick) were cast from allyl diglycol carbonate monomer manufactured by Arinor Ltd., Paris. We have employed this detector for the detection of 10-MeV protons, 70-MeV ^3He ions, and 52-MeV ^4He ions and have obtained a smooth variation of normalized track etching rate as a function of residual range. Our results also indicate that CR-39 will register perpendicularly-incident particles with a value of $Z\beta$ as low as 7.

2. ETCHING PROCEDURE AND MEASUREMENTS

Three stacks of CR-39 sheets were exposed to 10-MeV protons, 70-MeV ^3He ions and 52-MeV ^4He ions. For proton and ^4He irradiations, sheets of thin CR-39 (each 100 μm thick) were used, while for ^3He exposure sheets of thick CR-39 (each 500 μm thick) were employed. In all these radiations the beam was normally incident to the surface of the detector.

The etching procedure was described by Rao *et al.* (1981) in an earlier publication. The stacks exposed to protons, ^3He ions, and ^4He ions were etched for 74, 49.5 and 47 h, respectively, in a solution of 6.25 N NaOH at 50°C. In order to distinguish background against tracks due to beam particles, a virgin sheet of CR-39 was etched simultaneously. To estimate the value of the bulk etching rate (V_b) for CR-39, small areas of detectors were irradiated in vacuum with fission fragments from a ^{252}Cf source and then etched for a definite period of time. The bulk etching rate is given by $V_b = D/2t$, where D is the diameter of normally-incident fission-fragment tracks and t is the etching time.

Precision measurements were made on the surface diameter of tracks due to protons, ^3He ions, and ^4He ions in all sheets. The measurements were made with a Koristka R4 microscope using a X80 Zeiss dry objective and $\times 10$ widefield American Optical eyepiece. It should be pointed out that no

attempt was made to follow individual tracks into various sheets. Rather, a large sample of tracks was measured on each surface of the detector, and the mean diameter was computed. The track etching rate was estimated using the relation:

$$V_t/V_b = \frac{h^2 + r^2}{h^2 - r^2}, \quad (1)$$

where V_t is the track etching rate, V_b is the bulk etching rate, r is the surface radius, and $h (= V_b t)$ is the amount of bulk material removed from one surface during an etching time t .

The particle's residual range is determined by adding the thickness of each sheet from the stopping point to the top of the stack, taking into account the surface layer removed during etching. The residual ranges of 10-MeV protons, 70-MeV ^3He ions, and 52-MeV ^4He ions were compared with range-energy tables of Holeman *et al.* (1980) and found to be in good agreement. For each value of track etching rate, an appropriate value of resi-

dual range was assigned to obtain an experimental point on an etching rate versus residual-range curve.

3. RESULTS AND DISCUSSION

Figure 1 shows the variation of normalized track etching rate as a function of residual range. Following the phenomenological approach of Price *et al.* (1967), the experimental data have been fitted with the function:

$$V = V_t/V_b = AJ^n, \quad (2)$$

where

$$J = (Z_{eff}^2 \beta^{-2}) [K + \ln \beta^2 \gamma^2 - \beta^2] \quad (3)$$

The effective charge, Z_{eff} , of an ion of atomic number Z and with a velocity β can be expressed as

$$Z_{eff} = Z[1 - \exp(-130 \beta Z^{-2/3})]. \quad (4)$$

A and n are constants.

*It should be pointed out that the detectors need protection during registration (O'Sullivan and Thor

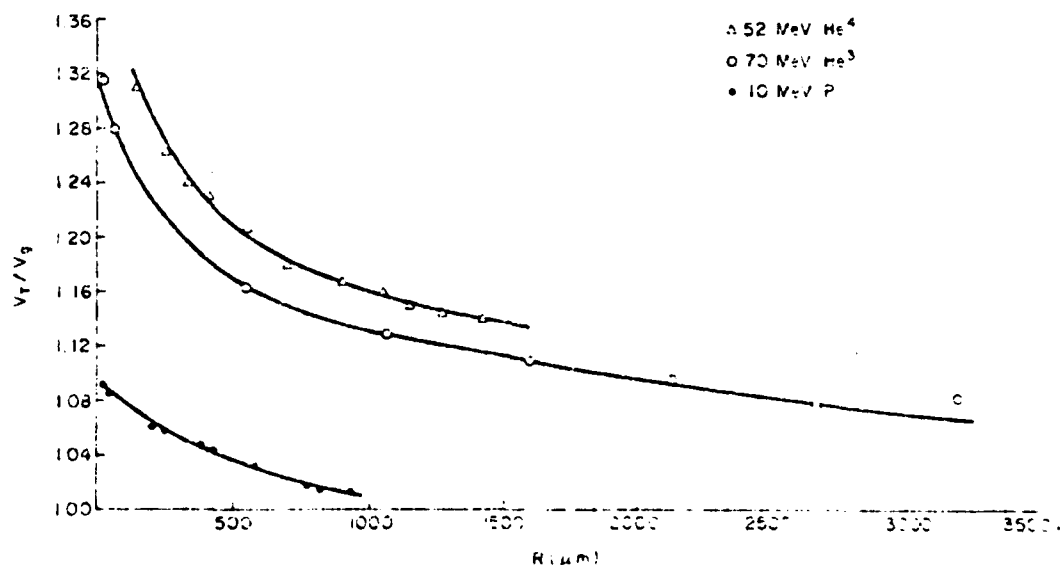


Fig. 1. Normalized track etching rate as a function of residual range for protons, ^3He and ^4He .

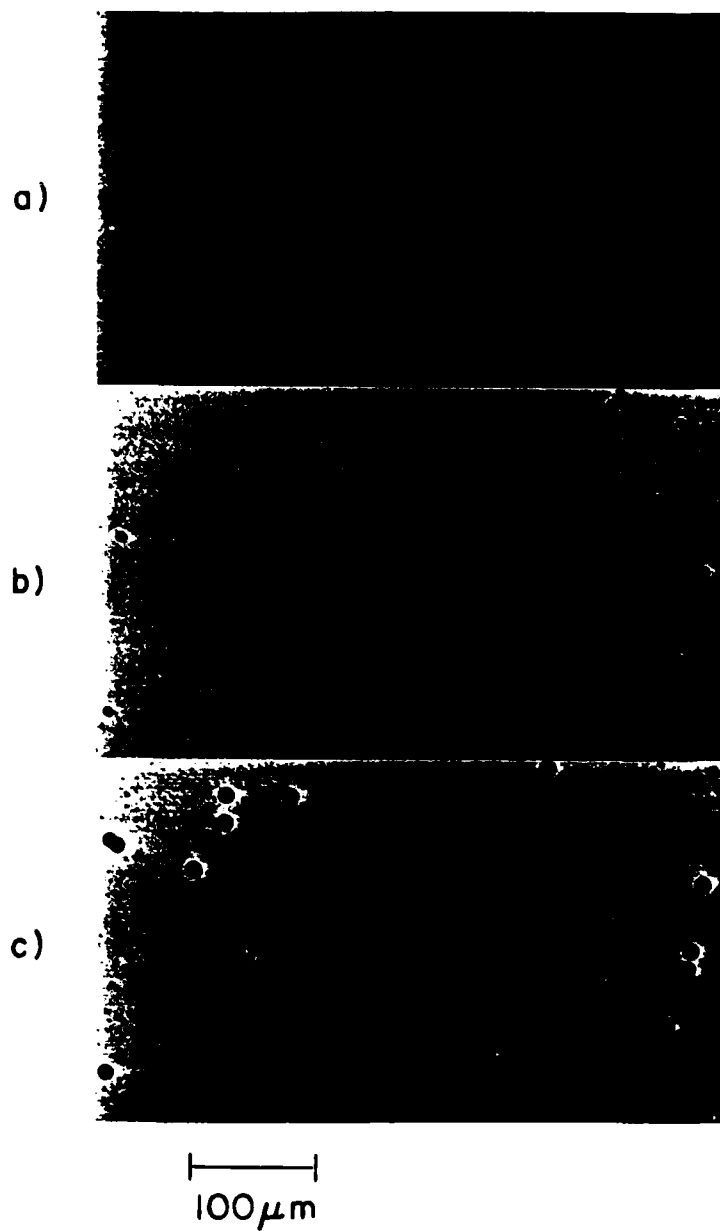


Fig. 2. Photomicrographs of the mouths of etched tracks of a) 10-MeV protons, b) 70-MeV ^3He and c) 52-MeV ^4He incident normally on CR-39 plastic sheet. In Fig. 2 a), the shallow low-contrast etched pits are due to 10-MeV protons.

Table 1. Detection thresholds for various track detectors

	Lexan Polycarbonate	Cellulose Nitrate	CR-39
Z/β	60	32	7

Assuming $K = 20$, the data have been fitted with the above function. Our results suggest that the response of CR-39 to protons can be represented as a function of $V = 0.801 J^{0.006}$, while $V = 0.516 J^{0.112}$ for the ^3He and ^4He .

A CR-39 detector is being developed for inclusion in the Long-Duration-Exposure Facility of NASA (DiBattista, 1977) to study the flux and energy spectra of trapped protons in near-Earth orbits. It is an extremely suitable* detector for this experiment because very low-energy proton tracks are registered and good discrimination is possible between protons and heavier particles. The track etching rate is only slightly greater than bulk etching rate for protons, and hence normally-incident protons are recorded. The latent damage trails produced in the detector are stable thermally (Khan and Khan, 1980) and this, in effect, reduces the thermal problems encountered with other passive detectors.

Recently there have been several investigations of light-ion production associated with collimated fast-neutron beams (August *et al.*, 1979; Lambert *et al.*, 1980). A significant component of light-ion flux has been attributed as responsible in part for the greater-than-anticipated late-skin reactions observed in connection with fast-neutron cancer therapy. Also, by identifying the light ions, it is possible to estimate roughly their contribution to the epidermal and subcutaneous doses in tissue. By exposing stacks of thin CR-39 sheets to fast-neutron beams, and with subsequent etching and precision measurements, it is also possible to estimate the light-ion component in neutron therapy beams.

In Table 1 are presented the detection thresholds for various track detectors. A value of $Z/\beta = 7$ for CR-39 plastic makes it an excellent detector to study the charge composition of heavy cosmic rays over a wide range of Z . Hayashi and Doke (1980) arrived at similar conclusions from a study of relativistic heavy primary cosmic rays.

Finally, a comparison was made between track densities due to protons, ^3He ions, and ^4He ions in CR-39 sheets and the counts given by the silicon detector, and it was found that the registration efficiencies were close to 100%. In Fig. 2 are shown photomicrographs of mouths of etched tracks of protons, ^3He ions, and ^4He ions incident normally on CR-39 plastic sheet.

Acknowledgement—The work at Emmanuel College was supported by Air Force Geophysics Laboratory under Contract No. F19628-79-0102. The authors thank Mr E. Holeman for the programming assistance and Mr A. Davis for his part in the initial phase of this work.

REFERENCES

- August L. S., Shapiro P. and Beach L. A. (1979) Light-ion production associated with collimated fast-neutron beams in air. *Bull. Am. Phys. Soc.* **24**, 855.
- Benton E. V., Preston C. C., Ruddy F. H., Gold R. and Roberts J. M. (1980) Proton and alpha particle response characteristics of CR-39 polymer for reactor and dosimetry applications. In: *Proc. 10th Int. Conf. Solid State Nuclear Track Detectors*, Lyon, pp. 459-467, Pergamon Press, Oxford.
- Cartwright B. G., Shirk E. K. and Price P. B. (1978) A nuclear-track-recording polymer of unique sensitivity and resolution. *Nucl. Instrum. Meth.* **153**, 457-460.
- DiBattista J. D. (1977) Long duration exposure facility—a free-flying experiment carrier. *Space Research* **17**, 847-853.
- Hayashi T. and Doke T. (1980) Characteristics of plastic CR-39 for detection of relativistic cosmic ray heavy nuclei. *Nucl. Instrum. Meth.* **174**, 349-355.
- Holeman E., Spencer T., Rao Y. V. and Hagan M. P. (1980) A table of parameters for heavy ion tracks in CR-39 nuclear track detector. *U.S. Air Force Geophysics Laboratory Report No. AFGI-TR-80-0035*, pp. 1-38.
- Khan H. A. and Khan N. A. (1980) A new plastic track detector for fast neutron dosimetry. *Int. J. Appl. Radiat. Isotopes*, **31**, 775-779.
- Lambert J. M., Treado P. A., Vyas R. G., Peterson E. J. and Shapiro P. (1980) Charged-particle detector—telescope measurements of the light-ion flux from collimated and uncollimated high energy neutron beams. *Bull. Am. Phys. Soc.* **27**, 558-559.

- O'Sullivan D. and Thompson A. (1980) *Nucl. Tracks* 4, 271-276.
- Price P. B., Fleischer R. L., Peterson D. D., O'Ceallaigh C., O'Sullivan D. and Thompson A. (1967) Identification of isotopes of energetic particles with dielectric track detectors. *Phys. Rev.* 164, 1618-1620.
- Rao Y. V., Davis A., Filz R. C., McNulty P. J. and Shirley D. (1979) Detection of protons in CR-39 plastic track detector. *Bull. Am. Phys. Soc.* 24, 650.
- Rao Y. V., Davis A., Spencer T. and Filz R. C. (1981) Diameter evolution of proton tracks in CR-39 detector. *Nucl. Instrum. Meth.* 180, 153-156.
- Rao Y. V., Davis A., Hagan M. P. and Filz R. C. (1981a) CR-39 plastic track detector experiment for measurement of charge composition of primary cosmic rays. In *Origin of Cosmic Rays* (Eds. G. Setti, G. Spada and A. W. Wolfendale) D. Reidel Publishing Company, Dordrecht-Holland-Boston-U.S.A. pp. 37-38.
- Somogyi G. and Hunyadi I. (1980) Etching properties of the CR-39 polymer nuclear track detector. In: *Proc. 10th Int. Conf. Solid State Nuclear Track Detectors*, Lyon. Pergamon Press, Oxford. pp. 443-452.

0.1 - 100 MeV PROTON FLUXES AT THE OUTER EDGE
OF THE INNER TRAPPED REGION

R. Filz (Air Force Geophysics Laboratory,
Hanscom AFB MA 01730)

D.R. Parsignault (Emmanuel College,
Boston MA 02115)

E. Holeman (Emmanuel College, Boston
MA 02115)

Charged particle telescope flown on S3-2 and S3-3 Air Force satellites have provided data on trapped proton fluxes, in the 0.1 - 100 MeV energy range, during 1976 and 1977. While these instruments were designed for soft proton spectra which typically occur in solar events, reliable data were obtained at the outer edge of the inner trapped region ($2 \lesssim L \lesssim 4$), and at minimum mirror point altitudes $100 \text{ km} \lesssim h_{\text{min}} \lesssim 4000 \text{ km}$.

We report proton fluxes over the 0.1 - 100 MeV energy range for the 1976-1977 time period, and compare them to earlier measurements. Energy spectra which cannot be fitted by a single distribution (exponential or power) are also presented.

1. 1980 Spring Meeting

2. AGU

3. Corresponding address:

D.R. Parsignault
Emmanuel College
400 The Fenway
Boston MA 02115

4. SM (Magnetospheric Physics)

5. (None)

6. 0

7. 0%

8. a. Emmanuel College
Business Office
400 The Fenway
Boston MA 02115

b. P.O. #3531

c. N/A

9. C

ELECTRON FLUXES OVER THE POLAR CAPS

D.R. Parsignault (Emmanuel College, Boston
MA 02115)
(Sponsor: Dave Hardy)

Observations of electron precipitations (0.050 - 20 keV) over the polar cap regions ($\text{Lat} \gtrsim |82^\circ|$) were made using the electrostatic analyzer on board the DMSP-F2 satellite, from February 13-17, 1978. This period coincided with a large PCA event.

Increases in the electron fluxes from $\sim 10^6$ el/cm²-sec-ster were observed to coincide with the onset of the PCA event (9:30 UT, Feb 13, 1978) associated with a hardening of the energy spectrum. The following polar passes on February 14, 15 showed an increase of at least one-order of magnitude, especially over the South polar cap region. On February 16, 0:10 UT the flux over that region reached 7.5×10^7 el/cm²-sec-ster. Sporadic electron acceleration in the keV region is evident during the period of observation. Comparisons with electron data from ISEE-B are made.

1. 1980 Spring Meeting
2. AGU
3. Corresponding address:
D.R. Parsignault
Emmanuel College
400 The Fenway
Boston MA 02115
4. SM (Magnetospheric Physics)
5. DMSP Special Session
6. 0
7. 0%
8. a. Emmanuel College
Business Office
400 The Fenway
Boston MA 02115
b. P.O. #3531
c. N/A
9. C

A 13-YEAR CONTINUOUS DECREASE IN THE 8-25 MeV PROTON POPULATION AT LOW L VALUES

D.R. Parsignault, E. Holeman (Emmanuel College
Boston MA 02115)

R.C. Filz (AFGL Bedford MA 01731)

A five-year continuous observation, 1963 to 1968, of the 8-25 MeV proton population, at $L < 2.0$, had shown a monotonic decrease in this population (Bostrom *et al.*, 1971). This decay on the different field lines had gone, until now, unverified and unexplained.

We have observed the same proton population from 1970 to 1976, using experiments flown on several USAF satellites (72-1, S3-2, S3-3). Using these data together with published data from the DIAL satellite, we show that the decreases in the proton fluxes first observed by Bostrom *et al.* have continued unabated, at least until August 1976, and with the same original mean lives. For example, the proton flux at $L = 1.35$ decayed over the 13-year period (1963-1976) with a mean life, $\tau = 6.0 \pm 1.0$ years. At $L = 1.35$, the mean life, $\tau = 4.55 \pm 0.16$ years. However, the proton flux at $L = 1.20$, which had first been reported as constant, started decreasing ~ 1970 to 1976 with $\tau = 3.06 \pm 0.25$ years.

Possible explanations for this observed phenomenon can be divided into the two categories of natural and artificial effects. We review these different effects and we are driven to the conclusion that we are seeing the decay of the high energy protons injected by the "Starfish" high altitude nuclear explosion.

Bostrom, C.O., Beall, D.S., and Armstrong, J.C., "Time history of the inner radiation zone October 1963 to December 1968", Models of the Radiation Environment, Volume VII: Long Term Variations, 25-35, 1971.

1. 1980 Fall Meeting
2. PARS202289
3. Corresponding address:
D.R. Parsignault
Emmanuel College
400 The Fenway
Boston MA 02115
4. SM (Magnetospheric Physics)
- 5.
6. 0
7. 15% (at 1980 Spring Mtg.)
8. a. Emmanuel College
Business Office
400 The Fenway
Boston MA 02115
b. P.O. #4369
c. N/A
9. C

THE GENERALIZED GEOMETRICAL FACTOR

OF

PARTICLE TELESCOPES FOR TRAPPED RADIATIONS

P. S. Young

Physics Department, Mississippi State University
Mississippi State, Mississippi 39762 U. S. A.

E. G. Holeman, D. R. Parsignault and M. P. Hagan
Physics Research Division, Emmanuel College
Boston, Massachusetts, 02115 U. S. A.

R. C. Filz

Air Force Geophysics Laboratory
Bedford, Massachusetts, 01731 U. S. A.

ABSTRACT

In analyzing the trapped proton data obtained by the instruments on board the U. S. Air Force Satellites S73-6 and S74-2, the formulation of the Generalized Geometrical Factor, $G(n, \lambda)$, for the particle detector telescopes has been developed, taking into account the anisotropy of the trapped radiations. The numerical and Monte Carlo methods were used to evaluate this G-factor. The results were applied to the reduction of the proton data in the energy range from 0.1 to 6 MeV.

In this paper, we present the mathematical formulism of the Generalized Geometrical Factor and some sample data which demonstrate the importance of this factor in the analysis of the pitch angle distributions and the energy spectra of the trapped radiations.

1. Introduction

Solid state electronic detectors of AFGI* have been flown in the near earth space on the U. S. Air Force Satellite S73-6 and S74-2 since 1975. The detectors were the P- α telescopes and LEPS (Low energy proton spectrometer). These instruments were designed to detect the trapped protons of energy ranging from 0.1 to 6 MeV through eleven channels.

In analyzing our vast data of the low energy protons, the generalized geometric factor for the detector systems has been formulated and calculated by using the numerical integration and Monte Carlo Method. Since the factor depends on the radiation's anisotropy and the effective area of the detector system, its numerical values are applicable to our data only. However the formulation of the factor and its variation with the

* Air Force Geophysics Laboratory

index of the pitch angle distribution as well as the spin-geomagnetic angle are worth reporting. For they should clearly illustrate the significance on the data-analysis and the conditions of the data-collection performed by our satellite-borne telescopes.

Under these considerations, this paper briefly reports the development of formulating the generalized factor. In addition, this paper presents some samples of analyzed data of the low-energy protons--the pitch angle distribution and energy spectra.

2. Method

In presenting the formulation of the generalized geometric factor G , it is necessary to emphasize its importance. It is the factor used to reduce the unidirectional particle flux of energy E , $J_{\perp}(E)$, from the counting rate dN/dt , where the subscript " \perp " refers to the flux of the incoming particle perpendicular to the local geomagnetic field \vec{B} . The relations among J_{\perp} , G , and dN/dt can be expressed by:

$$J_{\perp}(E) = \frac{dN/dt}{G \epsilon(E)} \quad (1)$$

where $\epsilon(E)$ is efficiency of the detector for detecting particles of energy E .

Since G represents the gathering power of the detector telescope with respect to the incoming particle flux, it is a function of the angular distribution $f(\theta', \phi')$ of the flux and the effective area A_{eff} of the telescope. It is defined as follows:

$$G = \int_{\Omega} \int_{A_{\text{eff}}} f(\theta', \phi') d\Omega \hat{p} \cdot d\vec{A} \quad (2)$$

where \hat{p} is the unit vector opposite to the direction of the incoming particle; θ' , the polar angle between \hat{p} and the local magnetic field \vec{B} ; ϕ' , the azimuthal angle of \hat{p} with respect to \vec{B} ; Ω , the solid angle defined by the telescope's aperture; and A_{eff} , the effective area in the telescope. Figs. 1 and 2 illustrate the geometry.

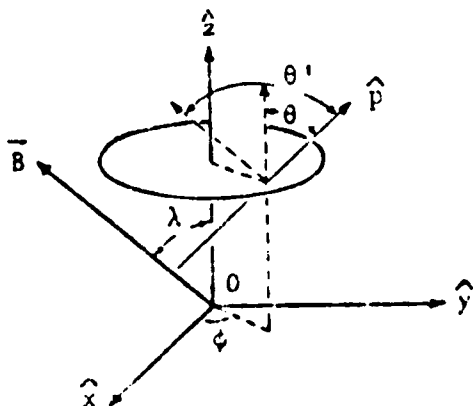


Fig. 1. Satellite Coordinate System

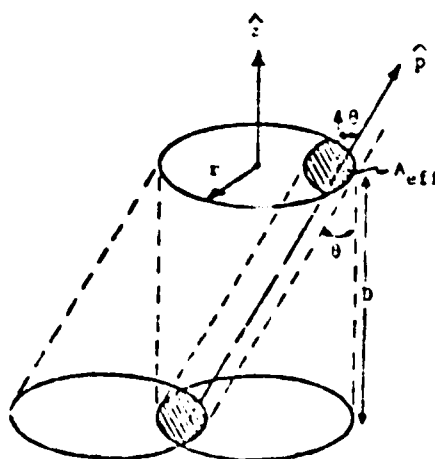


Fig. 2. Effective Area in Telescope

Under stationary conditions, the angular distribution $f(\theta', \phi')$ is axisymmetric with the local magnetic field \vec{B} but anisotropic in θ' . The θ' dependence can be described by $(\sin \theta')^n$ where n is the parametric index to be determined empirically. Hence Eq. (2) leads to

$$G = \int_{\Omega} \int_{A_{\text{eff}}} (\sin \theta')^n d\Omega \hat{p} \cdot d\vec{A} \quad (3)$$

In evaluating G for our data analysis, the conditions for data-collection must be taken into consideration. The Air Force Satellites S73-6 and S74-2 spin approximately four revolutions per minute. The detecting instruments (i.e. the P- α telescopes and LEPS) aboard the satellites had quite fast response. The slowest time period for recording the counting rate at various energy channels was one second. Therefore, during each counting period, the telescope axis can be regarded as being stationary. For the convenience of mathematical operation of Eq. (3) we choose the telescope axis as the \hat{z} -axis, the \vec{B} - \hat{z} plane as the \hat{y} - \hat{z} plane and the mid-point of the telescope as the origin. Fig. 1 illustrates this choice which enables us to convert Eq. (3) into the following form (see AFGL TR-78-0137):

$$G(n, \lambda) = 2r^2 \int_{\phi=0}^{2\pi} \int_{\theta=0}^{\theta_M} (\cos \theta \sin \phi) \left[1 - (\cos \lambda \cos \theta - \sin \lambda \sin \theta \sin \phi)^2 \right]^{n/2} \\ \times \left\{ \cos^{-1} \left(\frac{D}{2r} \tan \theta \right) - \left(\frac{D}{2r} \tan \theta \right) \times \left[1 - \left(\frac{D}{2r} \tan \theta \right)^2 \right]^{1/2} \right\} d\theta d\phi \quad (4)$$

where $\theta_M = \tan^{-1} \left(\frac{2r}{D} \right)$ (maximum polar angle for an incoming particle to pass through the top and bottom detector surfaces of the telescope).

Equation (4) was first calculated by use of the numerical integration method. Then we used the Monte Carlo method for a double check. The results from the two methods were found in excellent agreement. When the tabulated $G(n, \lambda)$ was being applied in deducing J_1 from the sorted data, λ was determined by knowing the relative position of the telescope with respect to \vec{B} and n by fitting the measured angular distribution of the data with $(\sin \theta')^n$. In the next section, some sample results are presented.

3. Results and Discussions

Because of the limited space of this report only one set of $G(n, \lambda)$, three pitch angle distributions, and two energy spectra are plotted in four figures below.

Although the value of $G(n, \lambda)$ varies with the detector's dimensions we still can see its typical form from Fig. 3. First of all, at $n=0$, $G(n, \lambda)$ does not depend on λ and is simply the built-in pure geometric factor of the detector. For instance, it is equal to $0.0139 \text{ cm}^2\text{-ster}$ for the LEPS with a narrow full opening angle of 23° . Second, all curves of $G(n, \lambda)$ converge to the pure geometric factor when λ approaches to 90° . Third, $G(n, \lambda)$ descends steeply with the increasing n .

In Fig. 4, the theoretic pitch angle distributions are plotted against the actual proton fluxes measured at the magnetic shells: $L=1.95 R_E$, $2.70 R_E$, and $3.74 R_E$. Although the magnetic field for Fig. 4(a) was found a little higher than the other two, they can be considered identical. Based on this consideration, the variation of the distributions can be attributed to the magnetic shell L and the pitch angle θ' . It is very

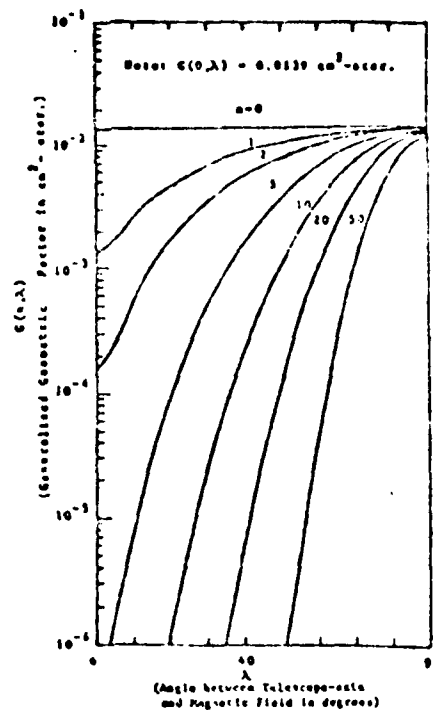


Fig. 3 $G(n, \lambda)$ versus λ for narrow-angle LEPS ($r = 0.147 \text{ cm}$, $D = 3.175 \text{ cm}$)

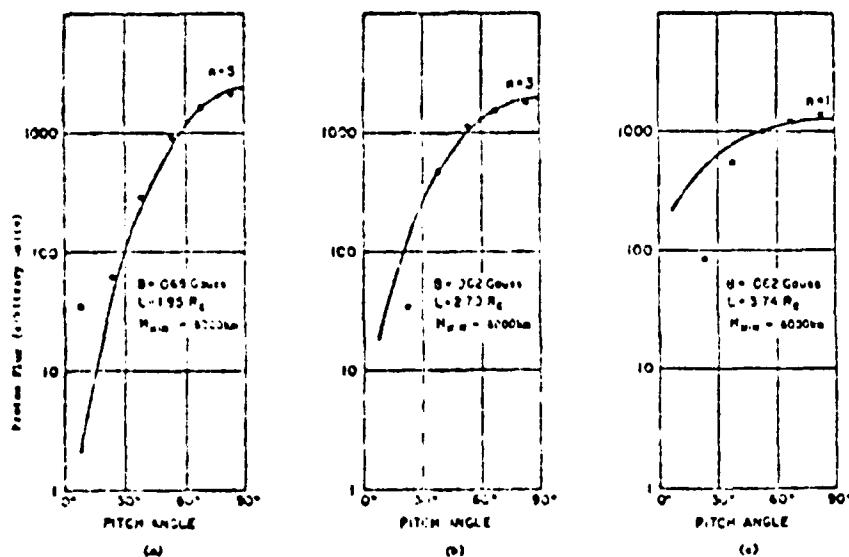


Fig. 4 Pitch Angle Distribution of 300 keV Protons

Measured by a LEPS with 2° opening angle. (1) a, a narrow LEPS 317 mm by 476 mm, $n = 60$ per degree (July 1976)

clear from this figure that n decreases when L increases. Furthermore the actual distributions seem to be steeper than the theoretical ones when the pitch angle drops to lower than 40° .

The two energy spectra plotted in Figs. 5 and 6 demonstrate the general feature that the flux of higher energy protons is smaller than that of lower energy ones in the regions of equal magnetic field. Another feature indicated by this figure is that the flux belonging to any energy level at a region of lower magnetic field is higher than those of the same energy level at a higher field region. Although a very few points do not follow this pattern, we may regard them as the spurious points of statistical nature. Finally it should be noted that the magnitude of the fluxes, ranging from 10^4 to 10^7 , agrees with the previous observations of other workers.

4. Conclusions

From the results presented in preceding section, we can reach the following temporary conclusions:

The fast response of the P- α telescopes and LEPS has simplified our formulation of the G factor because of no need of taking the time average of counting rates.

Since the pure geometric factor $G(0,1)$ and maximum angle of acceptance $\theta_M = \tan^{-1}(2r/D)$ for the narrow-angle LEPS are equal to $0.0139 \text{ cm}^2\text{-ster}$ and 12.3° respectively, the instrument provided us with a sharp angular discrimination.

The set of G curves as plotted in Figure 3 has shown that, at $\lambda > 80^\circ$ the G factors become almost independent of the anisotropy of the flux. This serves us a criterion for selecting particular data for the reduction of the information

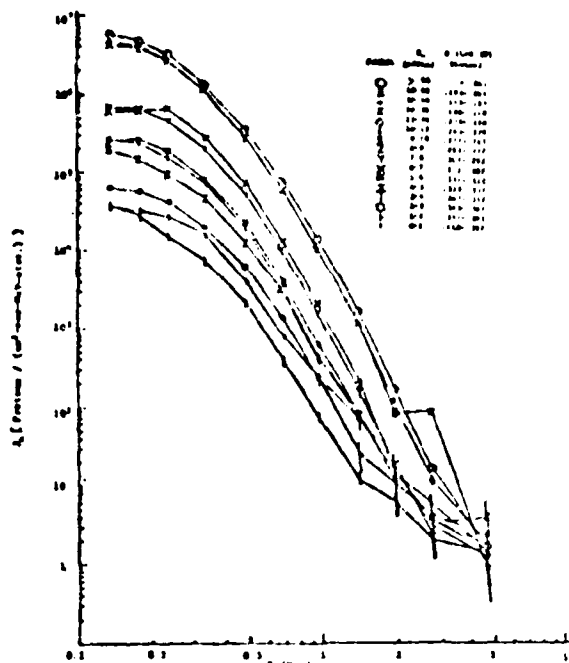


Fig. 5 Energy Spectra (Directional) Proton Flux Density J versus Energy E at various Minimum Voltages V_m and Earth Magnetic Field B to $L = 3.1$. (Stored Data from the P- α Telescopes 374-1, July, 1976)

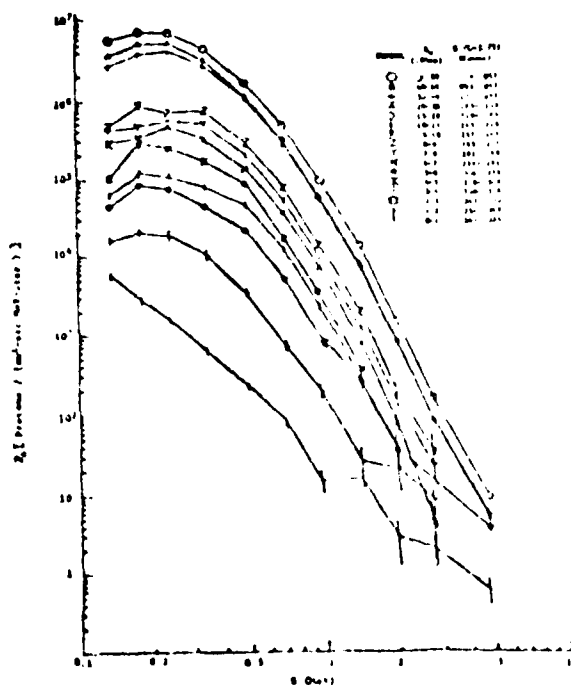


Fig. 6 Energy Spectra (Directional) Proton Flux Density J versus Energy E at various Minimum Voltages V_m and Earth Magnetic Field B to $L = 3.1$. (Stored Data from the P- α Telescopes 374-1, July, 1976)

other than the angular distribution.

Although the objectives of this paper do not include the interpretation of the measured pitch angle distribution and energy spectra, we would like to point out our observations: (i) the anisotropy seems to fit the function $(\sin \theta')^n$ very well from $\theta' = 90^\circ$ down to $\sim 40^\circ$ with one value of n . At the smaller angles the distribution tends to have a steeper slope which may imply that more complicated processes are needed for interpretation: (ii) the magnitude and shape of the energy spectra as shown in Figs. 5 and 6 are found to be largely consistent with those as reported by Mihalov and White in 1966. A compilation of similar data for the last solar cycle should provide adequate information to determine the temporal and spatial fluctuation of the low-energy proton flux.

5. Acknowledgement

The authors wish to thank Robert Vesprini and Thomas Spencer for their assistance in computer programming for this work. Also we acknowledge the valuable contribution of John Pantazis and Alan Huber in designing the detector telescopes.

6. References

The following list consists of only one part of the references which are either directly related to this work or representative of previous works.

- Filz, R. C., Space Res. 14, 321 (1974).
Fischer, H. M., Auschrat, V. W., and Wibberenz, G., J. Geophys. Res. 82, 537 (1977).
Hammer, M. and Crannel, C. J., Goddard Space Flight Center Report X-661-73-218 (1973).
Holeman, E. G., Davis, A. F., and Hagan, M. P., Air Force Geophys. Lab. Report TR-74-0531 (1978).
Pantazis, J., Hubert, A., and Hagan, M. P., Air Force Geophys. Lab. Report TR-75-0637 (1975).
Thomas, G. R. and Willis, D. M., J. Phys. E: Solen. Inst. 5, 260 (1972).
White, R. S., Phys. Today 19, 25 (1966).
Young, P. S., Vesprini, R., Holeman, E. G., Spencer, T., and Hagan, M. P., Air Force Geophys. Lab. Report TR-78-0137 (1977).
Young, P. S., Vesprini, R., Holeman, E. G., and M. P. Hagan, Air Force Geophys. Lab. Report TR-78-0146 (1978).

Solar Cycle Induced Modulation of the 55-MeV Proton Fluxes at Low Altitudes

DANIEL R. PARSIGNAULT AND ERNEST HOLEMAN

Physics Research Division, Emmanuel College, Boston, Massachusetts 02115

ROBERT C. FILZ

Air Force Geophysics Laboratory, Hanscom Air Force Base, Massachusetts 01731

Experiments flown on U.S. Air Force Satellites from 1961 until 1976 have measured the 55-MeV proton flux at low altitudes, between 275 km and 600 km. The analysis of these data shows that in spite of all the uncertainties involved, the agreement obtained between the theoretical calculations and the data is quite good. We conclude that the major determining factors of the 55-MeV proton fluxes in the inner zone are a nearly constant source coupled with a solar cycle varying atmospheric ionization loss process.

INTRODUCTION

Measurements of the 55- to 65-MeV proton population at low altitudes (275–600 km) have shown large changes in the fluxes closely following the solar cycle induced atmospheric density changes. Heckman and Nakano [1969] examined in detail the inner radiation belt protons at low altitudes for a period concurrent with the solar-minimum activity (September 1962–June 1966). They reported a high degree of stability during that period. As solar activity increased after mid-1966, these same authors observed a decrease in the 63-MeV proton population [Nakano and Heckman, 1968] and by mid-1969 (solar maximum) this same population had decreased by about a factor 2 relative to the solar minimum period.

Similarly, Filz and Holeman [1965] carried out comparable experiments, starting August 1961 until 1964, at the same altitudes, and reported that the 55-MeV proton flux closely followed the modulation expected from the variations of the earth's atmospheric density over that part of the solar cycle. These authors also observed on July 9, 1962, a sudden increase in the flux intensity, at the same energy, attributed to the high-altitude nuclear explosion, 'Starfish.' This increase could be explained by nonadiabatic redistribution of the inner-zone protons [Filz and Holeman, 1965]. Macy et al. [1970] further extended the period of this investigation to 1969 and found a rather good agreement of their data with a theory that took into account only atmospheric ionization losses.

In this report we present results obtained over the period October 1972 to August 1976, by three charged particle telescope experiments flown on U.S. Air Force satellites. We also have added to the emulsion data previously published [Macy et al., 1970] and some unpublished results for the 1969–1971 period. Using a simple transport equation, we then show that the 55-MeV proton flux modulation at low altitudes, from 1961 to 1976, can be reasonably well accounted for by the atmospheric density changes induced by the 11-year solar cycle. In particular, the high fluxes measured in 1976 are in good agreement with those observed in 1965, following a decrease to a minimum flux around 1968–69.

THE EXPERIMENTS

The measurements of the 55-MeV proton fluxes from 1961–1971 involved the use of emulsions carried on oriented, recov-

erable, polar orbiting Air Force satellites. These experiments as well as the data analysis, up until 1969, have been described in detail elsewhere [Filz and Holeman, 1965; Macy et al., 1970]. The data obtained from 1972 to 1976 were obtained with instruments flown on-board the polar orbiting Air Force satellites, 72-1, S3-2, and S3-3. The relevant orbit parameters for these satellites are shown in Table 1.

A solid state particle identifier telescope was flown on 72-1 [Morel et al., 1972; Filz et al., 1974]. Two identical solid state proton-alpha telescopes were used on S3-2 and S3-3, and these have been described in another paper [Morel et al., 1974].

DATA ANALYSIS

The data obtained with the particle identifier telescope on 72-1 has been reported previously [Filz et al., 1974; Holeman and Filz, 1975]. The final data tabulations gave the directional and omnidirectional fluxes sorted in various L groupings and 100 km- H_{min} intervals. The 72-1 data, covering an L region of 1.14–3.40 R_E , and H_{min} of 100–700 km were presented as a function of pitch angle for each of the 5 energy channels (5–45 MeV). Preliminary data analysis of the S3-2 and S3-3 experiment was also reported [Holeman et al., 1978]. These later data have been analyzed in final form and will be published shortly [Holeman et al., 1981]. The S3-2 and S3-3 data gave an excellent coverage of the region ' L - H_{min} ' space including $1.16 \leq L \leq 3.00$, $240 \leq H_{min} \leq 1400$ km, and $1.20 \leq L \leq 3.80$, $250 \leq H_{min} \leq 6900$ km, respectively. The energy range covered was 5–100 MeV, in 5 energy channels.

For this present investigation, we sorted our data in appropriate L - H_{min} bins, and the total fluxes were calculated for circular orbits of appropriate altitudes, i.e., 275 through 600 km. At each altitude and for a circular polar orbits, the fluxes at 55 MeV were averaged at each latitude ($\Delta\lambda = 2^\circ$) over all longitudes ($\Delta\phi = 5^\circ$). These integrations corresponded to a complete coverage of the SAA and thus could be compared directly to the rather uniform coverage of the SAA by the 3–4 day duration of the Air Force Satellite flights from 1961–1971.

THEORETICAL CALCULATION OF THE TIME DEPENDENCE

The trapped protons are lost from the radiation belts by ionization and excitation of atoms and by nuclear interaction with the nuclei in the upper atmosphere. However, at the en-

TABLE 1. Orbit Parameters of Air Force Satellites 72-1, S3-2, and S3-3

	72-1	S3-2	S3-3
Launch Date	Oct. 2, 1972	Dec. 3, 1975	July 8, 1976
Inclination, deg	98.4	96.3	97.5
Period, min	91	96.3	176.6
Apogee, km	750	1558	7856
Perigee, km	729	236	246

ergy of interest of ~ 55 MeV, we can safely ignore nuclear interactions. Additional losses are caused by pitch angle scattering by hydromagnetic waves and by diffusion across magnetic field lines at times of magnetic storms and by violation of the third adiabatic invariant. At the low altitudes under consideration, 275–600 km, we neglect all loss mechanisms, but the atmospheric ionization loss. The agreement of the theoretical curve with our data justifies this assumption. We thus consider the continuity equation in energy space,

$$\frac{\partial J(E, t)}{\partial t} + \frac{\partial}{\partial E} \left[J(E, t) \frac{\partial E}{\partial t} \right] = S(E) \quad (1)$$

where E is the proton energy and t is the time. The second term on the left represents the loss term and the term on the right, $S(E)$, is the source. This source is assumed to be constant in time but may vary with energy and altitude. This source includes the cosmic ray albedo neutron decay, CRAND, which varies by $\sim \pm 12\%$ from its mean value during the solar cycle [Blanchard and Hess, 1964]; the solar neutron decay injection source SND [Clafin and White, 1970]; the inward radial diffusion and magnetic field decay. The magnitude of this source is determined from the data of the 1963–1965 period by assuming $\partial J(E, t)/\partial t = 0$. We consider a power law type source of the form $S(E) = SE^{-\alpha}$. The loss term may be written as [Dragt *et al.*, 1966]

$$\frac{\partial}{\partial E} \left[J(E, t) \frac{\partial E}{\partial t} \right] = \frac{\partial}{\partial E} \left[J(E, t) \frac{\partial E}{\partial x} \right] \quad (2)$$

where we write the variable x , the proton velocity, as $AE^{-1/2}$ and $\partial/\partial x = BE^{-3/2}$. Then the partial derivative can be carried out and the differential equation solved for a constant atmospheric density ρ over a finite period of time t [Dragt, 1971; K. Yates, private communication, 1979]

$$J(E, t) = \frac{S}{E^\alpha} \left\{ 1 - \left[\frac{ABD}{E^\beta} (t+1) \right]^{(1-\alpha+\beta)/\beta} \right\} + J_0(E) \left[\frac{ABD}{E^\beta} (t+1) \right]^{(1-\alpha+\beta)/\beta} \quad (3)$$

where $J_0(E) = J(E, 0) = R_0 E^{-\alpha}$ is the initial power law spectrum. In the energy range of interest, $\alpha = 0.48$, $\beta = 0.77$, and $A = 0.048c$, where c is the speed of light. $B = 8 \times 10^{-22} \rho$, where ρ is the average atomic electron density in electrons/cm³ [Macy *et al.*, 1976]. Then $\beta = \alpha + 1$, and the solution to the equation (3) can be written in terms of the equilibrium power-law spectrum (taken to be at time 1963–65, when $dJ/dt = 0$), $J_0(E) = R_0 E^{-\alpha}$ as

$$J(E, t) = \frac{R_0 \rho_0}{E^\alpha} \left\{ 1 - \left[\frac{ABD}{E^\beta} (t+1) \right]^{(1-\alpha+\beta)/\beta} \right\} + \frac{R_0 \rho_0}{E^\alpha} \left[\frac{ABD}{E^\beta} (t+1) \right]^{(1-\alpha+\beta)/\beta} \quad (4)$$

This solution is more convenient than the iterative computer solutions, since it is stable regardless of the length of time considered (t need not be small). For the present calculations, we use $t = 1$ month. High altitude atmospheric densities vary both in magnitude and composition with a number of parameters that include magnetic storm strengths, daily, monthly and yearly variations and with the solar cycle. Since our study extends over a 15-year period, we are justified in considering only the solar cycle variation and smoothing the other shorter time fluctuations over the solar cycle. The atmospheric densities are thus represented by the average monthly values, which is the most convenient form when performing trapped proton calculations. A finer scale would be meaningless since proton lifetimes are long when compared to one month, and in any case, more precise calculations cannot be made since only one indicator is available over the whole period, i.e., the S number (10.7-cm radio wave data). By treating the density as a constant over a given monthly period, the continuity equation (4) can be solved exactly by using the previous month's solution as input to the next month. We estimate that any error introduced by this method must be far less than that caused by our ignorance of the large daily fluctuations and by our averaging method. Effectively, we use a density average derived from observed satellite slow down and apply it to high-energy proton slow down. Our calculations follow very closely those of Macy *et al.* [1970], and the method used here gives essentially identical results to the iterative solutions.

Furthermore, we found experimentally, for the anomaly observed proton fluxes, that K does not vary much over a solar cycle and therefore set it equal to the average index of 0.76 observed by Nakano and Heckman [1968], which is also consistent with our data. These authors also found no measurable change in K during the period of their observations.

To correlate the emulsion data that are integrated over the South Atlantic Anomaly with ρ , the atmospheric densities, we used the comparably integrated densities of Macy *et al.* [1970]. From 1970 to 1977, we compute new densities from the Macy *et al.* data, taking into account the actual measured variations

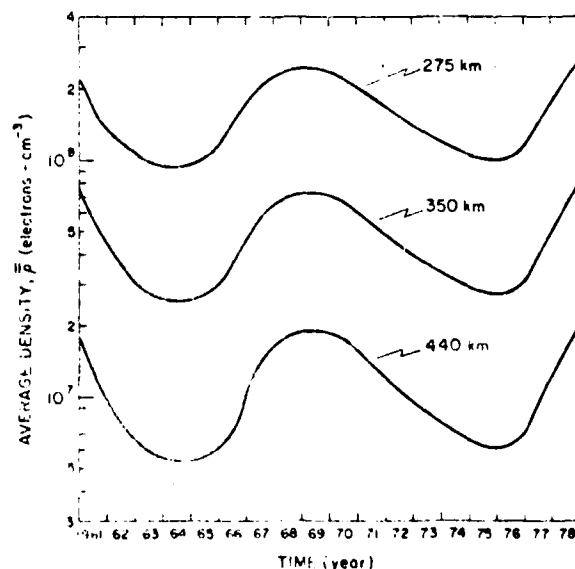


Fig. 1. The trajectory-averaged, Anomaly-averaged free electron densities, ρ (electron cm⁻³), at 275, 350, and 440 km.

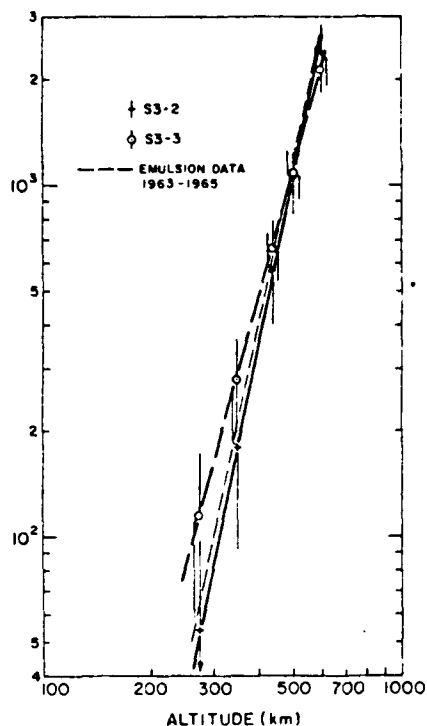


Fig. 2. Proton flux intensities (protons $\text{m}^{-2} \text{s}^{-1} \text{MeV}^{-1}$) as a function of altitude for a polar circular orbit, as calculated from the data of S3-2 and S3-3 (July 1976), for $E_p = 55 \text{ MeV}$.

of the Harris and Priester S numbers (10.7 cm) during that time period, smoothing out with a 2.5 year running mean. This S number is related to \bar{F} , the solar flux parameter, by Harris and Priester [1963]. The trajectory-averaged, anomaly-averaged \bar{p} , in electrons/cm², are given for 275, 350, and 440 km in Figure 1.

Figure 2 shows the proton flux intensity as a function of altitude for a polar circular orbit, as calculated from the data of S3-2 (January 1976) and S3-3 (July 1976). We fitted the data

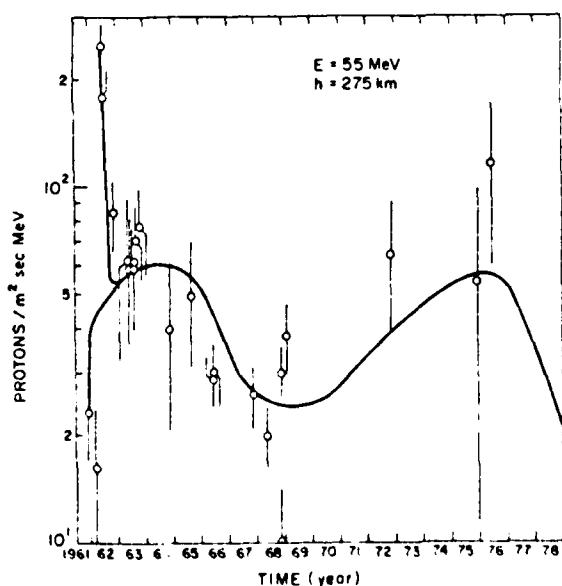


Fig. 3. Proton flux intensity (protons $\text{m}^{-2} \text{s}^{-1} \text{MeV}^{-1}$) as a function of time, at 275 km, for $E_p = 55 \text{ MeV}$.

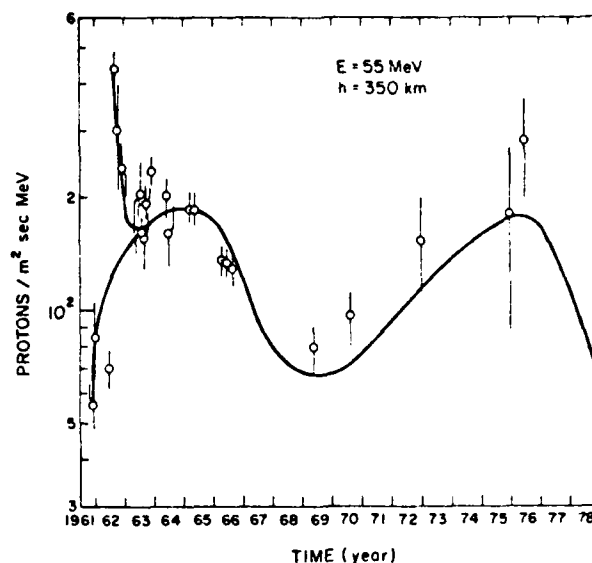


Fig. 4. Proton flux intensity (protons $\text{m}^{-2} \text{s}^{-1} \text{MeV}^{-1}$) as a function of time, at 350 km, for $E_p = 55 \text{ MeV}$.

to a power law of the form $J(H_c) = C(H_c)^K$, where H_c is the guiding center altitude and $J(H_c)$ is the omnidirectional flux in protons/ $\text{m}^2 \text{s} \text{MeV}$. We find $C = 7.00 \times 10^{-11}$ and $K = 4.878$ for the S3-2, data and $C = 8.16 \times 10^{-8}$ and $K = 3.750$ for the S3-3 data.

These two curves agree very well, both in slope and intensity, with the various curves obtained with the emulsion data ~11 years before [Fitz, 1968].

DISCUSSION

The theoretical time dependence curves presented here differ slightly from those presented by Macy *et al.* [1970] because we have attempted to obtain a 'best fit' to the data of the last solar minimum (1976) and thus evaluated the measurements taken during the current solar minimum. One sees in Figures 3, 4, and 5 that the emulsion data are fitted very well with the following exceptions:

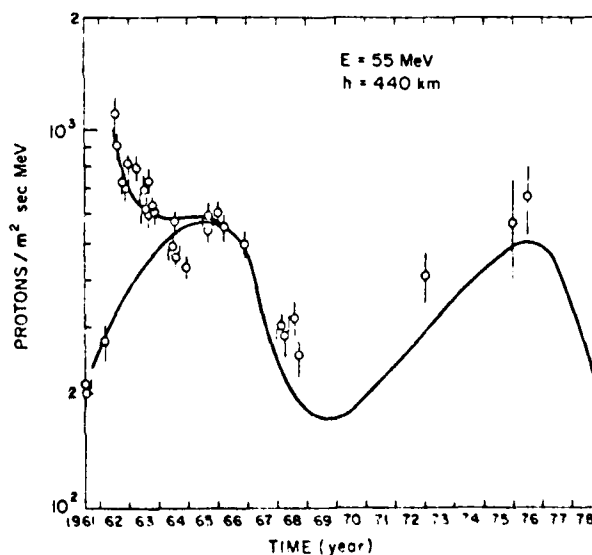


Fig. 5. Proton flux intensity (protons $\text{m}^{-2} \text{s}^{-1} \text{MeV}^{-1}$) as a function of time, at 440 km, for $E_p = 55 \text{ MeV}$.

1. The pre-starfish data at 275 km and 350 km are too low by about a factor of 2 from the levels required to fit the post-starfish data. This is revealed in the sharp initial rise in the theoretical curve in 1962.

2. The 1968, 1969, and 1970 data at 350 and 440 km are about 30% too high in comparison with the theoretical predictions.

These two exceptions mutually oppose each other if an attempt is made to obtain a better solution by adjusting the theoretical parameters. For example, an increase in the assumed equilibrium flux in 1963-1965, at 440 km, would yield a better agreement in 1968, but a worse agreement with the pre-starfish (1963-1965) data. A better fit to the data would require a solar cycle time-dependent source out of phase with the density. The neutron albedo source does have a solar cycle dependence but of the wrong phase and with only an expected peak to peak amplitude of 25%. However, if the neutron albedo source were to contribute through an inward radial diffusion mechanism such as the one suggested by Farley and Walt [1971], then a reduced amplitude in the solar cycle dependence would result. Farley and Walt [1971] state explicitly that 'some protons will be drawn down from the large reservoir in the heart of the inner zone, partially compensating for the enhanced atmospheric losses.' Such an effect, if of sufficient magnitude, would certainly help to explain our apparently too large 1968 proton fluxes.

Another possible source variation that would improve the fit to the data would be a source strength monotonically increasing as a function of time. An increase in the source strength of about 5% per year would bring the theoretical curves in better agreement with the data.

While many new models of the upper atmosphere have more recently been developed [Jacchia, 1977; Hedin et al., 1977a, b], these models are primarily aimed at improving the knowledge of the chemical composition and its time variation and have not resulted in substantial changes in the overall average densities. The density versus temperature curves for the various altitudes of interest here, as given by Jacchia [1977], are almost identical to those given by Harris and Priester [1963]. While the use of the newer models could possibly result in changes in the curves presented here of the order of 20%, the accuracy of our calculations and indeed of the newer atmospheric models themselves does not justify the extensive calculations which would be involved.

CONCLUSION

We have examined 55-MeV proton data taken at low altitudes, between 275 and 600 km from 1961 until 1976. We find that in spite of all the uncertainties involved, the agreement obtained between the theoretical calculations and the data is quite good, and it is concluded that the major determining factors of the inner zone proton fluxes are a nearly constant source coupled with a solar cycle varying atmospheric ionization loss process.

Acknowledgments. We thank M. P. Hagan for his support in carrying out this research. This work was supported in part under Air Force contract number F19628-79-C-0012.

The Editor thanks A. J. Dragt for his assistance in evaluating this paper.

REFERENCES

- Blanchard, R. C. and W. N. Hess, Solar cycle changes in inner zone protons, *J. Geophys. Res.*, **69**, 3927-3938, 1964.
- Clafin, E. S., and R. S. White, Injection of protons into the radiation belt by solar neutron decay, *J. Geophys. Res.*, **75**, 1257-1262, 1970.
- Dragt, A. J., Solar cycle modulation of the radiation belt proton flux, *J. Geophys. Res.*, **76**, 2313-2345, 1971.
- Dragt, A. J., M. N. Austin, and R. S. White, Cosmic ray and solar proton albedo neutron decay injection, *J. Geophys. Res.*, **71**, 1293-1304, 1966.
- Farley, T. A., and M. Walt, Source and loss process of protons of the inner radiation belt, *J. Geophys. Res.*, **76**, 8223-8240, 1971.
- Filz, R. C., Observations of inner zone protons in nuclear emulsions 1961 to 1966, in *Earth's Particles and Fields*, edited by B. M. McCormac, pp. 15-22, Reinhold, New York, 1968.
- Filz, R. C., and E. Holeman, Time and altitude dependence of 55 MeV trapped protons, August 1961 to June 1964, *J. Geophys. Res.*, **70**, 5807-5822, 1965.
- Filz, R. C., L. Katz, B. Sellers, F. A. Hanser, and E. Holeman, Observations of 5-45 MeV protons at $L \leq 3$ and $L \geq 7$, *Space Research*, **15**, 321-326, 1974.
- Harris, E. G., and W. Priester, Relation between theoretical and observational models of the upper atmosphere, *J. Geophys. Res.*, **68**, 5891-5894, 1963.
- Heckman, H. H., and G. N. Nakano, Low-altitude trapped protons during solar minimum period, 1962-1966, *J. Geophys. Res.*, **74**, 3575-3590, 1969.
- Hedin, A. E., J. E. Salah, J. V. Evans, C. A. Reber, G. P. Newton, N. W. Spencer, D. C. Kayser, D. Alcayde, P. Bauer, L. Cogger, and J. P. McClure, A global thermospheric model based on mass spectrometer and incoherent scatter data MSIS, 1, N_2 density and temperature, *J. Geophys. Res.*, **82**, 2139-2147, 1977a.
- Hedin, A. E., C. A. Reber, G. P. Newton, N. W. Spencer, H. C. Brinton, H. G. Hayr, and W. E. Potter, A global thermospheric model based on mass spectrometer and incoherent scatter data MSIS, 2, Composition, *J. Geophys. Res.*, **82**, 2148-2156, 1977b.
- Holeman, E., and R. C. Filz, Protons flux data obtained on Air Force Satellite 72-1 over the period October 1972-February 1973, *Sci. Rep. 2, AFCL-TR-73-0377*, Air Force Cambridge Res. Lab., Bedford, Mass., June 1975.
- Holeman, E., A. F. Davis, and M. P. Hagan, Analysis of data from research satellites, *Final Rep. AFGL-TR-78-0187*, Air Force Cambridge Res. Lab., Bedford, Mass., July 1978.
- Holeman, E., D. R. Parsignault, M. P. Hagan, and R. C. Filz, Proton fluxes (0.01-100 MeV) as measured by the Air Force satellites S3-2 and S3-5, *Final Rep.*, Contract AFGL-F19628-79-C-0102, Air Force Cambridge Res. Lab., Bedford, Mass., in press, 1981.
- Jacchia, L. G., Thermospheric temperature, density and composition: New models, *Spec. Rep. 375*, Smithsonian Astrophys. Observ., Cambridge, Mass., March 1977.
- Macy, W. W., R. S. White, R. C. Filz, and E. Holeman, Time variation of radiation belt protons, *J. Geophys. Res.*, **75**, 4322-4328, 1970.
- Morel, P. R., and B. Sellers, Design and fabrication of a heavy particle identification instrument for satellite, *Rep. F19628-69-C-0234*, Panametrics Inc., location, December 1972.
- Morel, P. R., F. A. Hanser, and B. Sellers, A satellite telescope for protons and alphas, *Final Rep.*, AFCL-TR-74-0531, Panametrics Inc., Wilham, Mass., Nov. 1974.
- Nakano, G. N., and H. H. Heckman, Evidence for solar cycle changes in the inner-belt protons, *Phys. Rev. Lett.*, **20**, 8060, 1968.

(Received February 17, 1981;
revised July 16, 1981;
accepted July 17, 1981)

Long-Term Intensity Decrease in the 8- to 25-MeV Proton Fluxes at Low L Values

DANIEL R. PARSIGNAULT AND ERNEST HOLEMAN

Physics Research Division, Emmanuel College, Boston, Massachusetts 02115

ROBERT C. FILZ

Air Force Geophysics Laboratory, Hanscom AFB, Massachusetts 01731

A five year continuous observation, 1963–1968, of the 8- to 25-MeV proton population, at $L < 2.0$, had shown a monotonic decrease in this population. We have observed the same proton population from 1970 to 1976, using experiments flown on several USAF satellites (72-1, S3-2, S3-3). These data, together with published data from the DIAL satellite, show that the decreases in the proton fluxes first observed from 1963 to 1968 have continued unabated, at least until August 1976, and with the same original mean lives. The proton flux at $L = 1.35$ decayed over the 13-year period (1963–1976) with a mean life τ of 5.7 ± 0.5 years. At $L = 1.90$, τ was 4.55 ± 0.16 years. However, the proton flux at $L = 1.20$, which had first been reported as constant, started decreasing ~ 1970–1976 with $\tau = 3.07 \pm 0.25$ years. Possible explanations for this phenomenon can be divided into the two categories of natural and artificial effects. We reviewed these different effects and conclude that most likely we are seeing the decay of the high energy protons redistributed by the 'Starfish' high-altitude nuclear explosion.

INTRODUCTION

The long-term monitoring of the trapped particle fluxes in the earth's magnetosphere should be of considerable help in the understanding of its dynamics. However, the long-term behavior of the trapped protons is far from being understood, and several outstanding questions remain unexplained, among which is the apparent decrease of the proton fluxes, at low L values in the 8- to 25-MeV energy range, observed over a period of five years (1964–1968) by *Bostrom et al.* [1971].

In this paper, we report the results of several measurements of 8.5- to 25-MeV proton fluxes made over several time periods of approximately six months long each, between 1972 and 1976. Our results indicate that the decrease in the fluxes first observed by *Bostrom et al.* have continued unabated, at least until August 1976.

INSTRUMENTATION

Our data were obtained using instrumentation flown on board the polar orbiting Air Force satellites 72-1, S3-2, and S3-3. The relevant orbit parameters for these satellites are shown in Table 1.

A solid state particle identifier telescope was flown on 72-1. For a description of this instrument, the reader should refer to papers by *Morel et al.* [1972], and *Filz et al.* [1974]. Two identical solid state proton telescopes were used on S3-2 and S3-3, and these have been described in another paper [*Morel et al.*, 1974].

DATA ANALYSIS

The data obtained with the proton telescope on 72-1 have been reported previously [*Holeman and Filz*, 1975]. The final data tabulations gave the directional and omnidirectional fluxes sorted in various earth radii L , groupings and 100-km H_{min} intervals. The magnetic field model used in the analysis was IGRIF 1965 model. The relevant magnetic field for the year of a particular series of observations was then calculated

by using the secular change coefficient. The 72-1 data covering an L region from 1.14 to 3.40 earth radii, and H_{min} of 100–700 km were given as a function of pitch angle for each of the 5 energy channels (5–45 MeV). Preliminary data analysis of the S3-2 and S3-3 experiments were also reported [*Holeman et al.*, 1978]. These data have now been analyzed in a final form and will be published shortly [*Holeman et al.*, 1981]. The S3-2 and S3-3 data gave an excellent coverage of the region in ' L - H_{min} ' space including $1.16 \leq L \leq 3.0$, $240 \leq H_{min} \leq 1400$ km; and $1.20 \leq L \leq 3.80$, $240 \leq H_{min} \leq 6900$ km, respectively. H_{min} is defined as follows: For a given set of B , L values, B - L iso-contours are drawn in the northern and southern hemispheres. The minimum altitude for each set of these iso-contours is called H_{min} . This minimum value occurs in the southern hemisphere, in the South Atlantic anomaly, owing to the offset of the earth's dipole. The energy range covered was from 5 to 100 MeV, in five energy channels.

The data from 72-1 were recorded over a six-month period starting October 1972 and ending May 1973. During this time period no significant intensity fluctuations were observed in the regions of interest. The data from S3-2 consisted of 186 orbits from December 1975 to March 1976, and for S3-3 we analyzed 383 orbits from July 1976 until January 1977. The data from S3-3 used in the present analysis were for the July–August 1976 period. In addition, we used selected data from the German satellite DIAL which were recently published [*Fischer et al.*, 1977]. These data were recorded in April 1970.

EXPERIMENTAL RESULTS

The original data recorded by the satellite 1963-38C spanned a time period starting October 1963 and ending January 1969. During this period, the 8.2- to 25-MeV proton fluxes were monitored at L values between 1.20 and 2.60. Between $1.35 \leq L \leq 2.20$, the proton fluxes were observed to decrease monotonically as a function of time.

We selected data, taken with our three experiments on board the three Air Force satellites, at the same B and L posi-

TABLE 1. Orbit Parameters of Air Force Satellites 72-1, S3-2, and S3-3

	Satellite		
	72-1	S3-2	S3-3
Launch date	10/02/72	12/03/75	07/08/76
Inclination, deg	98.4	96.3	97.5
Period, min	91	96.3	176.6
Apogee, km s	750	1558	7856
Perigee, km s	729	236	246

tions. These coordinates are listed in Table 2 together with the mirroring proton fluxes observed (protons/cm² s sr MeV).

For the instruments on-board S3-2 and S3-3, the energy interval under consideration corresponded to channels 2 and 3 (8.0-13 and 13-25 MeV, respectively) of the 5-energy channel spectrometer of each instrument. The closest channels of the spectrometer on 72-1 which coincided with the energy range of interest, were channels 2, 3, and 4 (7.0-12.2, 12.2-18.2, and 18.2-28 MeV). We interpolated the data to cover the energy range 8-25 MeV, and took into account these corrections as part of the uncertainties in the data points thus calculated. Similar corrections were applied to the DIAL satellite data.

The values for the 1963-38C were taken from Figure 6 of *Bostrom et al.* [1971]. The uncertainties were estimated from the scattering of the data points for the curve at $L = 1.35$. We assigned the same percentage uncertainties to the data points at $L = 1.20$ and $L = 1.90$.

The data points of April 1970, recorded by the DIAL satellite, were taken from Figures 5 and 6 in the paper by *Fischer et al.* [1977]. Our interpolation of the data to cover the 8- to 25-MeV range together with the scattering of the data at each of the particular (B , L) coordinate points, determined the uncertainties assigned to these data.

Figure 1 shows the directional proton intensities (J_i) in protons/cm² s sr MeV versus time, from January 1964 until August 1976, starting with the five-year continuous measurements of 1963-38C represented by the heavy lines.

In order to calculate the mean lives of the proton flux decreases, we performed a weighted least-square fit to a simple exponential $J_i = J_0 \exp(-t/\tau)$. As far as the 1963-38C data were concerned, we took the intensities at the beginning and end of the measurement period. At $L = 1.20$, this satellite measured a constant flux during the 5-year measurement period. However, since our data clearly show a steady decrease in the proton flux on that field line starting somewhere after

January 1969, we only consider in the fit the flux intensity at that time together with the three other data points recorded between 1970 and 1976.

Table 3 shows the resulting mean lives calculated from the data. The mean lives at $L = 1.35$ and 1.90 , as calculated with the data available from 1964 to 1976, are in very good agreement with the original mean lives as measured by 1968-38C satellite. Our data at $L = 1.20$ clearly shows a decrease on that field line, in contrast with the constant flux measured during 1964-1968, period.

DISCUSSION

Possible explanations for the observed behavior of the 8- to 25-MeV trapped proton fluxes can be divided into the two categories of natural and artificial phenomena. But the empirical data indicate that during our period of observation (1964-1976) the proton fluxes had to exceed those which would otherwise have been balanced by natural sources over more than one 11-year solar cycle.

For this reason, any explanation of a natural origin of the phenomenon for injection requires large perturbation event(s) not seen in the present 11-year solar cycle. *McIlwain* [1965] has observed changes in proton fluxes at higher L values during major magnetic storms. In particular, variations of the 2.2- to 8.2-MeV proton fluxes were observed during the spectacular May 26, 1967, magnetic storm by *Bostrom et al.* [1971]. However, these same authors saw no variation of the 8.2- to 25-MeV proton fluxes at $L \leq 2$.

The order of magnitude decay of the 8- to 25-MeV proton fluxes seen here between 1964 and 1976 at $L = 1.20, 1.35$, and 1.90 suggests that any increases caused by an earlier magnetic storm (prior to 1964) must have been very large indeed. However, the rather exceptionally large May 1967 event was observed to have no effect whatsoever at these L values [*Bostrom et al.*, 1971]. While storms comparable to this May 1967 event ($Dst = -418 \gamma$) were seen in 1958 and 1959 ($Dst = -422 \gamma$ and -436γ , respectively), no significant larger storms were seen during the last two solar cycles. No magnetic storms with $Kp > 9$ were observed from 1947 through 1956, [*Cage and Zawalick*, 1972; *Mayaud and Romana*, 1977], and the 4 September 1957 storm was not as large as the May 1967 storm judging by the Dst measurements.

Several times during the previous and present centuries, outstanding tropical aurorae have been observed, coinciding with periods of exceptional activity on the sun [*Chapman*, 1957]. This type of magnetic storm could be responsible for the very large injection of protons necessary to explain our

TABLE 2. Mirroring Proton Fluxes ($8 \leq E_p \leq 25$ MeV) at $L = 1.20, 1.35$, and 1.90 as Measured from January 1964 until August 1976 by Satellites 1963-38C, DIAL, 72-1, S3-2, and S3-3

	Proton Fluxes, J (p/MeV cm ² s sr)					
	Jan. 1964	Jan. 1969	Apr. 1970	Jan. 1973	Feb. 1976	Aug. 1976
$0.180 \leq B \leq 0.190$ $100 \leq h_{min} \leq 800$ $B/B_0 = 1.00$						
$L = 1.20$	$25 \pm 2^*$	$28 \pm 2^*$	$21.5 \pm 1.5^*$	6.3 ± 1.0	3.0 ± 0.4	
$0.170 \leq B \leq 0.180$ $800 \leq h_{min} \leq 900$ $1.31 \leq B/B_0 \leq 1.35$						
$L = 1.35$	$206 \pm 14^*$	$102 \pm 7^*$	$95 \pm 10^*$		20.0 ± 3.0	23.0 ± 3.0
$0.205 \leq B \leq 0.225$ $600 \leq h_{min} \leq 800$ $4.25 \leq B/B_0 \leq 5.35$						
$L = 1.90$	$135 \pm 10^*$	$42 \pm 3^*$		16.5 ± 1.1	9.4 ± 0.4	

* Estimated uncertainties in the proton fluxes as taken from Figure 6 in the work of *Bostrom et al.* [1971].

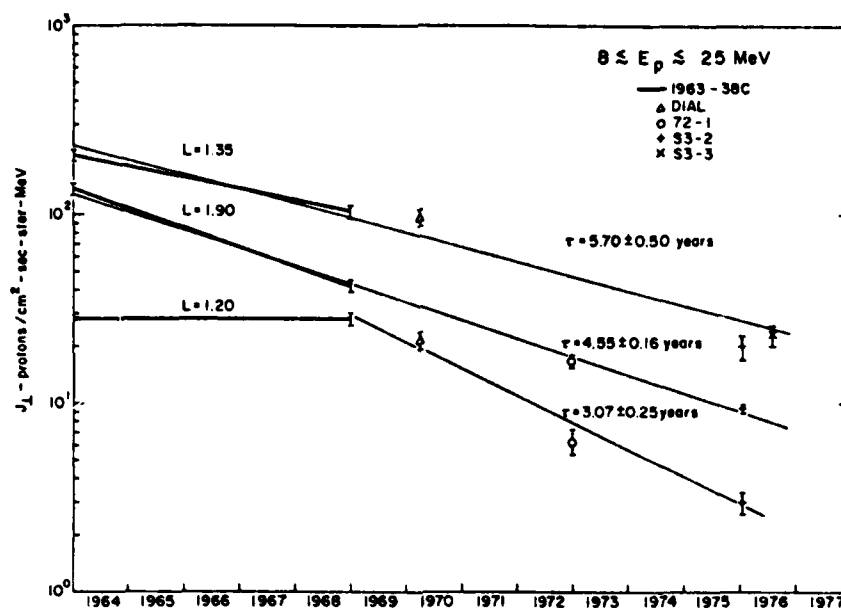


Fig. 1. Mirroring proton fluxes ($8 \leq E_p \leq 25$ MeV) as measured by satellites 1963-38C, DIAL, 72-1, S3-2, and S3-3, from January 1964 until August 1976.

observations. However, there is no quantitative theory that can be used to correlate such an injection with the low latitude precipitation. (Note added in proof: The recent tropical aurora observed April 13, 14, 1981, coincided with very large solar flares and had a $Dst \approx -300$ γ (J. C. Private Communications, Joselyn, 1981; M. Sugiura, Private communication, 1981).)

Looking back over the past observations, the only increase of some significance in the inner zone of trapped protons was revealed by the measurements made by *Filz and Holeman* [1965] at low altitudes, of the 55-MeV trapped proton fluxes immediately following the 'Starfish' high-altitude nuclear explosion. Their observations were consistent with a simple 2° equatorial pitch-angle redistribution that moved particles down the field lines. Subsequent analysis by *Cladis et al.* [1970], while making this interpretation plausible has not yielded quantitative proof of this hypothesis. Although the observations here at $L = 1.90$ could be explained by a pitch angle redistribution caused by 'Starfish,' the necessary increase at $L = 1.20$ could not be accounted for by the same redistribution since this observation was made at the equator ($B/B_0 = 1.00$). To explain the order of magnitude increase at $L = 1.20$ would necessitate a redistribution in L and/or an acceleration mechanisms.

Further evidence for 'Starfish' having caused the increase in the proton fluxes is the observation by *Fischell et al.* [1966], who reported that damage to solar cells of the 1961 $\alpha 1$ and 2 satellites following the nuclear explosion which could 'not be explained by an omnidirectional fission-electron spectrum.' These authors postulated 'a significant increase in the number of protons with $E > 4.5$ MeV being redistributed at least to an altitude range between 400 and 1200 km' by 'Starfish.' Thus, if the 8- to 25-MeV protons were to have been introduced by 'Starfish,' it would provide a resolution to this long outstanding problem.

Another curious aspect of the $L = 1.20$ observations that must be explained by any source is the constancy of the flux

from 1964 to 1968. A similar constancy in the 55-MeV proton fluxes was observed at lower altitude in the measurements of *Filz and Holeman* [1965], *Filz* [1967], and *Heckman and Nakano* [1969]. These authors showed that this could result from a chance coincidence between the rapid flux decay following 'Starfish' and the decreasing atmospheric density correlated to the approaching solar minimum. While the atmospheric density-solar cycle relationship is not well established at the higher altitudes considered here, it would seem to be a likely explanation for these present results at $L = 1.20$ as well.

In order to investigate the possibility that the 8- to 25-MeV protons reported here were present prior to 'Starfish,' a close examination of pre-'Starfish' data was made. Unfortunately, very little directional flux data was obtained prior to this artificial event, and geiger counter data cannot be used for quantitative comparisons. The NERV nuclear emulsion data [*Naugle and Kniffen*, 1961, 1963] would be the most reliable for determining proton fluxes in this energy interval, but there is some absolute flux uncertainty due to the spinning of the rocket. The NERV 'point B' that corresponds to $L = 1.72$ and $B = 0.198$ (see Figure 11 in *Naugle and Kniffen* [1963]) is closest to our data point at $L = 1.90$ ($B = 0.215$). The proton energy spectra at the NERV 'point B' when properly interpolated, would give 8- to 25-MeV proton fluxes in reasonable agreement with an extrapolation of our $L = 1.90$ data back to 1960. *Naugle and Kniffen* [1963] suggested that the main source of the upturn at the low energies in the proton spectra results from the injection of the albedo neutrons by solar protons (SPAND).

TABLE 3. Mean Lives, τ (years) of the Proton Flux Decay at $L = 1.20, 1.35$, and 1.90

L	1963-38C	Total Data
1.20	Constant	3.07 ± 0.25
1.35	7.1 ± 1.4	5.70 ± 0.50
1.90	-4.3 ± 0.4	4.55 ± 0.16

The low energy protons observed at $L = 1.72$, $B = 0.198$ (NERV 'point B') seems to disappear at $L = 1.64$, $B = 0.196$ ('point C'). These same authors interpret this observation as resulting from the transition from the SPAND source to the equatorially shadowed (from the polar cap) region where the CRAND source predominates. Our present data however, shows intense fluxes of low energy protons down to $L = 1.35$, a region in L space that is inaccessible to SPAND.

For the SPAND process to contribute, one would also have to assume that the major contribution came from the large solar flares that occurred during the 1950's and that the absence of large proton producing flares in the 1960's has led to the decay. The August 1972 flare was large enough but still probably less than 1/10th the size of the sum of the 1950's flares and hence would probably not contribute sufficient low-energy protons to be observed because of the uncertainties of comparing different data sets.

Another possibility to explain these protons is that they could have been brought onto the lower L values by inward radial diffusion processes such as those proposed by Farley and Walt [1971]. However, they should be present in the NERV data as well. Finally, an alternative hypothesis is that the low L regions were populated with low-energy protons by 'Starfish' and that the high L regions were populated with low-energy protons by 'Starfish' and that high L regions were populated by the SPAND process. Thus, the NERV data does suggest a source of low energy protons, which if redistributed a few degrees in equatorial pitch angle by 'Starfish,' might account for the high fluxes at the lower L values reported by Bostrom et al. [1971].

CONCLUSION

Although we cannot completely explain the observed phenomenon, i.e., the steady decrease of the 8- to 25-MeV proton fluxes at $L \leq 1.9$ over the 13-years observation period, it is nevertheless well established from 5 independent sets of observations that the originally observed decay of the proton fluxes between 1964 and 1968, at $L = 1.35$ and 1.90 has continued unabated until at least August 1976.

This decrease in the fluxes, which spans approximately 13 years, cannot be related to the 11-year solar cycle. Indeed, for the solar minima that occurred in ~1965 and ~1976, any solar-induced modulation of the proton fluxes would have resulted in comparable flux intensities at these 2 times.

There is no doubt, based on three independent sets of observations, that the flux at $L = 1.20$, which was observed to be constant up until 1969, started decaying at approximately that time with the shortest mean life observed in our data, i.e., 3.07 ± 0.23 years.

While it is possible that the 8- to 25-MeV protons that we are observing were originally introduced by some large magnetic storm in the 1960's, this explanation seems unlikely; most probably, we are simply looking at protons redistributed in L value and pitch angle by the 'Starfish' high-altitude nuclear explosion on July 9, 1962.

Acknowledgments. We thank M. Patricia Hagan for her support in carrying out this research. This work was supported in part under Air Force contract number F19628-79-C-0102.

The Editor thanks J. B. Blake for his assistance in evaluating this paper.

REFERENCES

- Bostrom, C. O., D. S. Beall, and J. C. Armstrong, Time history of the inner radiation zone October 1963 to December 1968, in *Models of the Trapped Radiation Environment: Long Term Time Variations*, vol. 7, NASA SP-3024, pp. 25-35, 1971.
- Cage, A. L., and E. Zawalick, A discussion of the geomagnetic indices K_p and a_p , 1932 to 1971, Rep. AFCRL-72-0693, Air Force Cambridge Res. Lab., Bedford, Mass., November 1972.
- Chapman, S., The aurora in middle and low latitudes, *Nature*, 179, 7-11, 1957.
- Cladis, J. B., G. T. Davidson, W. E. Francis, R. K. Jaggi, G. H. Nakano, and S. L. Ossakow, Redistribution of trapped protons by Starfish nuclear explosion, *J. Geophys. Res.*, 75, 57-68, 1970.
- Farley, T. A., and M. Walt, Source and loss processes of protons of the inner radiation belt, *J. Geophys. Res.*, 76, 8223-8240, 1971.
- Filz, R. C., Comparison of the low altitude inner zone 55-MeV trapped proton fluxes measured in 1965 and 1961-1962, *J. Geophys. Res.*, 72, 959-963, 1967.
- Filz, R. C., and E. Holeman, Time and altitude dependence of 55 MeV trapped protons, August 1961 to June 1964, *J. Geophys. Res.*, 70, 5807-5822, 1965.
- Filz, R. C., L. Katz, B. Sellers, F. A. Hanser, and E. Holeman, Observations of 5-45 MeV protons at $L \leq 3$ and $L \geq 7$, *Space Res.*, 14, 321-326, 1974.
- Fishell, R. E., J. H. Martin, W. E. Radford, and W. E. Allen, Radiation damage to orbiting solar cells and transistors, in *Radiation Trapped in the Earth's Magnetic Field*, edited by B. M. McCormac, pp. 793-807, D. Reidel, Hingham, Mass., 1966.
- Fischer, H. M., V. W. Auschra, and G. Wibberenz, Angular distribution and energy spectra of protons of energy $5 \leq E \leq 50$ MeV at the lower edge of the radiation belt in equatorial latitudes, *J. Geophys. Res.*, 82, 537-547, 1977.
- Heckman, H. H., and G. H. Nakano, Low-altitude trapped protons during solar minimum period, 1962-1966, *J. Geophys. Res.*, 74, 3575-3590, 1969.
- Holeman, E., and R. C. Filz, Proton flux data obtained on Air Force Satellite 72-1 over the period October 1972-February 1973, *Sci. Rep. 2, AFCRL-TR-75-0377*, Emmanuel College, Boston, Mass., June 1975.
- Holeman, E., A. F. Davis, and M. P. Hagan, Analysis of data from research satellites, *Final Rep. AFGL-TR-78-0187*, Air Force Geophys. Lab., Bedford, Mass., July 1978.
- Holeman, E., D. R. Parsignault, M. P. Hagan, and R. C. Filz, Proton fluxes (0.08-100 MeV) as measured by the Air Force Satellites S3-2 and S3-3, *AFGL Rep.*, contract F19628-79-C-0102, Air Force Geophys. Lab., Bedford, Mass., in press, 1981.
- Mayaud, P. N., and A. Romana, Supplementary geomagnetic data 1957-1975, *IAGA Bull.*, 39, pages, 1977.
- Mellwain, C. E., Redistribution of trapped protons during a magnetic storm, *Space Res.*, 4, 374, 1965.
- Morel, P. R., and B. Sellers, Design and fabrication of a heavy particle identification instrument for satellite, *R&D Equipment Information Rep.*, Contract F19628-69-C-0234, Panametrics, Inc., Waltham, Mass., December 1972.
- Morel, P. R., F. A. Hanser, and B. Sellers, A satellite telescope for protons and alphas, *Final Rep. AFCRL-TR-74-0531*, Panametrics, Inc., Waltham, Mass., November 1974.
- Naugle, J. E., and D. A. Kniffen, Flux and energy spectra of protons in the inner Van Allen Belt, *Phys. Rev. Lett.*, 7, 3, 1961.
- Naugle, J. E., and D. A. Kniffen, Variations of the proton energy spectrum with position in the inner Van Allen belt, *J. Geophys. Res.*, 68, 4065-4078, 1963.

(Received February 18, 1981;
revised May 5, 1981;
accepted June 5, 1981.)

END

FILMED

1-83

DTIC